PHENIX

Technical Design Report of the Forward Silicon Vertex Tracker (FVTX)

6 November 2007

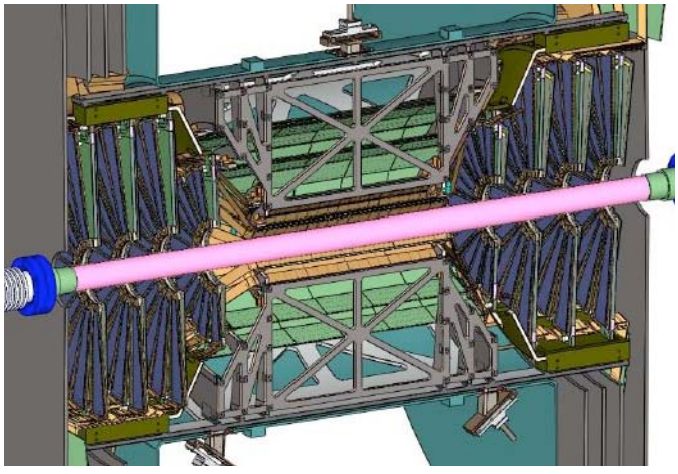

Proposal for a Forward Silicon Vertex Tracker (FVTX) for the PHENIX Experiment

R. K. Choudhury, P. Shukla, D. Dutta, A. K. Mohanty
Bhabba Atomic Research Centre, Mumbai, India

R. Pak
Brookhaven National Laboratory, Physics Dept., Upton NY USA

K.A. Drees
Brookhaven National Laboratory, Collider Accelerator Dept., Upton NY USA

H. Pereira
CEA Saclay, Gif-sur-Yvette, France

M. Finger Jr., M. Finger, M. Slunecka
Charles University, Prague, Czech Republic

M. Virius
Czech Technical University, Prague, Czech Republic

P. Freundlich, J. Popule, L. Tomasek, M. Tomasek, V. Vrba
Institute of Physics, Academy of Sciences, Prague, Czech Republic

B. Cole, E. Mannel, D. Winter, W. Zajc
Columbia University, NewYork, NY

J.C. Hill, J.G. Lajoie, C.A. Ogilvie, A. Lebedev, H. Pei, G.Skank,
A. Semenov, G. Sleege, F. Wei
Iowa State University, Ames, IA 56011, USA

Naohito Saito
High Energy Accelerator Research Organization (KEK), Tsukuba, Japan

T. Murakami, K. Tanida
Kyoto University, Kyoto 606, Japan

J.G. Boissevain, M.L. Brooks, S. Butsyk, C. M. Camacho, G. Grim, H.W. van Hecke, J. Kapustinsky, A. Klein, G.J. Kunde, D.M. Lee, M.J. Leitch, H. Liu, M.X. Liu, P.L. McGaughey, A.K. Purwar, W.E. Sondheim
Los Alamos National Laboratory, Los Alamos, NM 87545, USA

Hisham Albataineh, G. Kyle, V. Papavassiliou, S. Pate, X.R. Wang
New Mexico State University, Las Cruces, NM, USA

T. Alho, M. Bondila, R. Diaz, D. J. Kim, J. Rak,
University of Jyvaskyla, Finland

B. Bassalleck, D.E. Fields, M. Hoeferkamp, M. Malik, J. Turner
University of New Mexico, Albuquerque, NM, USA

J.H. Kang, Y. Kweon
Yonsei University, Seoul, Korea

Other Interested Institutions:

A.D. Frawley
Florida State University, Tallahassee, FL 32306, USA

B. Hong
Korea University, Seoul, Korea

List of Figures

List of Tables

1 Executive Summary

The main goal of the RHIC heavy ion program is the discovery of the novel ultra-hot high-density state of matter predicted by the fundamental theory of strong interactions and created in collisions of heavy nuclei, the Quark-Gluon Plasma (QGP). From measurements of the large elliptic flow of light mesons and baryons and their large suppression at high transverse momentum p_T that have been made at RHIC, there is evidence that new degrees of freedom, characteristic of a deconfined QCD medium, drive the dynamics of nucleus-nucleus collisions. It has been recognized, however, that the potential of light quarks and gluons to characterize the properties of the QGP medium is limited and the next phase of the RHIC program calls for the precise determination of its density, temperature, opacity and viscosity using qualitatively new probes, such as heavy quarks. We propose the construction of two Forward Silicon Vertex Trackers (FVTX) for the PHENIX experiment that will directly identify and distinguish charm and beauty decays within the acceptance of the muon spectrometers. The FVTX will provide this essential coverage over a range of forward and backward rapidities ($1.2 < |y| < 2.4$) – a rapidity range coverage which not only brings significantly larger acceptance to PHENIX but which is critical for separating cold nuclear matter effects from QGP effects and is critical for measuring the proton spin contributions over a significant fraction of the kinematic range of interest. In addition, the FVTX will provide greatly reduced background and improved mass resolution for dimuon events, culminating in the first measurements of the ψ' and Drell-Yan at RHIC. These same heavy flavor and dimuon measurements in p+p collisions will allow us to place significant constraints on the gluon and sea quark contributions to the proton's spin and to make fundamentally new tests of the Sivers function universality.

Current results from single non-photonic electron suppression and flow suggest that the heavy quark quenching and thermalization and flow are very large and present the biggest puzzle so far to heavy ion theory[xii]. An explosion of theoretical activity in the past couple of years has aimed at understanding the interaction mechanisms of heavy quarks in the plasma[x,xiv,xv.] Advances have been made in understanding the collisional component to parton energy loss in addition to the radiative one. Moreover, novel heavy flavor suppression mechanisms based on heavy flavor dissociation in the QGP have been proposed and shown to be very successful in describing the quenching of the non-photonic electrons and it has been argued that insight from string theory might be useful in understanding the properties of strongly coupled systems[xvii]. It is widely recognized in the theoretical and experimental communities that a breakthrough in this area requires direct and separate measurements of the charm and beauty meson quenching and flow with excellent precision. With the baseline PHENIX detector, these questions cannot be addressed because the heavy flavor measurements have very large systematic error bars due to large backgrounds and there is no capability for separating charm and bottom; therefore, the various model predictions cannot be separated from each other. The FVTX detector will provide precisely this experimental capability to answer the call of the theoretical community, provide the definitive determination of the heavy flavor modification mechanism in the QGP and quantitatively pinpoint its properties.

The FVTX detectors will address these questions, and many more that we will outline, and will extend the vertex capabilities of the PHENIX Silicon Vertex Tracker (VTX) to cover a much

larger rapidity interval, including forward and backward rapidities, and allow displaced track and secondary vertex measurements in conjunction with the PHENIX muon arms. The heavy flavor measurements provided by these detectors will move us from making qualitative statements that heavy flavor is suppressed in heavy ion collisions to being able to distinguish among models which include radiative energy loss, collisional energy loss, and/or collisional dissociation for light and heavy quarks—a distinction which is not possible without the addition of a vertex detector, and without which there remains large uncertainty in what the various suppression mechanisms are for light and heavy quarks and what the extracted properties of the medium should be. By adding vertexing capability covering the muon arms we not only increase the acceptance for physics observables by a factor of 3-10 but also allow coverage in the forward rapidity regions – coverage which is critical to separate cold nuclear matter effects from QGP effects, and critical for understanding the geometric extent of the medium.

J/ψ vector mesons are also considered to be a very sensitive probe of the dense matter created in heavy ion collisions and have been shown to be highly suppressed at RHIC[xxii]. At SPS the suppression of J/ψ production was one of the measurements given to support the statement that a new state of matter (the QGP) was formed[i], so the RHIC J/ψ results have been highly anticipated and are of great interest to the heavy-ion community. The baseline PHENIX detector was designed to provide good measurements of inclusive J/ψ production; however, to quantitatively understand the modification of J/ψ production in the medium, these measurements must be coupled with precise open heavy flavor measurements that can be used with recombination models to determine the contribution to J/ψ production that comes from random c and cbar pairs combining to form J/ψs as opposed to prompt J/ψ production. Since J/ψs produced by recombination have different kinematic distributions from prompt J/ψ production, and will *enhance* J/ψ production rather than suppress the production, the recombination contributions must be understood to extract the amount of medium-induced suppression. The FVTX will provide the needed precision open heavy flavor measurements to allow for a much better understanding of J/ψ production via recombination. Together with this, we need to measure production of other vector mesons such as ψ' and χ_c to understand Debye screening contributions. The different vector mesons have different screening radii, so measuring the difference in their suppression patterns allows one to infer the radius at which Debye screening becomes significant. Additionally, the ψ' and χ_c contribute to J/ψ production via feed-down, so measuring their suppression pattern allows one to understand how much of the J/ψ suppression is inherited from ψ', χ_c suppression and how much is suppression of prompt J/ψ production. With the addition of the FVTX detector, we will be able to separate the ψ' and J/ψ production through improved mass resolution and enhanced background rejection. These new measurements, coupled with the J/ψ measurements should significantly advance our understanding of J/ψ suppression in heavy ion collisions.

The RHIC spin program was developed to determine the gluon and sea quark contributions to the proton's spin and (possibly) put constraints on the angular momentum contributions to the spin. With the addition of the FVTX detectors, we will significantly extend the x coverage for gluon spin measurements in PHENIX by adding precision heavy flavor asymmetry measurements at forward and backward rapidities which are sensitive to the gluon spin distribution. These measurements cannot be made with the baseline detector alone. Measuring the gluon spin

distributions over a large x coverage is critical for extracting $\Delta G = \int \Delta G(x)dx$. The FVTX detector will provide precise Drell-Yan measurements (in conjunction with the muon arms), which will allow measurements of sea quark contributions to the proton's spin because the Drell-Yan production asymmetry is sensitive to the ubar polarization. This provides us a unique opportunity to produce a sea quark measurement which is complimentary to the W measurements that are proposed. The FVTX will also provide unique track reconstruction constraints which will help reject hadronic backgrounds which contribute to the single muon spectra. The single muon spectra will be used to measure sea quark contributions to the proton spin by extracting the $W \rightarrow \mu X$ single spin asymmetry at high p_T so background rejection at high p_T is essential to making a precision measurement.

The Drell-Yan measurements with polarized proton beams will also allow for a new fundamental test of QCD theory. Sivers-type single-spin asymmetry has been observed in semi-inclusive DIS at HERMES and COMPASS very recently[ii,iii]. A fundamental prediction of QCD is that such effects will give an opposite sign in the transverse single spin asymmetry in DY production in p+p collisions[iv]. Its verification (or not) will be an important milestone in our study of the strong interaction, as it tests all concepts for analyzing hard-scattering reactions that we know of today.

The FVTX detectors, covering forward and backward rapidities ($1.2 < |y| < 2.4$) are ideally suited to study the fundamental QCD interactions in d+A collisions at RHIC. Light hadron results indicate that the suppression pattern observed at forward rapidity is suggestive of nuclear shadowing or saturation physics at small values of Bjorken-x. It has been found, however, that such attenuation is not consistent with the measured shadowing in the nuclear structure functions in DIS[v,xxx]. Preliminary measurements have instigated recent theoretical activity which suggests that the physics of d+A collisions is much more complex[vi]. Nuclear effects that potentially play a role are the Cronin effect, cold nuclear matter energy loss (stopping power of large nuclei) and dynamical shadowing from coherent multiple scattering. The FVTX upgrades will help open new physics channels for precision measurements, such as the Drell-Yan process, where initial- and final state-effects can be separately investigated.

In addition, the FVTX detectors will provide moderate rapidity gap correlation measurements (when combined with the midrapidity PHENIX detectors) and large rapidity gap (when the forward and backward FVTX are used) for studying di-jet correlations. It has been argued in the framework of CGC phenomenology that the dominant particle production mechanism in d+A reactions is 2-to-1 processes, such as gluon fusion and quark scattering on a background gluon field. In contrast, the lowest order process in collinear factorized pQCD is 2-to-2 scattering which would produce a clear di-jet signal. Therefore, to validate or disprove theoretical models of jet production in d+A collisions jet-jet correlation measurements, including heavy quark triggered jets, are of critical importance.

With the present PHENIX detector, heavy-quark production in the forward and backward directions has been measured indirectly via the observation of single muons. The current measurements are inherently limited in accuracy by systematic uncertainties resulting from the large contributions to the single muon spectra from prompt pion and kaon semi-leptonic decays and from pion and kaons which punch through the entire muon system and are mistakenly tagged

as muons. In addition, the analysis does not allow for a model-independent separation of the charm and bottom contributions. The FVTX detector will provide vertex tracking with a distance of closest approach (DCA) resolution in r-z that is better than 100 μm over a large coverage in rapidity ($1.2 < |\eta| < 2.2$) and with full azimuthal coverage. This will allow for vertex cuts which separate prompt particles from decay particles and short-lived heavy quark mesons from long-lived light mesons (pions and kaons). In addition, bottom measurements can be made directly via $B \rightarrow J/\psi+X$ by looking for a displaced J/ψ vertex, and this will allow charm and bottom contributions to be separated in semi-inclusive single lepton measurements. Therefore, with this device fundamentally new measurements can be made and current muon measurements will be significantly enhanced.

The precision of the J/ψ and other dimuon measurements in AuAu collisions is currently limited by the large amount of combinatorial background that must be subtracted from the opposite sign dimuon signal obtained with the muon tracker and by the inherent mass resolution. With added rejection power for pion and kaon decays, the significance of all dimuon measurements will be greatly improved. Further improvement in these measurements results from the improved mass resolution, which will be attained because of the more accurate determination of the opening angles of the dimuons. All together, this will result in improved dimuon data as well as provide access to several new measurements: separation of ψ' from J/ψ, extraction of a Drell-Yan signal from the dimuon continuum, extraction of $B \rightarrow J/\psi$ and measurement of upsilons at central rapidity.

The FVTX adds several additional enhancements to PHENIX:

- Enhances tracking resolution for tracks passing through the muon system by adding measurement points close to the vertex
- Provides a fast data path for a Level-1 FVTX trigger
- Helps with electron/photon separation for the Nose Cone Calorimeter
- Improves event vertex location determination for triggering and offline analyses
- Gives an event topology cut capability for heavy quarks
- Provides unique track cuts which allow rejection of hadronic backgrounds in the single muon spectra
- Provides reaction plane measurement.

As a result of this proposed upgrade, numerous areas of physics exploration will become accessible, as summarized here in three broad classes associated with the type of collision:

- A+A collisions and the Quark Gluon Plasma:
    - Study of energy loss and flow of heavy quarks into very forward and backward rapidity regions using robust charm and bottom measurements over a broader x range than available with the barrel VTX detector alone and with greater precision than is possible with the muon detectors alone. This allows the extension of studies of the geometrical and dynamical effects of the hot-dense matter created in high-energy heavy ion collisions into the forward and backward rapidity regions and will allow for the first time separate measurements for charm and bottom.

- Precise open charm and bottom measurements will provide a solid "denominator" for comparison with production of bound states of heavy quarks (J/ψ and ϒ). These comparisons will allow for the isolation of common physics, e.g., initial-state effects such as those on the gluon structure function and physics that only affects the bound states, e.g., final-state absorption. These measurements will also provide strong constraints on production of J/ψs from recombination by determining a precise open-charm cross section over a broad rapidity range.
- Direct measurement of ϒs at mid-rapidity will be possible by eliminating the large random backgrounds from light-meson decays. Will also improve the mass resolution and signal/background for J/ψ production and enable improved separation of the J/ψ from the ψ'.
- Unambiguous measurement of the Drell-Yan and heavy-flavor dimuon continuum by separating background muons from light meson decays, muons from heavy flavor decay and prompt muons.
- An accurate reaction plane measurement will be provided by the FVTX.
- Flow in the forward and backward regions will be able to be measured.

- p(d)+A collisions and small-x or gluon saturation physics:

  - The study of the gluon structure function modification in nuclei at small (and large) *x* values, where gluon saturation or shadowing (anti-shadowing) is thought to be important will be possible, by adding precision open charm and bottom measurements at forward rapidity.
  - Determine the initial state for AA collisions and provide a robust baseline for cold-nuclear matter effects in studies of hot-dense matter in heavy ion collisions, again by adding precision heavy flavor measurements at forward rapidity.
  - Help untangle the intricate physics of J/ψ and ϒ production in cold nuclear matter by providing robust measurements of open-heavy quark production that can, by contrast, separate initial and final-state physics for these resonances.
  - Allow for a clean measurement of Drell-Yan which can further help untangle production issues for the J/ψ.

- Polarized p+p collisions, and the contributions to the spin of the nucleon:

  - Provide an increased x range (up to $x \approx 0.2$ and down to 10^{-3}) over which the mostly unknown gluon polarization ($\Delta G/G$) can be determined through open heavy flavor measurements. Without the FVTX the range covered is likely to be insufficient to study the shape of any polarization or to determine its peak value.
  - Allow for a direct measurement of the spin asymmetry in bottom production, which is expected to be different from open charm and light hadrons, thus providing much-needed cross checks.
  - Add background rejection capabilities for W and Z bosons measurements (which give information about the sea-quark contributions to the spin) by rejecting muons from light and heavy hadron decays which contribute to the high p_T muon spectra and by adding the possibility of event topology cuts.

- Enable Drell-Yan asymmetry measurements, which can give information about the sea quark polarization distributions.

The FVTX will be composed of two endcaps, with four silicon mini-strip planes each, covering angles ($1.2 < |\eta| < 2.2$) that match the two muon arms. Each silicon plane consists of wedges of mini-strips with 75 μm pitch in the radial direction and 3.75° wide strips in phi, which translates to lengths in the phi direction varying from 2.8 mm at small angles to 12.1 mm at 35 degrees. An r-z DCA resolution of 100 μm can be achieved with a maximum occupancy per strip in central Au+Au collisions of less than 2.8%. A picture of the detector is shown in Figure 1. The four stations of the North and South FVTX arms are circled in red, the central support structure for the VTX system can be seen between the two, and the large gray planes surrounding the FVTX sensors are the planes that will hold the readout electronics for the VTX and FVTX systems.

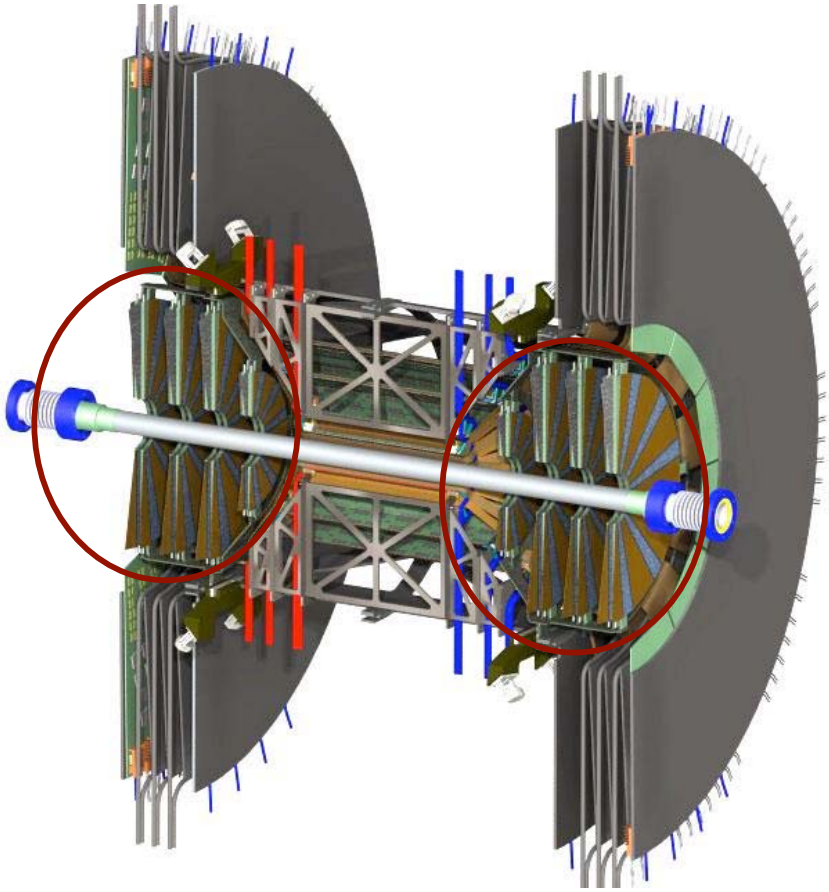

Figure 1 Conceptual layout of the PHENIX FVTX showing the four vertical planes of each endcap in the red circles.

The FVTX will consist of approximately 1.1 million mini-strips that will be read out with an IC chip (FPHX) to be designed by Fermilab, which is wire-bonded directly to the mini-strips. This chip will provide analog and digital processing with zero-suppression and produces a digital output which is "data-pushed" at 200 Mbps to intelligent readout boards containing FPGAs. The data are then transformed into the standard PHENIX format and transmitted to the PHENIX

DAQ system via fiber optics. In parallel, a fast "level-1" trigger algorithm can be run on the data to select interesting heavy-quark events.

The FPHX is a custom IC being designed by engineers in the Fermi National Accelerator Laboratory Particle Physics Division. The chip design borrows heavily from previously successful IC designs, FPIX2, FSSR, SVX4, etc. Standard p-on-n silicon strip technology, which has been the baseline detector technology for dozens of silicon trackers in Nuclear and High Energy physics experiments, will be used for the FVTX mini-strips sensors.

A collaboration of 16 institutions with approximately 60 physicists and engineers has been formed to carry out this project. The collaboration brings expertise in silicon vertex detectors from the FNAL E866, SSC, L3, Atlas and BTeV experiments together with general experience on construction and operation of large detector subsystems such as the PHENIX muon arms. Members of the collaboration come with extensive experience in heavy-quark and J/ψ physics, small-x nuclear effects, gluon structure functions and polarization, various other physics projects with muons, and expertise in simulations and analysis to support those measurements.

With the help of an LDRD Exploratory Research (ER) grant from LANL during FY02-FY04 we were able to develop a conceptual design of the FVTX and to settle many of the R&D issues necessary to advance to a full proposal. A new LDRD Directed Research (DR) project at LANL (FY06-FY08) will produce a small prototype detector covering approximately 1/8 of one muon arm, to be installed in the RHIC beam at the same time as the barrel pixel detector. As part of this effort we will advance the R&D for the FVTX by fully designing the interface electronics that connects the FPHX read-out chip to the PHENIX Data Collection Modules (DCMs) so that it will seamlessly provide data to the existing PHENIX DAQ. In addition, the LDRD DR project will support part of the design of the cooling system and support structure. Other experience relevant to the full detector will be obtained, such as measurements of single muon rates and noise. We will not describe further details of this effort here, but they are available on our LDRD-DR part of the FVTX web page[vii] and in the proposal listed there.

We request that the full project be funded by the DOE Office of Nuclear Physics at a total cost of $4.68M ($3.72M + 26% contingency in at-year dollars). Construction of the full FVTX detector should proceed starting in early FY08 on a time scale that will allow it to be completed and begin commissioning by the end of FY10.

A preliminary management plan of the FVTX detector project, which also discusses the roles and expected responsibilities of the participating institutions, is included in this document.

The proposal has the following structure:

- The physics motivation for the upgrade and the simulated physics performance is given in Section 2
- The general detector simulations and its performance is documented in Section 3.
- Section 4 gives a detailed description of the forward vertex tracker and the technical aspects of the proposed project.
- Section 5 discusses our R&D plan.

- A draft of our management plan, section 6, specifies deliverables and institutional responsibilities.
- Section 7 lays out the budget request and the proposed schedule.

2 Physics Goals of the FVTX Endcap Upgrade

In this section we outline the physics goals of the FVTX detector and present the physics performance of the trackers related to these goals.

The PHENIX Forward Vertex Detector (FVTX) endcaps complement the barrel vertex detector (VTX) already being built for PHENIX by providing increased coverage in rapidity (two additional units of rapidity compared to about one), extending the sensitivity to gluon momentum fraction (x) up to x~0.2 and down to $x\sim10^{-3}$, providing a broad reach in transverse momentum, and allowing a larger portion of the dynamical geometry of the hot dense matter created in heavy ion collisions to be explored. Heavy-quark mesons and bound states of heavy-quarks (quarkonia) coming from bottom meson decay can be identified with the FVTX by their short detached vertices. The light-meson yields that ordinarily comprise most of the backgrounds to these measurements can be largely eliminated because of their large detached vertices. Prompt muons and kaons which punch through the muon system can be eliminated by their lack of a displaced vertex. Dimuon measurements of open charm, quarkonia and Drell-Yan signals can be improved by rejecting light meson decay particles which contribute to the background and by improving the opening angle resolution, and thus mass resolution of dimuons.

We will now discuss the main physics goals by starting with those that are important in heavy ion collisions, then those of interest in proton or deuteron nucleus collisions, and finally those that are probed in polarized proton collisions.

2.1 Heavy ion Collisions and the Quark Gluon Plasma

The main goal of the RHIC heavy ion program is the identification and study of the hot high-density matter created in heavy ion collisions, i.e. the Quark Gluon Plasma (QGP). The energy loss of fast quarks or gluons traversing this dense matter is very large, leading to the observed suppression of high transverse momentum light hadrons and nearly comparable suppression of electrons arising from non-photonic decays, presumably from heavy mesons. This, along with large elliptic flow, suppression of J/ψ, and other signatures observed by the RHIC experiments point to rapid thermalization, extremely high energy density, and partonic rather than hadronic interactions. The dense matter formed at RHIC apparently has the properties of a perfect liquid, rather than an ideal gas. However, the composition of this high-density matter, whether or not it is truly deconfined, and what the degrees of freedom are, are still unknown. Addressing these questions requires measurements over a larger kinematic reach, along with additional observables. The FVTX detector coupled with the muon detector systems will allow for precision measurements of open charm and bottom versus rapidity, p_T and reaction plane, much improved measurements of vector mesons (J/ψ, ψ', ϒ) as well as first measurements of dimuons from the Drell-Yan process in heavy ion collisions. It is hoped that these precision measurements will allow one to understand heavy quark energy loss and flow in heavy ion collisions, understand how prompt production and quark recombination contribute to

charmonium production, how initial-state and final-state interactions modify charmonium production, and provide important reference measurements by studying the Drell-Yan process.

2.1.1 Energy Loss and Flow of Heavy Quarks

One of the most significant physics results produced in the first several years of RHIC operations was the measurement of strong suppression of high-p_T light particle production in Au+Au collisions. This is illustrated by measurements with the PHENIX detector, shown in Figure 2 and Figure 3. Figure 2 shows the suppression factor for charged and neutral pion production in Au+Au and d+Au collisions, with respect to p+p collisions. The suppression factor for d+Au is typically greater than 1 while the suppression for Au+Au collisions is approximately 0.2, indicating that the large suppression seen in Au+Au collisions comes from final state interactions with the produced medium and is not due to initial state interactions or interactions within the Au nuclei. This statement is further supported by the data shown in Figure 3 where the light meson suppression factor for Au+Au collisions is shown compared to a direct photon measurement. The direct photons, which do not interact with the medium, show no suppression with respect to p+p collisions. The strong suppression observed for the light mesons is interpreted as energy loss of the outgoing particles or jets[viii,ix,x] in dense matter with densities up to 15 times normal nuclear matter inferred. This energy loss shifts the produced particle spectra to lower energy, effectively suppressing the production at a given p_T. These densities are much larger than what is needed to dissociate the nuclear matter into quarks and gluon.

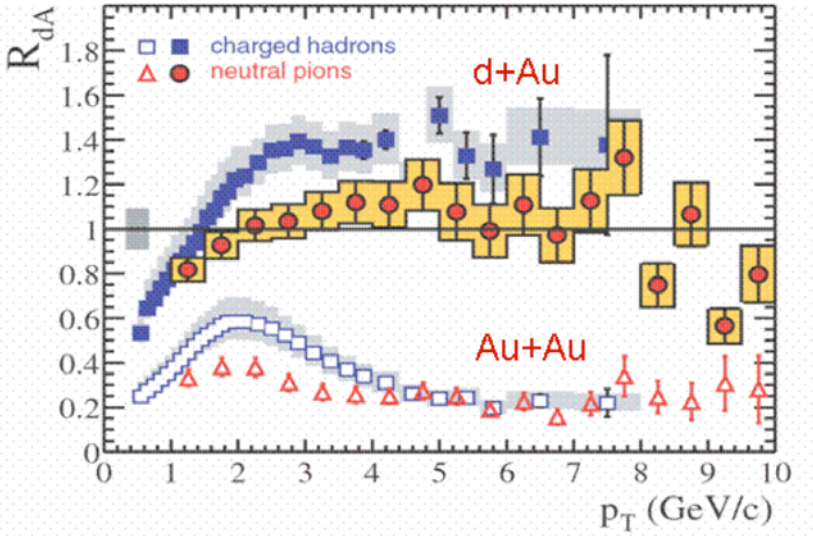

Figure 2 - Suppression of high-p_T hadrons and pions as seen in Au+Au vs d+Au collisions, measured by PHENIX and published in PRL.

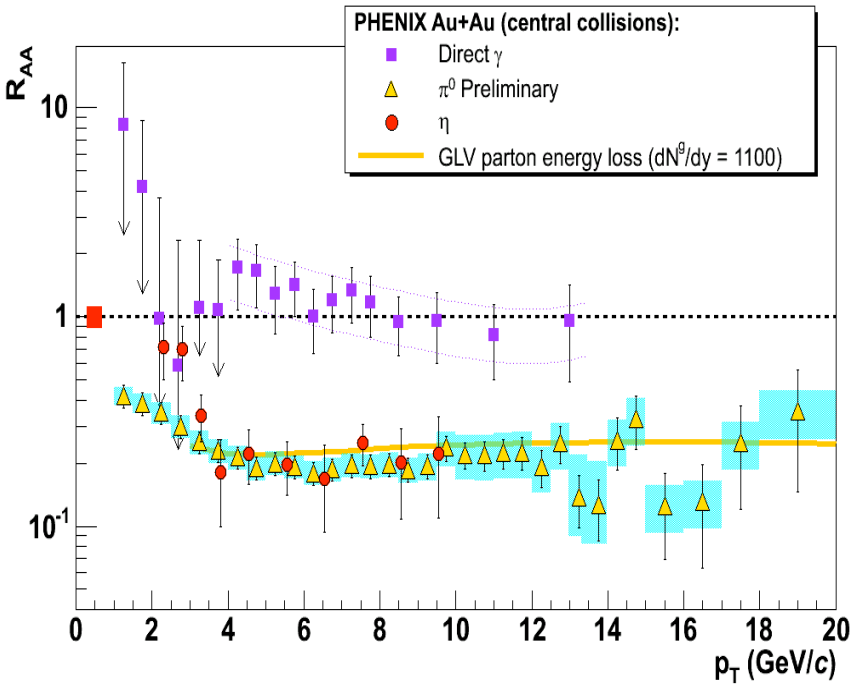

Figure 3 – High-p_T suppression of π^0's and η's – indicative of energy loss in large density matter; compared to no suppression of direct photons which indicates that the initial-state is not modified.

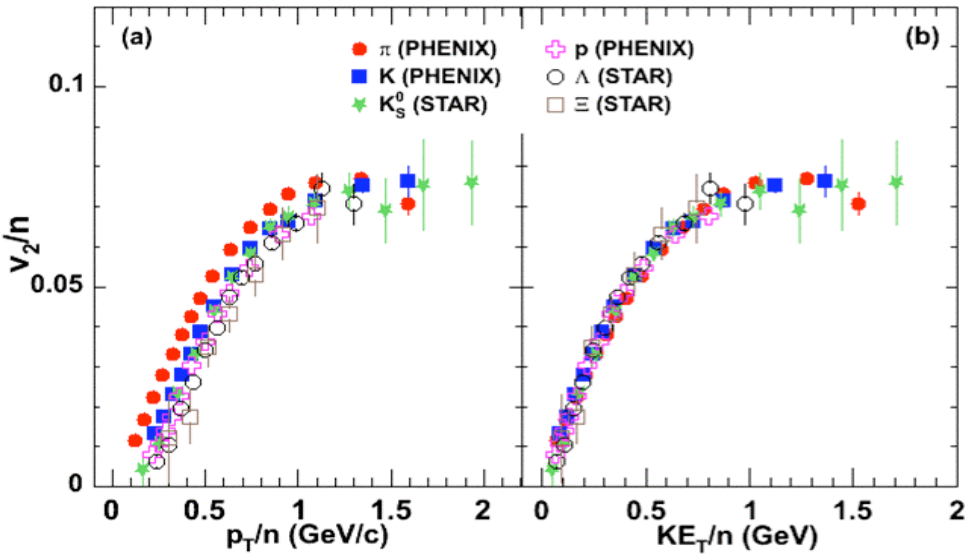

Figure 4 – The large elliptic flow for light hadrons in Au+Au collisions is near the hydrodynamic limit[xi] and scales with the number of valence quarks (n) in the observed hadron when plotted vs transverse kinetic energy (KE_T).

A large elliptical flow (momentum asymmetry with respect to the reaction plane) is also seen for the light hadrons as shown in Figure 4 and a universal behavior is seen when v_2 of the flow per

valence quark in the hadron that is observed is plotted versus transverse kinetic energy. The large flow indicates a strongly interacting medium is produced and thermalization is achieved relatively quickly. The scaling of the flow with the valence quarks indicates the flow is a reflection of partonic matter flow as opposed to hadronic flow.

More recent measurements of heavy flavor measured via single leptons at central rapidity[xii] indicate that heavy quarks (charm and bottom) also suffer substantial suppression (see top half of Figure 5 where a PHENIX measurement of the heavy flavor suppression factor is shown for Au+Au collisions). In the most recent measurements, they even appear to flow, though the flow measurements at high p_T are rather imprecise (see bottom half of Figure 5).

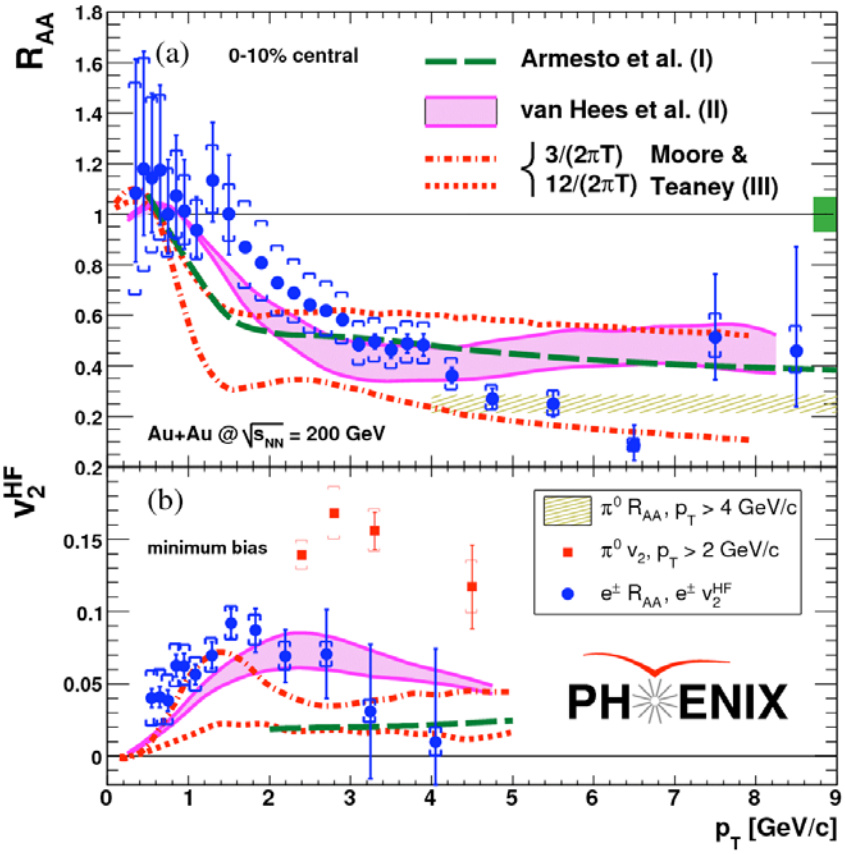

Figure 5 – Heavy quark suppression and flow vs p_T from PHENIX measurements using electrons in 200 GeV Au+Au collisions at mid rapidity[xii].

In all of these measurements large backgrounds coupled with the necessity to calculate non-heavy-quark contributions to the single lepton spectra and then statistically subtract these to isolate the heavy-quark component result in large systematic errors, severely limiting the accuracy of these measurements. In addition, once the heavy quark component is identified, there is still no clean way to separate the charm and bottom components of the resulting subtracted spectra. The FVTX detector will address both of these issues. Because of their higher mass, b quarks are expected to have substantially smaller energy loss and be much more difficult to thermalize and flow along with the medium. Consequently the large suppression of the electrons,

especially at high p_T where bottom contributions are expected to dominate, is quite mysterious. The expected reduction in flow appears consistent with the data, but the error bars at high p_T are too large to make any definitive statements about comparisons to models. What is really needed are much more precise measurements which include separation of D and B decay sources of single leptons.

The measurement of large suppression of heavy flavor production came as a surprise because a few years ago theoreticians predicted that heavy quarks would not lose much energy in the hot-dense matter due to the "dead-cone" effect[xiii] -- seemingly inconsistent with the recent results. This dead-cone effect refers to the reduction in phase space that is available for radiated gluons as you move to higher quark mass, thus resulting in less predicted radiative energy loss for heavy quarks than for light quarks. A number of different theoretical models now attempt to explain the unexpected large suppression of heavy quarks:

- Some studies suggest that the magnitude of the dead-cone[xiv,xv,xvi] may be similar between heavy quarks and light quarks, unlike the predictions in reference xiii, which would lead to an energy-loss for heavy quarks closer to that for light quarks..
- M. Djordjevic[11] suggests that collisional energy loss accounts for the extra suppression that is seen in the measurements. In this model, the charm suppression reaches approximately the levels of the measured inclusive heavy quark suppression and the bottom suppression would be much less than the charm suppression.
- A. Adil, I. Vitev [xvii] takes into account the formation time which is long for light quark mesons (relative to the lifetime of the medium) but short for heavy quark mesons. Because of the short lifetime, dissociation of the heavy quark mesons inside the medium is calculated to contribute to suppression of heavy meson production in addition to the heavy quark energy loss. In this model, the bottom component suffers less suppression than the charm component at low p_T, but the two become comparable at as low as 10 GeV.
- Cold nuclear matter (CNM) effects will provide additional suppression of heavy flavor production, especially at forward rapidity. A rapidity dependence measurement helps allow separation of CNM effects and dense medium effects since CNM.

The various suppression models also give different predictions for flow of heavy flavor mesons, as indicated in Figure 5. In general, models which predict larger suppression will also tend to predict larger flow because the suppression is larger perpendicular to the reaction plane (where it passes through more medium) than in the reaction plane (where less medium is traversed). This leads to an asymmetry in production which is reflected in a v_2 measurement. The combination of precision flow and R_{AA} measurements, along with separation of charm and bottom components, should allow us to clearly determine which among the different suppression mechanisms that have been proposed is correct.

The predictions of these models for charm plus bottom production, relative to p+p production, are indicated in Figure 6 and will be described in the next section. To distinguish among these various models higher precision measurements of heavy quark production are required to compare quantitatively the amount of suppression seen in Au+Au collisions compared to p+p

collisions, separation of charm and bottom will allow the collisional energy loss and formation time models to be clearly distinguished, and a measurement across a large rapidity range further distinguishes the models and helps understand the cold nuclear matter effects. We will now show the heavy flavor measurement precision that we expect to obtain with the FVTX detector.

2.1.2 Charm and Bottom Measurements with the FVTX

The signal to background improvements in charm and bottom that are obtained with the FVTX and discussed in Section 3.4 can be used to determine the precision of an R_{AA} measurement of open charm and bottom using the FVTX detector.

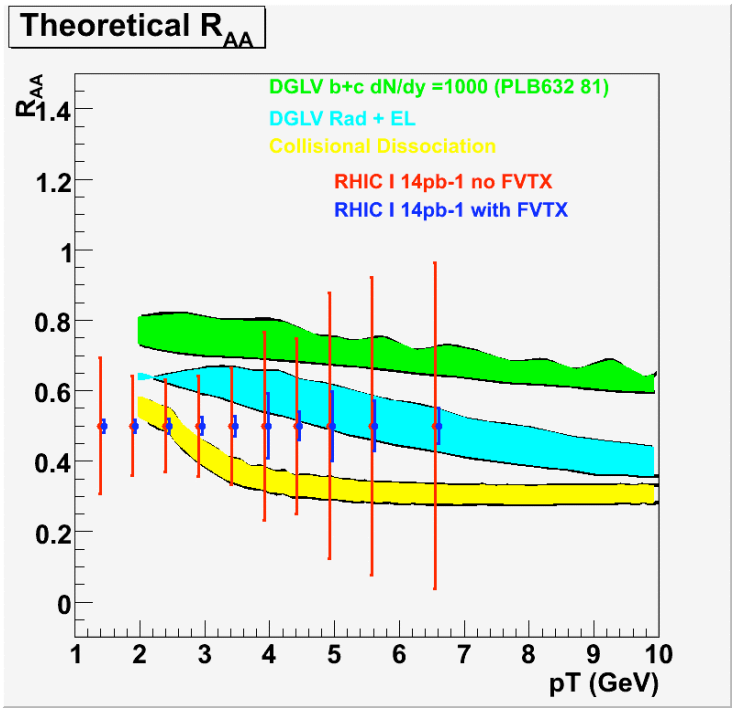

Figure 6 Heavy flavor R_{AA} measurement that can be achieved with RHIC Run 5 p+p statistics, with the FVTX detector (blue error bars) and without the FVTX detector (red error bars). Theory predictions which include radiative energy loss (green band), radiative energy loss plus elastic scattering energy loss (blue band) and radiative energy loss plus dissociation (yellow band) are shown for comparison.

The resulting predicted measurement capabilities are shown in Figure 6. The red error bars indicate the measurement precision that can be obtained without the FVTX detector, using RHIC Run 5 p+p statistics and the blue error bars indicate the precision that can be obtained with the same integrated luminosity run but using the FVTX in the analysis. Also shown are theory predictions which include radiative energy loss (green band), radiative energy loss plus elastic scattering energy loss (blue band) and radiative energy loss plus dissociation (yellow band).

2.1.3 Separating Charm and Bottom

There are a few possible methods for separating charm and bottom production using the FVTX system:

- Since bottom mesons have a larger lifetime than charm mesons (especially the D^0), and the decay muons are typically produced at a larger angle with respect to the parent meson, it is possible to separate the charm and bottom in single muons from semi-leptonic decays by placing a p_T dependent cut on the DCA of the tracks.

- The topology of B events is somewhat different from D events, and will be shown in section 3 later. Both the multiplicity and physical size of a heavy quark jet is different for B and D events. Selective kinematic cuts may greatly enhance the B signal from muons with respect to the D signal from muons (or vice versa).

- The decay channel $B \rightarrow J/\psi+X$ produces J/ψs that are displaced from the collision point by about one mm in Z. The FVTX can separate these from the prompt J/ψ and thus provide a direct B measurement channel..

- When the dimuons are tagged to come from a displaced vertex, bottom dominates the like-sign dimuon production.

2.1.3.1 Separating Charm and Bottom by Distance of Closest Approach (DCA) and p_T

Figure 7 shows the sigma of the distance of closest approach of the lepton track for simulated distributions of prompt particles (black), muons from D decay (blue), muons from B decay (red) and muons from π/K decay (green). As seen, the B decay muons have systematically larger DCAs than the D decay muons. Therefore, we hope to use a cut on DCA to help enhance heavy quark muons in the single muon spectra from the light quark muons.

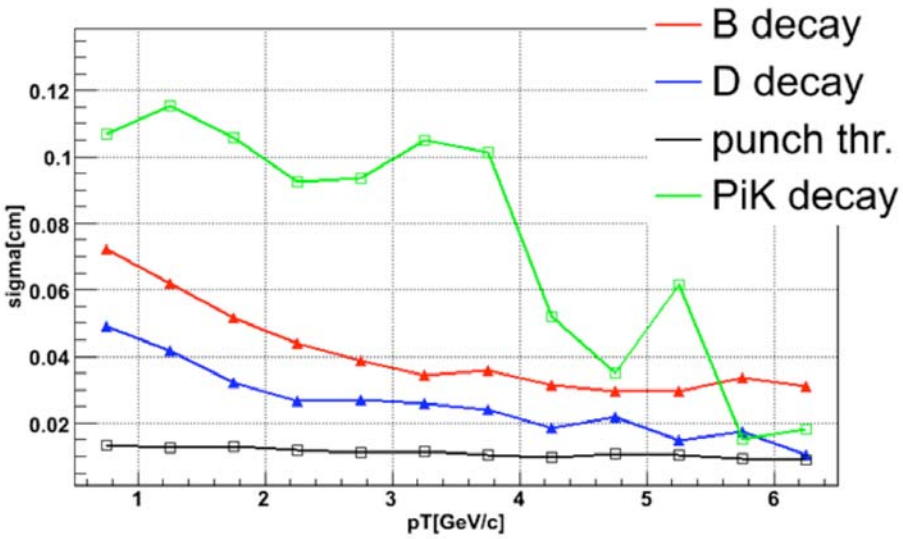

Figure 7 – The DCA for semi-leptonic decays of charm (blue) and bottom (red), light meson decays (green), and prompt punch-through hadrons (black).

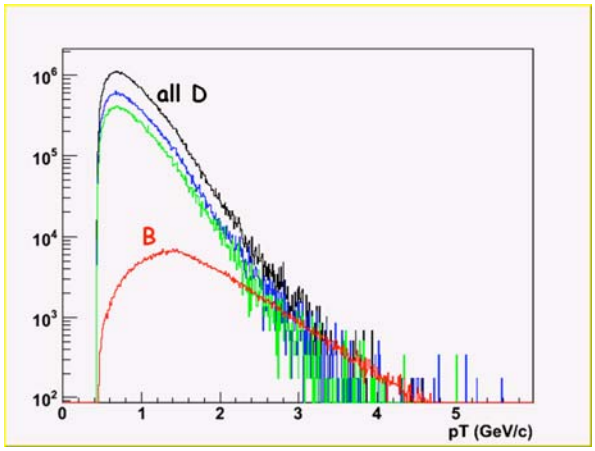

Figure 8 – Transverse momentum spectrum for charm and bottom decays. The different colored curves show the spectra for muons from Bs (red) charged Ds (green) and neutral Ds(blue).

Figure 8 shows the p_T spectra for muons from D decays (black) and muons from B decays (red), produced by PYTHIA and accepted into the muon arms. Although there is currently uncertainty in the relative cross sections of charm and bottom at RHIC energies, you can see that at low enough momentum the D decay muons will dominate and at high enough momentum the B decays will dominate. This can be used as a crude tool to separate Ds and Bs and/or as a way to check whether cuts are correctly separating the two contributions. See section 3.4 for more on this possibility.

2.1.3.2 Separating Charm and Bottom by Event Topology Cuts

Because of the larger mass of the B mesons with respect to the D mesons, the decay muon that comes from a B typically has a larger p_T with respect to the original meson than the decay muon that comes from the original D meson. This is illustrated in Figure 9 where the p_T spectrum of the decay muon with respect to the parent meson is shown for B muons and D muons. The two spectra have been normalized to each other to take into account the cross sections and branching ratios for each process. If we can effectively measure the momentum vector of the jets, by measuring the average vector of all the charged particles from the jet in the FVTX detector, we can then measure the decay muon with respect to the meson and we may be able to place a cut on the muon that would enhance the B signal in single muons relative to the D signal, or vice versa.

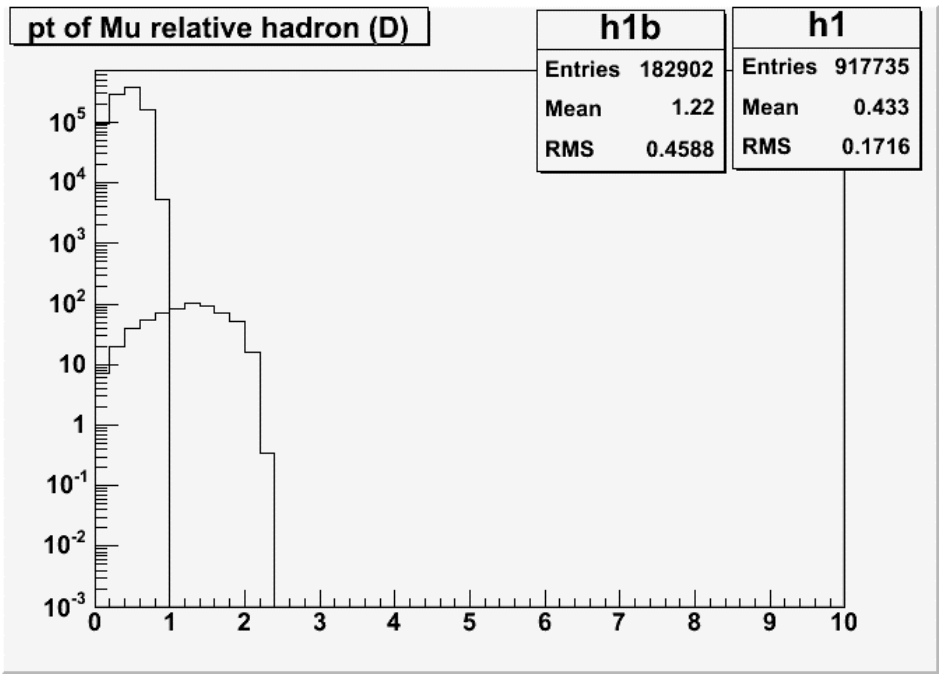

Figure 9 The p_T of the decay muon from D mesons (lower average value) and from B mesons (larger average value) is shown, properly normalized by their respective cross section and branching ratios.

2.1.3.3 Displaced Vertex for B Meson Decays: $B \to J/\psi \to \mu^+\mu^-$, $B \to \mu X$

Bottom measurements can be made directly by reconstructing B→J/ψ→$\mu^+\mu^-$. With the FVTX detector, J/ψs from B decay can be tagged by measuring the displaced vertex.

We simulated our performance for this direct bottom measurement by using PYTHIA to simulate B decays and tracking the decay muons through the silicon and muon spectrometers using PISA. The B→J/ψ decay muons have an impact resolution with respect to the displaced vertex of ~55 μm, better than single muons from D decays, due to their larger average momentum. The muon pair z-vertex resolution of the prompt J/ψ is ~133 μm, while the mean decay length is ~1.1mm, and this is indicated in Figure 10 where the reconstructed Z-vertex distribution for the J/ψ from B decays and prompt J/ψ (scaled down by a factor of 100) are shown. With a downstream pair z-vertex cut of 1 mm, we found 39% of the B decays are retained, while the prompt J/ψ are attenuated by a factor of 2×10^{-4}, leaving a sample which is dominated by B→J/ψ.

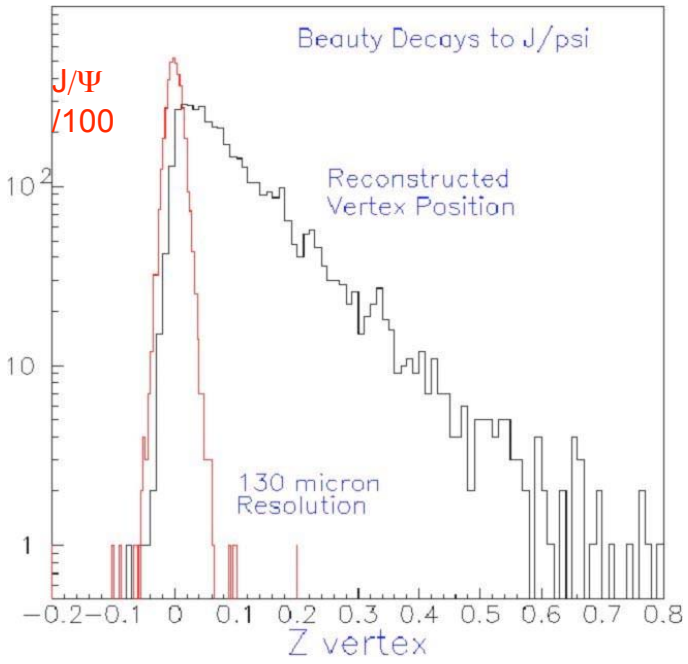

Figure 10 - The reconstructed Z-vertex distribution for J/ψ from B decays (black line) and for prompt J/ψ (red line). Note that the prompt J/ψ yield has been scaled down by a factor of 100. The relative yield of J/ψ from B decays versus prompt J/ψ is estimated to be about 1%.

The rates of bottom from single muons and of B→J/ψ events have been calculated using the following assumptions. We have assumed a total $b\bar{b}$ cross-section of 2 μb and 4 μb for J/ψ production. The branching ratio (BR) of 1.09% for B→J/ψ+X has been previously measured. The total acceptance for these events into one Si Endcap is ~ 4.6%. Assuming an integrated RHIC-II p-p luminosity per week of 33 pb^{-1}, about 650 B→J/ψ+X events would be reconstructed after the application of a 1 mm vertex cut. For $B \rightarrow \mu X$, the acceptance is ~4.5%. The corresponding yield is ~880,000 reconstructed events over the acceptance of the muon and FVTX arms.. See rate details in Appendix C (Section 8). Thus, an excellent *B* measurement is possible.

2.1.4 Open Charm Enhancement

It has been predicted that open charm production could be enhanced in high-energy nucleus-nucleus collisions relative to the expectation from elementary collisions[xviii,xix,xx]. Heavy quarks are produced in different stages of a heavy ion reaction. In the early stage charm and bottom are formed in collisions of the incoming partons. The yield of this component is proportional to the product of the parton density distributions in the incoming nuclei (thus giving binary scaling). If the gluon density is high enough, a considerable amount of charm can be produced via fusion of energetic gluons in the pre-equilibrium stage before they are thermalized. Finally, if the initial temperature is above 500 MeV, thermal production of charm can be significant. The last two mechanisms (pre-equilibrium and thermal production) can enhance charm production relative to binary scaling of the initial parton+parton collisions. These are the same mechanisms originally proposed for strangeness enhancement, but in the case of charm may reveal more about the

critical, early partonic-matter stage of the reaction since the rate of heavy-quark production is expected to be negligible later when the energy density has decreased. In comparison, strangeness production is expected to continue even in the final hadronic stages of the reaction.

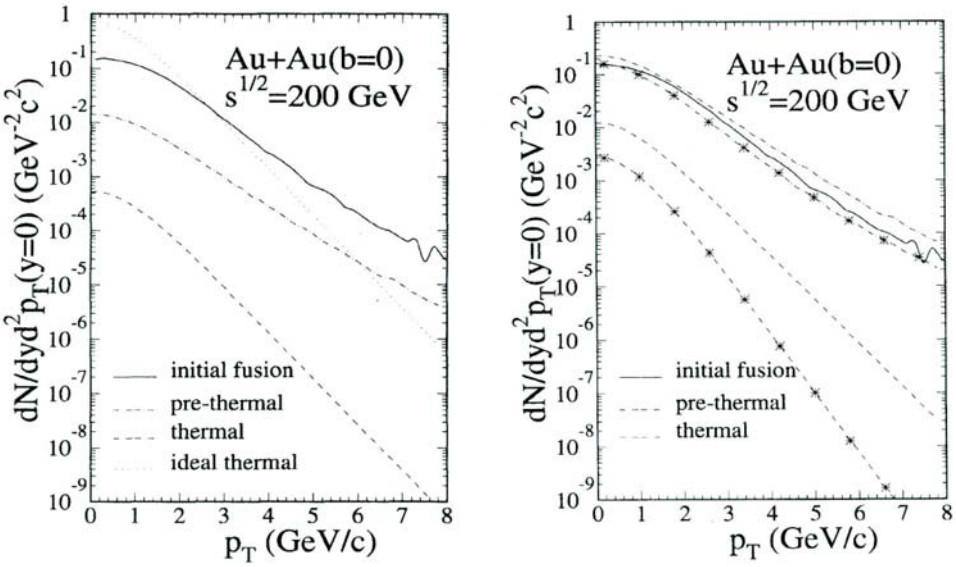

Figure 11 - Charm enhancement expected at RHIC from ref. xix. In both panels, contribution from the initial gluon fusion (solid), pre-thermal production (dot-dashed), and thermal production (dashed, lowest) are shown. The left panel is the calculation with energy density of 3.2 GeV/fm^3, while the right panel shows the case with energy density 4 times higher. The barely visible dotted curve in the left panel figure is the thermal production assuming an initially fully equilibrated QGP. In the right panel the curves with stars are the same as the corresponding curves without stars except that the initial temperature is reduced to 0.4 GeV (compared to 0.55 GeV).

At RHIC energies the anticipated enhancement is a small effect[xix,xx]. The contributions to charm production from various stages of a Au+Au collision are shown in Figure 11 (taken from reference xix). From the left panel of the figure it is evident that for an initial energy density of 3.2 GeV/fm^3 the pre-thermal or pre-equilibrium production contributes about 10% of total charm production, while the thermal contribution is negligible. However, the yield is very sensitive to the initial density, and with 4 times the energy density the pre-equilibrium contribution can be as large as the initial fusion. This is illustrated in the right panel of the figure. Present single electron measurements of PHENIX indicate that within ~25% systematic uncertainty charm production approximately scales with the number of binary collisions. Thus, charm enhancement, if it exists, cannot be a large effect. A measurement of the charm yield with substantially higher accuracy is therefore required to establish a potential charm enhancement.

The FVTX combined with the muon spectrometers will allow measurements of charm and bottom over a broader range in p_T. This will extend the single muon measurement to the p_T region near 0.5 GeV/c. Since more than half of the yield from charm decays is in this p_T region, this is essential for an accurate determination of the p_T integrated charm yield at forward and backward rapidities. Approximately one third of the total charm cross section is expected to come from the rapidity range measured by the FVTX, as shown in Figure 12. Combined with the central rapidity ($|y|<1.2$) measurement from the VTX detector, this will allow an accurate

measurement of the total charm cross section which then allows us to see a potential charm (or bottom) enhancement.

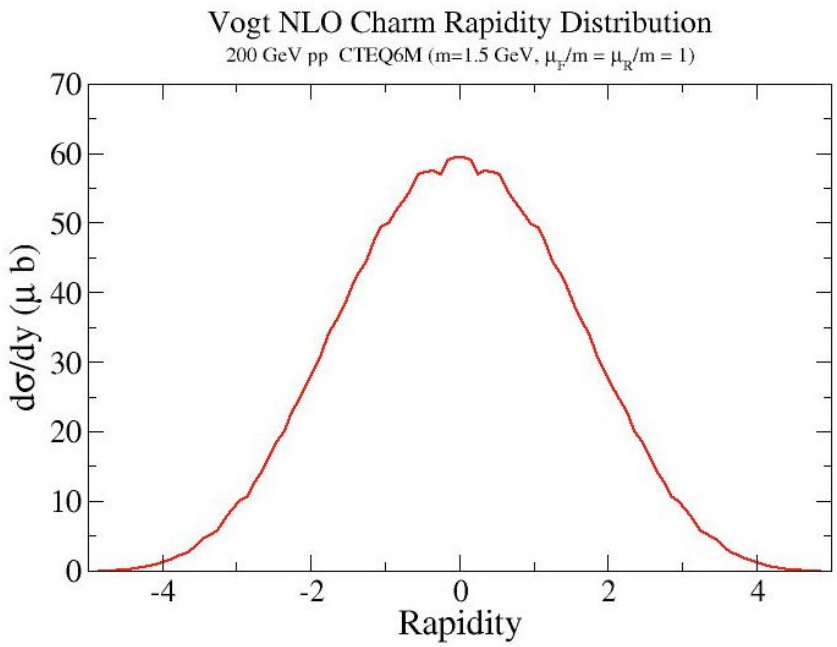

Figure 12 - Rapidity distribution from Vogt[xxi] for charm in pp collisions at √s = 200 GeV. One third of the total cross section comes from the region of the FVTX coverage, |y|>1.2

2.1.5 J/ψ Suppression and Comparisons with Open charm, ψ' and ϒ

J/ψ production in heavy ion collisions has long been considered a very sensitive probe of the quark gluon plasma. Its formation is expected to be suppressed because the c and cbar pair are screened from each other by the high density of quarks and gluons in the plasma and cannot form a bound state. However, the J/ψ production is a complicated process that is potentially modified at several stages of the collision process. J/ψ production can be modified in Au+Au collisions with respect to p+p collisions by changes in the gluon distribution functions in a nucleus compared to a nucleon (gluon-gluon fusion is a primary production mechanism for J/ψs so modified gluon distribution functions mean modified J/ψ production), energy loss of the composite charm quarks in the medium will modify the distribution of J/ψs that are produced, having additional contributions to the production from recombination (if the charm density is high enough) can *enhance* production, and one can have suppression due to the Debye screening mentioned above.

The most recent J/ψ measurements from PHENIX are shown in Figure 13, where one can see a large suppression at central rapidity (red points) and a substantial difference in suppression between mid and forward rapidity for the mid-central collisions.

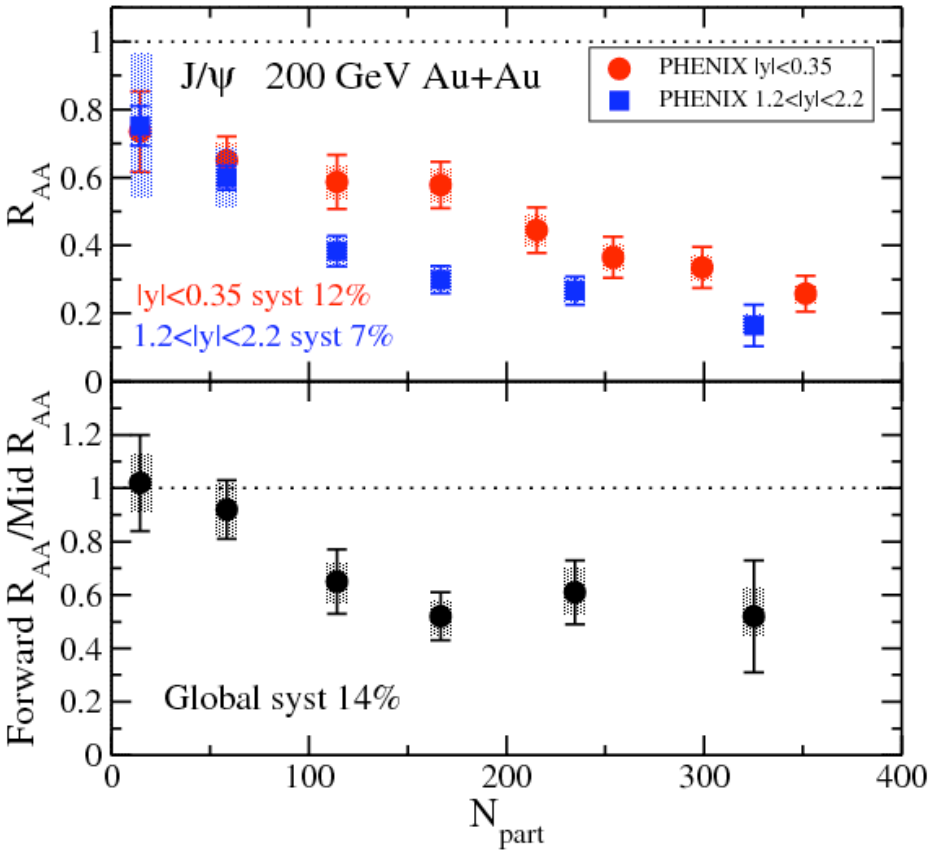

Figure 13 – J/ψ results for 200 GeV Au+Au collisions[xxii]. (a) (top) Nuclear modification factor for J/ψ at mid (red) and forward (blue) rapidity, and (b) (bottom) the ratio of these suppressions for forward/mid rapidity, all vs centrality in terms of the number of participants (N_{part}).

The suppression measured at central rapidity is similar to the amount of suppression measured at lower energies at the SPS, though many predictions expected the suppression to be larger at RHIC because of the higher density state that is achieved at RHIC energies. Recombination of c and cbar pairs would enhance production and may account for less suppression than expected at RHIC. This can, in principle, be checked by measuring p_T and rapidity distributions which are different for J/ψ from recombination than from prompt production, and by having precise open charm measurements so that we can estimate the contributions from recombination. The difference in suppression at forward rapidity compared to central rapidity may come from cold nuclear matter effects, which tend to give larger suppression at forward rapidity, but cannot be precisely checked currently because of the poor precision of d+Au collision data. The Debye screening effects can be checked by looking at other vector mesons like ψ' because the different sizes of the different vector mesons lead to different suppressions within the plasma.

The FVTX detector can help untangle the mechanisms that modify J/ψ production in heavy-ion collisions by, (1) allowing for precision open charm measurements which helps in the understanding of the initial c and cbar production, (2) improving the J/ψ measurements by reducing the background dimuons from π and K decay and improving the J/ψ mass resolution, which will allow more precise measurements to be made for a given integrated luminosity, and (3) allowing additional vector meson measurements like ψ' , and ϒ at mid-rapidity using the

muon arms to be added to the suite of PHENIX measurements. The open charm measurements have already been covered, so we show here the improvement to the vector meson measurements.

Figure 14 shows the estimated composition of the background in the J/ψ mass region. The vertical axis is the ratio of background events containing a decay muon to the total background. Based on this plot, the FVTX detector can eliminate about 60% of the total background at the J/ψ peak, by rejecting the dimuons which contain a decay muon. The punch-through hadrons cannot be eliminated by a vertex cut, since they are prompt, as is the signal.

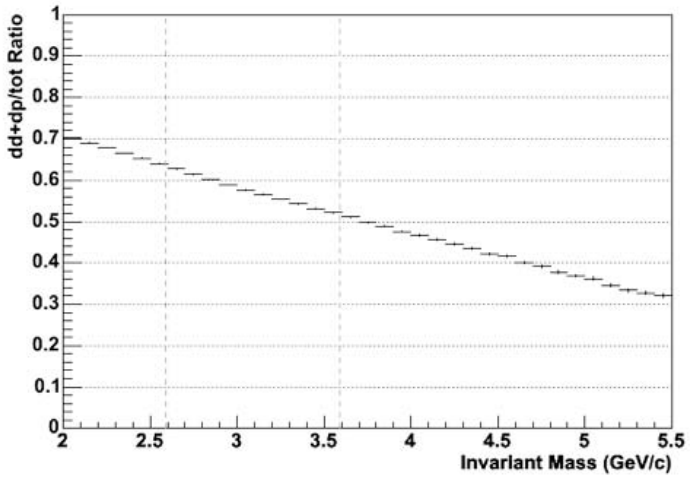

Figure 14 – Fraction of dimuon pair background containing decay muons versus dimuon mass. At the J/ψ mass (3.1 GeV), about 60% of the total background contains at least one decay muon, which can be rejected using the FVTX.

The mass resolution of the J/ψ measured by the muon arms is currently determined primarily by the uncertainty in energy loss in the absorber material that is in front of the muon arms and the uncertainty in the opening angle of the dimuon due to the multiple scattering in the absorber material. The latter can be removed from the resolution contributions by accurately measuring the opening angle with the FVTX. This results in a reduction in the J/ψ mass resolution from ~150 MeV to ~100 MeV.

Simulations of the improvement of the dimuon mass spectrum, when the light meson decay muons are rejected and with the expected mass resolution improvement, are shown in Figure 15 for p+p collisions and in Figure 16 for minimum-bias Au+Au collisions. For the p+p spectrum the signal-to-background for the J/ψ is already quite good, so the improvement of the J/ψ is not as dramatic, but the improvement of the separation of the J/ψ and ψ' is. For the Au+Au collisions, especially those for central Au+Au, the J/ψ peak is very hard to see until the FVTX eliminates the light hadron decays and the improvement is quite dramatic. The ψ' is not quite as dramatic because the backgrounds have not been subtracted, but even in these plots the improvement is quite clear. The yields are representative of those expected for RHIC-II luminosities and the starting signal-to-background ratios are taken from recent runs for Au+Au.

We also expect that with more sophisticated cuts in the future, we will be able to eliminate some of the punch-throughs and further improve the signal-to-backgrounds shown here.

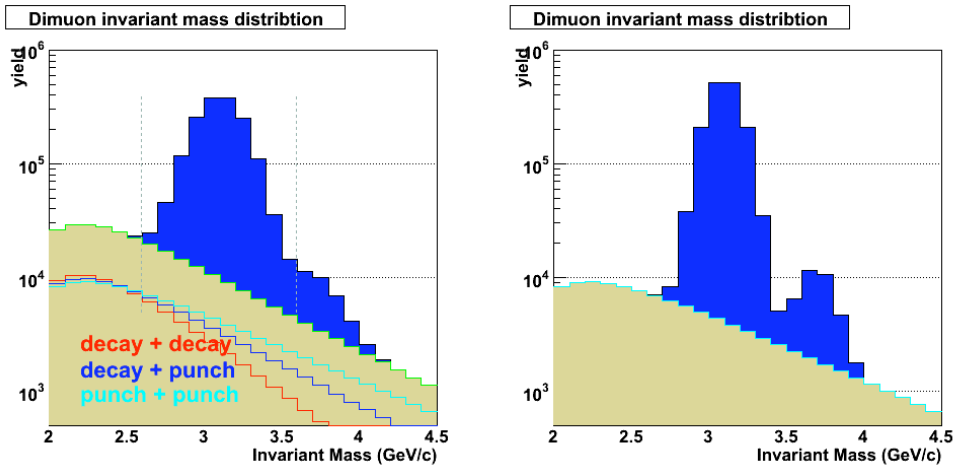

Figure 15 - Simulated dimuon mass spectrum for p+p collisions before (left) and after (right) FVTX vertex cuts are applied to eliminate the light meson decay backgrounds. The mass resolution of the J/ψ and ψ' are improved from 150 MeV to 100 MeV, as shown, by the FVTX. These plots correspond to a 10 week RHIC-II run and the initial J/ψ signal/noise (before the FVTX cuts) is set according to that observed in the 2005 p+p run. There are about 1.5 million J/ψ and 27,000 ψ' entries in the peaks.

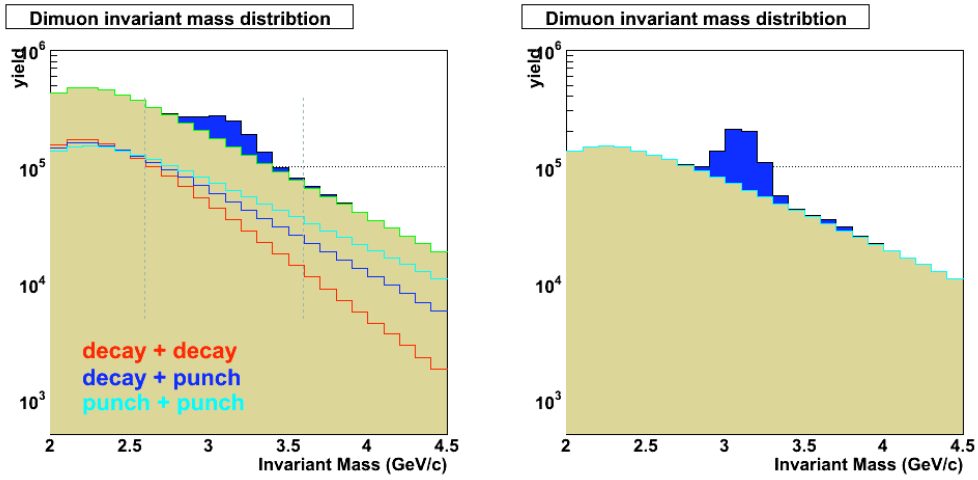

Figure 16 - Simulated dimuon mass spectrum for minimum bias Au+Au collisions before (left) and after (right) FVTX vertex cuts are applied to eliminate the light meson decay backgrounds. The mass resolution of the J/ψ and ψ' are improved from 150 MeV to 100 MeV, as shown, by the FVTX. These plots correspond to a 10 week RHIC-II run and the initial J/ψ signal/noise (before the FVTX cuts) is set according to that observed in the 2004 Au+Au run. There are about 400,000 J/ψ and 7,100 ψ' entries in the peaks.

Figure 17 shows the dimuon mass spectra after background subtraction, again for minimum bias Au+Au events. As can be seen, the ψ' peak becomes much more prominent with the FVTX improvements.

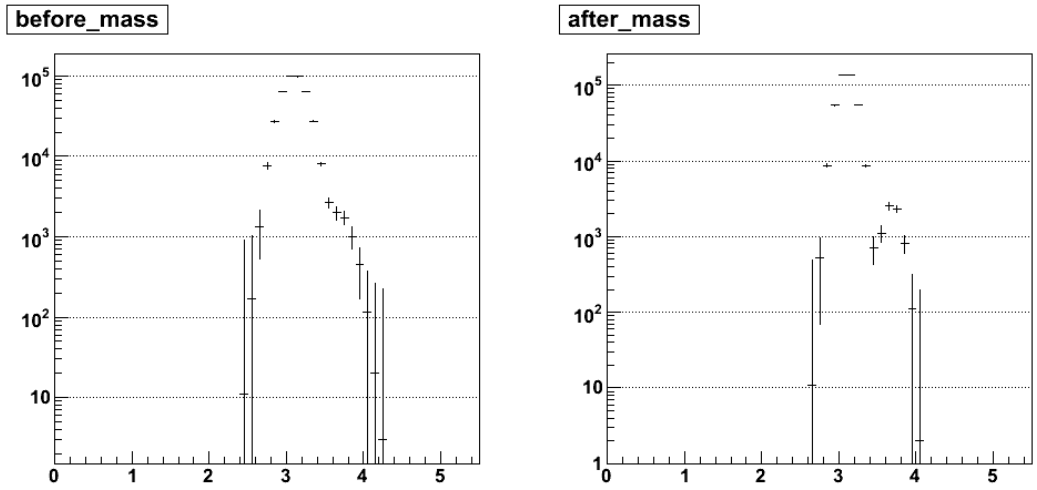

Figure 17 The simulated dimuon mass spectrum for minimum bias Au+Au collisions, with background subtraction, before (left) and after (right) FVTX vertex cuts are applied. As can be seen, the ψ' peak becomes much more prominent after the FVTX improvements.

For the ϒ family resonances, since the mass resolution is dominated by the momentum resolution obtained by the muon tracker, this resolution is not expected to improve much from the FVTX tracker. On the other hand, the backgounds from decays of light mesons will be decreased in the same way as they are for J/ψ. The rejection of backgrounds will be especially important if we try to measure ϒ at mid-rapidity through detection of one muon in each muon arm. Here, the backgrounds are larger (because of the smaller momentum needed to make high mass) and must be reduced if we are to extract the upsilon signal.

Another dimuon measurement that becomes possible with the addition of the FVTX is measurement of Drell-Yan. The dimuon continuum between the vector meson resonance peaks is comprised of Drell-Yan, dimuons from (correlated and uncorrelated) open heavy flavor, and combinatorial background from decay muons from pions and kaons and punch-through hadrons. With the FVTX detector prompt dimuons from Drell-Yan can be separated from dimuons which contain a decay muon from heavy flavor or light mesons, leaving a much cleaner Drell-Yan signal. Since Drell-Yan dimuons are produced in the initial hard-scattering, the production of the muons does not suffer from any interactions with the medium, making Drell-Yan a good measurement for helping to separate final state interactions with the medium from initial-state interactions.

2.1.6 Reaction Plane and Azimuthal Asymmetries

The large increase in the overall solid angle for observing charged particles provided by the FVTX and the more optimal rapidity coverage will result in a substantial improvement in the reaction plane resolution, compared with the baseline PHENIX measurements, which will aid in the study of many signals in PHENIX versus reaction plane. Many physics measurements made by PHENIX with respect to the reaction plane are more limited by the reaction plane resolution than by other systematic or statistical errors, so it is critical to maintain this capability to the PHENIX physics program.

2.1.6.1 Reaction Plane

The determination of the reaction plane for heavy ion collisions from charged particle asymmetries is very important for it allows the measurement of observables (e.g. charm R_{AA}) as a function of path length in the medium. It is generally agreed that in mid-central collisions, the path length in plane is much smaller than out of plane due to the almond shaped overlap zone. A binning of the reaction plane orientation into e.g. 3 bins would therefore allow for path length dependency study of various physics signals with a 60 degree separation of in and out of plane bins (±30 degrees).

In order to avoid auto correlations, the reaction plane has to be determined in a region that does not overlap with the actual measurement, e.g. current central rapidity measurements with respect to the reaction plane use the BBC information at much higher rapidity to determine the reaction plane. Figure 18 shows a measurement with the MVD pad detectors for minimum bias Au+Au collisions from run4, and demonstrates that the elliptic flow at the shaded rapidity region for the former MVD pad detectors and the currently proposed FVTX exhibits a stronger v2 signal than at BBC rapidity and should therefore provide a reaction plane measurement with better resolution.

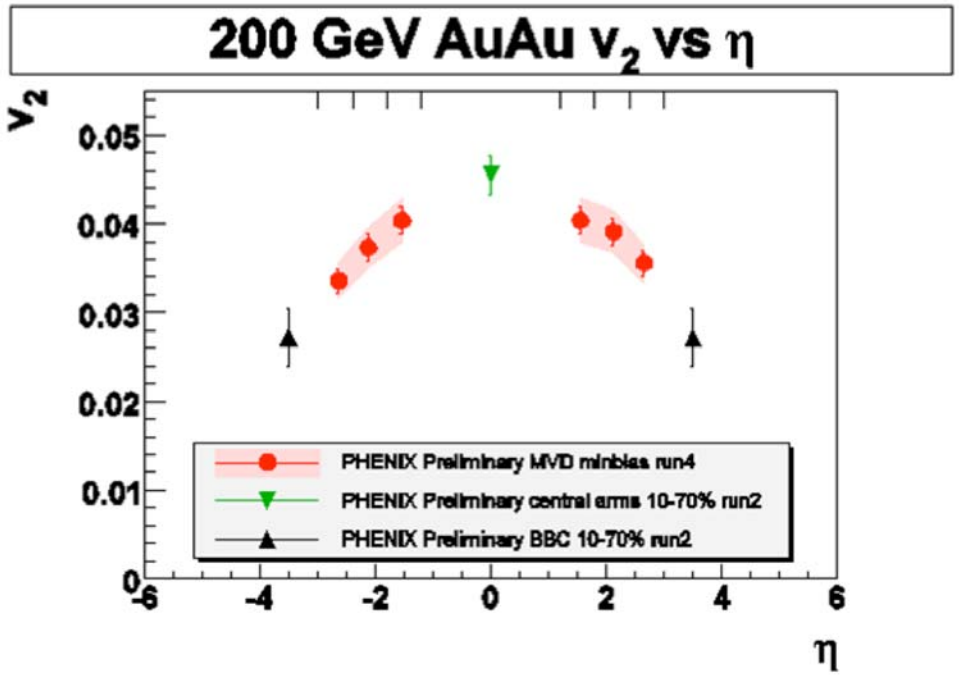

Figure 18 - Azimuthal asymmetry v2 as function of pseudo rapidity for minimum bias A-A collisions at 200 GeV. The measurement from run 4 with the MVD pad detectors is colored in magenta; the FVTX will cover the same range in pseudo rapidity.

A simulation has been performed to study the reaction plane resolution and confidence levels for providing 'reaction plane bins'. The typical way to measure or report a reaction plane resolution is quoting the square root of two times the mean cosine of the difference between reaction planes obtained from two subsets of tracks, in this case the north and south tracks. As this is a rather

complex variable, we choose to first represent it in Figure 19 and then translate it into a more intuitive variable in Figure 20, namely a confidence level of having made the right determination.

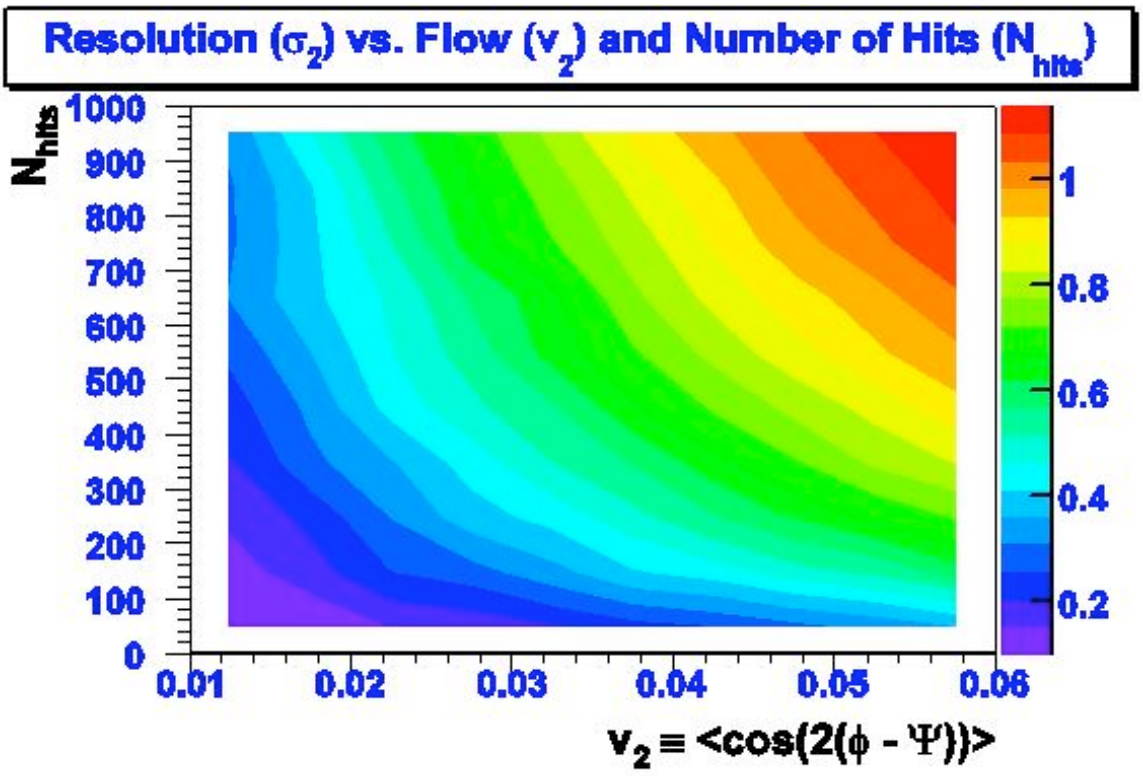

Figure 19 - The two dimensional color representation of the mean reaction plane resolution as function of the charge particle multiplicity Nhits and the elliptic flow signal v2 present in the rapidity interval of the FVTX detector. The total number of charge tracks expected for a mid central Au+Au collision at 200 GeV is simulated to be about 800 traversing the FVTX silicon detector, the previously measured elliptic flow signal v2 is on the order of 0.035, the resulting expected mean reaction plane resolution is approximately 0.75.

Figure 19 shows in color the square root of the mean cosine of the reaction plane difference between north and south FVTX detector as function of the track multiplicity (here called Nhits), i.e. the reaction plane resolution on the ordinate. The flow signal v2 present in the given rapidity interval of the detector is shown on the abscissa. The general trend visible is that the reaction plane resolution is increasing (improving) with the number of charged tracks and increasing with the strength of the elliptic flow signal v2. The red colored top right corner marks the area which yields the best resolution. (Note that since this is cosine of the difference, a value of 1.0 indicates the reaction plane difference is zero and a value of 0.0 indicates they are 90 degrees apart, i.e. a larger number means a smaller resolution)

Studies from HIJING have shown that the mean number of charged tracks to be expected for the FVTX is on the order of 400 tracks per endcap, i.e. about 800 charged tracks total.

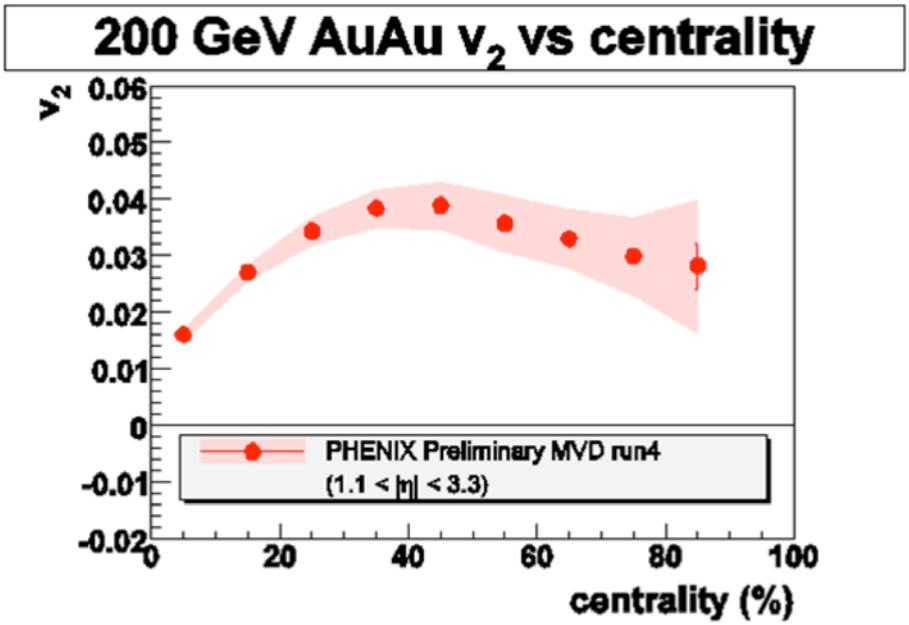

Figure 20 - Azimuthal asymmetry v2 (elliptic flow) as function of centrality for A-A collisions at 200 GeV. The measurement was obtained with the MVD pad detectors which covered in run 4 the same pseudo rapidity rage as the FVTX will in the future.

The elliptic flow measurement v2, shown in Figure 20 as a function of centrality for Au+Au collisions at 200 GeV, indicates that the expected value v2 is about 0.035 for mid central collisions. The expected reaction plane resolution we obtain via Figure 19 is therefore about 0.75.

Figure 21 shows in color the expected confidence levels as function of the reaction plane bin size. For a given reaction plane bin size in delta phi one can see that the confidence level that the actual reaction plane lies in the measured reaction plane bin increases with the reaction plane resolution. It also shows that a 2 sigma confidence level can only be reached in the limit of two broad bins in and out of plane with a nearly perfect detector.

If we interpret Figure 21 with the number for the reaction plane resolution obtained above (0.75) and assume that we want to have 3 bins in reaction plane as mentioned earlier (i.e. ±30 degrees around the major axis plus a 60 degree gap), then we obtain a confidence level of about 65 percent; two broad bins in vs. out will have a confidence level of 85 percent, a very good measurement.

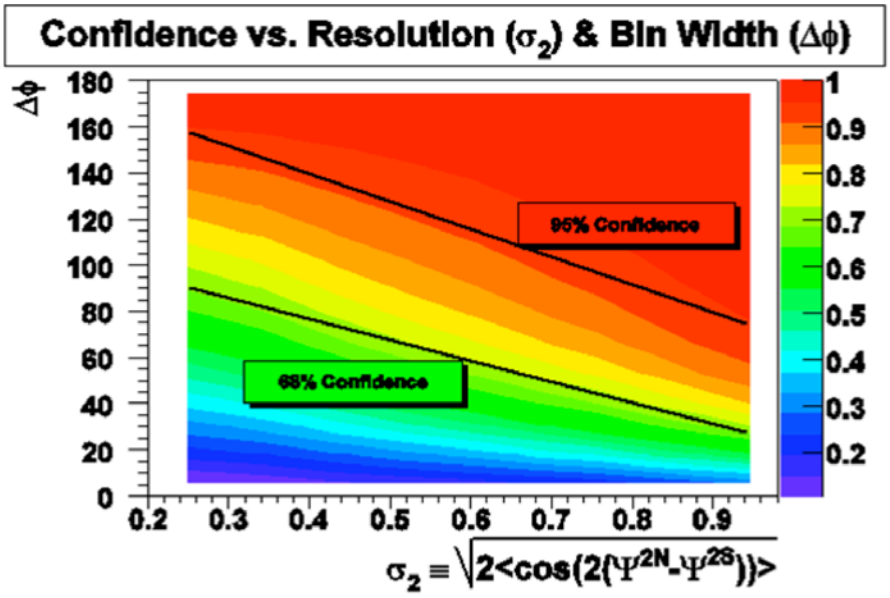

Figure 21 - Three dimensional representation of confidence level (0 to 1 corresponds to 0 to 100 percent) of a given delta phi bin as function of the mean reaction plane resolution for the FVTX. The reaction plane resolution of 0.75 estimated in figure 4 would result is a 65 percent confidence level if binning the reaction plane into 3 bins. Two bins (delta phi = 90 degrees) will give a confidence level of 85 percent for the 'true reaction plane' being in the measured bin.

2.1.6.2 Flow Measurements

In addition to providing a reaction plane for the central detector measurements, the FVTX can obviously measure the actual elliptic and directed flow signal. In the following we discuss the measurements obtained with the MVD pad detectors in run 4 which covered about the same rapidity range and were already shown above in the context of the reaction plane measurements.

Figure 18 shows the measurements of the azimuthal asymmetry v2 as function of the pseudo rapidity with three sets of PHENIX detectors. The measurement obtained with the MVD is colored in magenta, it shows a sizeable v2 which translates into a good reaction plane measurement. The FVTX has an improved granularity and the same rapidity coverage as the former MVD pad detectors. In addition the measurement of asymmetries and reaction plane will be improved by using tracklets in the four FVTX planes rather than just hits as was done in the MVD analysis.

Figure 20 and Figure 22 show elliptic and directed flow measurements with the MVD pad detectors as function of centrality for Au+Au collisions. The proposed FVTX will provide for the same measurements, but with better statistical and systematic error bars.

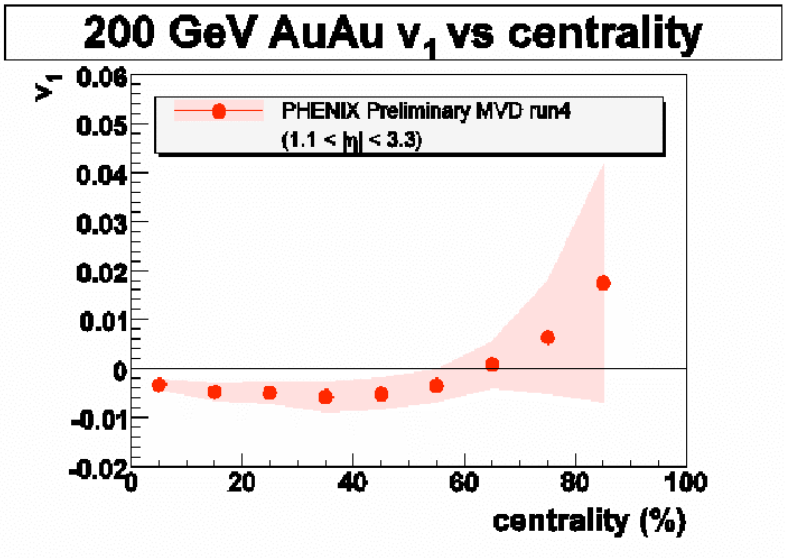

Figure 22 - Azimuthal asymmetry v1 (directed flow) as function of centrality for A-A collisions at 200 GeV. The measurement was obtained with the MVD pad detectors which covered the same pseudo rapidity rage as the FVTX will.

2.2 Proton(Deuteron) + Nucleus Collisions and Nuclear Effects on Quarks and Gluons

Proton-nucleus collisions not only provide important baseline information for the study of QCD at high temperatures, they also address fundamental issues of the parton structure in nuclei. Since the discovery of the EMC effect in the 1980s, it is clear that the parton-level processes and the structure of a nucleon are modified when embedded in nuclear matter[xxiii]. These changes reflect fundamental issues in the QCD description of parton distributions, their modifications by the crowded nuclear environment of nucleons, gluons and quarks, and the effect of these constituents of the nucleus on the propagation and reactions of energetic partons that pass through them.

There are many ways that cold nuclear matter can affect particle production and propagation. Initial state effects, which occur before the incoming parton undergoes a hard scattering, include parton shadowing, energy loss and multiple scattering. These generally conserve the incident parton flux, but change their kinematics. Final state effects, which take place after the hard scatter occurs, include energy loss, multiple scattering and dissociation of bound states. For some processes the hard scattering part may not factorize from the soft collisions, resulting in additional process-dependent effects. These are usually minimized by choosing reactions with sufficiently large Q^2.

2.2.1 Heavy-quarks in d-Au Collisions: Charm and Bottom Mesons

The most compelling physics issues that can be studied using single heavy quarks include:

- Gluon shadowing or saturation effects for single heavy quarks. To be contrasted with similar studies of quarkonia.

- Energy loss and multiple scattering of heavy versus light quarks in cold nuclear matter.
- Accurate heavy quark cross section measurements over large rapidity and p_T ranges in order to constrain recombination models for quarkonia ($c\bar{c}$ or $b\bar{b}$ bound states).

2.2.1.1 Shadowing or Gluon Saturation via Heavy-quarks Measurements

A cold nuclear matter effect that is of particular interest is the apparent depletion of low momentum partons (gluons or quarks) in nuclei, called shadowing, which can result from the large density of low momentum partons. For gluons with very low momentum fraction, $x < 10^{-2}$, one can assign, following the uncertainty principle, a large distance scale. These gluons will then interact strongly with many of their neighbors and by gluon recombination or fusion are thought to promote themselves to larger momentum fraction, thus depleting the small x region. In most models the overall momentum is conserved in this process, so that the small x gluon region is depleted while the moderate x region is enhanced. This shift of the gluon distribution function translates into a shift in particle production. Production via low-x gluons is reduced and production via high-x gluons is enhanced. The kinematic acceptance of the PHENIX detector is such that the low-x particle production has good acceptance in one muon arm (in the direction of the deuteron beam in a d+Au collision) and high-x production has good acceptance in the other muon arm (i.e. the direction of the Au beam in a d+Au collision). Therefore, particle production measurements in the muon arms potentially provide measurements of gluon shadowing.

However, modification of the gluon distribution function is not the only way that particle production can be modified to give less particle production at small x. In recent years a model for gluon saturation at small x has been developed by McLerran and collaborators[xxiv]. Gluon saturation affects both the asymptotic behavior of the nucleon's gluon distribution as x approaches zero and causes shadowing.

It should also be noted that a model from Qui and Vitev[xxv] involving higher-twist (power corrections) effects predicts a similar suppression of the cross sections at forward rapidity. These effects arise from coherent multiple scattering of the final state parton, in contrast to shadowing, which occurs in the initial state. If the energy loss of the outgoing partons is added to the model, even larger suppression is seen at forward rapidity.

Kopeliovich has argued that suppression at large rapidity may be caused by Sudakov suppression[xxvi]. In this case, energy conservation results in particle production in p+A collisions going to zero as $x_F \rightarrow 1$.

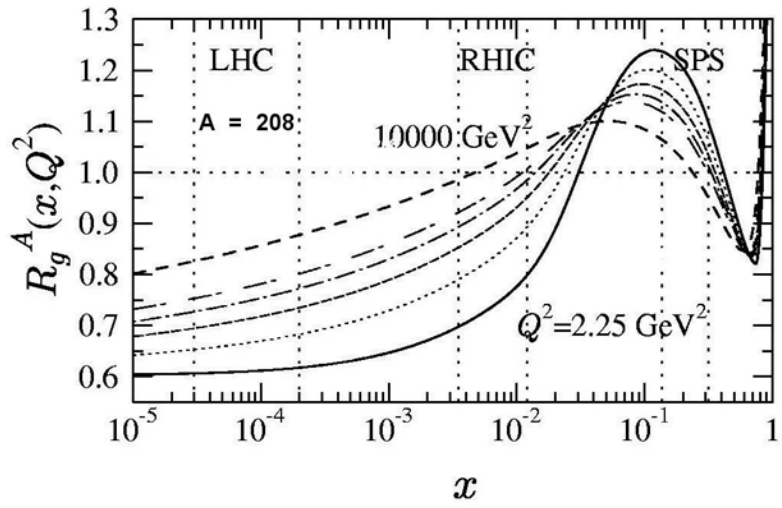

Figure 23 - Gluon shadowing from Eskola[xxvii] as a function of x for different Q^2 values: 2.25 GeV^2 (solid), 5.39 GeV^2 (dotted), 14.7 GeV^2 (dashed), 39.9 GeV^2 (dotted-dashed), 108 GeV^2 (double-dashed) and 10000 GeV^2 (dashed). The regions between the vertical dashed lines show the dominant values of x_2 probed by muon pair production from charm pairs at SPS, RHIC and LHC energies.

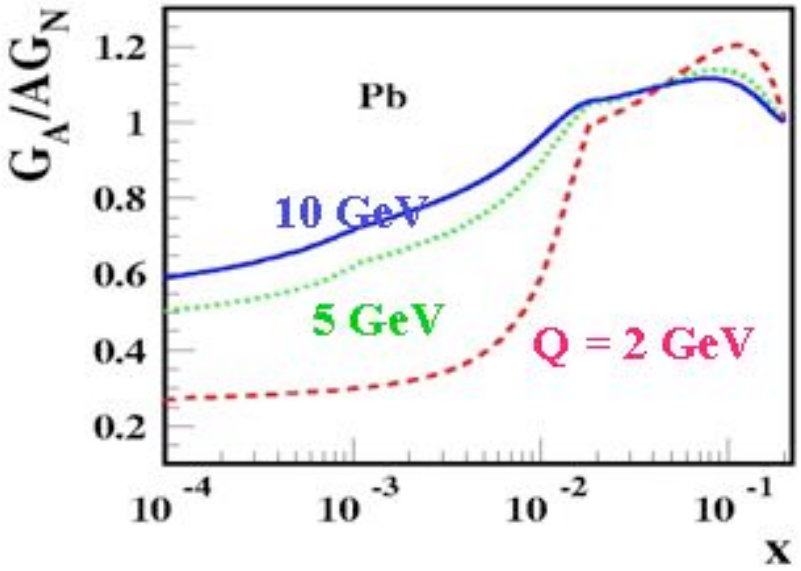

Figure 24 - Gluon shadowing calculations from Frankfurt and Strikman[xxviii] that predicts substantially larger shadowing than that of EKS[xxvii].

At RHIC energies many of the observables are affected by gluon distributions at small *x* where nuclear shadowing is thought to be quite strong. However, theoretical predictions of the amount of shadowing differ by factors as large as three. For example, in the production of J/ψ in the large rapidity region covered by the PHENIX muon arms, models from Eskola et al (EKS) (Figure 23) predict only a 30% reduction due to gluon shadowing, while those of Frankfurt & Strikman[xxviii] (Figure 24) or Kopeliovich[xxix] predict up to a factor of three reduction.

Figure 25 shows the different regions of evolution in Q^2 and x, highlighting the region at small x and Q^2 where the non-linear processes described by the Color Glass Condensate (CGC) model become important and reduce the gluon density. Since these effects are amplified in a nucleus (a factor of ~5 in a Au nucleus), they also produce a shadowing effect where the gluon density per nucleon is reduced at small x.

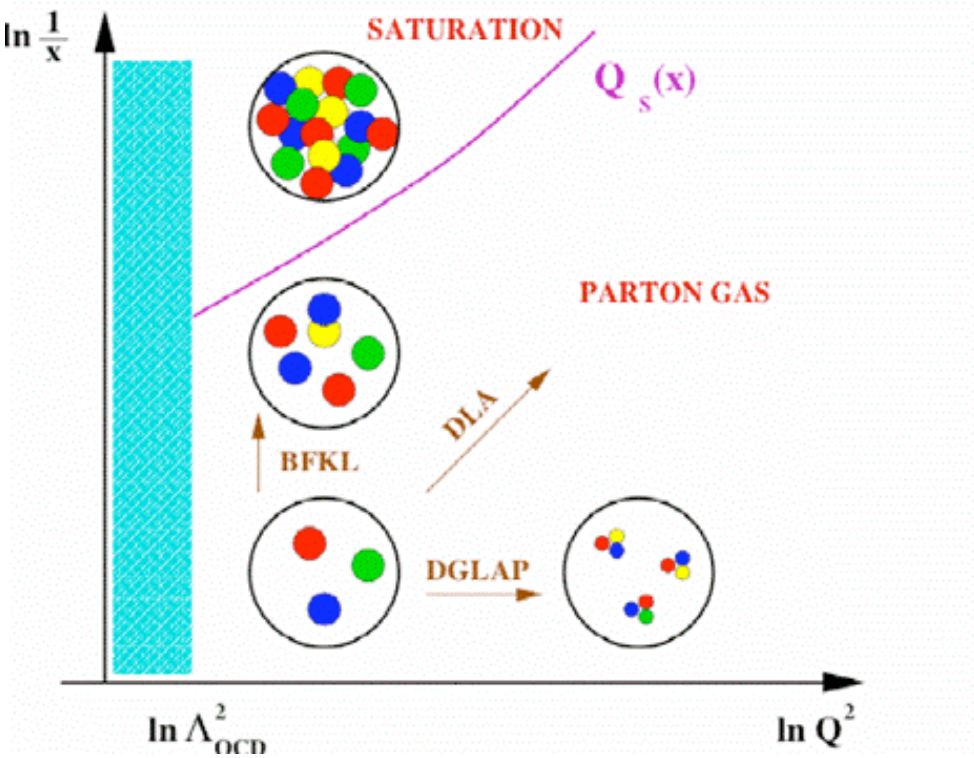

Figure 25 - Diagram showing the gluon saturation region at small x and Q^2.

The coverage in *x* for the FVTX is indicated in Figure 26, superimposed on calculations of the ratio of nuclear to nucleon gluon structure functions. The red bars indicate the additional coverage provided by the FVTX upgrade compared to the baseline of the PHENIX detector. The FVTX extends the *x*-range from the anti-shadowing region into the shadowing domain, which means we will be able to establish the shape of the gluon structure function in nuclei. The shadowing region ($x < 10^{-2}$) is not accessible at the central rapidity covered by the VTX barrel. J/ψ and open charm production in the forward direction covered by the FVTX would be affected by shadowing. For the J/ψ, final state effects such as absorption complicate the connection to the gluon structure function, while for open charm and bottom there is some uncertainty about whether the dominant production mechanism is gluon fusion or flavor excitation. Therefore, comprehensive measurements of both open and closed heavy flavor are necessary to obtain a reliable measure of the modification of the gluons. Given sufficient RHIC luminosity, it would also be quite instructive to measure for bottom the same observables as for charm, since open-bottom production should be largely unaffected by shadowing.

The additional coverage in the anti-shadowing region (x ~ 0.1) is also important. Many models of shadowing predict that the momentum of the shadowed partons collects in this region. Anti-shadowing has only been observed for quarks, not for gluons, so a good measurement would have a strong impact on theory. The suppression of quarks at large x in nuclei (EMC effect) is well characterized, but the situation for gluons is unclear.

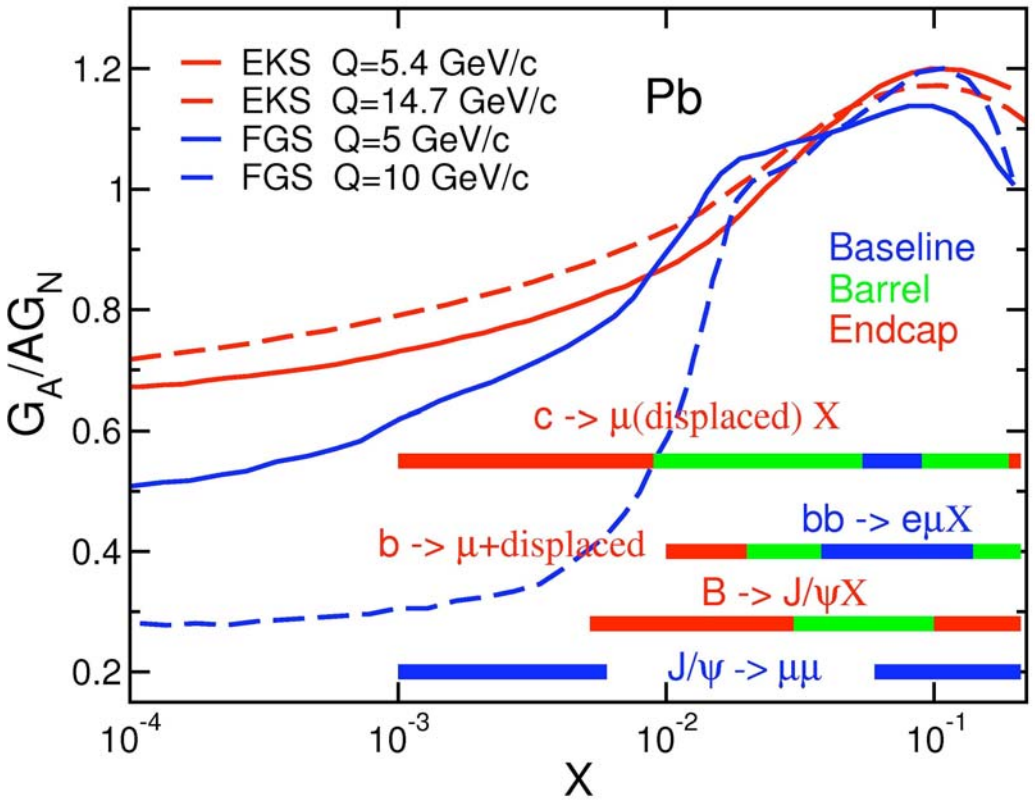

Figure 26 - Gluon shadowing predictions along with PHENIX coverage. The red bars indicate the additional range provided by the FVTX upgrade, green bars are for the barrel (VTX) upgrade, while the blue bars cover the PHENIX baseline. The red and blue curves are the theoretical predictions for gluon shadowing from EKS[xxvii] and FGS[xxviii] for different Q values.

2.2.1.2 Energy Loss and Multiple Scattering of Quarks and Gluons in Nuclei.

As discussed above, measurements of single heavy quarks (charm and bottom) are sensitive to the gluon distributions and their modification (shadowing) in nuclei. They provide a complementary view to that provided by studies of quarkonia as they involve the same initial-state gluon distributions but have quite different, and probably simpler, final-state effects than those of the J/ψ. For example both quarkonia and single heavy quarks can experience energy loss and multiple scattering in the final state, while quarkonia also have potentially large effects from absorption (i.e. disassociation of the two heavy quarks that would otherwise form the heavy quark-antiquark bound state).

Energy loss of partons in the initial state was thought to have a small effect at RHIC, since the energy loss per unit length in many models is thought to be approximately constant and small

compared to the initial-state parton momenta at RHIC, but no definitive data were available to confirm these models or energy loss values. Recently, Vitev et. al.[xxx] have shown that *significant* energy loss in the initial state is consistent with the nuclear dependence seen for prompt muons from PHENIX as shown in Figure 27 where the production suppression factor is shown for dAu collisions versus p_T. These issues are very important in the high-density regions created in heavy ion collisions, but we also need a baseline for normal nuclear densities from proton-nucleus collisions.

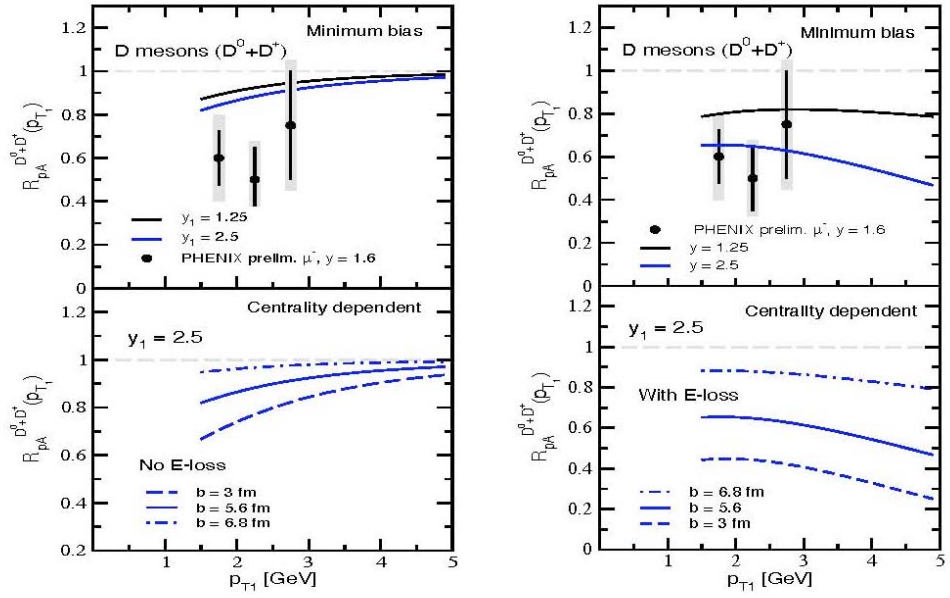

Figure 27 - Vitev, et. al.[xxx] predictions of coherent power corrections (left panel) and the sum of the power corrections and initial state energy loss (right) for the nuclear dependence of D meson production compared to prompt muon data from PHENIX fromn dAu collisions. Significant energy loss is predicted.

Another general feature of most produced particles comes from the multiple scattering of initial-state partons, which causes a broadening of the transverse momentum (Cronin effect) of the produced particles. Final-state multiple scattering can further broaden the transverse momenta.

A recent result for the p_T dependence of the nuclear modification factor for prompt muons is shown in Figure 28 from PHENIX[xxxi]. Data for prompt muons from d+Au collisions show a supression at forward rapidity (small *x* values) in Au where one would expect shadowing effects. At backward rapidity an enhancement that increases with p_T is observed which could be due to initial-state multiple scattering effects, but this data is in the anti-shadowing region where an enhancement that balances the depletion of the gluons at smaller x could also occur.

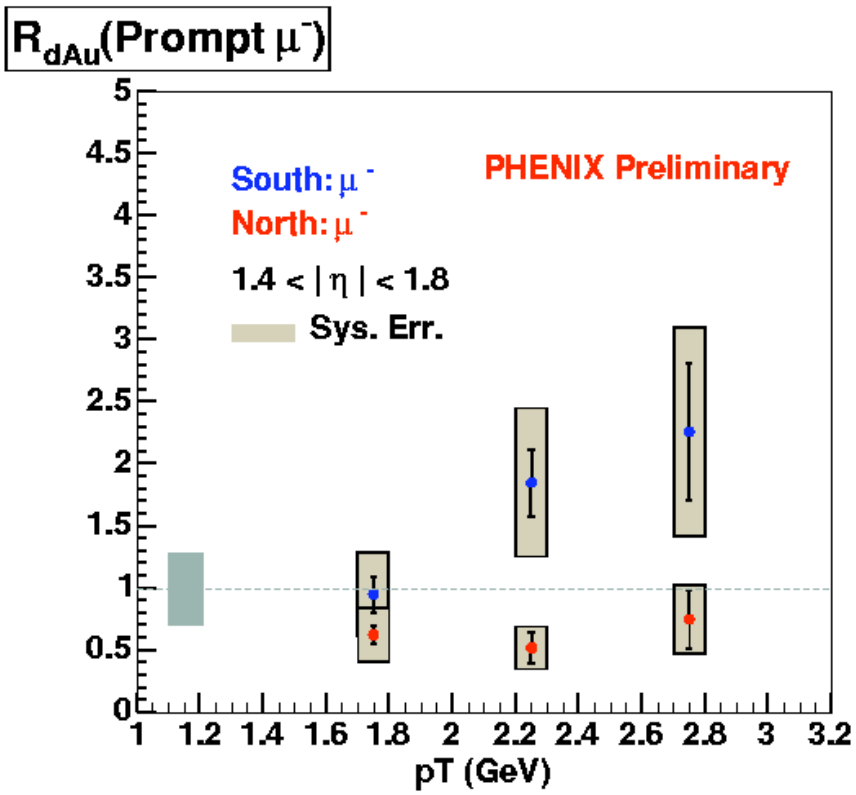

Figure 28 - Nuclear modification factor in d+Au collisions, R_{dAu}, for prompt muons in the forward and backward rapdity regions versus p_T. The prompt muons are primarily from the decays of charm and bottom mesons although perhaps 10% are from other processes such as light meson decays.

These results were obtained through a statistical method where the vertex distribution is used to determine and subtract the single muon component which comes from light meson decays. The punch-through hadrons were also removed through a statistical method by studying how many particles reach each layer of the muon identifier system. These statistical methods suffer from substantial systematic effects that are probably more than 20-30%. With the FVTX upgrade these events can be identified on an event-by-event basis and a much more robust and accurate heavy-quark semi-leptonic decay spectrum can be obtained. This will also allow measurements at p_T values down to 0.5 GeV by substantially reducing the low-mass meson decay backgrounds

2.2.1.3 Heavy Quark Cross Sections

Many models assume that heavy quarks are formed in pairs from a combination of gluon fusion and quark anti-quark annihilation. Next-to-leading-order calculations are performed using the appropriate parton distribution functions. In contrast to this conventional expectation, Vitev et al. have shown in their theoretical approach[xxx] that gluon fusion is not the dominant process for production of open charm. In their model "flavor excitation" diagrams, $cg \rightarrow cg$ and $cq \rightarrow cq$, dominate the production, rather than gluon fusion, $gg \rightarrow c\bar{c}$. Note that this mechanism produces

single charm quarks, not pairs. The relative contribution of these different processes versus transverse momentum at several different rapidities is shown in Figure 29.

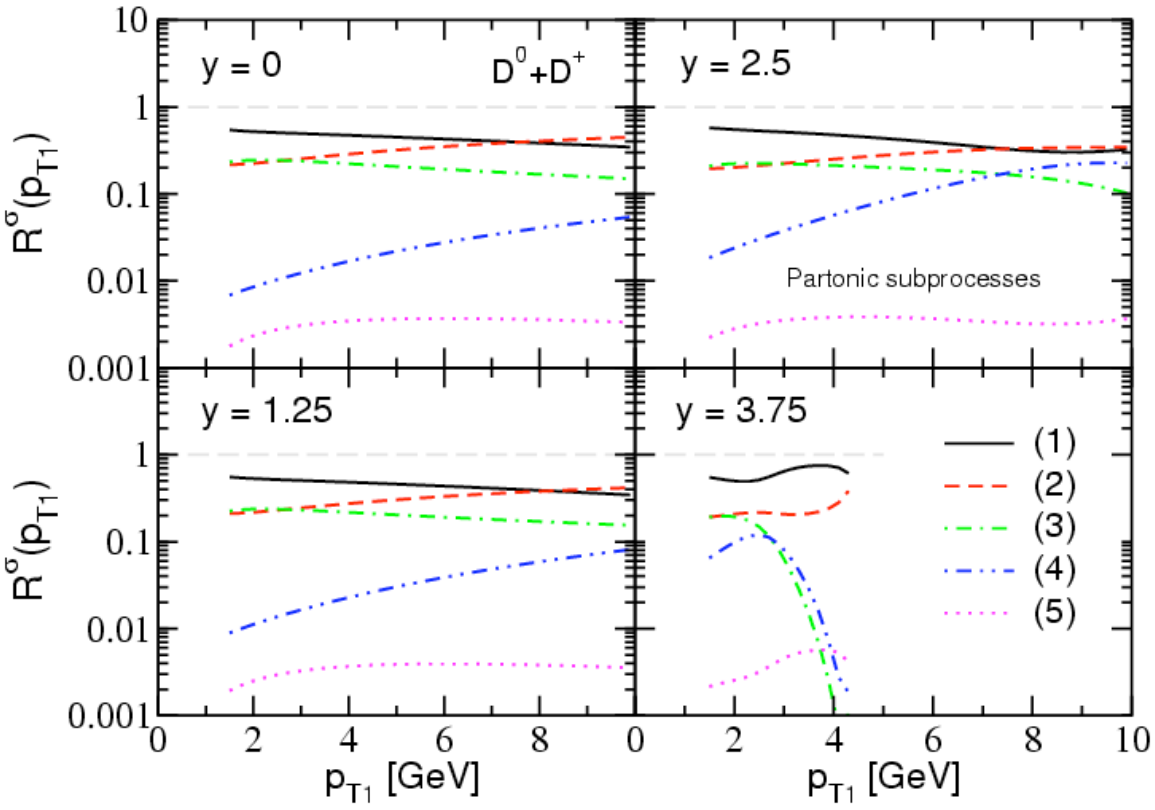

Figure 29 – Vitev's calculations[xxxii] show that gluon fusion is not the dominant process in open charm production at RHIC energies. Here he shows the fraction of the total cross section contributed by each process vs p_T for different rapidity values for the processes (1) $cg \rightarrow cg$, (2) $cq \rightarrow cq$ (where *q* is a light quark or anti-quark), (3) $gg \rightarrow c\bar{c}$, (4) $q\bar{q} \rightarrow c\bar{c}$ and (5) $c\bar{c} \rightarrow c\bar{c}$ (intrinsic charm).

If correct, this model implies that the initial state already contains the heavy quark, which complicates the interpretation of any nuclear effects. An accurate measurement of the heavy quark cross section is needed to determine the production mechanism for heavy quarks ranges and to constrain recombination models for quarkonia as discussed below.

2.2.2 Disentangling the Physics of J/ψ and ϒ Production in Nuclei

Recent measurements by PHENIX of the J/ψ nuclear dependence for d+Au collisions[xxxiii] are shown in Figure 30. The large rapidity region corresponds to small x in Au, the region where shadowing is thought to be important. Extraction of gluon densities from these measurements is not only hampered by the poor statistical precision of the present d+Au data, but also by theoretical issues including the possibility that much of the suppression at large rapidity might come from coherent multiple scattering as calculated in[xxx], initial-state energy loss of the incident gluon[xxxiv] or from Sudakov suppression of the final-state $c\bar{c}$ [xxxv]. Increased statistics together with definitive measurements of open charm and bottom will help constrain the underlying theoretical QCD processes, though additional measurements will likely be needed to

unambiguously determine what cold nuclear matter effects are contributing to particle production rates.

Different d+Au runs at different energies and rapidities will help since the relative contributions of energy loss and shadowing changes versus x_F. Adding Drell-Yan measurements to the mix will also help as Drell-Yan does not suffer from final-state effects. With the FVTX a Drell-Yan measurement becomes possible as we can reject the other dimuon backgrounds which contribute at the same mass as Drell-Yan (open heavy flavor and decay muons from pi and kaon decays). The potential additon of ψ' measurements (because background rejection and mass resolution improvement make the measurement possible) and upsilons at forward and mid-rapidity will further help to constrain models since ψ' does not suffer from feed-down and upsilons probe a different x-region.

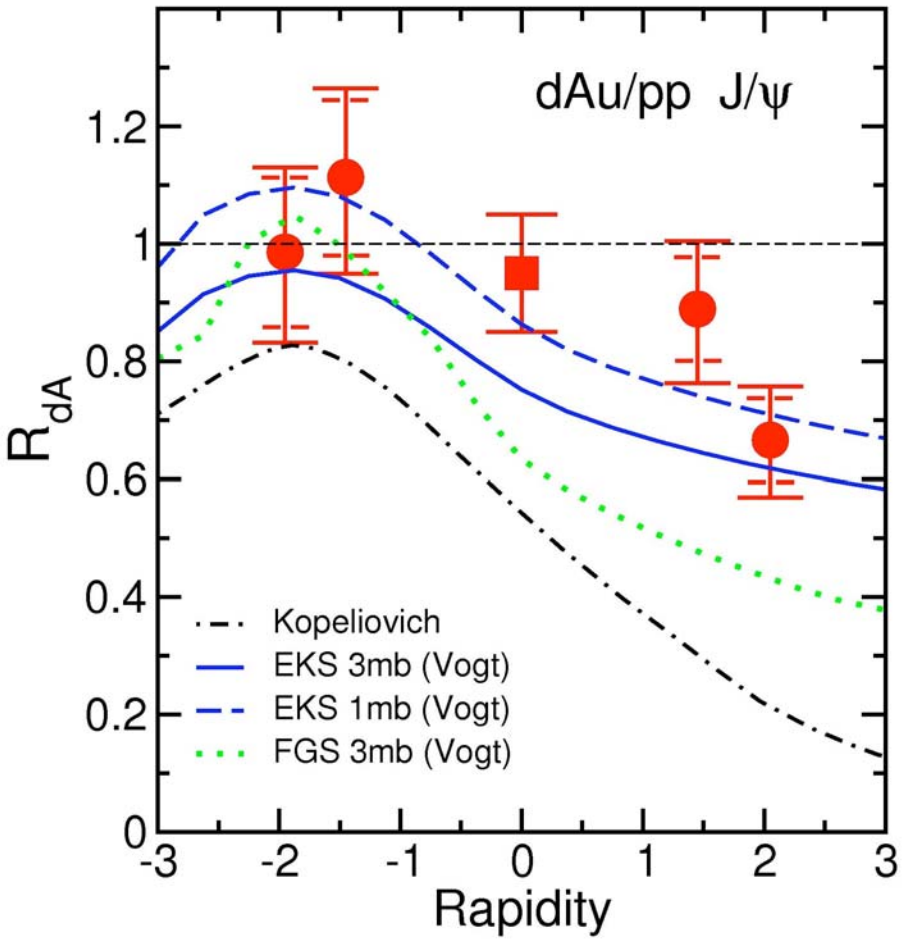

Figure 30 - J/ψ nuclear dependence versus rapidity, compared to theoretical predictions with two types of gluon shadowing[xxxiv].

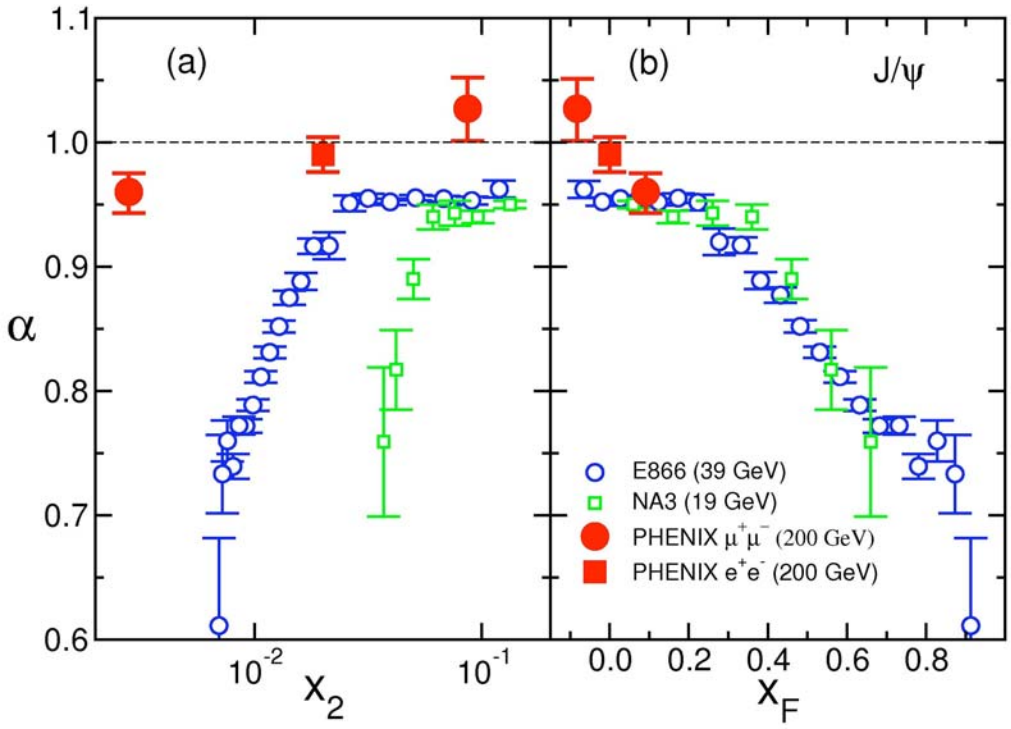

Figure 31 - The dependence of alpha on x_2 and x_F for J/ψ production shows that the suppression does not scale with x_2 but does exhibit approximate scaling with x_F. Alpha is defined as $\sigma_A = \sigma_p A^\alpha$, where σ_p (σ_A) is the nucleon (heavy nucleus, A) cross section. Data is from PHENIX (√s = 200 GeV)[xxxiii], E866/NuSea (√s = 39 GeV)[xxxv] and NA3 (√s = 19 GeV)[xxxvi].

Data from lower-energy fixed-target p+A measurements by E866 and NA3 have already provided some x_F dependent measurements and these are shown in Figure 31, compared to data from PHENIX. The experiments E866 and NA3 report stronger suppression at large x_F (or small x_2), where x_2 is the momentum fraction of the gluon in the nucleus and $x_F = x_1 - x_2$ (x_1 being the momentum fraction in the proton). A stronger absorption at mid-rapidity is also observed by the lower energy experiments. This lack of scaling versus x_2 for the three experiments indicates that the observed suppression is not dominated by shadowing, and suggests that energy loss or other nuclear effects are playing important roles in J/ψ production, at least at lower energies. Clearly, a larger x_F coverage by PHENIX is highly desired.

.

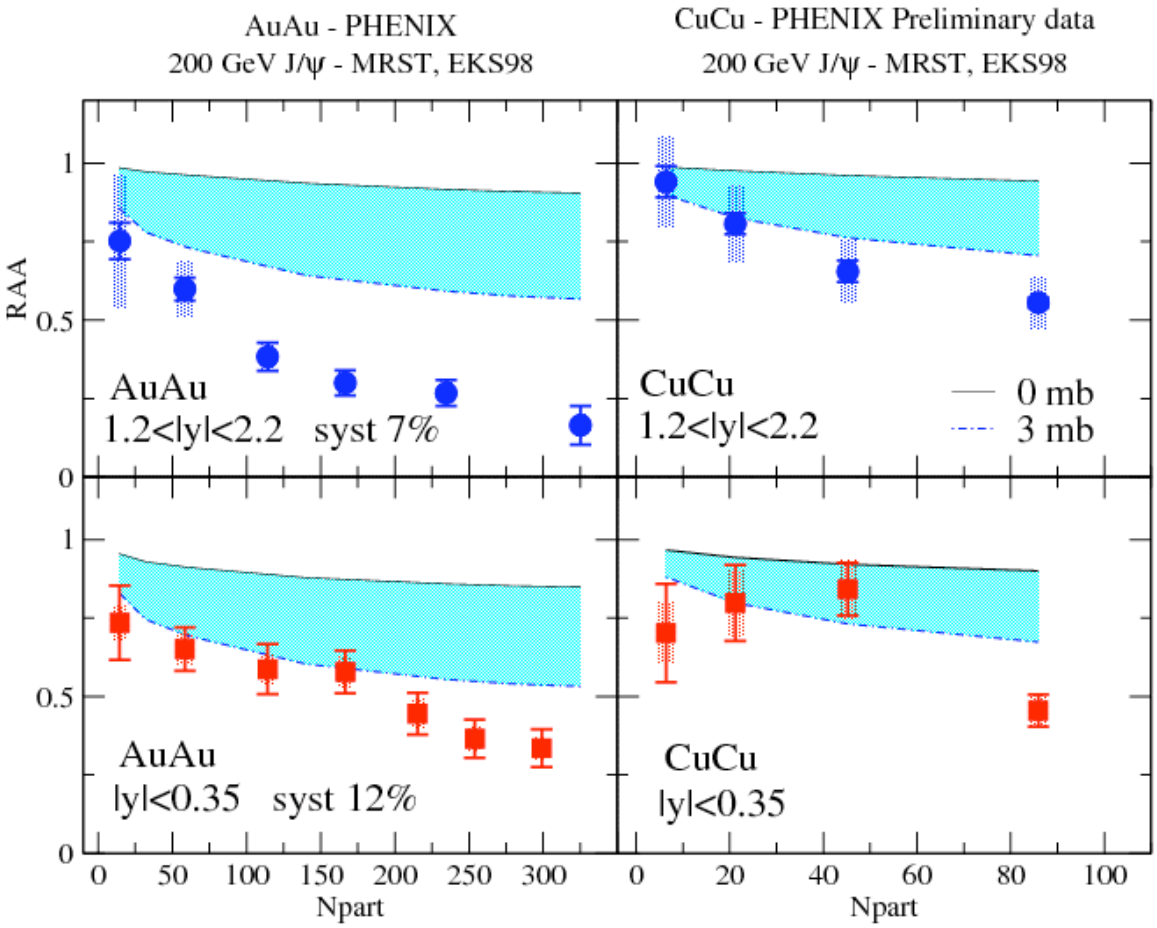

Figure 32 – PHENIX J/ψ nuclear depedence data for Au+Au and Cu+Cu collisions versus centrality at forward and mid rapidity. The shaded areas are EKS shadowing calculations with absorbtion cross sections between 0 and 3 mb.

Figure 32 demonstrates the uncertainty in the cold nuclear matter effects when extrapolated from d+Au collisions to Au+Au collisions. As seen by the large blue band, most of the suppression of J/ψ in Au+Au could be due to cold matter effects, with a factor of about two uncertainty. Although higher statistics data will help, one of the largest uncertainties comes from the subtraction of the combinatoric background due to random combinations of muons from light hadron decays. The FVTX will eliminate most of the hadron decays using the large DCAs of their decays to muons (see section 2.1.5), resulting in a statistics limited measurement rather than a systematics limited measurement.

2.2.3 Hadrons at Forward and Backward Rapidity

Light hadrons, π and K, can also be measured at forward and backward angles by the PHENIX muon arms using their decays into muons or by identifying those hadrons that "punch through" all layers of a muon identifier. These punch-through hadrons are identified by measuring particles which stop in the middle of the muon identifier planes and requiring that the momentum measured in the tracker is greater than the momentum of a muon that would stop in the same

plane. The decay muons from pion and kaon decays are measured by fitting the single particle spectra versus the z position of the event vertex. Since decay muons will contribute more for vertices far from the absorber than vertices close to the absorber, the decay component can be inferred from this fit.

Nuclear modification factors for light mesons (via their decay to muons) for d+Au collisions from PHENIX are shown for positive and negative rapidity in Figure 33. Similar to the prompt muon results shown earlier, these particles also exhibit suppression at forward rapidity and enhancement at backward rapidity. Hadron production at forward rapidity is sensitive to the gluon structure function and its modification in nuclei, e.g. shadowing. However, whether these hadron measurements actually probe small momentum fractions that lie within the shadowing region is unclear, as some theoretical calculations indicate that unless one measures two hadrons in the forward direction one does not actually sample small enough x values.[32]

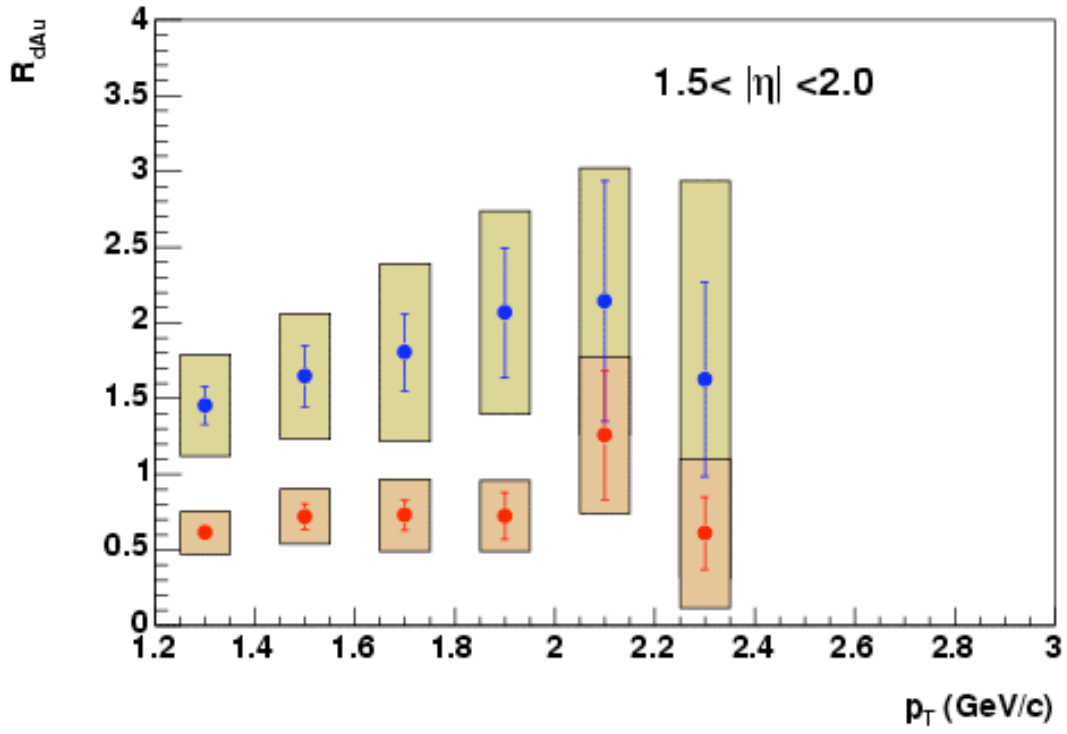

Figure 33 - Nuclear modification factor in d+Au collisions (R_{dAu}) for hadrons decaying into muons in the forward (red) and backward (blue) rapidity directions (PHENIX Preliminary).

Like the prompt muons discussed earlier, this method of measuring hadrons suffers from large systematic errors due to the statistical method used to separate prompt particles from light hadron decays. With the FVTX we will be able to cleanly separate the prompt component from that due to the decaying hadrons by measuring the displacement of tracks from the primary vertex. This will allow direct identification of the light hadrons, especially at larger p_T where the heavy-quark decays would normally start to dominate, and produce a cleaner result with much smaller

systematics. In addition, the FVTX can provide an independent sample of punch-through hadrons that can also be used to measure the forward and backward hadron spectra.

The ratio of yields for all particles measured in the muon arms in central divided by peripheral d+Au collisions is shown versus rapidity in Figure 34. Data for light hadrons and for the J/ψ show a surprisingly similar trend: suppression at forward rapidity and enhancement at backward rapidity. This has been interpreted as the consequences of nuclear shadowing. The FVTX will provide reduced systematic errors for all of the measurements at |y|>0 (include estimates or reference). Figure 33 clearly points to the importance of a broad rapidity coverage that can be provided by the FVTX.

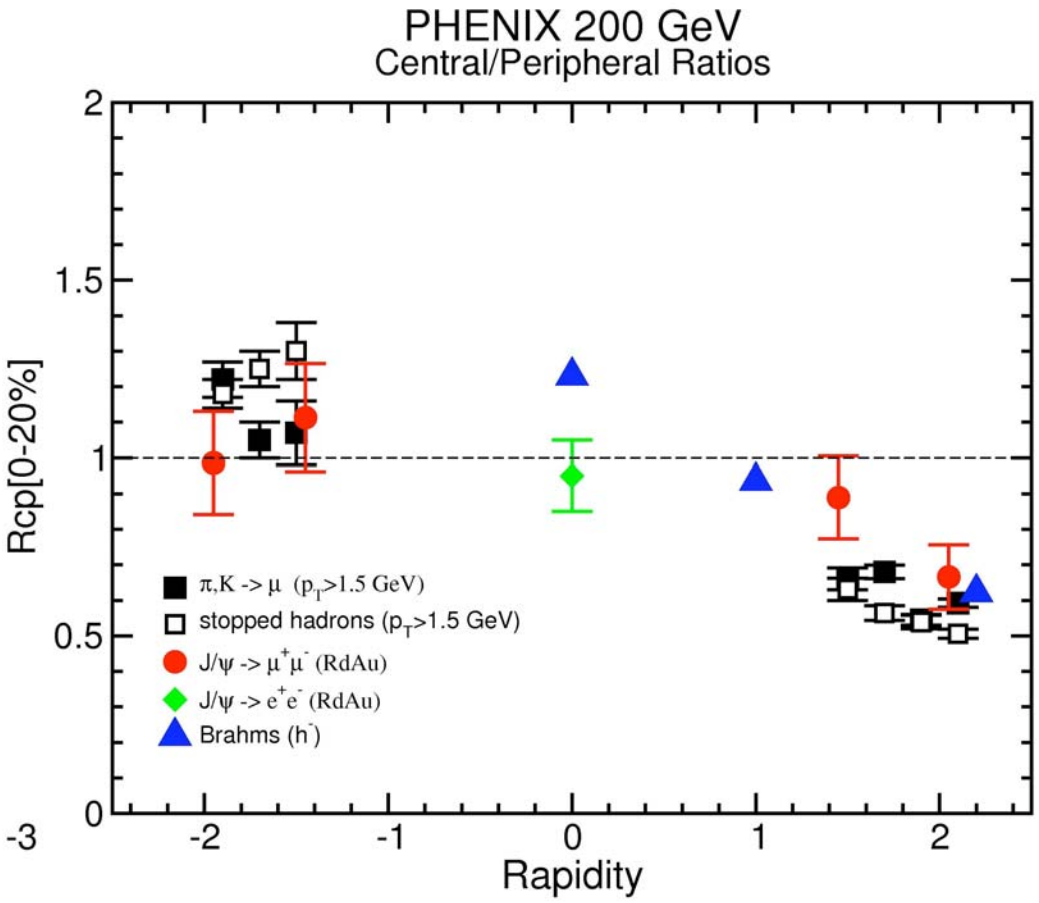

Figure 34 – Nuclear modification in d+Au collisions in terms of the ratio between central and peripheral collision yields, Rcp, for light hadrons that decay into muons from PHENIX, compared to similar results from Brahms and to PHENIX data for the J/ψ.

A different interpretation is provided by Vitev et al.[xxx] where the most important effect in the increasing suppression at large rapidity comes from energy loss in the initial state. In their calculations, shown in Figure 35, coherent multiple scattering plus a rapidity shift of Δy=0.25 providing a phenomenological energy loss gives suppressions very similar to both the hadron

and charm data. The calculations do not include initial-state p_T broadening (Cronin effect) which could slightly alter the comparison of the calculation to the data.

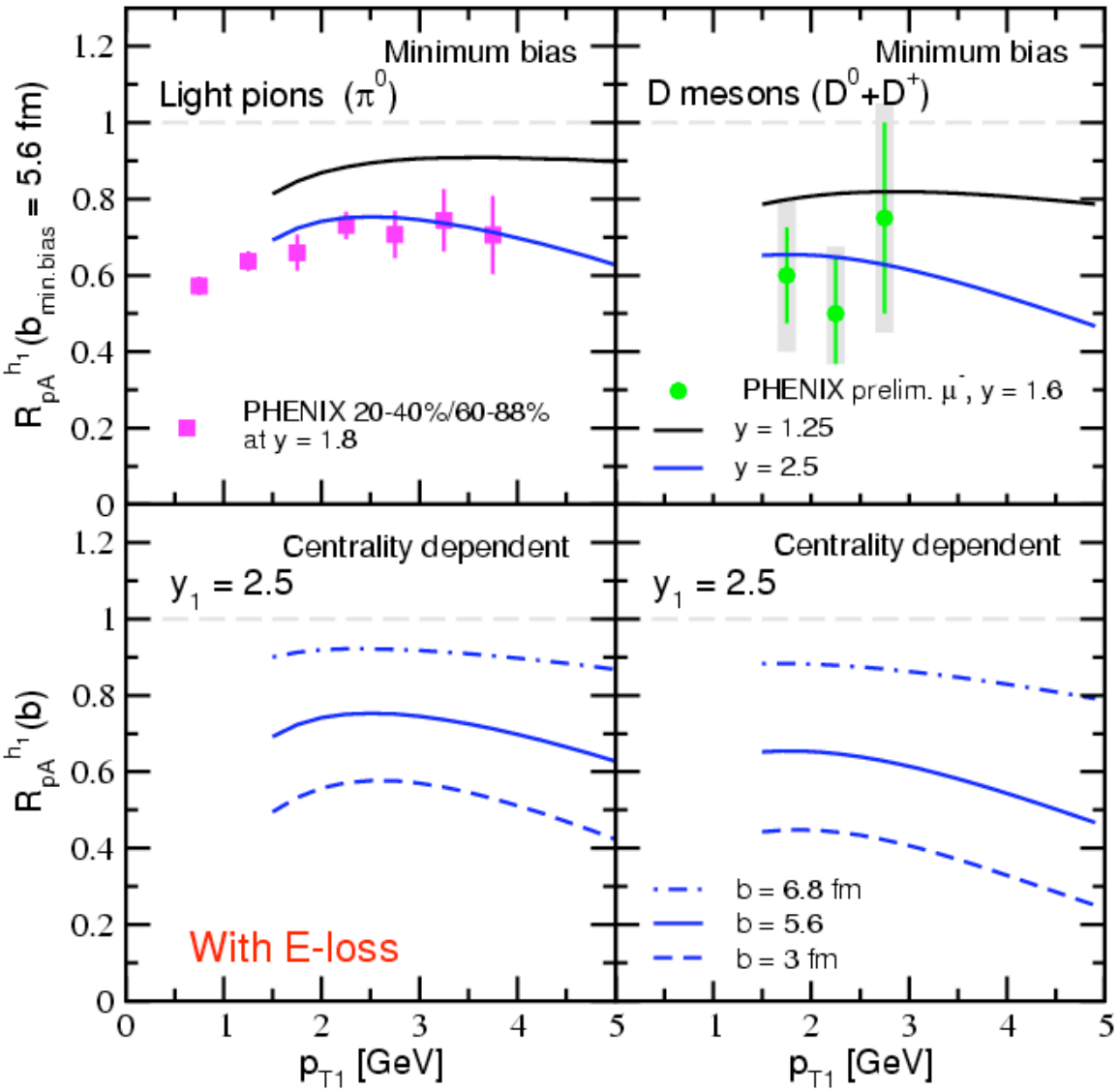

Figure 35 – Calculations from Vitev[xxx] Top: Suppression of the single inclusive hadron yields in d+Au collisions versus p_T for rapidities y_1 = 1.25 and 2.5. Bottom: Impact parameter dependence of the calculated nuclear modification for central, b=3 fm, minimum bias, 5.6 fm and peripheral, 6.9 fm, collisions.

One should also note that the model of Kopeliovich[xxix] which includes Sudakov suppression, provides a somewhat universal explanation for increasing suppressions at forward rapidity as well. As an example we show these calculations compared to the Brahms forward π^- suppression ratios in Figure 36.

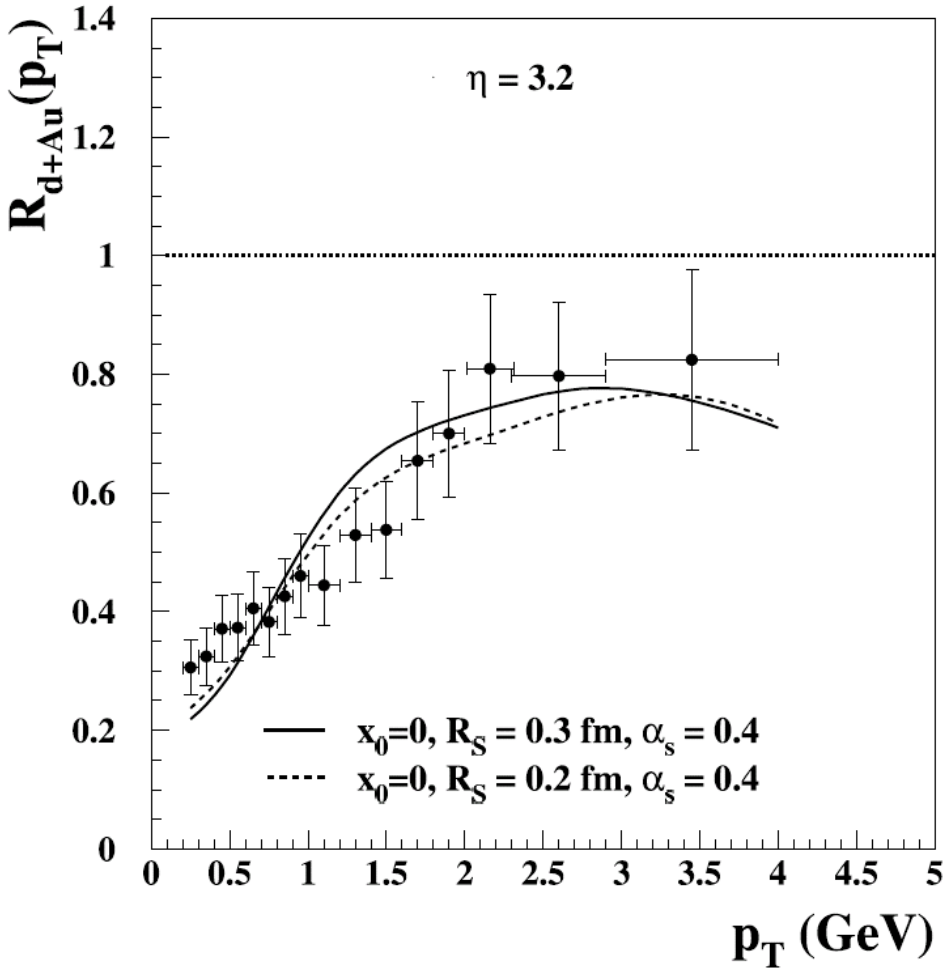

Figure 36 – Calculations from Kopeliovich[xxvi] Ratio of negative particle production rates in d+Au and p+p collisions as a function of p_T. Data are from Ref. [xxxvii], solid and dashed curves correspond to calculations with the diquark size 0.3 fm and 0.4 fm, respectively.

It is also important to study the modification of jets in the forward and backward directions from d+Au, both to understand the fragmentation and how it is modified in cold nuclear matter. Jet data will also provide a baseline for similar studies in nucleus-nucleus collisions where jets are one of our most important tools for studying the properties of the hot-dense matter (QGP) created in those collisions. The FVTX will detect all charged particles in the jet, rather than just the leading particle.

2.2.4 Drell-Yan Measurements

Drell-Yan events, which provide a direct measure of the anti-quark distributions in nucleons or nuclei, have always been limited in the past in their reach to low *x* by the inability to separate the Drell-Yan muon pairs below the J/ψ mass from copious pairs due to open-charm decays. For example, as shown in Figure 37, the FNAL E866 Drell-Yan data was limited to masses above 4 GeV, due to a significant contribution of randoms (charm decays) at lower masses. At RHIC energies, the backgrounds from charm decays are much worse.

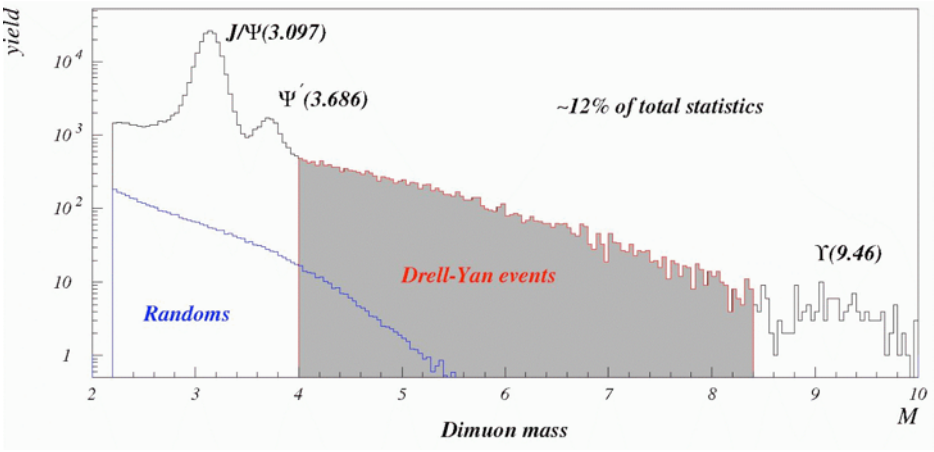

Figure 37 - Dimuon mass spectrum from E866/NuSea, showing the Drell-Yan mass region used in their analysis, which excluded masses below 4 GeV/c^2 because of the large backgrounds from open charm decays (labeled Randoms) in that region.

On the other hand, PHENIX, with the addition of the FVTX, should be able to identify and quantify the portion of the low mass dimuon continuum from charm decays and also remove the large numbers of random pairs from light hadron decays by measuring the displacement of the tracks from the primary vertex. This should allow Drell-Yan measurements over a broad mass range including values below the J/ψ, therefore spanning a large range of x with values well into the shadowing region. Since the relative Drell-Yan rates at RHIC are small, such measurements will still be a challenge, but with RHIC-II luminosities such measurements have the potential to provide information on the anti-quark distributions in nuclei at much smaller values of *x* than are currently accessible. At the same time, one would also learn more about charm production and the correlation of the charm pairs through the decay pairs found in the continuum.

2.2.5 Summary of Physics Addressed by the FVTX in d(p)+A Collisions

The FVTX addresses the following physics in d+A reactions:

- Probing the small-x shadowing region in nuclei through the production of single heavy quarks (c and b) and of bound states of heavy quarks (J/ψ, ψ' and ϒ).
- Comparison of light and heavy-quark p_T distributions to determine differences in energy loss and Cronin effects.
- Measurements of light hadrons to contrast with heavy quarks in the same kinematical regions.
- Bottom cross sections as a constraint on the contributions of $B \rightarrow J/\psi$ to J/ψ production.
- Measurements of the energy loss and multiple scattering of heavy quarks in cold nuclear.
- Disentangling various nuclear effects on J/ψ production by contrasting it with open charm production at large positive and negative rapidity.

- Separation of the ψ' from the J/ψ, leading to the first ψ' nuclear dependence data from RHIC.
- Drell-Yan measurements of anti-quark shadowing at small *x* values.
- ϒ and Drell-Yan nuclear dependence measurements at mid-rapidity where x is large.

2.3 Polarized Proton Collisions, and the Gluon and Sea Quark Spin Structure of the Nucleon

Understanding the substructure of the nucleon is of fundamental interest in nuclear and particle physics. The strong nuclear interaction observed between nucleons inside a nucleus is a residual "van-der-Waals" force arising from a more fundamental interaction, Quantum Chromodynamics, between the nucleon's partonic constituents, namely the quarks and gluons. Studying the partonic distributions inside the nucleon can shed light on why and how quarks and gluons are confined inside hadrons.

The striking results, first from the EMC experiment at CERN and then from subsequent experiments at SLAC, DESY, and Jefferson Lab, showed that the total spin of the quarks does not account for the total spin of the proton. These deep-inelastic scattering (DIS) experiments have established that only 10-30% of the proton spin is carried by the quarks and anti-quarks. The rest of the spin must come from the gluon spin and the parton orbital angular momentum. Figure 38 shows the AAC collaboration analysis of the polarized parton distributions for quarks and gluons. SU(3) flavor symmetry is assumed in the analysis, and for sea quarks it is assumed that $\Delta\bar{u} = \Delta\bar{d} = \Delta\bar{s}$. The sea quark polarization is poorly constrained (lower right panel) and gluon polarization is virtually unknown (upper right panel), with the present set of data.

The PHENIX spin program seeks to measure the gluon spin structure function in the proton. Shown in Figure 39 are the different channels that can be used for the extraction of the gluon spin structure function. The existing PHENIX capability is shown in the blue bars. However, precision measurements for heavy quarks with the separation of charm and bottom are only possible with the addition of a precision vertex tracking detector. The green bars display the additional capability supplied by the barrel VTX detector. However, there are significant gaps in this *x*-range that will make it difficult to fully address the spin issue. The FVTX proposed here extends the coverage (red bars) to the lowest and highest *x*-values, $0.001 < x < 0.3$, as well as providing significant regions where multiple channels overlap. These overlaps will provide vital cross-checks that will improve the reliability of global fits to the spin structure functions.

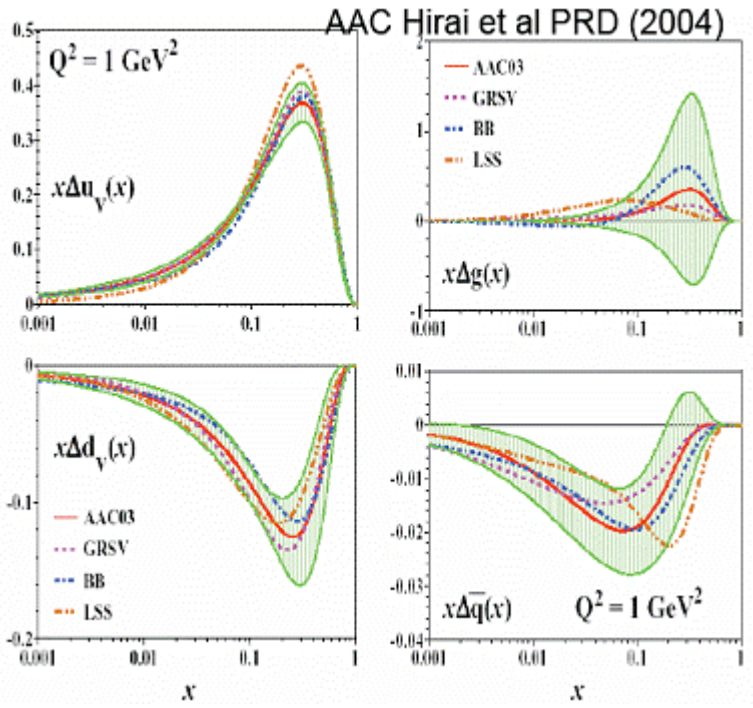

Figure 38 - Global polarized quark and gluon distributions from AAC collaboration. The red line is the result of their fit, and the green band is the total uncertainty with respect to the red line. The other colored lines are alternative parameterizations of these distributions.

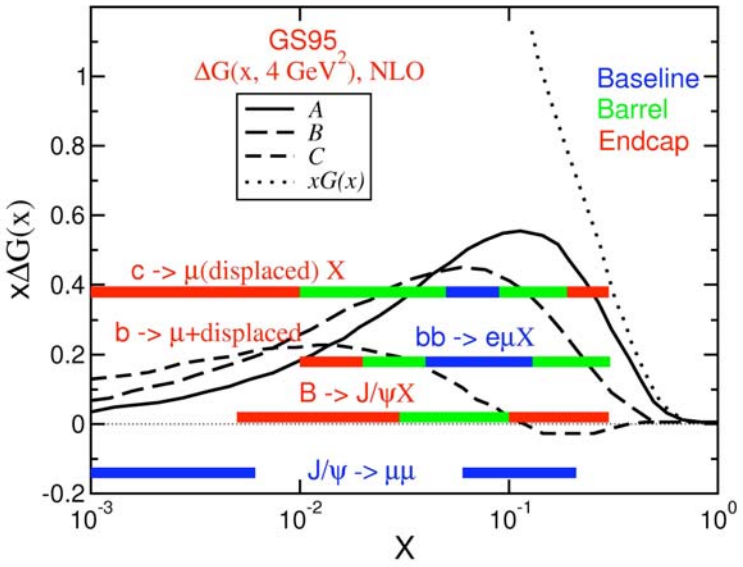

Figure 39 - Expected *x*-range for different channels used to extract the gluon spin structure function. The blue bars indicate PHENIX's existing capability, green bars are for the Barrel upgrade, while the red bars indicate the additional coverage provided by the proposed Endcap vertex upgrade. The curves show various estimates of the expected gluon polarization[xxxviii].

2.3.1 The Role of the FVTX Detector

The FVTX provides significant improvements in *x*-range coverage over a Barrel-only detector, as shown in Figure 39. It also provides a model independent clean separation of light hadron, charm and bottom production. The following list of measurements that are possible with the FVTX detector has been studied by simulating *p*+*p* collisions with PYTHIA and requiring sufficient counts in each exit channel to be able to make a reasonable measurement:

- $c\bar{c}$ production via gluon fusion, measuring D→μX. The *x*-range is extended considerably down to $x = 0.001$ and up to x~0.3, using $D \rightarrow \mu X$, with a displaced muon from charm decay.
- $b\bar{b}$ production via gluon fusion. With the upgrade we can identify displaced J/ψ from $B \rightarrow J/\psi$ decay. This provides coverage for $0.005 < x < 0.3$. The selection of semi-leptonic decays B→μX at high momentum is improved using displaced vertices. This extends the x_{gluon} coverage for these semi-leptonic decays to 0.01–0.3.
- π, K measurements via decay muons or direct measurement of punch-throughs
- Drell-Yan→$\mu^+\mu^-$
- Background suppression for *W* physics events. The main background for a *W* measurement with single muons is muons from heavy flavor decay and light hadron decay and/or punch-through. The heavy flavor background can be identified and rejected based on displaced vertices. The light hadron background can be suppressed with an isolation cut, DCA cuts, and χ^2 cuts on the MuTr+FVTX track fit and on the dE/dx measurement in the FVTX. This could also extend *W* physics to a broader kinematic coverage by measuring low p_T muons from *W* decays.

2.3.2 Polarized Gluon Distribution and Heavy Quark Production

The RHIC-SPIN program provides a new tool to directly collide polarized protons at high energy (shown at leading order in Figure 40) and as such PHENIX has a major goal of measuring the gluon spin-structure function of the proton. At RHIC energy, heavy flavor production is dominated by gluon-gluon interactions as is also shown in Figure 40, and is therefore sensitive to the polarized gluon distribution in polarized p+p collisions.

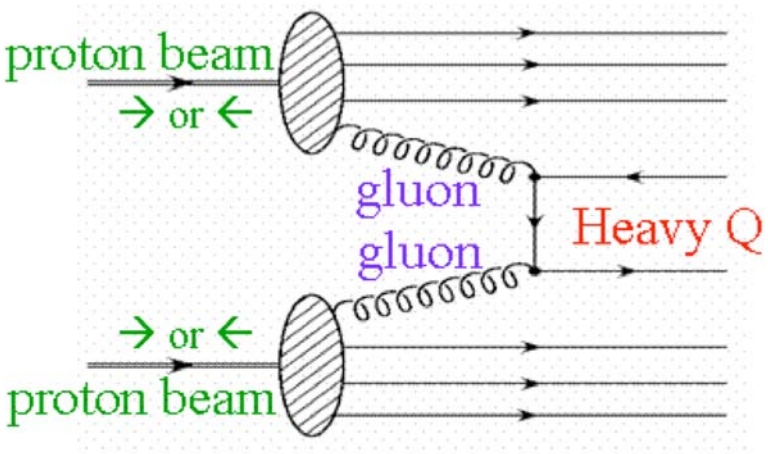

Figure 40 - At RHIC-SPIN, quarks and gluons interact directly at leading order.

Experimentally we measure the double spin asymmetry;

$$A_{LL}^{Q\bar{Q}} = \frac{\sigma^{++} - \sigma^{+-}}{\sigma^{++} + \sigma^{+-}} \sim \frac{\Delta G(x_1)}{G(x_1)} \otimes \frac{\Delta G(x_2)}{G(x_2)} a_{LL}(x_1 + x_2 \to Q\bar{Q} + X)$$

The partonic asymmetry $a_{LL}(x_1 + x_2 \to H + X)$ is normally calculated within the framework of pQCD. In the PHENIX experiment, we will measure the polarized gluon distribution $\frac{\Delta G(x)}{G(x)}$ using many different processes as indicated in [xxxix]. However, in reality, one always faces various backgrounds in the measurement, so the measured signal asymmetry is diluted,

$$A_{LL}^{Q\bar{Q}} = \frac{A_{LL}^{incl} - r \cdot A_{LL}^{BG}}{1 - r}$$

$$\delta A_{LL}^{Q\bar{Q}} = \frac{\sqrt{(\delta A_{LL}^{incl})^2 + r^2 \cdot (\delta A_{LL}^{BG})^2}}{1 - r}$$

where $r = \frac{N^{BG}}{N^{Q\bar{Q}} + N^{BG}}$ is the background fraction, A_{LL}^{incl} and A_{LL}^{BG} are the asymmetries of the inclusive signal and background, respectively. Normally, the background asymmetry itself is not well known, so it is very important to minimize the background fraction. The proposed FVTX detector will significantly improve the purity of the signals both for the light hadron and heavy quark measurements by permitting an additional cut on displaced vertex information.

2.3.2.1 Measurements of Open Heavy Quark Production

In section 3.1.2 a general discussion of the need to remove light hadron decays and punch through hadrons to get a clean measurement of charm and bottom decays is given. Those cuts

presented in that section are relevant here and have been studied in p+p measurements for charm and bottom. Methods for separating charm from bottom as defined in section 3.2 will also be applied to the p+p data.

We have simulated the improvement in determining the double asymmetry measurement A_{LL} for charm and bottom. Figure 41 shows projected experimental sensitivities of double spin asymmetry measurements with (blue) and without (red) the FVTX detector if we can identify prompt muons from open charm and open bottom decay. Also shown in the figure are theoretical predictions for the charm, bottom,and the sum, asymmetry using gluon spin distributions from the world's data fit. The error bars are derived in a similar manner as done in section 2.1.2. A very precise asymmetry measurement is possible over a large p_T range, allowing us to distinguish between zero asymmetries and asymmetries predicted for nominal gluon polarization, even without separating the charm and bottom components. In addition, if we can separate charm and bottom measurements, as was discussed in section 2.1.3, we will provide more sensitive asymmetry measurements as the charm and bottom asymmetries partly cancel over much of the p_T range. Therefore the individual asymmetries are expected to be much larger than the sum of the two. Note that the flavor excitation mechanism can contribute to open charm production, but has not been included in the theoretical asymmetries shown in Figure 41.

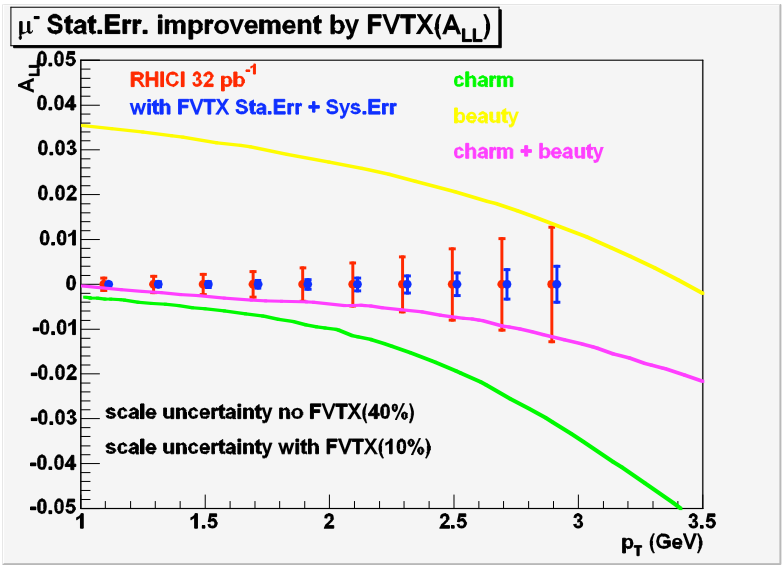

Figure 41 The error bars that would be obtained on an A_{LL} measurement, assuming 32 pb^{-1} integrated luminosity with (blue) and without (red) the FVTX detector.

2.3.2.2 Measurement of Light Hadron Production with the Muon Spectrometers

There is copious production of light hadrons at RHIC. Figure 42 shows the muon p_T spectra from different sources in 200 GeV $p+p$ collisions, where the muons from light charged hadron decays dominate at low p_T (< 3 GeV.) Using recently developed analysis techniques, we can measure inclusive light hadron production with the muon spectrometer, using event vertex and muon penetration depth analysis to statistically establish the hadron and muon event rates. This method

was used in the dAu analysis and is being used now for the 2005 *pp* data analysis of spin asymmetries. The proposed forward silicon vertex detector will enable us to identify muons from light hadron decay on an event-by-event basis, as they tend to have large vertex separations of order of few mm or greater. Furthermore, these light hadrons are dominantly produced through *gg* and *gq* scattering at low p_T, see Figure 43. Such samples can be used to explore gluon polarization since they have good statistics and also cover a wide range of momentum fraction *x*.

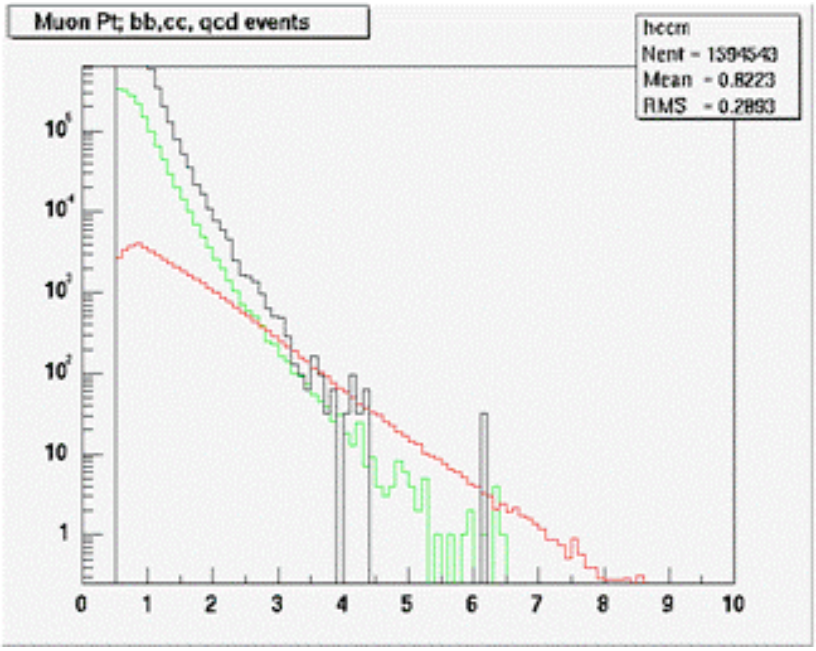

Figure 42 - Muon p_T spectra with different origins from Pythia simulation, as a function of p_T [GeV]. Muons from light charged hadron decays (black); from open charm (green); from open bottom (red).

The improvement in an A_{LL} measurement for hadrons, that can be obtained with the FVTX detector compared to without the FVTX detector is shown in Figure 44 along with theoretical predictions of the asymmetries for different gluon spin assumptions. With the FVTX we enter the realm of being able to distinguish among different gluon polarization predictions, whereas without the FVTX no discrimination can be made.

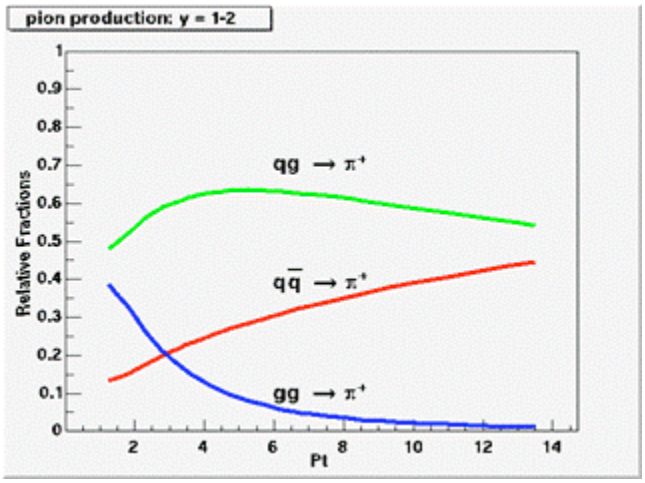

Figure 43 - Partonic origin of charged pions produced within the acceptance of muon spectrometer in pp collisions at $\sqrt{s}$ = 200 GeV.

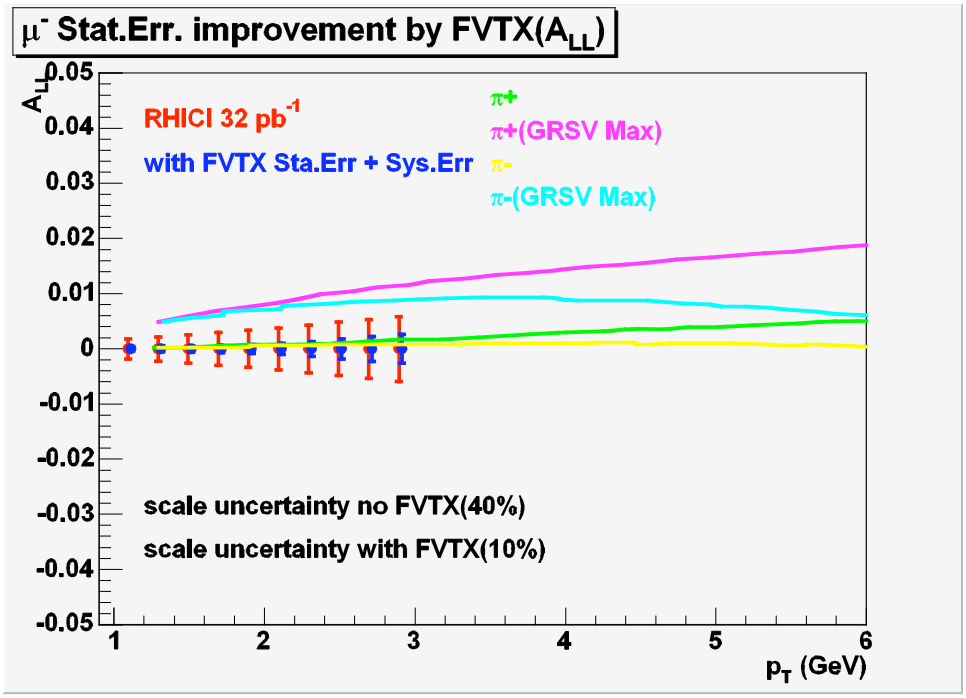

Figure 44 A_{LL} measurement for hadrons obtained with (blue) and without (red) the FVTX detector.

2.3.2.3 Measurements of Heavy Quarkonium Production

Presently the most accurate way to measure the polarized gluon distribution in the nucleon is to study those processes which can be calculated in the framework of perturbative QCD, i.e., those for which the involved production cross section and subprocess asymmetry can be predicted. Heavy quarkonium has been a useful laboratory for quantitative tests of QCD and, in particular, of the interplay of perturbative and non-perturbative phenomena, as the heavy quark pair production processes can be controlled perturbatively, due to the large mass of heavy quarks. The factorization formalism of non-relativistic QCD provides a rigorous theoretical framework for the description of heavy quarkonium production and decay. It successfully describes the inclusive cross section of charmonium production at the Tevatron and RHIC. In *pp* collisions, heavy quark pairs are mainly produced in gluon fusion processes, and therefore, asymmetries are expected to be sensitive to the polarized gluon distribution function in the proton. Another advantage of heavy quarkonium is that it provides a very good event-by-event measurement of gluon "*x*" values since we can almost fully reconstruct the parton collision kinematics. Production of the ground state quarkonia from decays of the higher levels is significant and needs to be taken into account.

During the RHIC run in 2005, PHENIX accumulated 3.8 pb^{-1} of integrated luminosity with an average beam polarization of 47%. This provides the first opportunity to explore the gluon polarization with heavy quarks at RHIC. Figure 45 shows the opposite charge dimuon pair mass

spectrum from run5 *pp* data. The J/ψ signal clearly stands out from the background. There were about 7300 J/ψ candidates from which the double spin asymmetry was measured, see Figure 46.

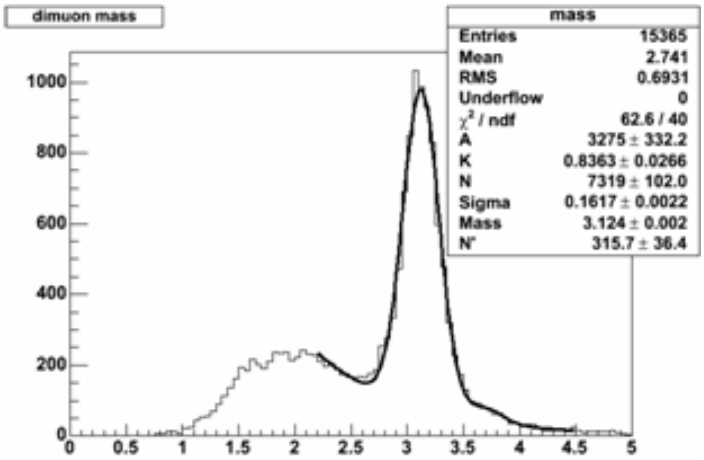

Figure 45 - J/ψ measurement from run5 pp run. The J/ψ peak clearly stands out from the background. The background fraction is about 25% under the J/ψ mass peak.

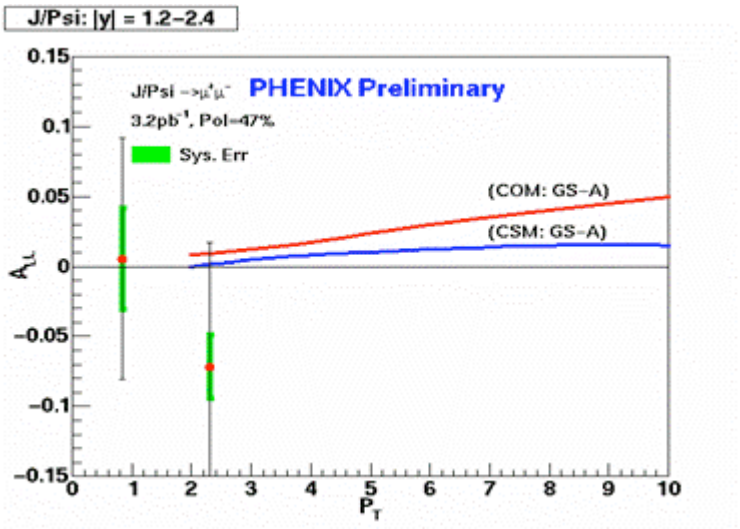

Figure 46 - The first measurement of double spin asymmetry from polarized *pp* collisions at RHIC.

The majority of the background under the J/ψ mass peak is from muons produced by open charm and light hadron decay. As in the case of single muons, at high p_T it is expected that the J/ψ sample will be also contaminated by J/ψ's from *B* decay. The proposed forward silicon vertex detector will help us to improve the prompt J/ψ signal purity by rejecting background muon pairs through a cut on displaced vertices since muons from prompt J/ψ decay point back to the original collision vertex and by improving the mass resolution which will also result in fewer background dimuons below the J/ψ peak.

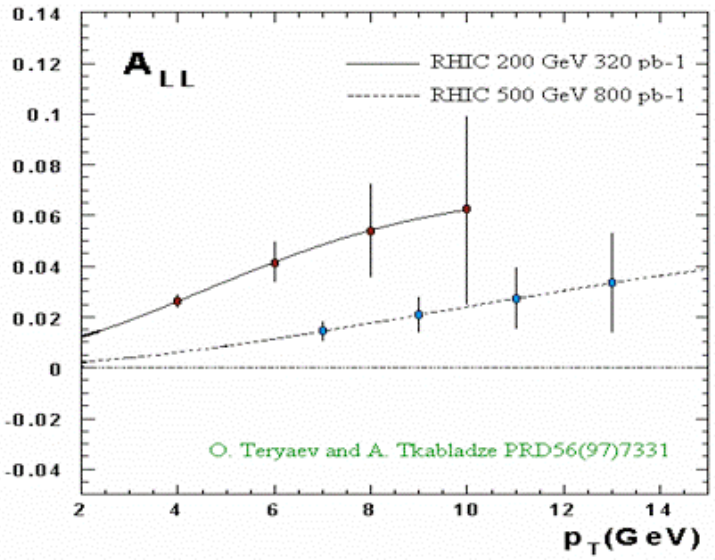

Figure 47 - Expected experimental sensitivities of double spin asymmetry measurements with prompt J/ψ (not from *B* decay).

Figure 47 shows the expected asymmetry measurements for prompt J/ψ (not from *B* decay) with projected luminosities at RHIC, without the FVTX detector. With the FVTX detector, the error bars will be improved because of the reduced systematic errors which come from smaller backgrounds below the J/ψ peak.

J/ψ from bottom decay can also be measured using the FVTX, as was indicated in section 2.1.3.3. Figure 48 shows the correlation between the x of the gluon and the p_z, p_T of the measured J/ψ.

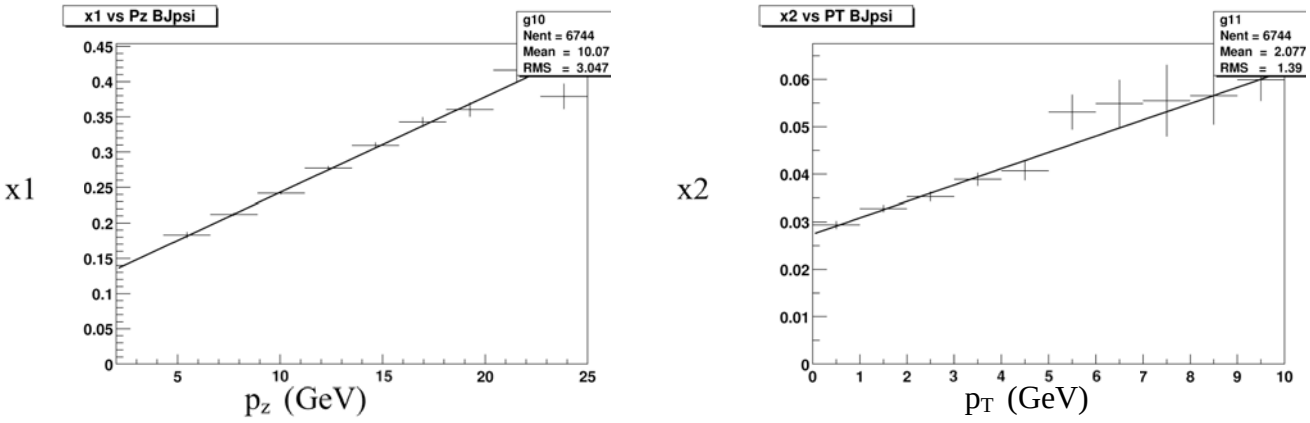

Figure 48 - Left panel: Correlation between gluon x1 and p_Z of J/ψ from B meson decays (PYTHIA simulation.) Right panel: Correlation between x2 and p_T.

2.3.3 Polarized Sea Quark Distributions and *W/Z* Production

W production at PHENIX presents a unique opportunity to study the flavor dependence of (polarized) quark and anti-quark distributions inside the proton. The W^+ is produced by collisions of up and anti-down quarks and identified experimentally through a decay muon (Figure 49):

$$u + \bar{d} \rightarrow W^+ \rightarrow \mu^+ + \nu$$

Similarly, for W^-, the process is:

$$d + \bar{u} \rightarrow W^- \rightarrow \mu^- + \bar{\nu}$$

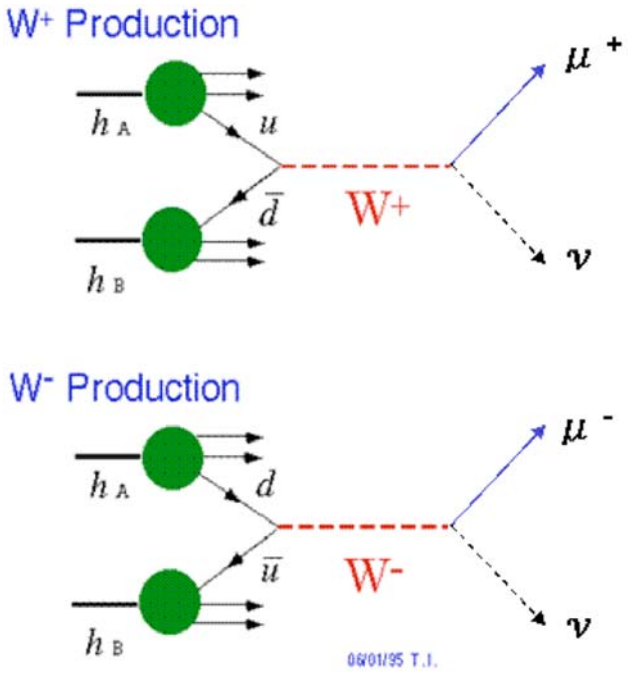

Figure 49 – W production and decay to a muon plus a neutrino.

A measurement of the single spin asymmetry of muons from W+ (W-) production yields a measure of the anti-d and u (anti-u and d) polarization. In order to make a sensitive measurement of these quark and anti-quark distributions, the lepton-ν decay channel should be clearly separated from other W decay channels and the muons in this decay channel should be clearly separated from other sources of muons. We can discriminate among the different decay channels using the FVTX detector by making an isolation cut (the μν channel will not have neighboring tracks from the W event but the other decay channels will) and a DCA cut (muons from hadron or τ decay will show a displaced DCA).

The main backgrounds for a *W* measurement are muons from heavy flavor decay, punch-through hadrons and low energy hadrons which decay within the tracker volume and are mis-

reconstructed into a high-p_T muon. The decay-in-tracker-volume component is shown in Figure 50, along with the muons from W decay. As seen in the figure, the lowest p_T bins (true momentum) make the largest contributions to the fake high p_T background for W measurements.

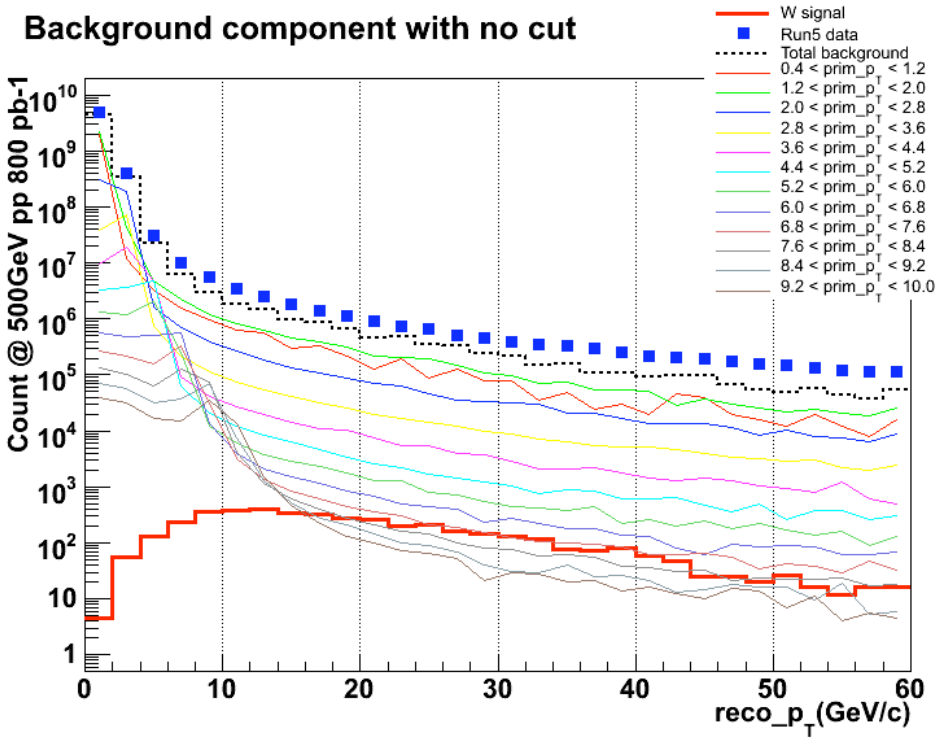

Figure 50 The single muons from W decay (red) and the muons from various p_T bins which are mis-reconstructed to higher momentum. As can be seen, the lowest (true) p_T bins make the largest contributions to the (fake) backgrounds at high p_T.

The background from heavy flavor decays can be identified and rejected based on a displaced secondary vertex; for light hadrons, an isolation cut can be used to suppress the background: in general, a muon from *W* decay has no accompanying jet, while a light hadron normally has associated jet particles around it, and for hadrons which decay in the tracker volume an isolation cut can also be used to reduce the background. Additional discrimination against in-tracker decays comes from a χ^2 cut on a full FVTX+Muon tracker fit,. Reduction of these backgrounds could also allow us to extend the *W* physics to a broader kinematic coverage by lowering the minimum p_T requirement for muons from *W* decays. Figure 51 shows the expected sensitivity and *x*-range for the flavor dependent polarized quark distribution functions measured by the PHENIX muon spectrometers at $\sqrt{s}$ = 500 GeV if we have a clean W measurement. In the next section we describe the performance for rejecting the background muons.

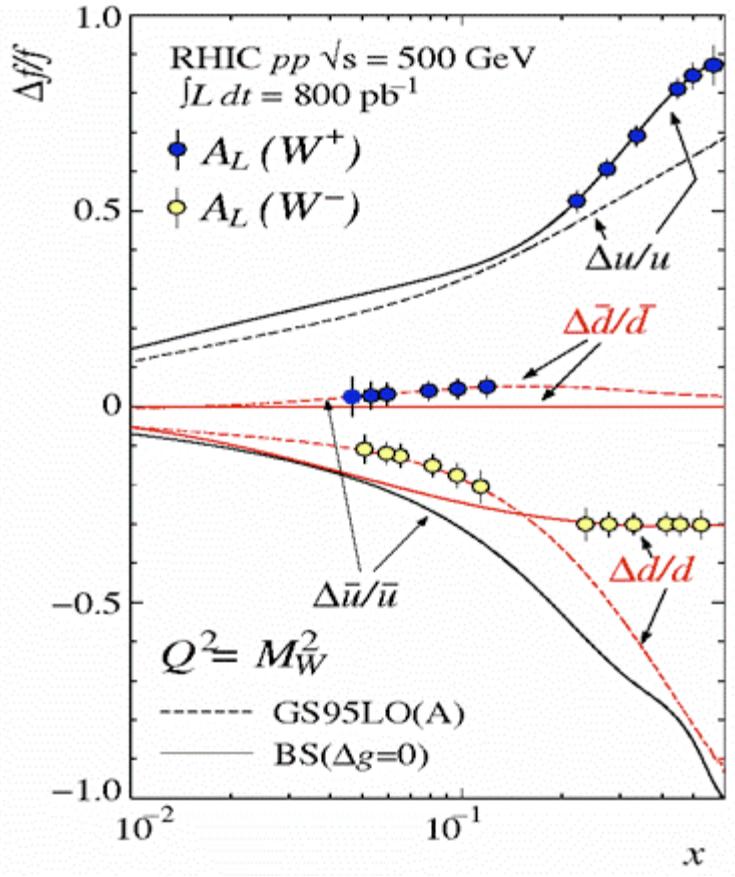

Figure 51 - Expected flavor dependent polarized quark distribution functions measured by the PHENIX muon spectrometers.

2.3.3.1 W Measurements via Single Muons

As indicated in Section 2.3.3 polarized sea quark distributions can be extracted from W measurements via single muons if the background muons are sufficiently low and the μν decay channel can be selected. The background from decay muons from light mesons can be reduced using the FVTX detector just as they are to be reduced for open heavy flavor measurements via a DCA cut on the muon. Pions and kaons which punch-through the muon system, and pions and kaons which decay within the tracker volume can not be removed via a DCA cut since they come from the same primary vertex as the W particles. However, they can be removed to some extent if an isolation cut is placed on the muon since the W decay muon typically has very few particles surrounding it in an event but the hadrons are typically produced within a jet of particles. An isolation cut is illustrated in Figure 52 where a primary particle and secondary particles within a

given cone are shown.

Figure 52 Schematic of an isolation cut: the number of particles in a given layer that are within a cone are counted and if the number found is less than some value the particle is considered to be "isolated" and if it is larger than that value it is not isolated. Left cone illustrates a muon from a W event and the right cone illustrates a hadron associated with a jet of particles.

The number of particle tracks that are found close to a muon are shown for all muons from minimum bias events (blue) and for muons from W decay (red) in Figure 53 versus momentum. As seen, the momentum of muons from W decay is typically much higher than the muons created in a minimum bias event and the number of tracks found surrounding the muon from W decay is typically zero while there are typically several other tracks found surrounding a background muon track. A combined cut on momentum and number of surrounding tracks will provide isolated high momentum tracks which are predominantly from W decay.

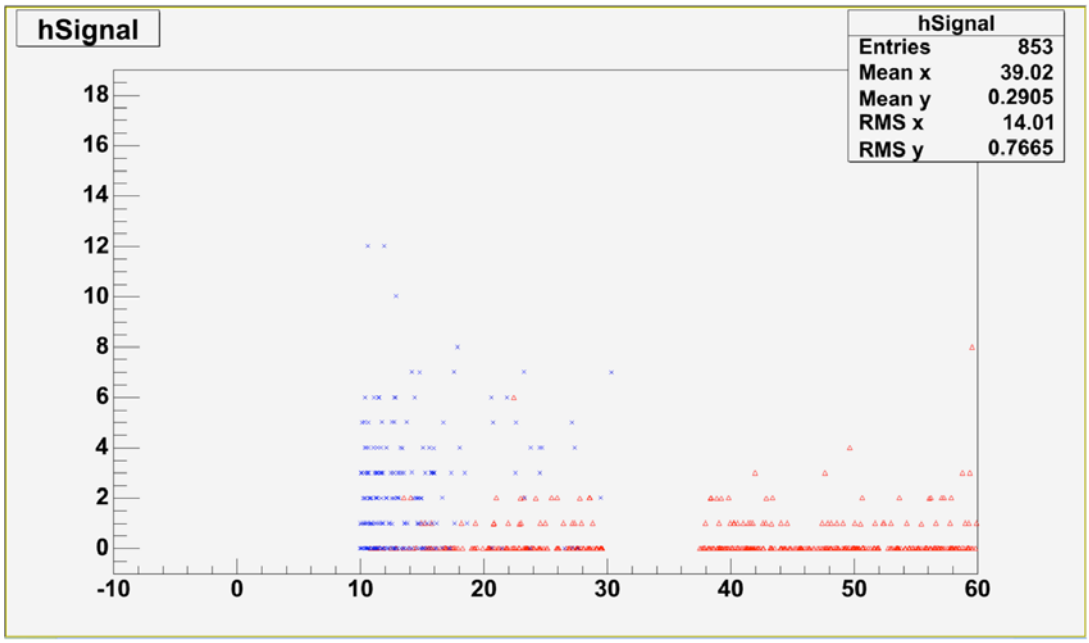

Figure 53 The number of particles (y axis) that are found in an event surrounding a muon from minimum bias events (blue) and muons from W events (red), versus momentum.

To understand the various contributions to the single muon spectrum, relative to the signal from W decays, 5 million minimum bias events and several hundred thousand W events were thrown using the PYTHIA event generator, run through our full simulation, and the number of tracks

reconstructed versus p_T was counted. Additionally, 1.9 billion single π and 1.9 billion single K particles were simulated to look at the contributions from mis-reconstructed particles which decayed in the muon tracker volume. These single particles were normalized based on PYTHIA-generated and UA1-generated events, and the contributions were shown in Figure 50. We then apply the various cuts that have been described above on all reconstructed tracks:

- ≥3 hits in the FVTX (to allow a track to be reconstructed)
- Muon Tracker quality cuts (track reaches last plane of MuID, $\chi^2 \leq 9$, DG0≤4.3, DDG0≤1.9, DS3≤10, DS0≤40, DS3ctpc≤5, DG4≤4.8, mutr_nhits>=12, ref_vtx_rdca≤1.5)
- Muon Tracker plus FVTX track fit $\chi^2 \leq 4$
- FVTX layer 4 measured position – MuTr projected position ≤ 0.5
- Hits in a cone of 0.3 rad <2 (isolation cut)

The background and signal efficiency that is achieved for each of these cuts is shown in Figure 54. The red line gives the efficiency for muons from W, and the other lines show the efficiency when successive cuts are applied to the background. The blue line is the background efficiency with the tight muon tracker quality cuts, the green adds the FVTX acceptance cut of ≥3 hits and MuTr+FVTX χ^2 and DGO cut and black adds the isolation cut. As seen, a large overall rejection factor is achieved for the background. The efficiency for the W is about 50-60%, but there is still room for optimization that would increase the W efficiency. Some caveats to note on the background rejection are: the track fitting uses perfect pattern recognition (we pick the Monte Carlo hits which are known to go with a particular track). We expect some reduction in the background rejection when full track finding is added to the simulation. However, the total rejection factor is already quite large (~ $1x10^5$) so we still expect to retain significant rejection of the backgrounds, allowing a very significant W measurement even if backgrounds are increased.

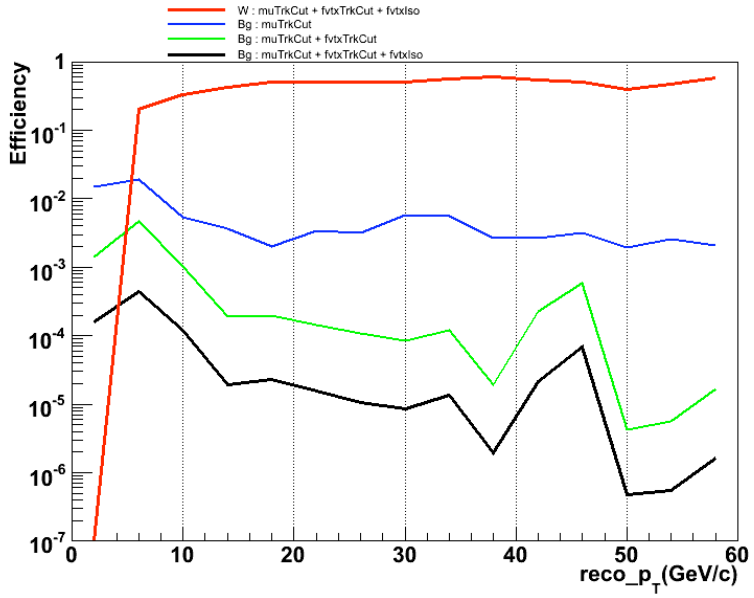

Figure 54 Efficiency for background and and signal tracks in the single particle spectrum, for each successive cut. Red is the W efficiency with all cuts, turquoise is the background with muon quality cuts and FVTX hits ≥3, green adds the MuTr+FVTX χ^2 cut and black adds the isolation cut.

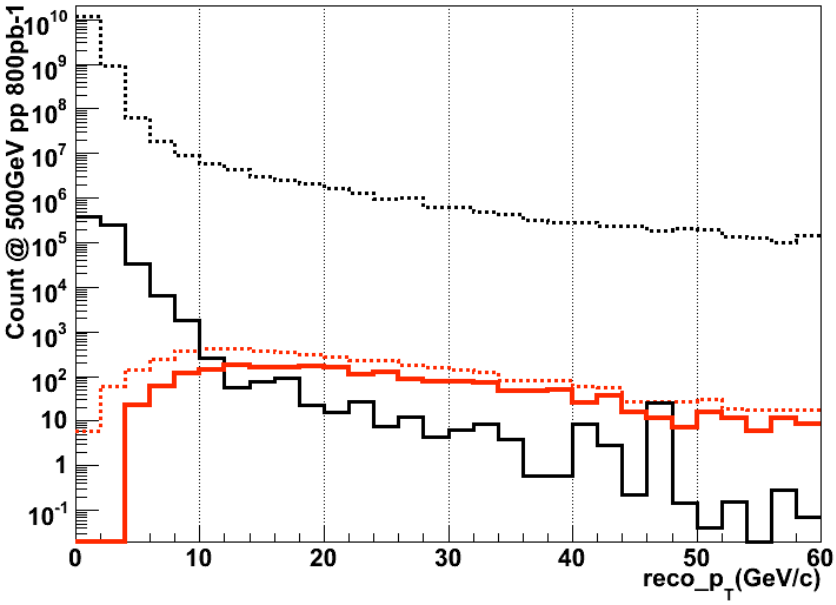

Figure 55 The W signal and background muon contributions before cuts (black dotted is background and red dotted is W signal) and after track cuts (black solid is the background and red solid is the W signal)

Figure 55 shows the signal to background which we achieve with the cuts applied, and the background tracks appropriately normalized to the W signal. The background (black dotted lines) and W signal (red dotted lines) are shown before any track cuts are placed and after the cuts are placed (black solid is the background and red solid is the signal). As seen, the current simulations give signal to background >1 above around 15 GeV p_T.

2.3.4 Physics with Transversely Polarized Beams

The aim of this section on transverse spin is to elucidate another unique measurement that the FVTX upgrade makes possible, namely the measurement of the Sivers gluon distribution in $p^{\uparrow} p \to DX$. To make this understandable, however, it is necessary to briefly introduce the phenomenology of transverse spin and transversity.

2.3.4.1 Introduction to Transverse Spin Phenomenology

In addition to the familiar unpolarized quark parton distribution function $q(x)$ measured in *ep* and *pp* scattering, and the polarized (helicity) distribution function $\Delta q(x)$ measured in $\vec{e}\vec{p}$ and $\vec{p}\vec{p}$ scattering, there is a third equally fundamental distribution function associated with the transverse polarization of the quarks, called the transversity distribution function $\delta q(x)$. In a basis of helicity spin states, the transversity distribution $\delta q(x)$ represents a spin-flip amplitude between two helicity states. However, in a basis of transverse spin states the transversity distribution $\delta q(x)$ has a probabilistic interpretation similar to that of $\Delta q(x)$ in a helicity basis.

For this reason, a measurement program involving transversely polarized protons has been developed at RHIC to measure $\delta q(x)$.

Transverse single spin asymmetries (SSAs) can be produced in a number of ways[xxxix]. The simplest mechanism is to observe the asymmetry proportional to the triple product of spin *S*, beam momentum *P*, and observed transverse momentum p_T , $A_N \propto S \cdot (P \times p_T)$, in inclusive hadron production $p^{\uparrow} + p \rightarrow h(p_t) + X$. However[xl] this asymmetry is suppressed by a factor $\alpha_s m_q / p_T$ and so this mechanism is not useful for the exploration of the transversity distribution function $\delta q(x)$.

Other mechanisms for SSAs arise when one (necessarily) takes into account the effect of initial-state parton transverse momentum k_T. Sivers showed[xli] that a k_T-dependent quark distribution for a transversely polarized nucleon, anti-symmetric with respect to nucleon spin-flip, can be a source of SSAs. This distribution (now called the Sivers distribution) describes an initial-state correlation between the transverse spin of the nucleon *S* and the parton transverse momentum k_T, and thus contains a tremendous amount of information about the structure of the nucleon. The asymmetry it produces is proportional to $A_N \propto S \cdot (P \times k_T)$.

Another mechanism involving parton transverse momentum k_T is the Collins-Heppelmann effect[xlii] whereby the final-state jet momentum P_{jet} is correlated to the spin and initial state k_T and produces an asymmetry $A_N \propto S \cdot (P_{jet} \times k_T)$.

The three mechanisms described so far all involve the transversity distribution $\delta q(x)$ through the transverse spin *S*. There is another mechanism to produce a transverse SSA, noted by Brodsky, Hwang and Schmidt[xliii]. Final state interactions between the struck quark and the spectator system can produce such asymmetries. We will not concern ourselves here with this mechanism, because the asymmetry we are most interested to discuss does not require this mechanism. However, such final state interactions could *modify* the asymmetry of interest.

The Sivers idea can be invoked to define a Sivers gluon function[xliv], and that is the topic of most interest to us here.

2.3.4.2 Measurement of the Sivers Gluon Distribution in $p^{\uparrow} p \rightarrow DX$

Recently[xlv] a new window into the gluon structure of the nucleon was opened by realizing that a measurement of the transverse single spin asymmetry in $p^{\uparrow} p \rightarrow DX$ is uniquely sensitive to the Sivers gluon distribution function, see Figure 56. There are two channels that dominate open charm pair production; *s*-channel quark annihilation $q\bar{q} \rightarrow c\bar{c}$, and the gluon fusion process $gg \rightarrow c\bar{c}$. Note that the possible production of charm due to flavor excitation has not yet been included. Gluons do not carry transverse spin, therefore for **both** of these channels there cannot be any polarization of the final state charm quarks if the initial state protons are only transversely polarized. The lack of final state quark polarization rules out any Collins effect, leaving the Sivers distribution as the only source of a single spin asymmetry.

The FVTX upgrade can make such a unique measurement idea into a reality. As already discussed in other sections of this proposal, *D* production can be tagged on an event-by-event basis, therefore a very clean sample of $p^{\uparrow}p \to DX$ events can be produced for subsequent SSA analysis. This same physics will also be accessible in the central arms, using the VTX upgrade, but this was not known at the time of the VTX proposal because the Anselmino et al. paper was not published.

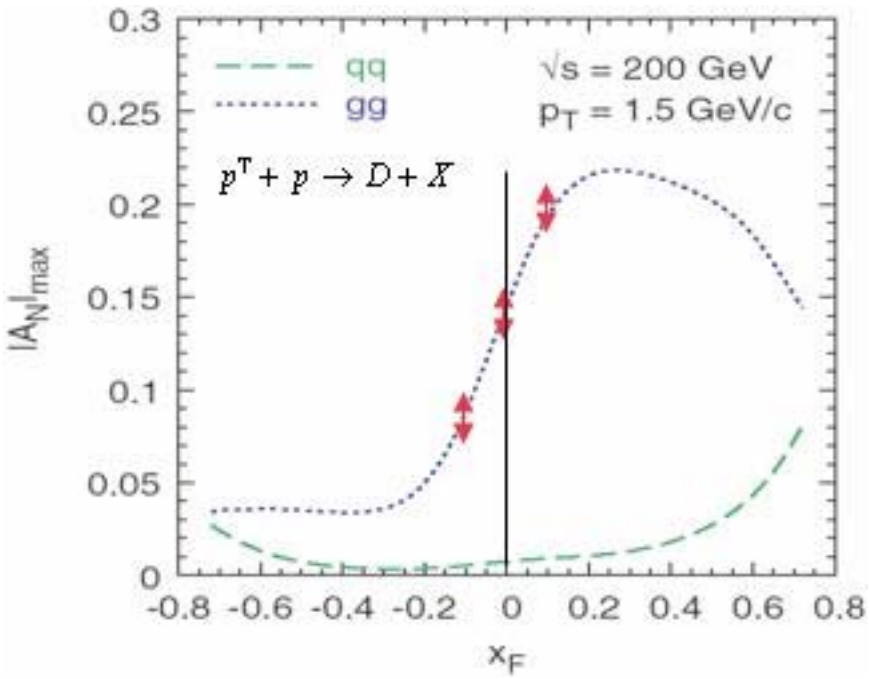

Figure 56 - Maximized values of transverse single spin asymmetry A_N for the process pp->DX as a function of x_F at fixed transverse momentum calculated using saturated Sivers function. The dashed line corresponding to a maximized quark Sivers function (with the gluon Sivers function set to zero), while the dotted line corresponding to a maximized gluon Sivers function (with the quark Sivers function set to zero). Red marks indicate the x_F range that the PHENIX upgrade detectors can measure.

2.3.5 Tests of pQCD Model Calculations and Providing a Baseline for pA and AA Measurements

Spin plays a key role in fundamental interactions. The experimental study of spin observables (polarization, spin correlations and asymmetries) provides information on the most important dynamical properties of particle interactions. Moreover, the spin studies give us more complete information than the measurements of spin-averaged quantities and allow us to make a detailed comparison of various theoretical model calculations with experiment. The fact that the nucleon spin composition can be measured directly by experiments has created an important frontier in hadron structure physics, has had a crucial impact on our basic knowledge of the internal structure of the nucleon, and will eventually lead us to a better understanding of strong interaction phenomena. As an example of how current theory can help us to understand spin dependent QCD dynamics, Figure 57 shows an NRQCD prediction for the double spin

asymmetry of the J/ψ in two different helicity states. Experimentally we can identify the helicity state by examining the dimuon angular distribution from the J/ψ decay.

Before using charm and bottom for spin and heavy ion physics, we need to test the next-to-leading-order (NLO) pQCD calculations for heavy-quark production. Qualitatively, low-p_T charm and bottom production are dominated by gluon-fusion, while production at high-p_T is expected to be dominated by the hard-scattered gluon splitting into a $Q\bar{Q}$ pair[xlvi]. Present data on charm and bottom production is scarce and of limited statistics. Data from polarized *pp* collisions at RHIC will provide critical information on heavy quark production mechanisms.

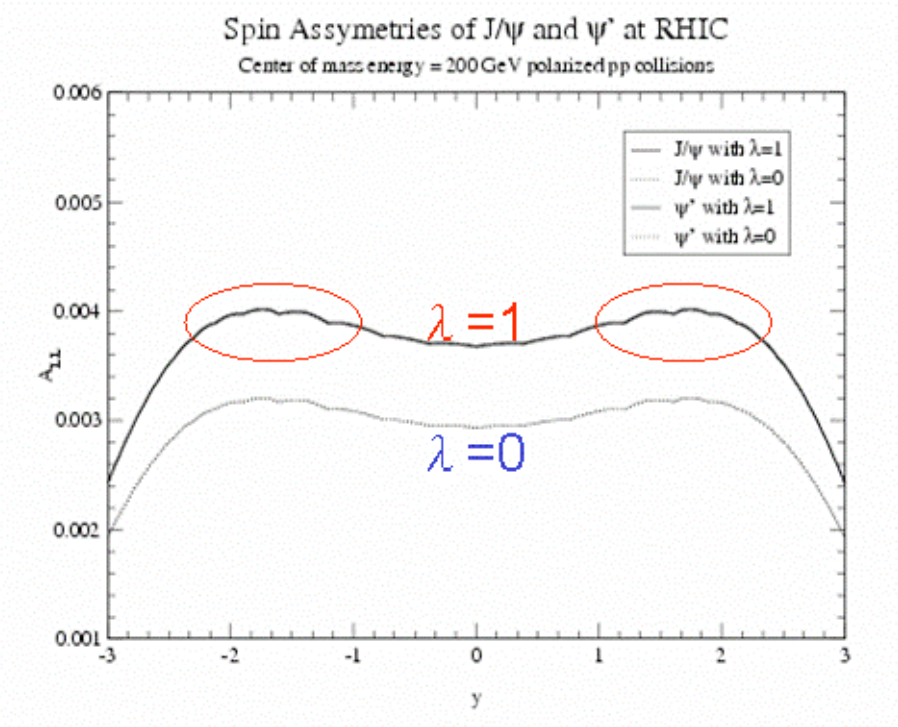

Figure 57 – Predicted double spin asymmetry for charmonium at RHIC[xlvii]. The asymmetry value depends on the final state charmonium polarization, which can be tested experimentally. The red circles indicate the acceptance region for the PHENIX muon arms and FVTX detector.

There is also significant uncertainty in the primary particle production mechanism for charm. Leading-order calculations typically calculate the production from gluon-gluon fusion (indicated in Figure 58, left) but flavor excitation (shown in Figure 58, right) is predicted to give comparable or even larger contributions to the open heavy-flavor production.

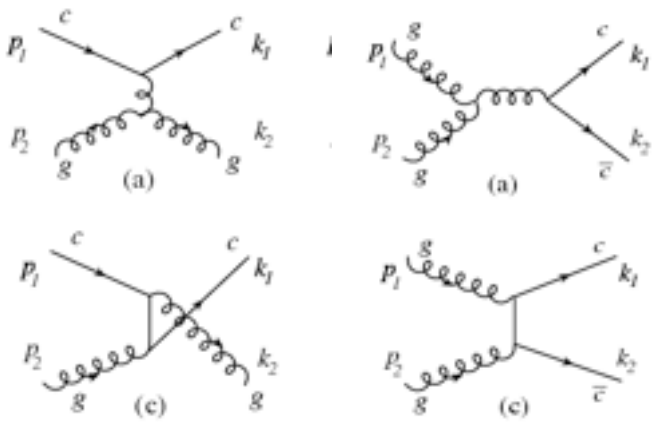

Figure 58 Heavy flavor production diagrams from flavor excitation (left) and gluon fusion (right)

In the first case, the correlated c-cbar production should give a strong back-to-back correlation in two-particle correlation measurements, and in the second case, there will be no correlation since the D mesons would come primarily from single charm production. The difference between these two correlation measurements is shown Figure 59 in where the gluon splitting (flavor excitation) shows no backward peak in a df spectrum, but the flavor creation process shows a strong backward peak in the df distribution. With the FVTX, we can measure the two particle correlations of c-cbar produced in each event and should be able to determine what the dominant production mechanism is.

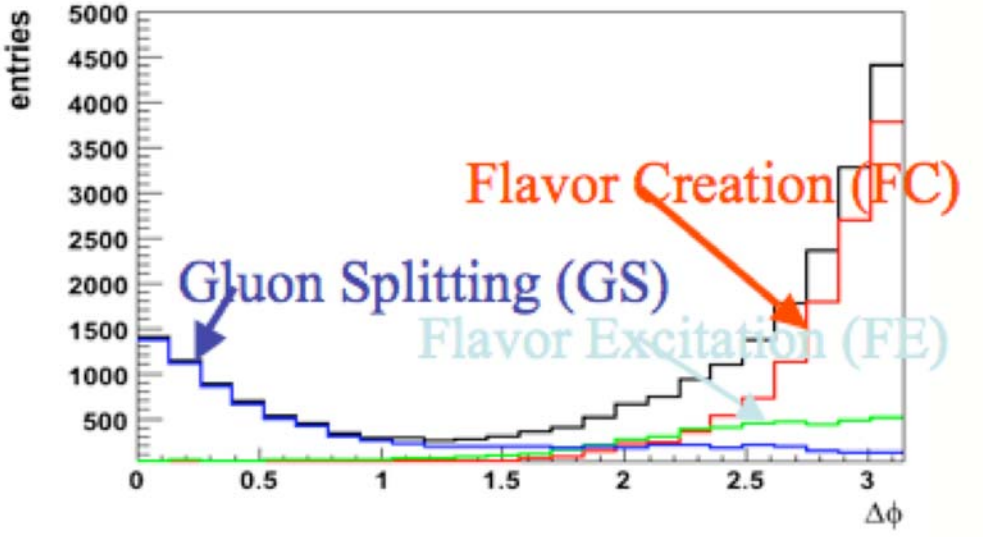

Figure 59 Back-to-back correlation expected for flavor excitation is shown in blue and for flavor creation (gluon-gluon fusion) is shown in red. Note the strong correlation when c-cbar pairs are created in flavor creation as opposed to the non-existent correlation that would be true if single charm production were the primary production mechanism.

2.3.6 Summary of Physics Addressed by the FVTX in Polarized *pp* Collisions

In summary, the FVTX detector will significantly improve on the following physics in polarized *pp* collisions:

- Probing the polarized gluon distributions via muons from light hadron, open charm and bottom decay.
- Measurement of flavor dependent polarized quark distributions via muons from *W* production and providing the first experimental test of SU(2) flavor symmetry for polarized sea quarks.
- Providing a vital cross check of pQCD calculations for light and heavy hadron production in polarized pp collisions.

2.4 Trigger Plans

An increasingly important issue as RHIC luminosities rise is to be able to capture all (or a sufficient) amount of the physics signals through the DAQ onto archival storage. The first line of attack on this issue is to use fast Level-1 triggers to identify interesting physics events and make sure as many of them as possible are read out, and are not prescaled away. Estimates of the needed rejection factors beyond those from the present muon identifier based level-1 triggers are estimated in Appendix C (Section 8). They are listed in Table 1.

Table 1 – Level-1 Rejection factors needed beyond those available from the present muon triggers.

	Single muons		Di-muons	
	p+p	Au+Au	p+p	Au+Au
2008 RHIC-I	~1/20		1	~1/5
RHIC-II	~1/100		~1/1.4	~1/40

Triggers involving new upgrade systems would probably be formed by first finding tracks in various subsystem independently (muon identifier, muon trigger upgrade, FVTX, etc.), then combining these in the final stages to allow matching of tracks and use of information such as a rough momentum determination from one subsystem in the final cut decisions applied to integrated tracks from both (all) subsystems. This would be implemented on high-speed level-1 trigger boards containing state-of-the-art FPGA's.

Physics triggers that are needed include:

- $B \rightarrow J/\psi+X$ where the existing muon trigger would identify a muon pair, the muon trigger upgrade would assure these tracks came from the primary vertex using its RPC pad pointing and time-of-flight information; and then this combined road would be matched to a FVTX pair which would be required to have a detached vertex ($\Delta Z_{vertex} >$ 0.1 cm).
- Other pair triggers (e.g. prompt J/ψ, ψ' and Υ) could be formed by requiring a prompt rather than downstream vertex.

- Single muon D and B decays using single-track combined roads matching FVTX tracks that have detached vertices. In this case a vertex cut of 400μm < ΔZvertex < 1 cm could be made, and for the lower momentum tracks (as identified by the muon trigger momentum measurement) where the rejection might not be sufficient a momentum-dependent prescale could be applied. While at higher momentum all detached vertex tracks could be kept.
- It might also be advantageous to use the FVTX for a more efficient minimum-bias (vertex) trigger in p+p collisions, because the present BBC-based trigger only achieves an efficiency of ~55% because of the low multiplicity of tracks in to the BBC in p+p collisions. The much larger acceptance of the FVTX should allow it to provide a much more efficient trigger..

More details on the developing trigger plans are discussed in Appendix B (Section 7), and further discussion of the synergy of the different subsystems and upgrades is discussed in Appendix D (Section 9).

The Iowa State University group is actively developing the trigger plans and associated hardware with the help of a STTR grant along with Northern Micro Design Inc.

After events are selected and passed on by the level-1 triggers, they can then be examined further by level-2 triggers implemented in a large array of parallel processors as has been done already at PHENIX. These processors can do fast reconstruction of the events including full combinations of the different subsystem information and could then make more refined cuts including mass cuts for pair triggers, or selecting high momentum tracks using the higher resolution information from the muon tracks which would only be available at level-2 and above (not in level-1). This resulting information could then be used to cut the data rate down further, or just to allow creation of filtered event streams enriched for the most important physics topics that would enable fast offline analysis for timely physics results.

2.5 Si Endcap Event Rates

The event yields in the previous sections are summarized below in Table 2. They assume an integrated p+p luminosity of 33 pb^{-1} and Au+Au luminosity of 2.5 nb^{-1}. The FVTX yields for semi-leptonic heavy quark decays are about an order of magnitude larger than for the VTX silicon barrel, due to the larger acceptance of the silicon endcap. The *B* decay rates would benefit most from the increased luminosity at RHIC II . Details of the rate estimates and additional count estimates for d+Au collisions and for p_T bins can be found in Section 8.5.

Table 2 – Triggered rates for RHIC-II p+p and Au+Au in one week of running. Integrated luminosities are 33 pb^{-1} for p+p and 2.5 nb^{-1} for Au+Au. The semi-leptonic decay rates are before application of a vertex cut.

Observable	Counts per RHIC-II p+p week	Counts per RHIC-II Au+Au week
D → μX	~ 71M	~180M
B → μX	~880k	~2.3M

$B \rightarrow J/\psi\ X \rightarrow \mu\mu$	~650	~1.7k

3 FVTX Detector Performance

In this section we will discuss the general performance of the FVTX and its simulation. The physics-driven requirements for the FVTX silicon endcap detector design includes:

- Sufficient position accuracy so that the displacement resolution of a track with respect to the collision point is less than the displacement produced by the $c\tau$ of charm and bottom decays
- Excellent accuracy for the primary vertex (<200 μm in z) using all tracks seen in the FVTX as well as those from the VTX (central rapidity barrel) vertex detector; with high efficiency (> 90%) even for p+p collisions.
- Low enough occupancy to allow accurate track finding in Au+Au central collisions. Occupancy levels of <2.8% are achieved.
- Ability to match tracks from the muon arm (muon tracker and muon identifier) to those in the FVTX silicon mini-strips, even in Au+Au central collisions..

In addition to these detector requirements, the FVTX detector provides a number of additional features which allow it to contribute to particle identification and identification of specific physics decay channels. These include:

- Full azimuthal and large rapidity coverage allow one to test whether a given particle was produced in isolation within the event or within a jet of other particles
- 3-bit ADC(or more) information is available from each hit strip, allowing the possibility of having energy loss information for a track
- Additional measurement points on the track trajectory provides improved dimuon mass resolution.
- χ^2 values for tracks passing through the silicon will be large if the momentum is small and has been mis-reconstructed to a large value. Therefore, cutting on the χ^2 should discriminate against mis-reconstructed tracks.

The discussion of the above requirements and the simulations that establish the FVTX performance to satisfy these requirements follows.

3.1 Simulation Code

The FVTX detector sensitive and non-sensitive volumes have been simulated in the PHENIX GEANT framework, PISA. The simulation includes the beam pipe, the central silicon barrels, support structures, and the forward silicon tracker. The radiation length per station in the forward region is ~1.8-2.4% . This 1.8-2.4% includes sensor, readout chips, readout bus, and support panels and varies from the inside radius to the outside radius. This radiation length is achievable

because we are implementing a design that has minimized the readout bus and the mechanical structure, and we are able to thin the chips. We are still striving to minimize this thickness, in particular for the critical first disk. The output of the PISA simulation includes a description of the materials and detector volumes in the GEANT simulation (to be used by the offline code) and the x, y and z positions of tracks that hit sensitive silicon volumes.

The detector volume description and the x,y,z positions are fed into the offline code (Fun4All) where the detector response is simulated and track reconstruction takes place. The simulation includes a full digitization of the PISA hits into hit silicon strips, cluster finding of strips which belong to one hit is performed, and a centroid fit is applied to each cluster. The centroid positions of the clusters belonging to a given track are then used in a Kalman Filter track fit. The parameters from the track fit are used to project the track to the event vertex and extract the distance of closest approach (DCA) of the track to the primary vertex. This DCA value is then used to discriminate among tracks which originate from the primary vertex and tracks which come from a displaced secondary vertex. In the simulations that include the muon spectrometers, tracks are found in the muon system and matched with tracks in the FVTX and a complete Kalman Filter track fit is applied to get the correct track in the FVTX. Missing in this full track reconstruction is a track finding algorithm for the FVTX tracks. While this algorithm will most likely be patterned after the MuTR track finding algorithm, we have not implemented this yet primarily because the occupancy in the FVTX is much less than that in the MuTR so FVTX track finding should be much easier. At this point, we use Monte Carlo information to combine hits together into tracks. See section 3.5 for a discussion of the occupancy.

3.2 Distance of Closest Approach Measurement

Figure 60 shows the basic principle of using the FVTX endcap silicon detector to detect secondary tracks which have been produced at a displaced vertex. A D meson is created at the primary vertex where the two beams collide. It travels a distance proportional to its lifetime and then decays semi-leptonically into a muon. The muon travels off at a different angle (due to the decay process), passing through four silicon planes with 75μm radial pitch. The reconstructed muon track has a small but non-zero *distance of closest approach* (DCA) to the primary vertex – typically 200-300μm - unlike particles from pion and kaon decays, which have a much larger average DCA and prompt particles which have a DCA that is nominally zero.

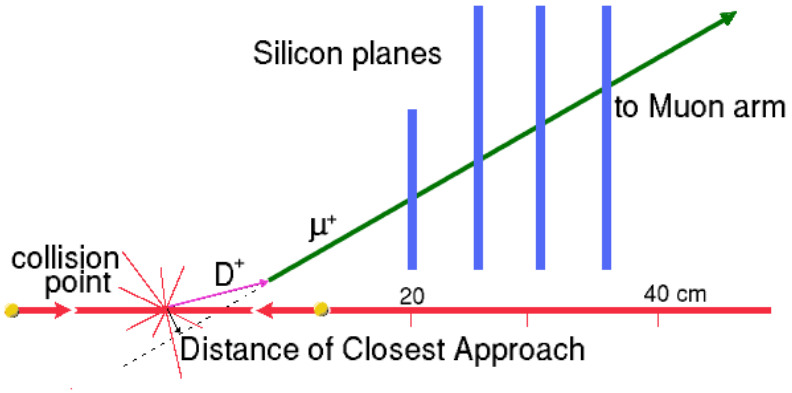

Figure 60 - Principle of operation of the FVTX silicon endcap detector in the r-z plane. A D meson is produced at the collision point. It travels a distance proportional to its lifetime (purple line), then decays to a muon (green line). The muon's trajectory is recorded in the four layers of silicon. The reconstructed muon track (dashed line) has a small, but finite distance of closest approach (dca) to the collision point (black line). The primary background is muons from pion and kaon decays, which have a much larger average DCA.

Figure 61 shows the number of layers of active silicon in the VTX and FVTX detectors traversed by muons as a function of the track angle (y-axis) and primary vertex position (x-axis). The crosshatched magenta region corresponds to tracks that hit all four of the FVTX silicon layers and the crosshatched red region corresponds to tracks that hit 3 layers, indicating that we have met our goal of 3 or more FVTX hits over much of the muon arm acceptance ($10° < \theta < 34°$). Most of the tracks also first traverse one or both of the central barrel silicon pixel layers (areas above the two blue 'barrel' lines). These additional hits will provide useful track confirmation for the pattern recognition, improve the DCA measurement, plus provide a precise measure of the azimuthal angle of the track, which the FVTX would otherwise only roughly reconstruct.

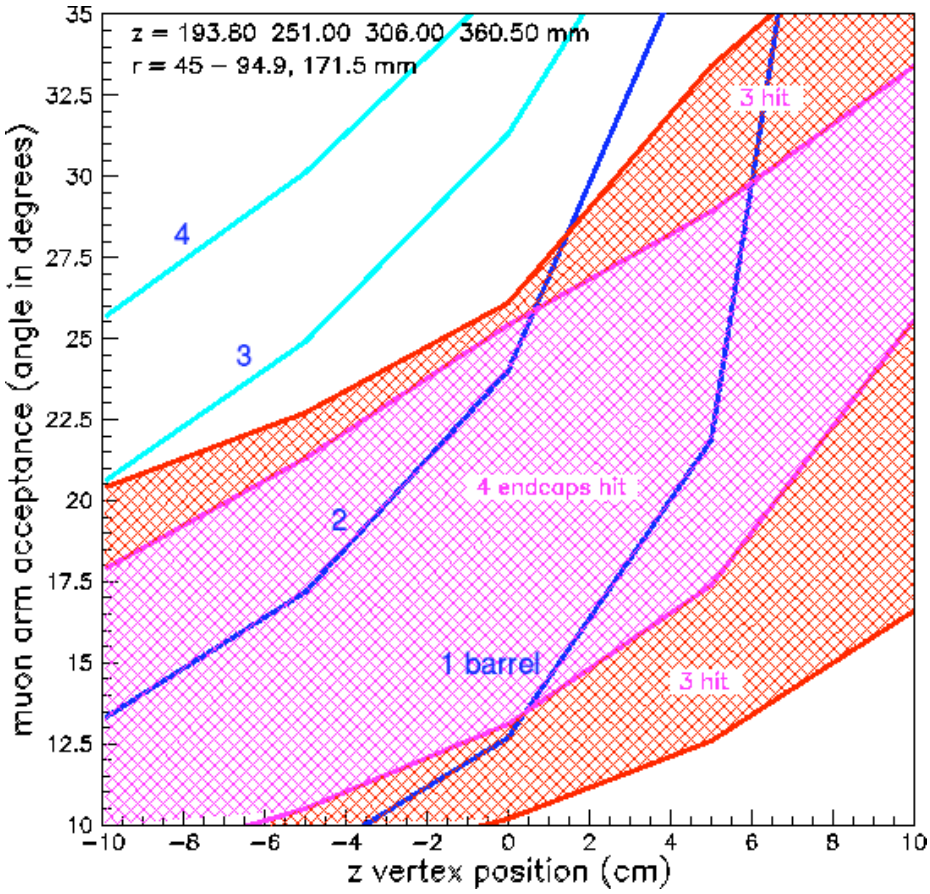

Figure 61 - Plot of vertex silicon layers hit as a function of muon track angle (y-axis) and primary vertex position (x-axis). The magenta crosshatched area includes tracks that hit all four FVTX layers (labeled endcap hits), while the red hatched area has three VTX hits. The area above the dark blue lines (labeled barrel) indicates the number of barrel pixel layers hit, either one or two. Over much of the FVTX active area, at least one barrel pixel layer is also hit.

The measured DCA distributions have been produced for prompt, single muons of various momenta using our simulation code, to establish the DCA resolution of the detector. In Figure 62 the sigma of the DCA distributions in r (resolution which is approximately perpendicular to the strips and gives the best measurement) and phi (resolution which is approximately parallel to the strips) are shown for the FVTX tracker alone (red) and the FVTX plus VTX trackers (black). The improvement in the DCA resolution for the combined system compared to the FVTX system alone comes because the first pixel layer in the VTX detector is typically much closer to the vertex point than the first FVTX layer, and this layer provides the first hit on a track for many tracks which pass through the FVTX system, as seen above. The resolution improvement is primarily in the phi direction, which is the good measurement direction for the VTX detector, and a small improvement is obtained in the r direction, which is the good measurement direction for the FVTX detector. All subsequent simulation results will be for the combined VTX plus FVTX systems.

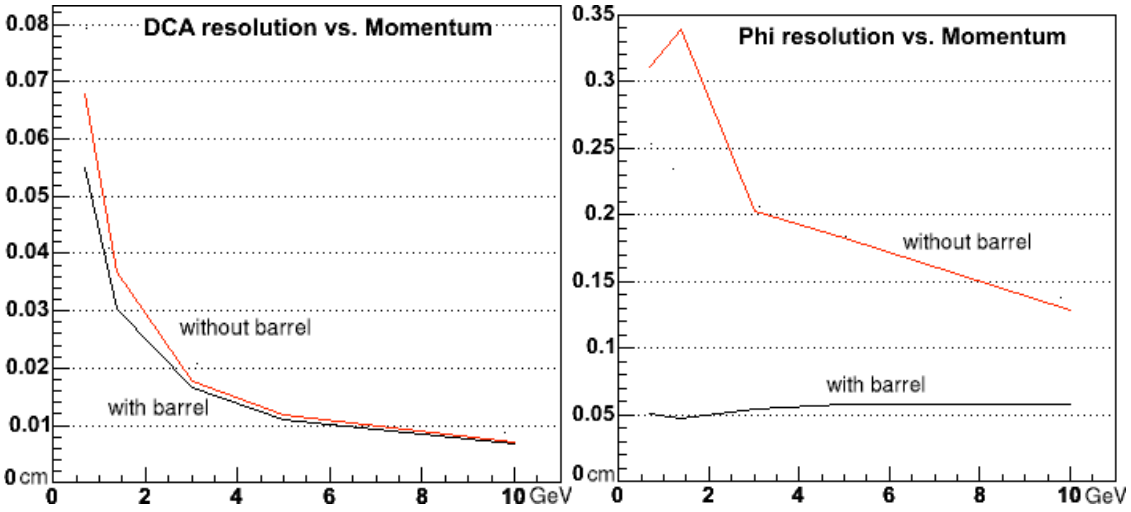

Figure 62 The DCA resolution in r (left) and phi (right) for just the FVTX (red) and for the FVTX plus VTX hits (black). Note that the resolution improvement is primarily in the phi coordinate, which is the good measurement direction for the VTX.

The DCA as a function of momentum and strip width, is shown in Figure 63. The resolution obtained in r is approximately 100 μm at high momenta and the resolution obtained in phi is approximately 500-600 μm.

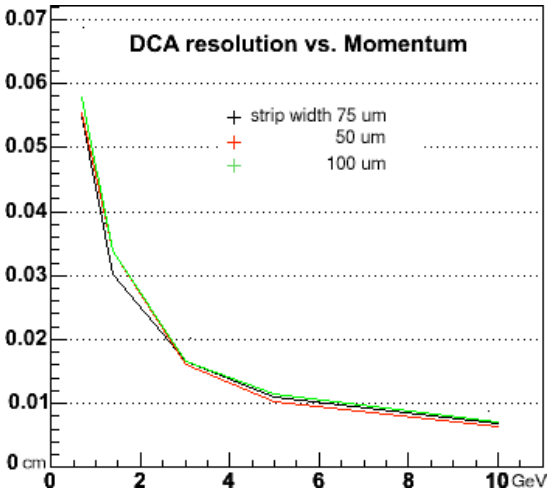

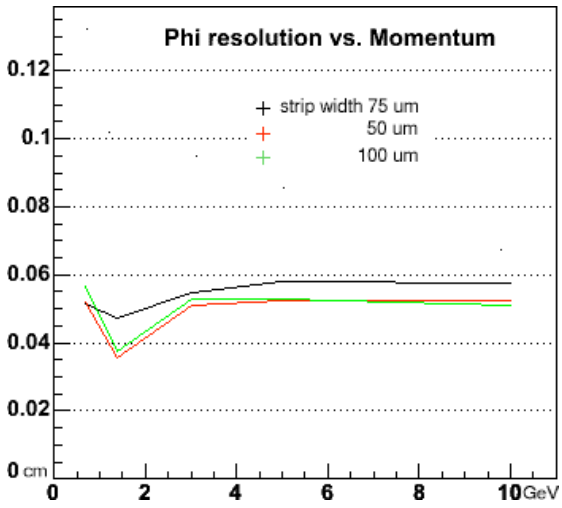

Figure 63 - Top panel: The DCA resolution in the r direction, versus ptotal, for prompt muons and a detector with 75 μm (red) and 50 μm (black) strip pitch. Bottom panel: the same, except the DCA resolution is in the phi direction.

The radial resolution is almost completely independent of the strip-width in this strip-width regime, indicating that the resolution is entirely dominated by the multiple scattering in the material. Since we get similar DCA resolutions for 50, 75 or 100 μm strips, we have chosen a strip pitch of 75 μm for our detectors primarily to minimize the number of channels required while keeping the occupancy in Au+Au events to a tolerable level. An additional factor that was considered was the implication on the physical size of the FPHX chip for different strip pitches. A 100 μm pitch would have given a chip that was > 1.2 cm, felt to be a little to long or would have required a pitch adaptor. Both are undesirable.

We are in the process of studying whether the strips in each station should be tilted with respect to each other to improve the phi resolution, and thus allow a tighter three-dimensional cut on the DCA of tracks. If the strips are tilted at 11° with respect to each other in two out of the four stations, then the phi resolution shown in Figure 64 is obtained. As can be seen from the figure, the r resolution is maintained and the phi resolution is improved by approximately a factor of two.

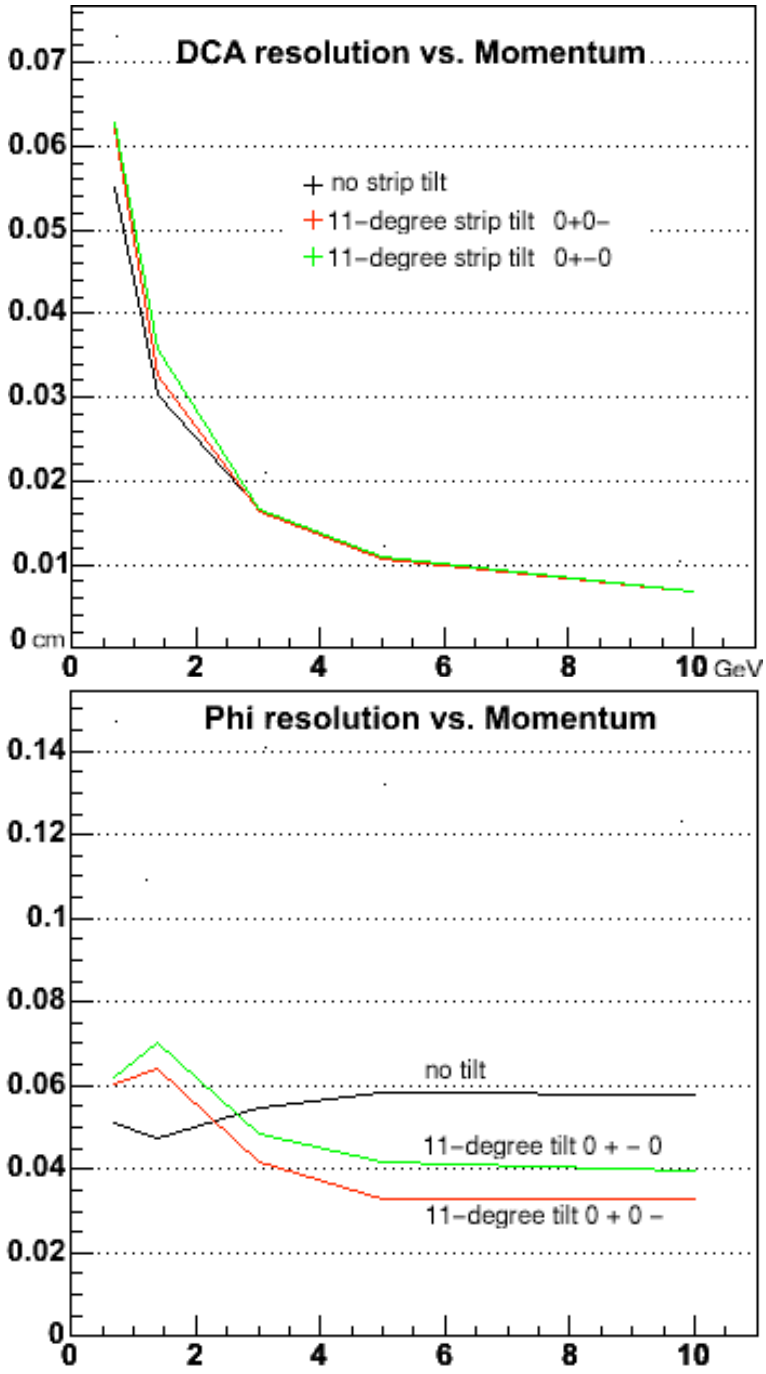

Figure 64 The DCA resolution in r (top) and in phi (bottom) for a detector which has all strips oriented with zero degrees with respect to a circular chord and the same for a detector which has two stations with strips oriented at 11 degrees with respect to the baseline strips.

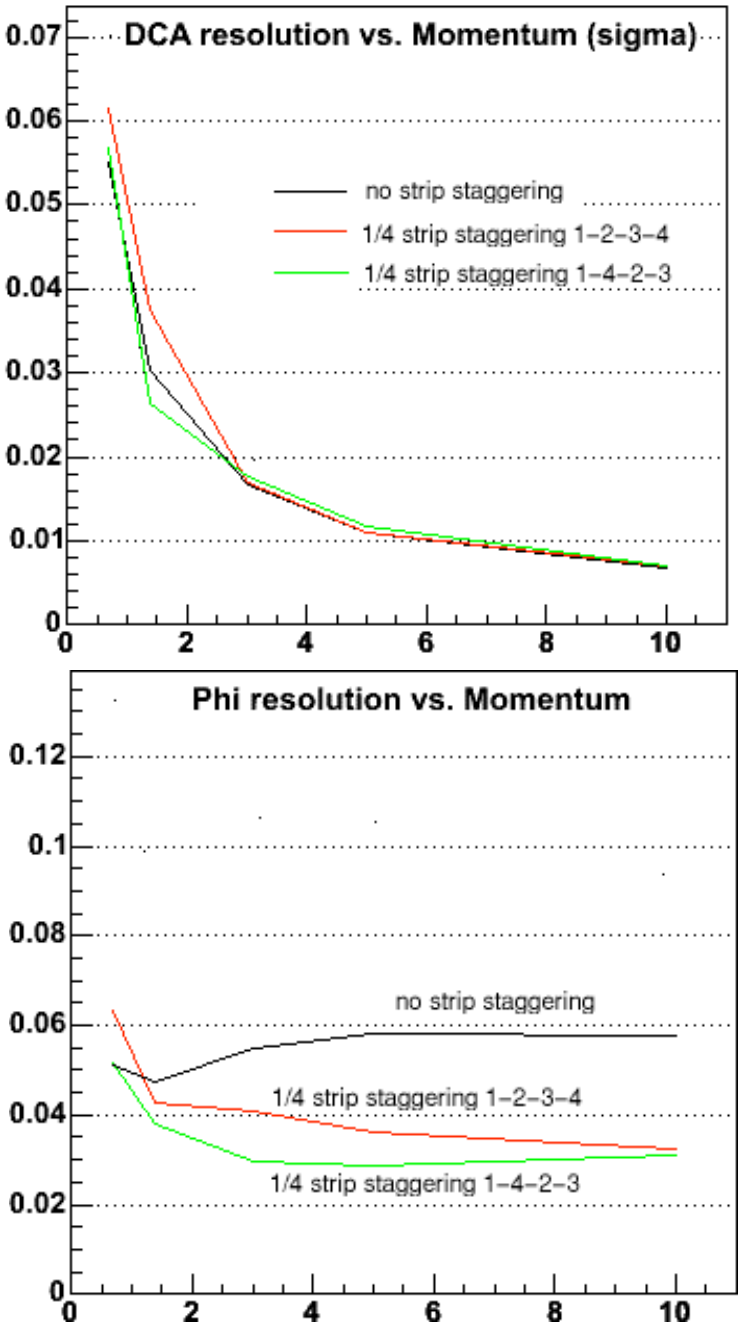

Figure 65 The DCA r resolution (top) and phi resolution (bottom) for a detector which has the sensors at all stations in the same phi positions, and the same resolutions for a detector which has the sensors in each station rotated by ¼ of a sensor width with respect to each other.

The DCA phi resolution can also be improved if the silicon sensors in each station are rotated by a fraction of the width of the sensor with respect to each other. Figure 65 shows the resolutions obtained if each station is rotated by ¼ of the width of a sensor. Again, the resolution is maintained and the phi resolution is improved by about a factor of 2.

Since the phi staggering involves changing only the position of each station, but no change to the sensor, we adopt phi staggering as a baseline and will continue to investigate the cost implications for adding stereo angles. It should also be noted though that having both stereo angles and phi staggering does not additively improve the phi resolution, but just improves the resolution of one of them alone by a small amount.

Based on the above plots, we are currently maintaining the following baseline detector configuration:

- 75 μm silicon strip pitch, in r
- 3.75° sensor wedges determining the strip width in phi
- The VTX points are included in track reconstruction whenever a hit is produced
- No stereo angles
- Phi staggering is included
- Two dimensional DCA cuts are used to discriminate between different decay particles, with one cut value used in the r direction and a larger cut value used in the phi direction.

3.3 Determining the Primary Vertex

Displaced vertices are measured with respect to the primary vertex in the event, so the primary vertex must be found with sufficient accuracy if the DCA resolution is to be maintained. This is true for both the offline event reconstruction of the FVTX as well as any level 1 trigger algorithm that attempts to identify tracks from heavy quark decays. We have studied the primary vertex resolution in p+p, p+Au and Au+Au central collisions, using HIJET together with PISA. For each beam species, the average number of particles traversing the FVTX was determined. These particles are typically soft pions with a mean momentum of about 1.4 GeV/c and most probable momentum of about 600 MeV/c. Each of these pions typically provides an impact parameter measurement with an accuracy of ~250 μm. Assuming that the accuracy of the vertex determination scales inversely as the square root of the number of measured tracks the primary vertex accuracies shown in Table 3 below are obtained.

Since these tracks are all in the FVTX, they are available to a level 1 trigger. Also shown in the table are the additional pions detected in the VTX, which can be used to improve the vertex determination offline. The VTX single-track vertex resolution provided by each of these is about 210 μm.

Table 3 - Determination of primary vertex using prompt pions, shown versus collision species.

Collision Species at √s= 200 GeV	Number of pions detected in FVTX	Accuracy of primary vertex determination from FVTX alone	Additional pions in VTX	Primary vertex accuracy with FVTX + VTX
p-p min bias	5.8	104 μm	~3	79 μm
p-Au min bias	11.2	75 μm	~6	56 μm
Au+Au central	1730	6 μm	~900	5 μm

3.4 Heavy Quark Measurements with the FVTX Using D, B→ μ X

Charm and bottom measurements can be made with the FVTX and muon arms using the semi-leptonic decay channels D→μX, B→μX. Figure 66 shows the contributions from charm+bottom decays ("Prompt" in the figure), light meson decays, and punch through hadrons to the single muon spectrum (based on real Run 2 p+p data). The light meson decays dominate the spectrum below p_T of 2 GeV/c and the punch-throughs become comparable to the heavy quark meson decays at ~3 GeV/c. These light meson contributions to the single muon spectrum must be rejected if a precision charm or bottom measurement is to be made. A DCA cut requiring DCA<DCA_{max} will reduce the muons from light meson decays, making a charm measurement possible at low p_T. A DCA cut requiring DCA>DCA_{min} will reduce the punch-throughs since the punch-throughs come from the primary vertex, allowing a heavy flavor measurement at moderate to high p_T.

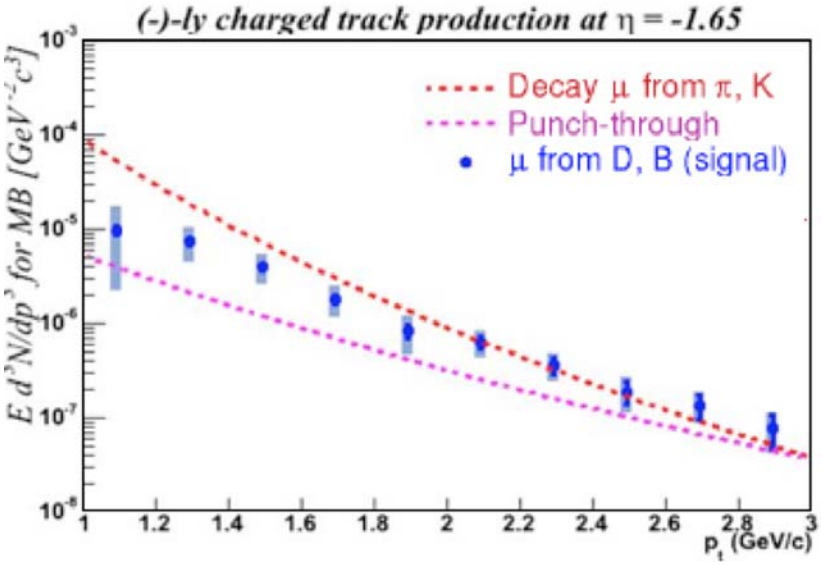

Figure 66 - The p_T distribution of negative prompt muons (muons from heavy quarks), decay muons from π and K and punch-through hadrons at pseudorapidity (η) = -1.65. The punch-throughs become the dominant background for p_T values above 3 GeV. The curves are simulations, based on real data extrapolations, while the data are PHENIX measurement.

We have looked at the signal to background improvement for D and B measurements by running full D, B and minimum bias PYTHIA events through our simulation and seeing what fraction of each particle type survives DCA cuts. Figure 67 and Figure 68 show how the signal to background for charm (D) and bottom (B) measurements improves when DCAmin<DCA<DCAmax cuts are applied. Figure 67 shows the signal to background improvement for particles decaying to μ^+ and Figure 68 shows the improvement for particles decaying to μ^-. There are more background muons for μ^+ signals than for μ^- signals.

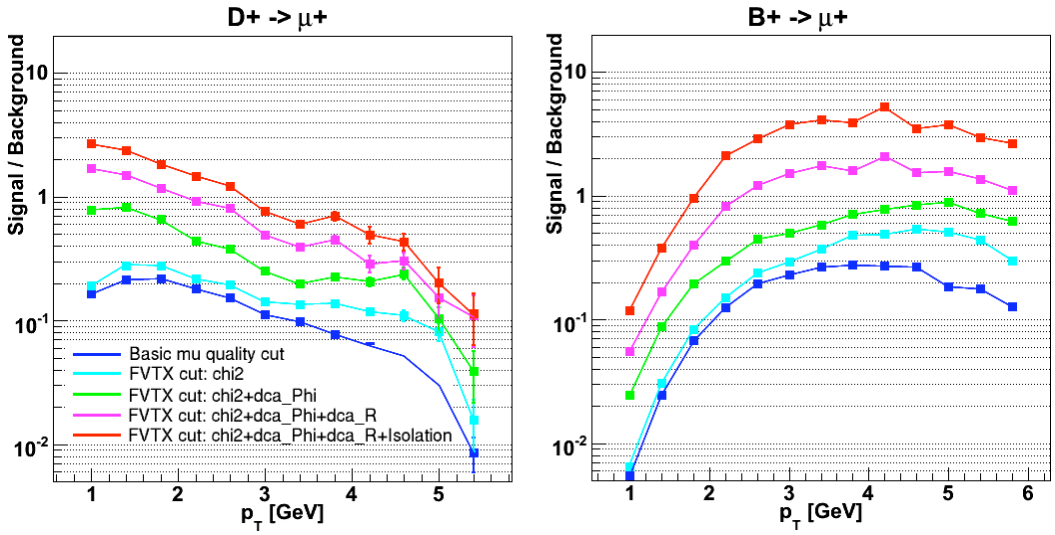

Figure 67 – Signal to background improvement for Ds (left) and Bs (right) which decay to μ^+ for no vertex cut and successive FVTX cuts. Cuts applied are χ^2 cut, DCA cut in the phi direction, and DCA cut in the r direction.

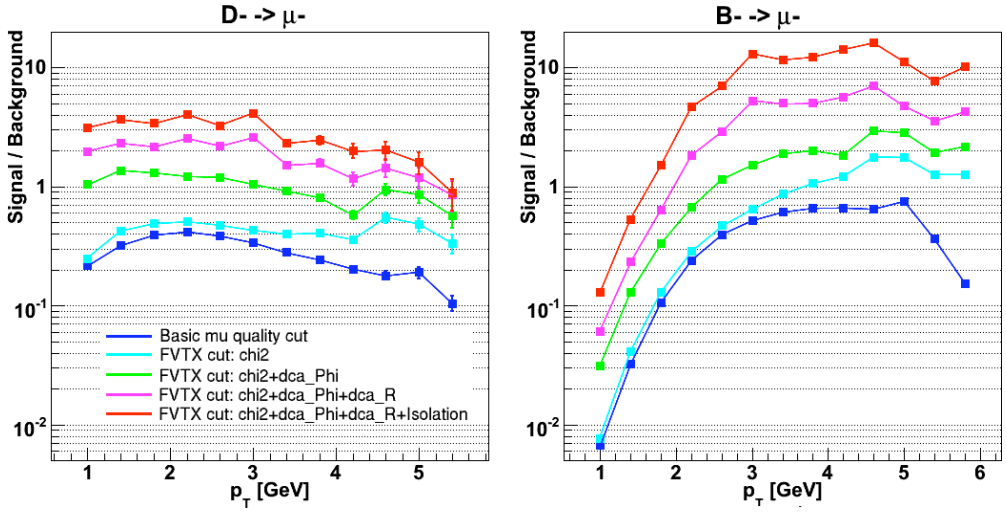

Figure 68 - Signal to background improvement for Ds (left) and Bs (right) which decay to μ^- for no vertex cut and successive FVTX cuts. Cuts applied are χ^2 cut, DCA cut in the phi direction, and DCA cut in the r direction.

For both charm and bottom, an improvement in the signal to background of about a factor of 10 is attained over most of the p_T range accessible by the FVTX and muon systems when DCA cuts are employed. These figures will enable us to determine which pt ranges we can use to enhance either B or D. Generally, D's dominate below 2 GeV and B's dominate above 3 GeV.

3.4.1 Error Bar Improvement on Single Muon Physics Measurements with the FVTX

The heavy flavor measurement improvement that we achieve with the FVTX comes about because the error bars on an open heavy flavor measurement get reduced when the signal to background improves. The statistical error will improve because less background needs to be subtracted to obtain the signal. This is indicated in the following equations where the error in the signal (S) is given with respect to the fraction (f) of the total counts which are background (B) counts.

$$S = N - B;$$

$$\delta S = \sqrt{\delta^2 N + \delta^2 B} = \sqrt{\delta^2 N + f^2 \delta^2 N};$$

$$here, \delta N = \sqrt{N};$$

$$N = S + B = S + fN \Rightarrow N = \frac{S}{1-f};$$

$$\delta S = \sqrt{\frac{S}{1-f}(1+f^2)} = \sqrt{S}\sqrt{\frac{1+f^2}{1-f}}$$

As seen, the statistical error will become smaller as the fraction (f), that is background, is reduced.

The systematic errors also improve because the uncertainty in the background normalization contributes less to the systematic error as the background gets reduced. This is indicated in the following equations where the systematic error is given as a function of the uncertainty of the fraction (f) of the counts which are background. As f becomes smaller, the contribution of δf/f to the systematic error also becomes smaller.

$$\delta S_{sys} = \delta B_{sys} = \sqrt{N^2 \delta^2 f} = N\delta f$$

$$= \frac{s}{1-f}\delta f = s(\frac{1}{1-f})\delta f = s(\frac{f}{1-f})(\frac{\delta f}{f});$$

If the improved signal to background ratio shown in Figure 67 and Figure 68 are used to calculate the statistical and systematic errors for an open heavy flavor cross section measurement, we obtain the reductions shown in Figure 69, where we have applied the improvement to a Run 2 single muon measurement.

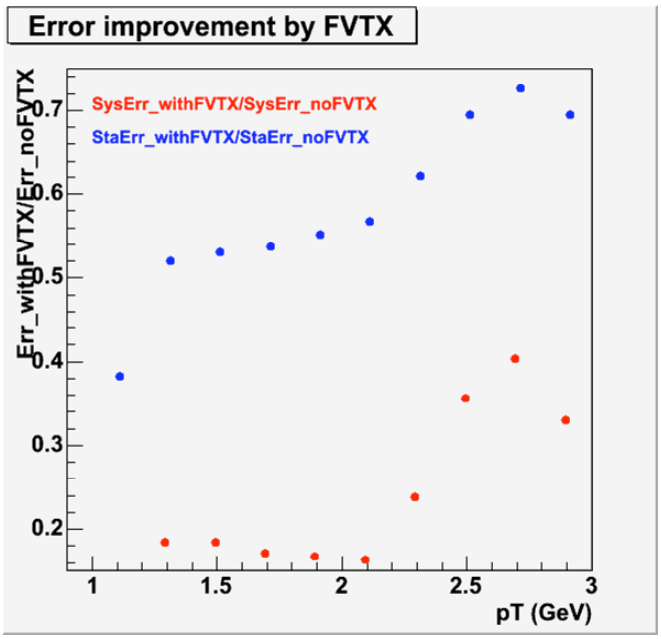

Figure 69 The fractional reduction in statistical and systematic error bars that we would obtain for Run 2 pp data cross section measurement if we had the FVTX included in the analysis. Note that additional statistical error bar improvements will be obtained just by increasing the integrated luminosity with respect to Run 2.

The systematic error gets reduced by a factor of approximately 2.5-10, depending on p_T, and the statistical error gets reduced by a factor that is somewhat smaller than 2 at all values of p_T. Note that any current or future measurement that has a larger integrated luminosity than Run 2 will have further improvement in the statistical error bar so the systematic error bar improvement is the most critical.

If these fractional improvements in statistical and systematic error bars are applied to the Run 2 published measurement, we get the reduced error bars indicated in Figure 70 where the Run 2 error bars without the FVTX are shown in red and the reduced statistical and systematic error bars that we would obtain with the FVTX detector are shown in blue. Note that the improvement is more dramatic for μ^+ than for μ^- because there are more μ^+ background particles than μ^-. The physics analyses that can be made with these improved heavy flavor measurements will be shown in the physics sections that follow.

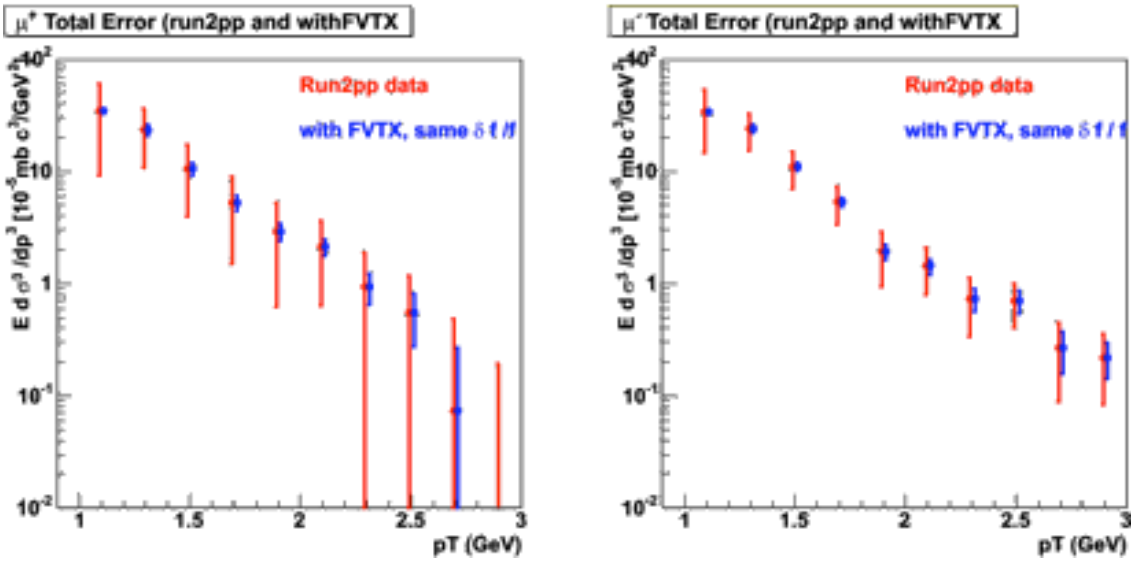

Figure 70 The statistical and systematic error bars from run 2 p+p data are shown for μ+ (left) and μ- (right) with (blue) and without (red) the FVTX.

3.5 Occupancy in Central AuAu Events

The endcap mini-strips have a radial pitch of 75μm and widths in ϕ (or mini-strip lengths) that are 3.75° wide and that therefore vary between 2.8 and 11.2 mm as the radius increases. The simulated hit density at the first silicon layer for central AuAu collisions, simulated by PISA, is shown in Figure 71. For $75\,\mu \times 2.8$mm strips at the smallest radii, a density of 7cm^2 translates into an occupancy = 1.5%. Accounting for charge sharing and the total yield of soft charged particles, the maximum occupancy is expected to be ~2.8% for Au+Au central collisions. We expect this occupancy to be low enough to allow accurate track finding even in the central-most AuAu collisions.

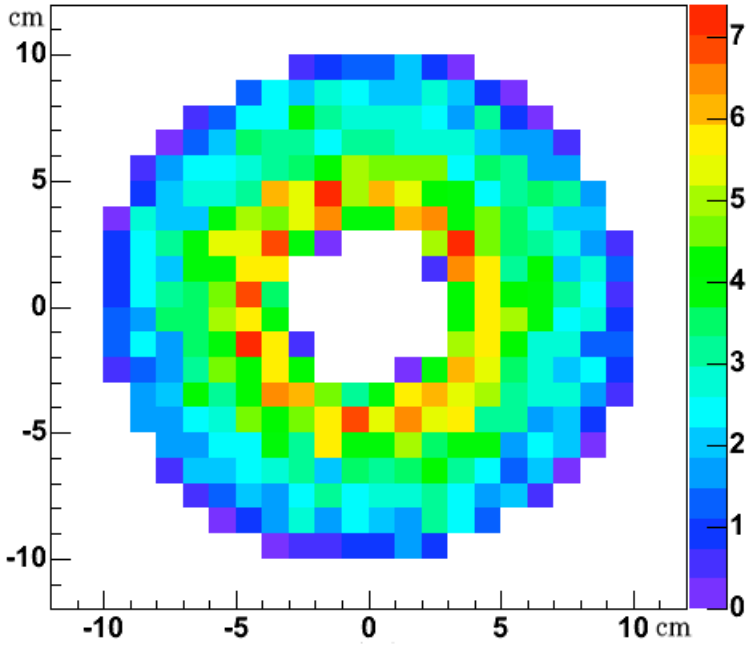

Figure 71 - Simulated occupancy at the first silicon plane for Au+Au central collisions using the HIJING model. The color scale is in units of hits per cm^2, with a maximum of 7 hits per cm^2 at the inner radius. The other silicon planes have lower occupancies.

3.6 Analog Information from the FVTX

The FPHX chip provides analog information in the form of a 3 (or more) bit ADC. We have begun a study of the use of this information in either triggering or in offline analysis. In the energy region of the particles of interest to PHENIX, we are sensitive to the relativistic rise of the energy loss with momentum. The relativistic rise is governed by the restricted Bethe-Block formula which predicts a rise for pions (muons) between 1 and 18 GeV of about 7%. Because of this relativistic rise, we can use the energy loss as a coarse measure of the momentum of the track in the FVTX that can then be matched to the muon spectrometer measured track. An analysis of the backgrounds in the measurement of muons from W decay has shown that a substantial portion of the backgrounds comes from low energy kaon decays in the muon spectrometer that mimic high energy muons. It may be possible to provide some discrimination of these low energy kaons by looking at the energy loss in the FVTX planes. We are currently validating the GEANT code to insure that the energy loss is calculated correctly and will then do a full simulation of the combined muon system and FVTX to determine at what level we can reduce the backgrounds for the W physics measurement.

3.7 Matching Tracks from the Muon Spectrometers to the FVTX

Track matching between the Si Endcaps and the Muon Spectrometers was studied by using HIJING Au+Au central collisions in a PISA simulation, followed by full offline reconstruction.

Au+Au central collisions produce nearly two thousand tracks in the FVTX. Since only a few of these particles manage to penetrate deep into the muon identifiers, it is important be able to correctly match the tracks found in the muon system to those found in the FVTX. We have performed a matching simulation by looking at matching in stages as follows: First, tracks are found in the muon spectrometers, seeded by roads in the muon identifiers, as done in all existing PHENIX muon analyses. Second, tracks from the FVTX are projected into the muon tracker station one where a momentum-dependent window is computed, based upon the expected amount of multiple scattering. The background FVTX tracks are found within that window. Finally, each of those tracks are joined to the muon track and fitted using a Kalman filter fit. The combined track with the best fit is retained.

PISA was used to simulate the projection accuracy for a 5.5 GeV muon from the FVTX into station one of the muon tracker. The window radius in station one for 99% efficiency of retaining the muon was 1.8 cm. The number of background pions within this window is 2.7. One can use a χ^2 cut on the track fit in the FVTX to remove some of the background pions but one is still left with one pion for every muon. A more efficient method for removing the background pions is to fit the muon track in the spectrometer with each of the tracks in the FVTX with the use of a Kalman filter.

With the Kalman filter it is possible to cut on the combined χ^2 of the fully fitted track. This χ^2 includes contributions from multiple scattering in the FVTX, as well as the track position and angle matches between the FVTX and muon tracker. It also takes the momentum dependence of these into account. Results for the χ^2 of the Kalman filter track in central Au+Au occupancy are shown for tracks which are incorrectly matched to background tracklets (black histogram) in the FVTX and for correct matches (red histogram) at 3 GeV (Figure 72) and 9 GeV momentum (Figure 73). A clear distinction in χ^2 is seen between the muon tracking matches with the background tracklets in the silicon or the correct muon tracklet. If one simply picks the best χ^2 track for the match in each case one gets an efficiency for picking the correct tracklet of 93% (9 GeV muon), 83% (6 GeV muon) and 75% (3 GeV muon).

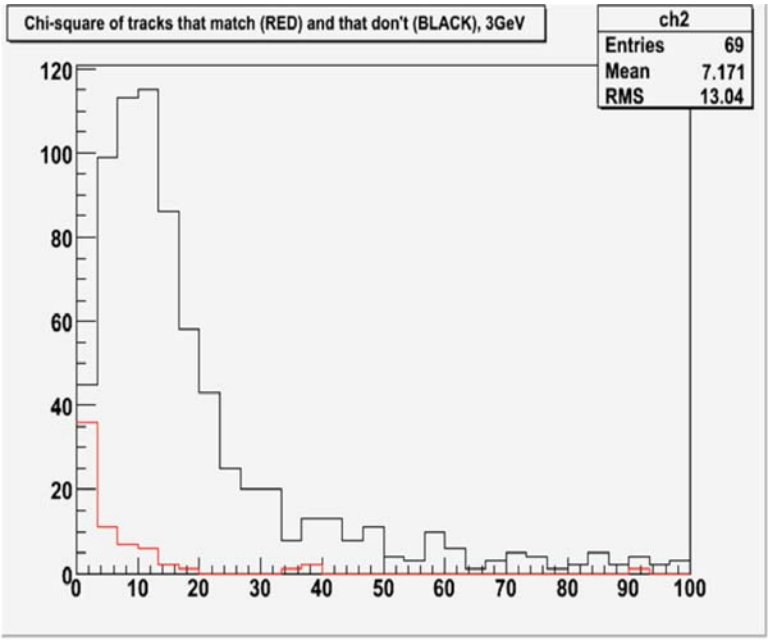

Figure 72 - Matching of 3 GeV muon tracking tracks with FVTX silicon tracks in central Au+Au collisions. The red historgram shows the Kalman filter χ^2 for the correctly matches tracks while the black histogram shows that for the soft pion background tracks. The correct FVTX track is matched 75% of the time.

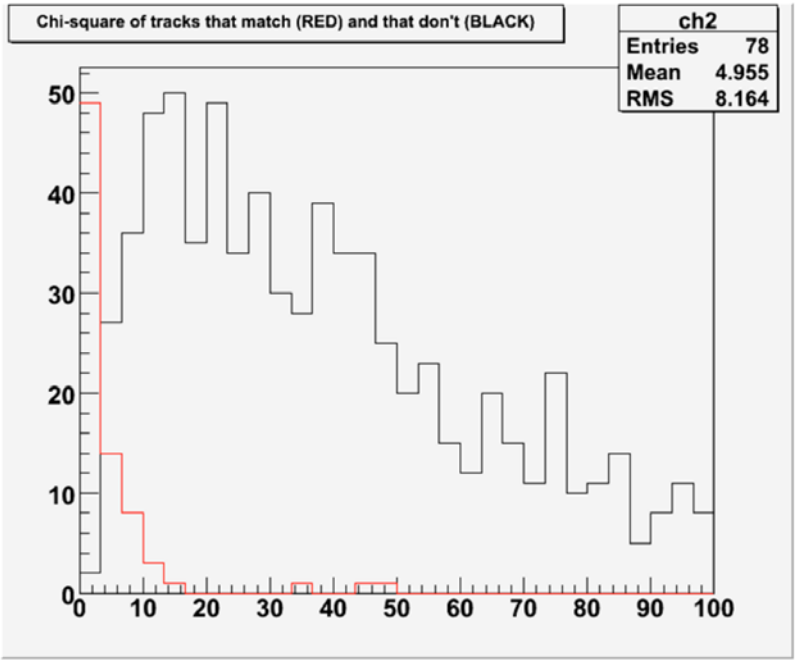

Figure 73 - Matching of 9 GeV muon tracking tracks with FVTX silicon tracks in central Au+Au collisions. The red histogram shows the Kalman filter χ^2 for the correctly matches tracks while the black histogram shows that for the soft pion background tracks. The correct FVTX track is matched 93% of the time

4 FVTX Detector system

4.1 Overview

The FVTX detector system is composed of two identical endcap sections, one in the front of the north muon spectrometer and one in the front of the south muon spectrometer. Figure 74 shows a three dimensional model of the two detectors, and the geometrical parameters are shown in Table 4. The VTX detector and the two FVTX endcap regions share an environmental enclosure. The environmental enclosure is needed because the barrel strip detectors must be operated at 0 deg C. The enclosure radius is 25 cm except close to the absorbers (the nose-cone surface) where the enclosure extends out to at least 50 cm. The larger radius ends are used for the barrel pixel layer transition electronics and all of the barrel bus cables, power and cooling lines plus all of the utilities and cables for the forward vertex system. An ongoing integration study of these utilities and cable routing is being pursued for the VTX barrel upgrade. The design of the enclosure and mechanical structure will include the needs of both the barrel and the forward upgrades.

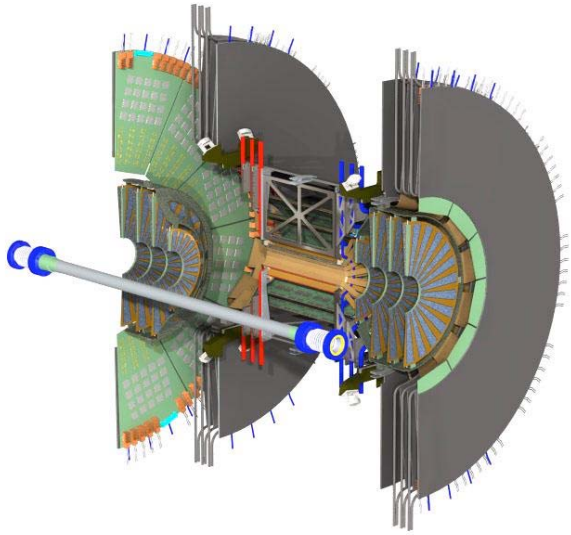

Figure 74 - 3-D model of the full vertex detector showing the barrel portion and the endcaps on left and on the right. The Readout Out Cards are at either end of the detector at a larger radius and visible in the exploded view on the left.

The four endcap disks contain 48 individual wedge shaped towers which are 7.5° wide and mounted on a carbon composite support substrate. Each wedge supports silicon sensors with readout chips lined up along the sides of the sensors and wire bonded to the sensors. Adjacent wedges overlap by about 0.5 millimeter to give hermetic coverage in the phi direction. The technology for the sensors will be p-on-n detectors with the strips oriented so that the strips are 75 μm wide and the strips nearest the beam pipe, at a radius of 4.5 cm are short, ~3.5mm long in the phi coordinate, and at the largest radius of 17 cm they are ~ 11.2 mm long, i.e. individual strips fan out from the center of the 7.5 deg wedge. The maximum occupancy at the inner strip is 2.9% in central Au+Au collision events. The total number of readout strips in each endcap is

~ 540,000. The FPHX chips on each edge of the sensor are connected to a flexible kapton bus that takes the data to the outer radius of the wedge.

Table 4 - Summary of the parameters of the FVTX disks.

FVTX	Disk	Z1	Z2	Z3	Z4
Geometrical	z (cm)	18.7.	25.1	31.5	37.9
Dimensions	R (cm) inner	4.5	4.5	4.5	4.5
	R (cm) outer	10.6	17.0	17.0	17.0
Unit Counts	# of wedges	48	48	48	48
	sensors/wedge	1	1	1	1
	readout chips	10	26	26	26
	Readout Channels	61.5k	160k	160k	160k
Radiation Length	Sensor (300 :m)	0.32	0.32	0.32	0.32
	Readout chip(300 :m)	0.32	0.32	0.32	0.32
	Bus	0.33	0.33	0.33	0.33
	Ladder	0.4	0.4	0.4	0.4
	total	1.1	1.1	1.1	1.1

The data from the readout chips will go through two successive boards before going in to the PHENIX DCMs, as indicated in

Figure 75. The first board, the ROC, will reside inside the enclosure and will perform the functions of: stripping the sync words out of the data, collecting the data of several chips together, serializing it and sending it out on optical fiber to the FEM. Additionally, the ROC will provide calibration pulses for the FPHX chips and route download and readback lines to and from the chips.

The second board, the FEM will reside inside the counting house and will receive data from the ROC(s), buffer it until a Lvl-1 accept is received, retrieve the data of interest for the Lvl-1 accepts and package the data for the DCMs. It will also perform the function of an overall slow-controls manager: passing data to and receiving data from the ROCs/FPHXs and the PHENIX DAQ system, and has the option to pass the data to a trigger board so that the FVTX can participate in Lvl-1 decisions.

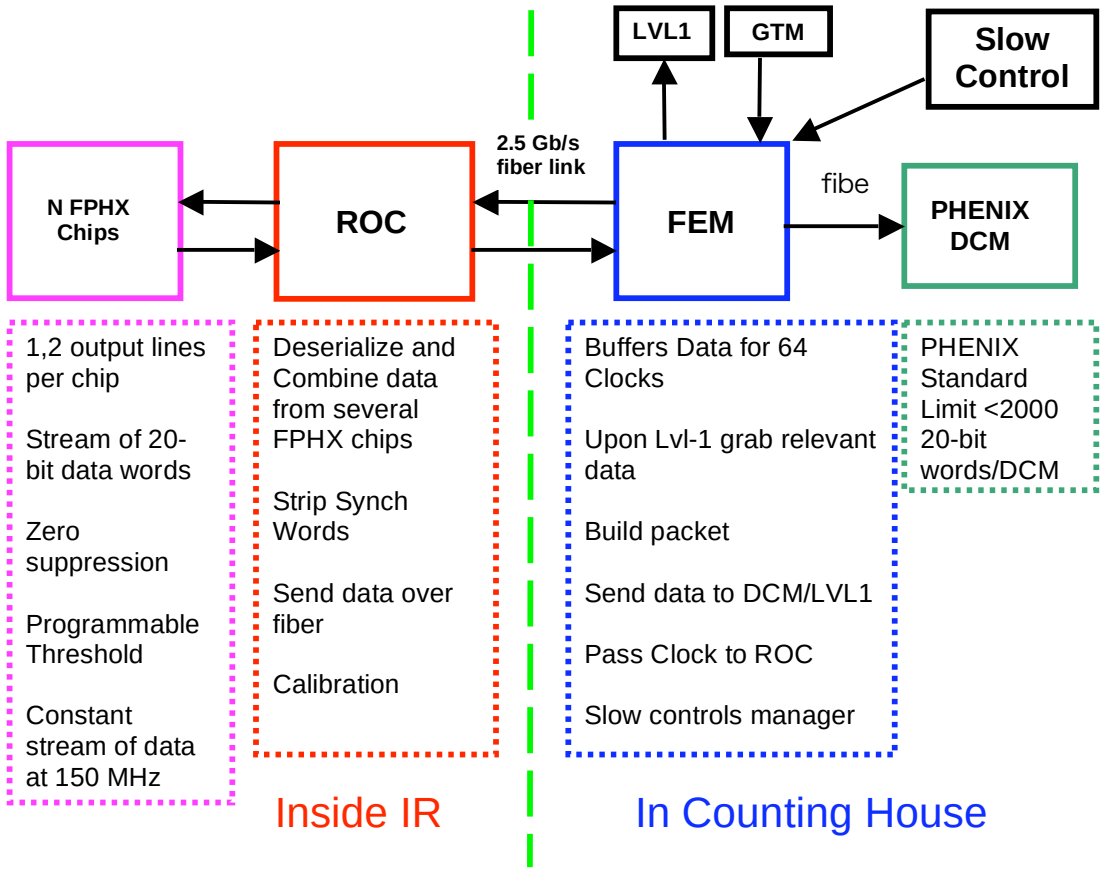

Figure 75 A block diagram of the readout system required for the FVTX. The red block (ROC) and blue block (FEM) are boards which will reside between the FPHX readout chip and the DCM and are currently under development.

4.2 FPHX Chip Development

The ASIC development Group at FNAL, led by Ray Yarema, has completed the design for a readout chip that is specifically tailored to the FVTX sensor. Within the Group, Tom Zimmerman is leading the analog section design, and Jim Hoff is leading the digital data acquisition design function of the chip. The chip design borrows heavily from previously successful IC designs, FPIX2, FSSR, SVX4, etc. The FVTX custom IC has been named the FPHX chip. Each chip is a 128 channel package with an input pitch that is slightly less than 70 microns.

The schematic for one channel is shown in Figure 76. The front end amplifier is designed to accept a positive charge (holes) input from the p-on-n silicon sensor. It is optimized for the input capacitance range of the strips from the inner most to outer most radius of the sensor. The

estimated capacitance range is 0.5 pF to 2 pF. The total charge gain of the fronte end integrator is 50 mV/fC. The dynamic range is 50,000 electrons, corresponding to 4X the average charge deposited per strip per hit (particles hit the strips at an angle so the average charge deposited in a strip is a fraction of the 24,000 electrons generated at normal incidence). The CR-RC shaper has a peaking time of 60 ns (see Figure 77), and the shaping time can be adjusted through a programmable shaper bias. The chip can operate in either AC or DC mode and in DC mode provides leakage current compensation up to 100nA per strip. The noise floor of the analog section is 150e and the noise slope is 140 e/pF Figure). The power consumption is 60-110 uW, depending on the transistor bias current that is set.

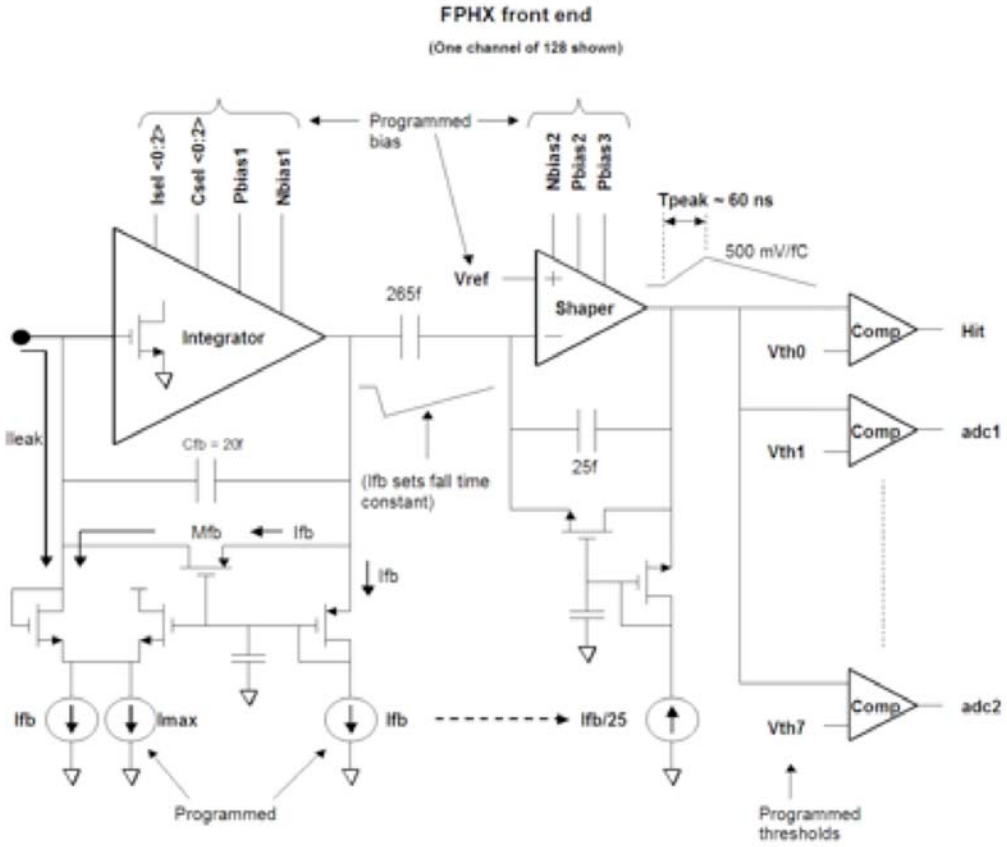

Figure 76 The FPHX amplifier front end.

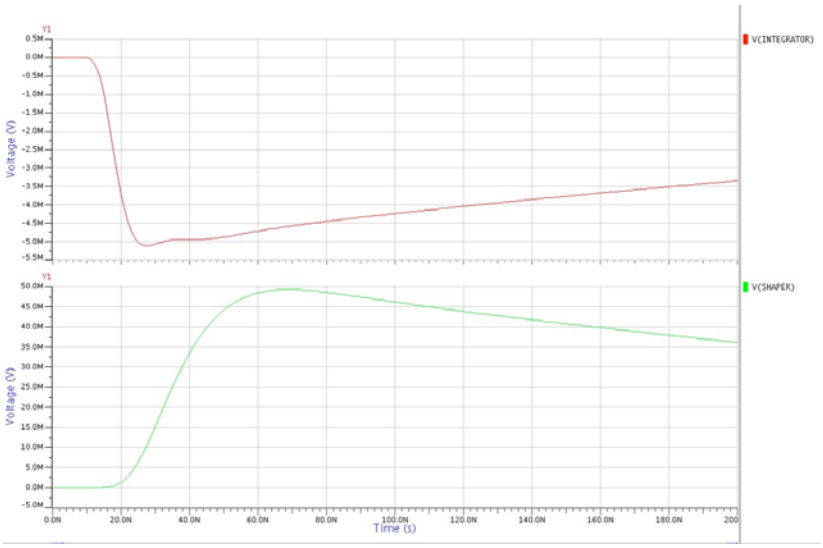

Figure 77 Pulse Shape before and after shaper.

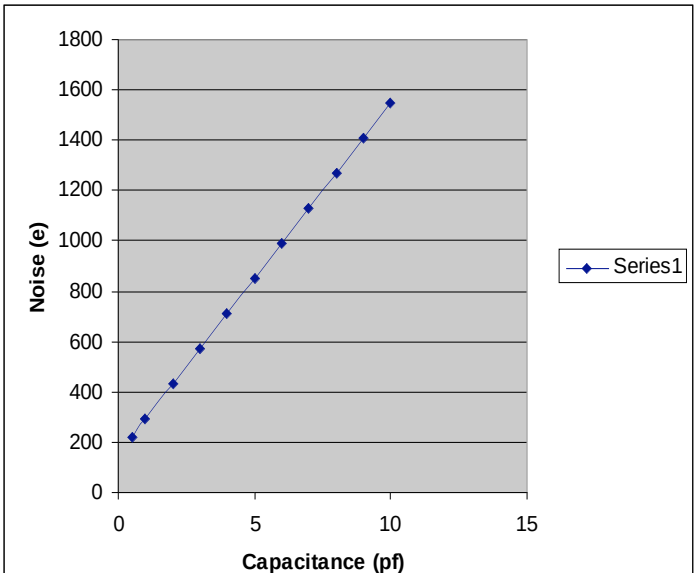

Figure 78 Noise vs. Capacitance.

A ~70 um pitch on the FPHX chip will allow us to wire bond directly from the sensor to the chip input without the need for an additional pitch adapter. The smaller pitch also allows for space between adjacent chips where bypass capacitors might be placed. One of the most important reasons that drove the design layout to locate the readout chips on each side of the sensor was to minimize possible noise problems associated with long signal return paths between the sensor and the chip. This mitigation is accomplished by locating a bias voltage bypass capacitor as close as possible to the readout chip ground reference and the silicon sensor bias.

The output, clock, and control pads are all located on the side of the chip opposite from the inputs and they are wire bonded to a high density interconnect (HDI) cable. The digital connections are arranged to minimize their effect on the analog inputs.

The FPHX is designed to be a data push architecture. It incorporates simultaneous read/write in a dead time free configuration. The FPHX output provides a 7 bit address, a 6 bit time stamp, and 3 bits of ADC for each hit. The chip will also output sync words comprised of 19 zeros followed by a one, which are used by the downstream acquisition to synchronize word boundaries. The functionality of the chip is separated into four distinct phases; analog process the hit, zero suppress, serialize1 and serialize2. The four-phase architecture assures that up to four hits from a single event can be processed and delivered within four beam crossover periods. In the rare case that there are events in sequential beam crossings, all the data will be output, but in more than four beam crossings.

4.3 Silicon Mini-strip Sensors and Wedge Assembly

We will use existing technology for the silicon sensor. Standard p-on-n silicon strip technology, which has been the baseline detector technology for dozens of silicon trackers in Nuclear and High Energy physics experiments, will be used for the FVTX mini-strips. In a p-on-n detector, the output signal is generated by the collection of positive charge carriers. The FPHX chip is being designed to be compatible with positive charge collection. The FPHX is also designed to have leakage current compensation at the front-end, up to 100 nA/ strip. This compensation circuitry allows the possibility of reading out sensors with dc output connections to the FPHX chip, however our baseline sensors are ac-coupled. The strips are ac-coupled directly on the sensor. The capacitor is made by depositing an oxide layer of approximately 200 nm on top of, and over the entire length of the p-implant. An aluminum metallization is placed on top of the oxide to complete the capacitor and to form the readout conductor. The bias connection to the p-implants is made by a polysilicon resistor of approximately 1.5 MΩ, which is electrically connected to a common bias ring on one end, and to the p-implant on the other end. There is an individual polysilicon resistor for each strip. There are three sets of pads on each strip. There is a spy pad which penetrates the oxide layer to allow probing of the dc characteristics of the strip. There are probe pads, which are dedicated for probing the ac characteristics of the strips. And there are bond pads which are only used to wire bond from the detector to the electronics. All non-metal surfaces of the top side of the sensor are covered with a passivation of silicon-oxide or silicon-nitride. A guard ring is implanted around the perimeter of the wedge between the bias ring and the cut-edge of the sensor to prevent breakdown at the cut-edge of the sensor under a normal range of bias voltage. The sensor breakdown voltage is specified to be $\geq$200V or $\geq$50V+ operating voltage, whichever is greater. There is no need to specify higher breakdown voltage, or to incorporate multiple guard ring structures, because an integrated 10 year radiation dose of 200 krads does not require it. Leakage current at 20˚ C is specified to be $\leq$ 160 nA/cm^2 at operating voltage. All of these processes and specifications are standard in the industry.

The sensor readout strips will operate at ground potential, and a positive bias voltage will be applied to the backside of the sensor to fully deplete the sensor volume for efficient charge collection. The large sensor wedge for disks 2, 3, and 4 is approximately 126.5 mm high, 8.7 mm wide at the inner radius, and 25.3 mm wide at the outer radius. The small sensor wedge for disk 1 is approximately 59.5 mm high, 8.7 mm at the inner radius, and 16.5 mm at the outer radius. Several, but not all vendors have 6-inch wafer processing capability. The advantage to a 6-inch

wafer is that an entire unit wedge sensor fits within the useable wafer boundary whereas, a 4-inch wafer forces us to design each full sensor wedge out of two component parts. We have chosen a 6-inch wafer as the baseline. Developing the masks for this effort will be done in concert with the vendors of the sensors. The material and electrical specifications for the sensors are listed below.

Production will be made in two stages. First, a minimum lot size to evaluate the process, followed by production of the balance of the order. It is assumed that the small wedges and the large wedges can be incorporated together on a single mask. We believe that 3 large wedges and, two small wedges will fit on one mask.

We require 288 large wedge sensors + 42 spares = 330 sensors
We require 96 small wedge sensors + 24 spares = 120 sensors

The numbers above suggest an order of approximately 110 wafers. This will result in an overproduction of the small wedge sensors, but at no additional cost.

MATERIAL SPECIFICATION:

Wafer diameter	6 inch preferred (152 mm**),** 4 inch (100 mm)
Crystal orientation	<111> or <100>
Thickness	300 μm +10 μm –20 μm
Uniformity (across wafer)	< 10 μm
Wafer bowing after processing	< 50 μm (sagitta)
Doping of starting material:	n-type
Resistivity:	2.0 – 5.0 KΩ
Polysilicon resistors	~1.5MΩ
Uniformity of resistivity (wafer to wafer)	±25%
Passivation:	Covering junction-side except for wire-bond pads and reference marks. It can either be silicon oxide or silicon nitride.

DESIGN PARAMETERS

- Devices shall be p-on-n ac-coupled mini-strips.
- The full design for the masks will be provided by us in electronic form, GDS file format.
- Vendor will finalize the design details according to their design rules and process, and will work with us on the final design and mask layout.
- Mask alignment precision within the same side : ±2um
- Mask Alignment precision between front and back side: ±5um

The arrangement of the readout chips on each of the large wedge assemblies is shown in Figure 79. The FPHX chips are located on the vertical edges of both sides of the silicon wedge. The two columns of strips are physically separated to the left and right of the centerline of the sensor wedge. The FPHX input pads are located directly opposite the strip bond pads, allowing for easy wire-bonding without the need for fan-in circuitry. The location of the chips close to the sensor

also facilitates the effectiveness of the bias voltage filters. The total number of 128-channel known-good FPHX chips that will be required is 11,290, which includes an estimate for spares. There are 3328(1280) independent strips per large (small) wedge arranged into 2 columns. The wedge assembly covers an angular range of 15 deg and the sensors cover an angular range of 7.5 deg with 0.5 mm added on each edge for overlap with the adjacent sensor located on the back side of a support plate.

The sensor wedge consists of a stack up of a carbon support backing, kapton HDI, and sensor and chips as shown pictorially in Figure 80. The carbon backing serves as a carrier on which the sensor, HDI, and chips can be mounted separately from the cooling plate. This modular arrangement allows us to fabricate and test all of the wedges separately.

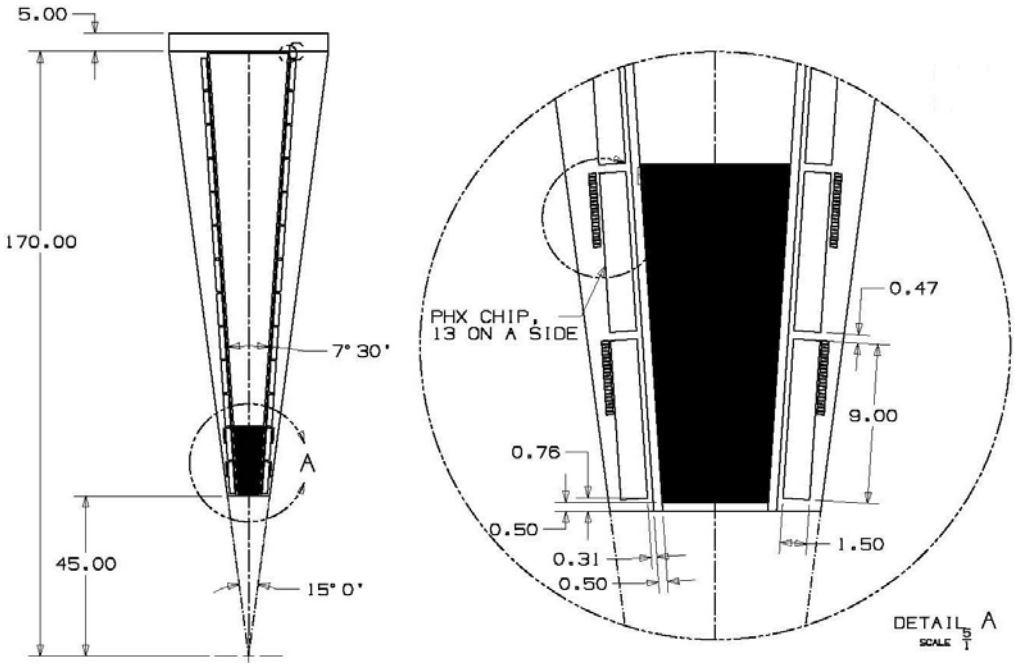

Figure 79 The large wedge assembly on the left showing the location of the sensor and chips and blow up the bottom of the wedge n more detail on the right.

The HDI stack up is shown on the left of Figure 80 and the wedge stack up is shown on the right. Indicated on the HDI stack up is one signal layer, one ground and two power layers. All control lines (which are not active during data taking) will be routed under the sensor and all output lines will be routed towards the edge of the wedge thus insuring that the output lines will not couple into the signal lines on the sensor. The number of lines required (8 pairs for the control lines and 2 signal pairs per chip for the output lines) will easily fit into the width of the HDI and the line pitch of the HDI will be very modest allowing us to use conventional kapton manufacturing techniques.

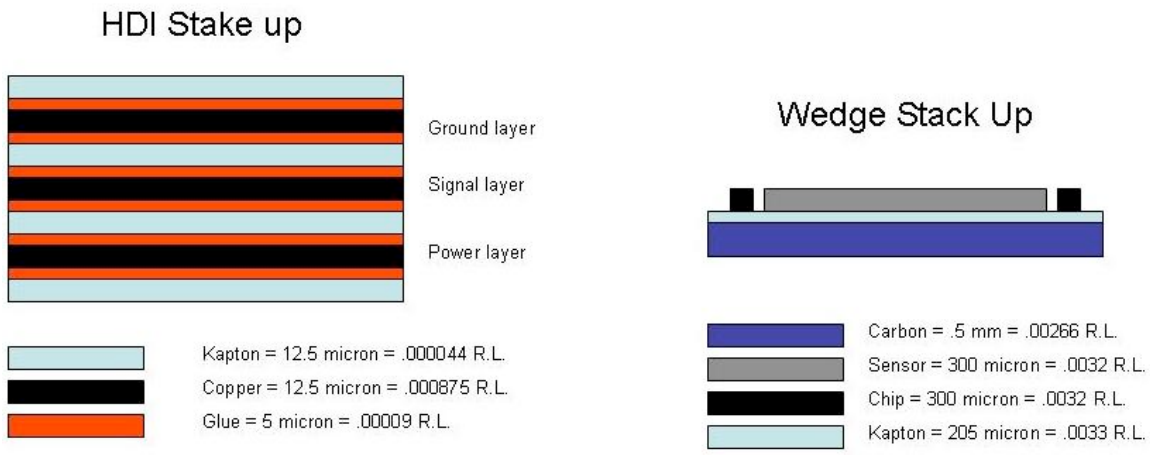

Figure 80 The HDI and wedge stack up. The radiation length of the wedge is 1.2%.

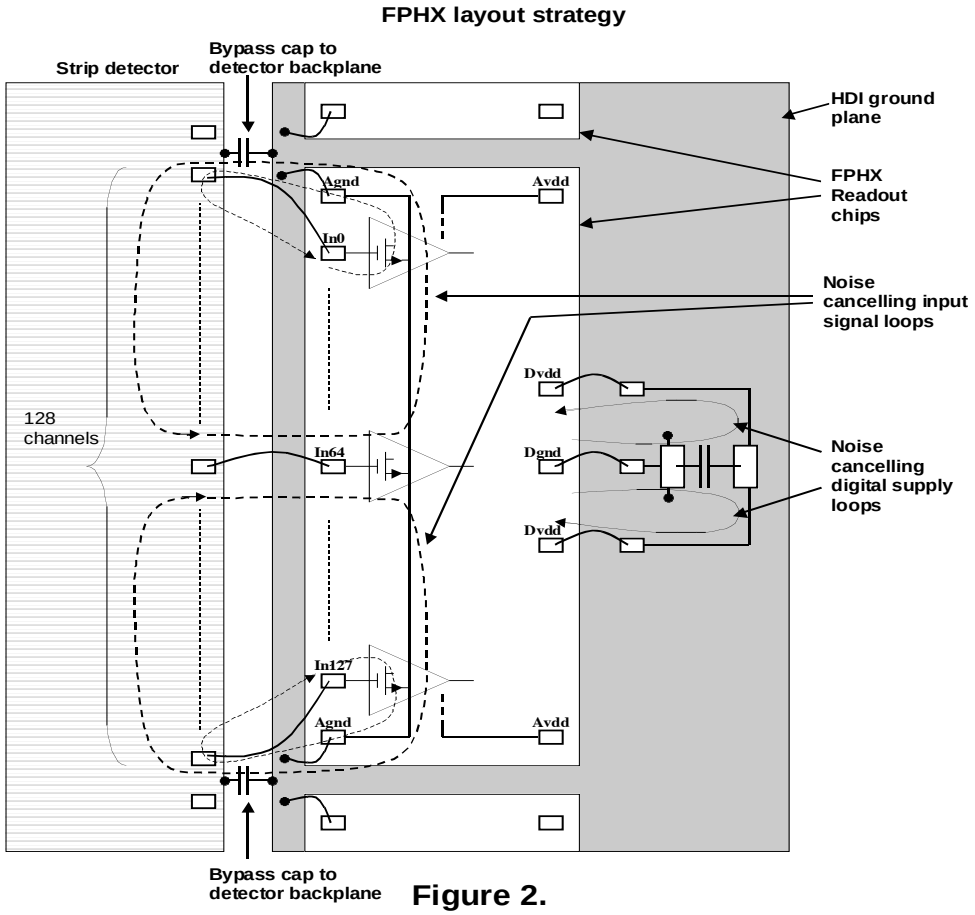

Figure 81 The noise canceling strategy for the HDI.

The layout of the wedge, chip, and HDI will have impact on the noise figure of the system. To facilitate the HDI layout, Tom Zimmerman of FNAL analyzed the electrical layout of the wedge assembly to insure we did not increase the noise. The strategy is shown in Figure 81 . In the

figure one notices the two noise canceling loops, one for the input side and one for the output side of the chip. The location of the bypass capacitors will be incorporated into the design of the HDI. In particular we will design the length of the chip to allow us to place the bypass capacitor to the backplane in between the chips. The digital supply bypass caps will located on the edge of the wedge.

4.4 Electronics Transition Module and FEM

As indicated in the block diagram in

Figure 75 there are two boards (the ROC and the FEM) which will need to be developed to get the data from the FPHX chips in to the PHENIX DAQ system.

The FPHX chip will have the following connections to the ROC:

- One calibration line per chip
- One analog and one digital voltage supply and associated grounds
- 6 LVDS lines required for downloading, clocking, and resetting the chip
- 2 LVDS data lines per chip sending the data out

The ROC will take the continuously streaming data (data-push) from 52 FPHX chips via flexible cables into an FPGA, strip the sync words from the data, combine the data of several chips, serialize it and send it out via fiber to the FEM and the Lvl-1 boards. The time to receive all of the data to pass to the Level 1 trigger is expected to be less than or equal to four beam clocks or 424 nsec. The location of the ROCs will be at the end of the silicon tracker enclosure in the “big wheel” area, as indicated in Figure 82. A block diagram of the ROC is shown in **Figure** 83 and a layout for a board which would service 4 layers*4 sensor wedges is show in Figure 84. Twelve ROC boards will be required to service one endcap and these boards will hold a total of 48 FPGAs.

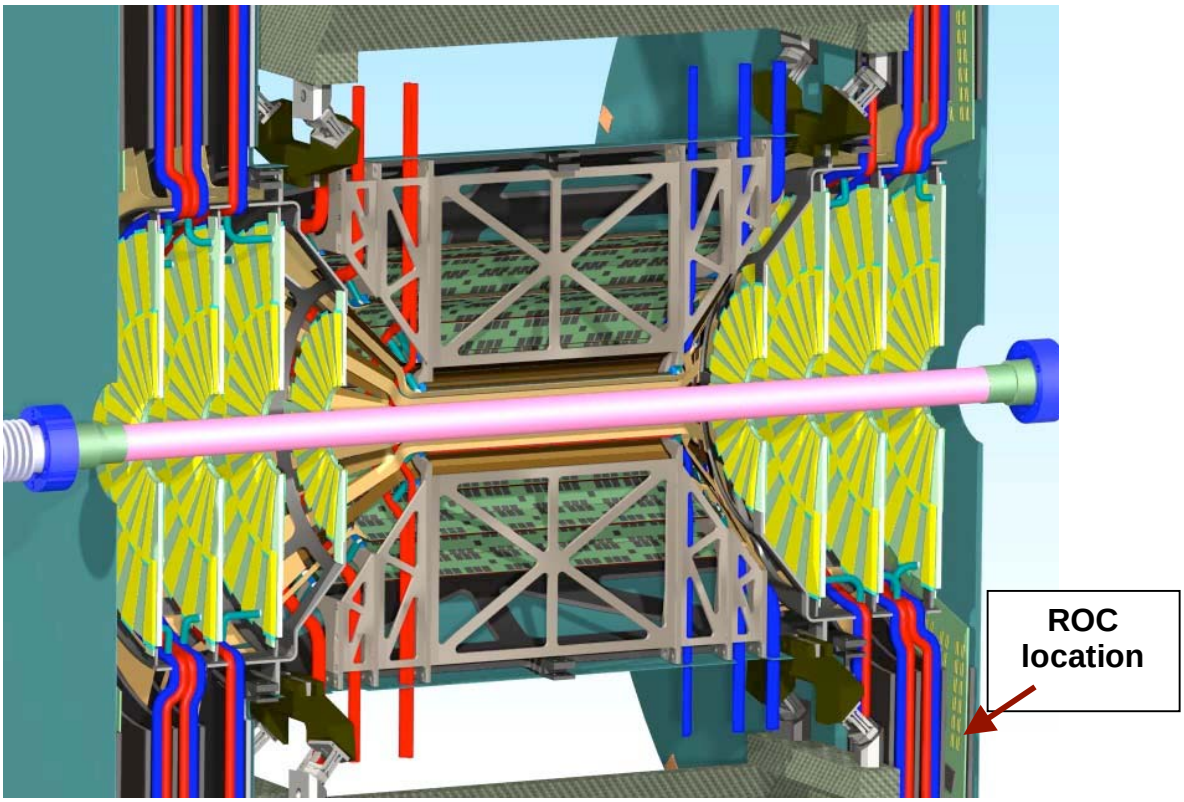

Figure 82 The silicon tracker region, indicating at the far right the location of the ROCs for the FVTX.

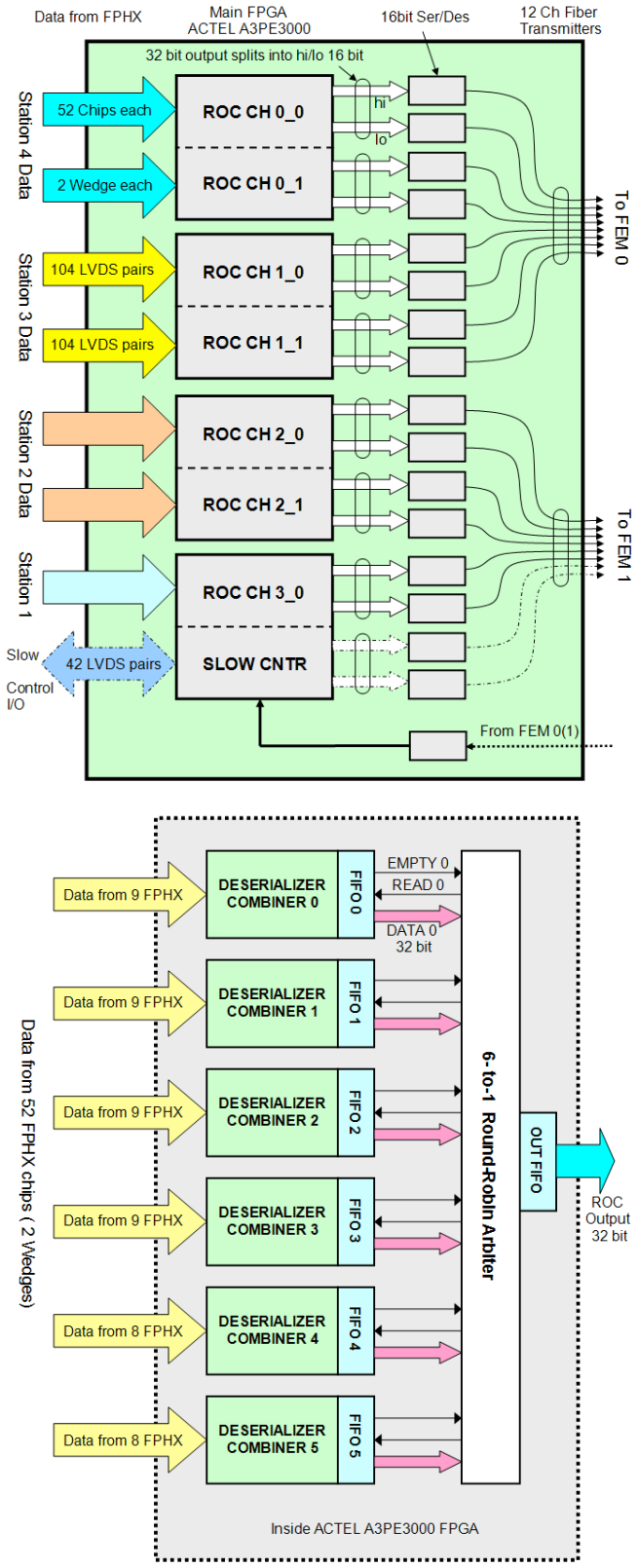

Figure 83 Block diagram of the ROC board and single ROC Channel which will take data from 52 chips, derserialize and strip off the sync words, serialze the data and send it out on fiber.

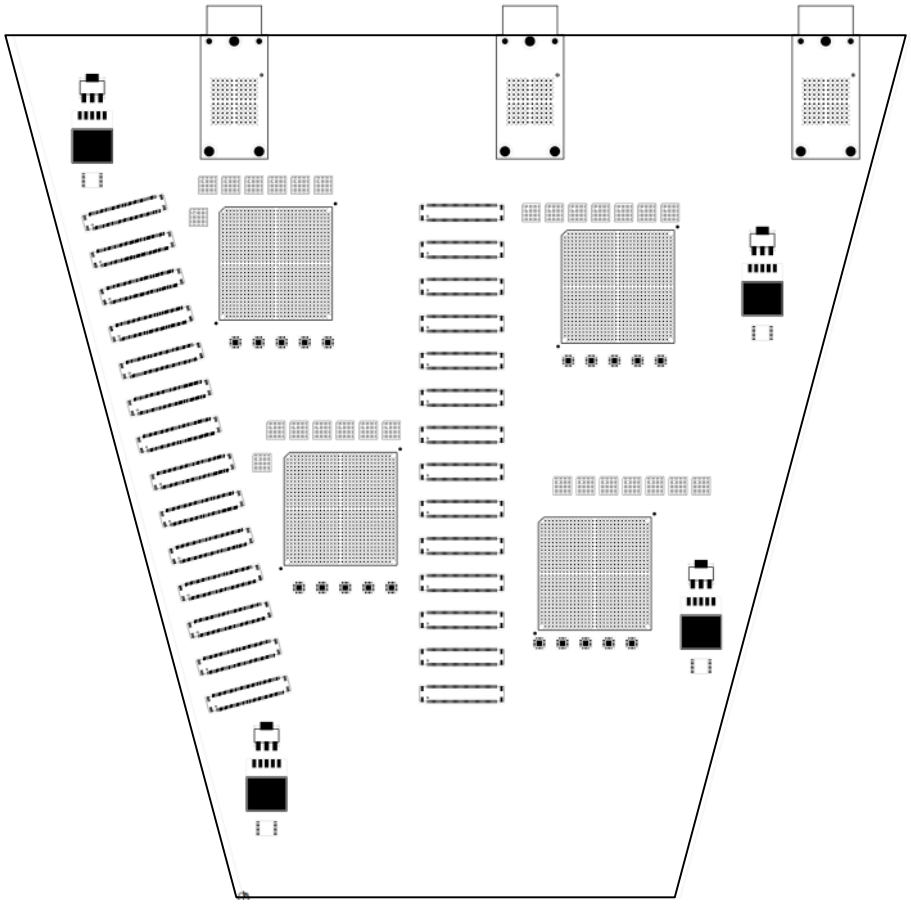

Figure 84 Layout of a ROC board which would span 30° and service 4 layers*4 sensor wedges. Shown are the connectors which would receive signals from and route signals to the FPHX chips, the FPGAs which would compress the data, serdes which serialize the data and fiber drivers which send the combined data to the FEMs and Lvl-1 boards. Voltage regulators and LVDS repeaters are also included above.

The power consumption required for the ROC is approximately 350 Watts per arm. The details of this are shown in Table 5.

Power Calculations		
#FPIX/FPGA	26	52
#I/O/FPHX	2	2
#SERDES (Data)	2	4
#LVDS Repeaters	5	5
FPGA	A3PE1500	A3PE3000
FPGA Core (V)	1.5	1.5
FPGA Core Quiescent (mA)	105	225
#2.5V CMOS I/O pins	48	96
#3.3V CMOS I/O pins	16	40
FPGA 3.3V CMOS I/O (mA)	0.84	2.11
FPGA 2.5V CMOS I/O (mA)	14.93	29.86
#LVDS I/O pins	116	160
FPGA LVDS I/O (mA)	116.00	160.00
FPGA Core RAM (mA)	97.2	97.2
FPGA Pins	180	296
FPGA 1.5 V Core Power (mW)	303.3	483.3
2.5V Power (mW)	827.3	974.6
3.3V Power (mW)	332.8	337.0
Total FPGA Power Dissapation (mW)	1463.4	1794.9
2.5V CMOS Frequency (MHz)	135	135
3.3V CMOS Frequency (MHz)	10	10
LVDS Frequency (MHz)	200	200
FPGA LVDS/Pin Pwr Dyn (uW)	1.20	1.20
FPGA LVDS/Pin Pwr Static (mW)	2.26	2.26
FPGA 2.5V CMOS/Pin Pwr (uW)	5.76	5.76
FPGA 3.3V CMOS/Pin Pwr (uW)	17.39	17.39
Pins/SERDES	24	24
SERDES (mA)	200	200
SERDES Power Dissapation (mW)	7500	8500
LVDS Repeater(mA)	100	100
FPGA Core RAM (uW/MHz)	1080	1080
Track Hits/FPIX	10	10
Noise Hits/FPIX	0.01	0.01
Track Data Size (24 bits/word)(bits)	6240	12480
Noise Data Size (24 bits/word)(bits)	6.24	12.48
BCO Clock (MHz)	9.96	9.96
Readout Clocks	4	4
Track Data Rate (Gbits/sec)	15.538	31.075
Noise Data Rate (Gbits/sec)	0.016	0.031
Total Data Rate (Gbits/sec)	15.553	31.106
FiberOptic Transmitters	2	2
FO Transmitter Current (+3.3)(mA)	415.00	415.00
FO Power Dissapation (mW)	2739	2739
Number of FPGAs	7	4
Max Power Dissapation per ROC	**20.48**	**18.42**

Table 5 Power consumption calculations for the FVTX ROC card components.

The FEM will buffer the data for 64 beam clocks (emulating the 64 beam clock analog buffer of current PHENIX detectors), grab the data from the appropriate beam clock upon a Level-1 trigger and reformat the data before it is sent to the PHENIX DCMs. The block diagram of a single FEM board and a single FEM channel is shown in Figure 85. There is a 64 FIFO array, with each FIFO storing the data from a particular beam counter. The FPHX data is routed to a FIFO, selected by the beam clock counter that is embedded in the data stream hits. The hits from a particular beam crossing stay in the FIFO for not more than 64 clocks, otherwise they are marked as expired. This strategy solves the problem of relatively short beam clock counter wrap around. The FPGA then allows the data from the appropriate beam clock to be sent to the DCM when a LVL-1 trigger accept is received. Upon readout of the FIFO the hits from the expired beam crossing are not being outputted. The existing PHENIX DCMs can be used without modification.

The current FEM channel design has been successfully implemented on an XC4VSX35 Vertex-4 XILINX FPGA and tested at design speed. The buffering block is capable of receiving 32 bit parallel data at up to 300 MHz and reliably sends the data to the output buffer at 300 MHz. Copying of the data from a particular FIFO to the output buffer should be done as fast as possible so that data from one beam crossing are fully emptied before data from another beam crossing arrives. The full design for FVTX readout will be implemented on the largest VSX series FPGA XC4VSX55, which has a sufficient number of FIFO blocks to accommodate 4 FEM Channels on a single chip. The data from all 4 channels will be combined on the output in order to reduce the number of DCM channels in readout.

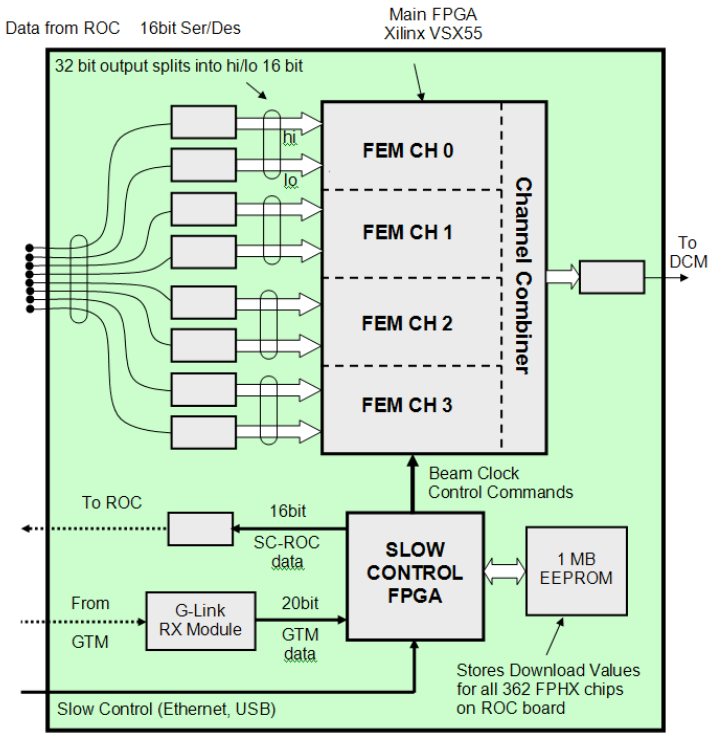

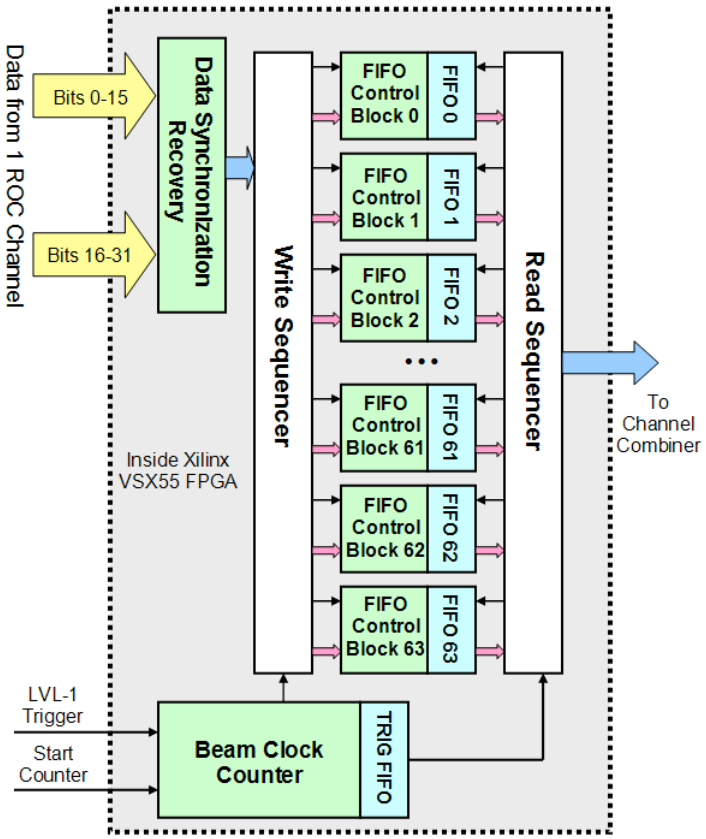

Figure 85 – Block diagram of FEM board and single FEM channel.

The buffering requirements of the ROC are expected to be modest with <20 kbits of data expected in Central Au+Au events for up to 56 chips serviced by the same FPGA. Noise hits are expected to take even less space. Some calculations of data sizes and readout times can be found in Table 6, for various options of readout lines, chip "ganging", and assuming the readout clock is synchronized to give an integral number of beam clocks needed per data word. The proposed granularity of the readout DAQ and the data rates at each point are shown in Figure 86.

Layers Ganged	channels/chip	chips/board	channels/board	Occupancy	Strips/Hit	Interactions/64 clocks	Real Hits/64 Clocks	Real data size/64 clocks (kbits)	Noise	Clocks	Noise Hits/64 Clocks	Noise data size/64 clocks (kbits)	Buffer needed for 64 clocks (kbits)	Number of Readout Lines	Readout Time/data word (nsec)	Readout Time (beam clocks)	Noise Hits/chip needed to Fall Behind	Noise Rate/chip	Readout Clock Speed (Mbps)
1	128	28	3584	0.028	1.0	1	100.352	1.71	0.001	64	229.4	3.9	7.9	1	85.0	4.2	1.2	0.1	200
4	128	56	7168	0.028	1.0	1	200.704	3.41	0.001	64	458.8	7.8	15.8	1	85.0	4.2	1.2	0.1	200
1	128	28	3584	0.028	1.0	1	100.352	1.71	0.001	64	229.4	3.9	7.9	2	42.5	2.6	2.4	0.1	200
4	128	56	7168	0.028	1.0	1	200.704	3.41	0.001	64	458.8	7.8	15.8	2	42.5	2.6	2.4	0.1	200
1	128	28	3584	0.028	1.0	1	100.352	1.71	0.001	64	229.4	3.9	7.9	4	21.3	1.8	4.7	0.1	200
4	128	56	7168	0.028	1.0	1	200.704	3.41	0.001	64	458.8	7.8	15.8	4	21.3	1.8	4.7	0.1	200
1	128	28	3584	0.028	1.0	1	100.352	1.71	0.001	64	229.4	3.9	7.9	6	14.2	1.5	7.1	0.1	200
4	128	56	7168	0.028	1.0	1	200.704	3.41	0.001	64	458.8	7.8	15.8	6	14.2	1.5	7.1	0.1	200

Table 6 - Buffer requirements for the transition module for most challenging case of AuAu events, various options of readout lines/chip, different levels of chip "ganging", and a extremely conservative noise estimate. In addition the time to readout an event is given for the same conditions.

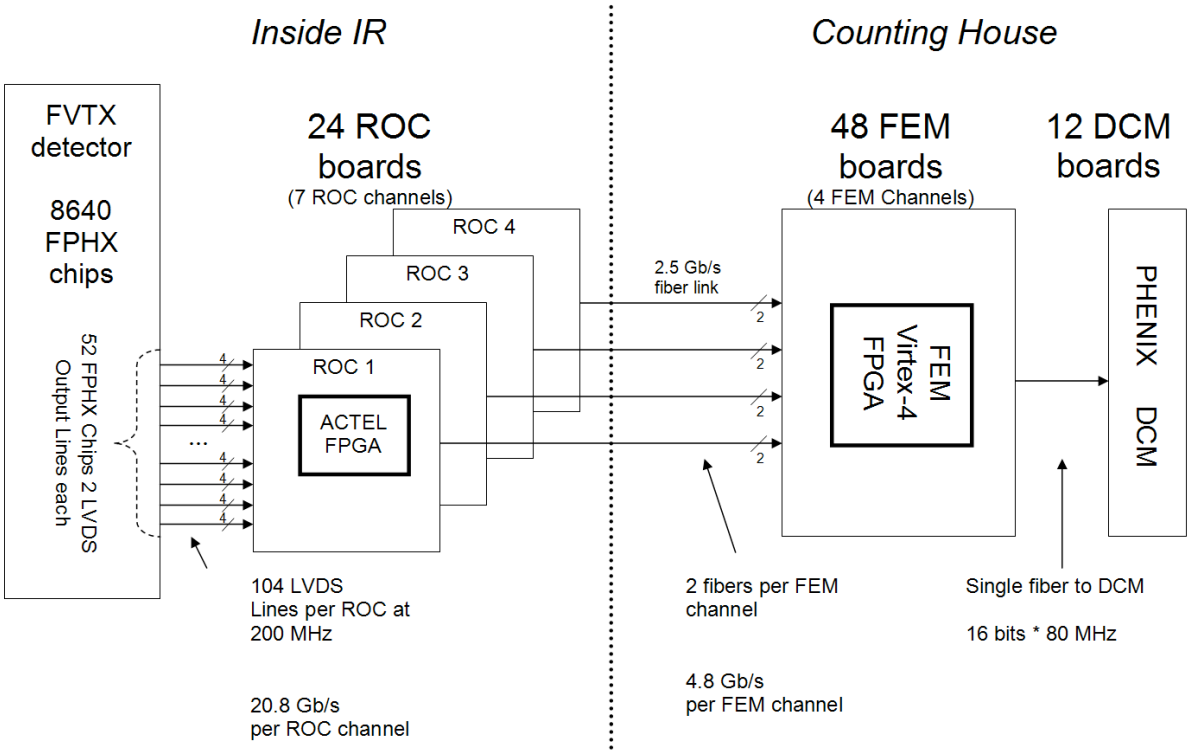

Figure 86 Block diagram of the FVTX readout electronics components.

4.5 Radiation Environment and Component Selection

The evaluation of the FPGA technology available for use on the FVTX Read-out Controller (ROC) primarily considers the effects of the radiation on the performance of the overall system. Additional considerations included I/O configurations, serial communication capabilities and reconfiguration of the device within the system. The choice of technology is primarily the choice of configuration memory technology as logic implementation and density do not really impact our application. The different configuration technologies and their suppliers under consideration are as follows:

SRAM	Altera, Xilinx
FLASH	Actel ProASIC3
Anti-fuse	Actel Axcelerator

The primary concern for FVTX about FPGAs is the ability to operate in a radiation environment. Considerable effort and investigation has gone into this question by such organizations as NASA, DOD and CERN. The concern here is to determine the radiation environment and its effects on FPGA performance for the FVTX system. The radiation environment for the FVTX is the environment of the PHENIX interaction area with either RHIC I or RHIC II luminosities. The master's thesis *A scalable analytic model for single event upsets in radiation-hardened field programmable gate arrays in the PHENIX interaction region* by Steven Skutnik provided

invaluable information on defining these environments as did the ASIC discussion section of the VTX TWIKI. The total integrated dose that the FVTX detector is expected to see is on the scale of 20 kRad/yr over 10 years, though the absolute value depends on the radial position of the components.

Based on the above, the upset rates in the PHENIX radiation environment at 10 and 40 cm are as follows:

RHIC I AuAu
10cm 1.6×10^{-6} /bit/hr
40cm 1.0×10^{-7} /bit/hr

RHIC II AuAu
10cm 1.6×10^{-5} /bit/hr
40cm 1.0×10^{-6} /bit/hr

RHIC II p+p
10cm 1.28×10^{-4} /bit/hr
40cm 8.0×10^{-5} /bit/hr

The primary elements of the FPGA that are affected by the radiation are the SRAM memory elements, clocks and sequential logic. The primary concern with Altera and Xilinx FPGAs is that the configuration or functionality of the device is contained in SRAM and upsets in this memory affect the function of the device and will cause it to no longer perform the function as it was initially programmed. Both Xilinx and Altera offer configuration "scrubbing" solutions that check the configuration but they require a reload of the configuration if an error is detected, which takes time. The configuration SRAM size dominates the FPGA SEU rates as it is 3 to 10 times the size of the data SRAM available. The configuration and data memory sizes for a mid-range Statix II GX part and a high-end Cyclone II part are shown below:

Altera EP2SGX60	Configuration SRAM = 16,951,824	Data SRAM = 6,747,840
Altera EP2C70	Configuration SRAM = 14,319,216	Data SRAM = 1,152,000

The SEU rates for the SRAM based FPGAs must include both configuration and data memories. The Altera and Xilinx devices are extremely similar in regards to their radiation susceptibility so we use just the Altera device as an example here. In consideration of the application in the FPGA for FVTX, data memory upsets are ignored and triple redundancy methods would be used on sequential logic to reduce upsets to negligible levels. Therefore, considering only configuration SRAM upsets, the upset rate for the Altera chips are as follows:

EP2SGX60	27.12 upsets/hr	RHIC I AuAu	10cm
EP2C70	22.91 upsets/hr	RHIC I AuAu	10cm
EP2SGX60	271.2 upsets/hr	RHIC II AuAu	10cm
EP2C70	229.1 upsets/hr	RHIC II AuAu	10cm
EP2SGX60	2170 upsets/hr	RHIC II p+p	10cm
EP2C70	1833 upsets/hr	RHIC II p+p	10cm

EP2SGX60	1.70 upsets/hr	RHIC I AuAu	40cm
EP2C70	1.43 upsets/hr	RHIC I AuAu	40cm
EP2SGX60	16.95 upsets/hr	RHIC II AuAu	40cm
EP2C70	14.32 upsets/hr	RHIC II AuAu	40cm
EP2SGX60	135.6 upsets/hr	RHIC II p+p	40cm
EP2C70	114.6 upsets/hr	RHIC II p+p	40cm

These upset rates are per device so the system upset rate is determined by multiplying these rates by the number of devices in the system. For the LDRD version of FVTX device count is between 12 (lower limit should be 8 if you follow our design) and 48 and for the DOE FVTX system the device count is between 48 and 192 devices. Even with configuration scrubbing the SRAM FPGAs have an unacceptable down time because the configuration reload time is between 1 and 2 seconds.

The Actel FPGAs do not have SRAM configuration memory so they are immune to this form of upset. FLASH memories exhibit dissipation of the charge on the floating gate after 20kRad of integrated dose. The dissipation is not permanent damage and is remediated by reprogramming the device. Flash memories also displayed SEE problems during programming during radiation exposure that included gate punch-through, a destructive effect. These types of SEEs are avoided by not programming the FLASH under radiation exposure conditions, namely during machine operation.

The Actel FPGAs have a decided advantage over the SRAM based FPGAs since they do not have configuration upsets.

The additional factors to consider for the selection of the FPGA are I/O configurations, serial communication capabilities and reconfigurability in the system.

The I/O configuration necessary for the ROC is to accept many input differential LVDS pairs as that is the native signaling mode for both the FPIX and PHX interface chips. The Actel devices allow for almost 100% of their I/O pins to be differential pairs. The Altera devices are both less than 50% necessitating the inclusion of LVDS to CMOS translators in order to use these devices.

The Altera Stratix II GX includes built-in SERDES for up to 6.375 Gbit/s data links (and Xilinx does too right?). None of the other devices have this feature and thus will require an external device for high speed serial communications protocols (> 600Mbits/sec). Each of the devices have the capability for moderate speed (600 Mbit/sec) communications.

Finally, in-system reconfiguration is available for the Actel ProASIC 3 Flash based FPGA and the Altera devices. The Actel Axcelerator is a one-time programmable device.

In consideration of all of these factors the Actel ProASIC 3 Flash based FPGA provides the best solution to the FVTX ROC FPGA requirements because it is immune to radiation problems, it provides the I/O capabilities required, it allows reprogrammability. The following table summarizes most of these factors for the different candidate FPGAs.

FVTX Read-out Controller FPGA Comparison

	Actel Axcelerator	**Actel ProASIC3**	**Altera Stratix II GX**	**Altera Cyclone II**
Model	AX 2000	A3PE3000	EP2SGX60	EP2C70
Configuration type	Anti-fuse	FLASH	SRAM	SRAM
Radiation Tolerance	200kRad	200kRad	50kRad	50kRad
Single-ended I/O / Differential I/O pairs	684 / 342	616 / 300	534 / 78	622 / 262
Voltages	1.5	1.5	1.2	1.2
Power (Quiescent)	22mA	25mA	820mA	250mA
Built-in SERDES	No	No	Yes	No
I/O Rates	LVDS - 700 Mb/s	LVDS - 700 Mb/s	LVDS-6.375 Gb/s	LVDS-622 Mb/s
Configuration Errors	No	No	Yes	Yes
SEE types	clocks, data memory	clocks, data memory	configuration, clocks, memory, SERDES	configuration, clocks, memory
SRAM Memory- Data	294912	516096	6747840	1152000
SRAM Memory- Configuration	0	0	16951824	14319216
FLASH Memory- Configuration	0	0	32 Mbyte	16 Mbyte
RHIC I AuAu SEU Rate - 10 cm /hr-chip	0.00	0.00	27.12	22.91
RHIC I AuAu SEU Rate - 40 cm /hr-chip	0.00	0.00	1.70	1.43
RHIC II AuAu SEU Rate - 10 cm /hr-chip	0.00	0.00	271.23	229.11
RHIC II AuAu SEU Rate - 40 cm /hr-chip	0.00	0.00	16.95	14.32
RHIC II p+p SEU Rate - 10 cm /hr-chip	0.00	0.00	2169.83	1832.86
RHIC II p+p SEU Rate - 40 cm /hr-chip	0.00	0.00	135.61	114.55
Total Integrated Dose	>200k	>200k	>50k	>50k

SEU Rates

RHIC I AuAu-10cm	1.60E-06
RHIC I AuAu-40cm	1.00E-07
RHIC II AuAu-10cm (200GeV)	1.60E-05
RHIC II AuAu-40cm (200 GeV)	1.00E-06
RHIC II p+p-10cm (500 Gev)	1.28E-04
RHIC II p+p-40cm (500 Gev)	8.00E-06

4.6 Mechanical Structure and Cooling

The mechanical structures and cooling are part of the integrated design of the barrel and endcaps. The majority of the support structure has been designed as part of the barrel effort and remaining issues concerning ladders and cooling specific to the endcaps will be part of this proposal. The cooling system is being designed for the VTX project where the heat load is ~ 2.5 kWatts. Since the FVTX total heat load is only ~ 100 Watts, the inclusion of the FVTX to the cooling system means only a small increase in the total required heat capacity.

A conceptual design of the silicon vertex detector was commissioned by the LANL group

to HYTEC, Inc. HYTEC provided the mechanical designs for the ATLAS silicon pixel group and has 15 years of design experience with silicon vertex detectors. For PHENIX they have also designed the station-1 muon detectors and the station-2 spider and they also did the finite element analysis for the station-3 octants. The VTX/FVTX mechanical conceptual design was completed and a report written.

http://p25ext.lanl.gov/~hubert/phenix/silicon/HTN-111003-0001.pdf

Recently, in 2005 and then again in 2007, the original concept was reanalyzed to incorporate changes that have occurred over the intervening years. The most recent report was issued in April 2007.

http://www.phenix.bnl.gov/WWW/publish/brooks/silicon/reviews/Nov07/

We summarize the results of both reports:

For the internal support and cooling of the VTX and FVTX detector, the major results of the conceptual design are:

- The use of sandwich composites will satisfy the radiation length requirements and provide the required stiffness.
- The outer frame structure should be a single diameter encompassing both the barrel and end-caps.
- The modular clamshell design can satisfy the stability requirements provided the connection issues are studied further.
- A circular arrangement is suggested to facilitate utility routing and fabrication.
- Structural end disks at either end of the structure are recommended to prevent deformation
- The ladders should have a simple support at one end and floating support at the other end to minimize thermal strains

The R&D issues identified are:

- Building prototypes of ladder assemblies to verify calculations.
- Building full-scale prototype to test static and dynamic stiffness.
- Develop connections of modules.
- Develop support design.
- Refine calculations and develop full concept for room temperature operation.

4.6.1 Design Criteria

The goal of the study was to establish a feasible design and to identify outstanding design issues. The study was based on a preliminary list of design requirements and a straw-man layout of the

detector structure. To adequately address all structural and mounting issues, a fully integrated design, which includes the barrel detectors and future end-caps extension, is needed. This design needs to address all integration issues not only for the barrel and the end-cap vertex trackers, but also with other potential PHENIX upgrades.

The design requirements of the conceptual study were,

- Modular Design
  - End-caps detectors can be mounted independently at a later time
  - Support structure separated vertically into two half shells
- Detector Coverage
  - Hermetic design
  - Four barrel layers
  - Four end-cap layers in each forward section
  - Fiducial volume < 20 cm radius, z < 40cm
- Radiation length goal < 2.7% per layer (VTX)
- Room temperature operation desirable, 0 deg Celsius if needed
- Dimensional stability < 10-15 microns

4.6.2 Structural Support

The selection of materials for the support structure is based upon the above criteria where the most important material properties are low radiation length, low density, high stiffness, and availability. Out of three candidates (i) beryllium, (ii) graphite fiber reinforced plastic (GFRP), and (iii) Carbon-Carbon, the GFRP was chosen for the study because of its wide availability, works well in sandwich composites, and has good radiation length and strength properties. The GFRP is still the material of choice.

4.6.2.1 Structural Analysis

The structural analysis includes two studies, a first study using finite element analysis models and the resulting modal frequencies to look at dynamic stiffness of tracker concepts and a second study to look at the static stiffness with mass loaded structures. The lower modal frequency limit is set at 70 Hz on a fully loaded structure so that the natural frequencies due to environmental conditions such as pumps, traffic, etc. do not couple into the structure and cause instabilities greater than 25 microns.

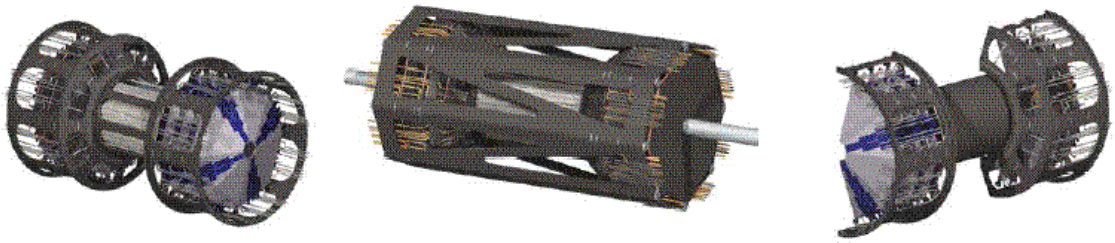

Figure 87 Design concepts studied for the vertex detector support structures. The center most concept with the constant outer diameter shell had the highest fundamental frequency.

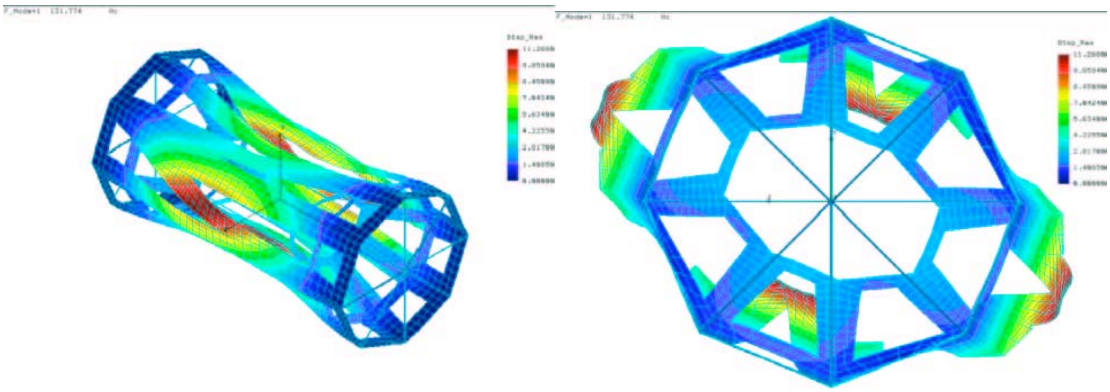

Figure 88 First mode shape that dominated the dynamic structural stiffness analysis

Various support structures shown in Figure 87 were studied. The center most structure has the highest frequency limit.

The dumbbell shaped structure has the lowest mode frequencies below 53 Hz while the concept with the uniform shell with constant outside diameter has the lowest fundamental mode at 132 Hz, well above 70 Hz. In Figure 88 the associated first mode shape of the concept that has the highest fundamental frequency is shown

The static analysis under gravitational load is shown in Figure 89 for the concept with the uniform shell. A 1.0 G load is applied vertically to the fully loaded structure. The maximum displacement is 14.5 microns and the maximum stress is 130 psi. These satisfy the design criteria so the uniform shell with constant diameter has been chosen as the concept to be pursued.

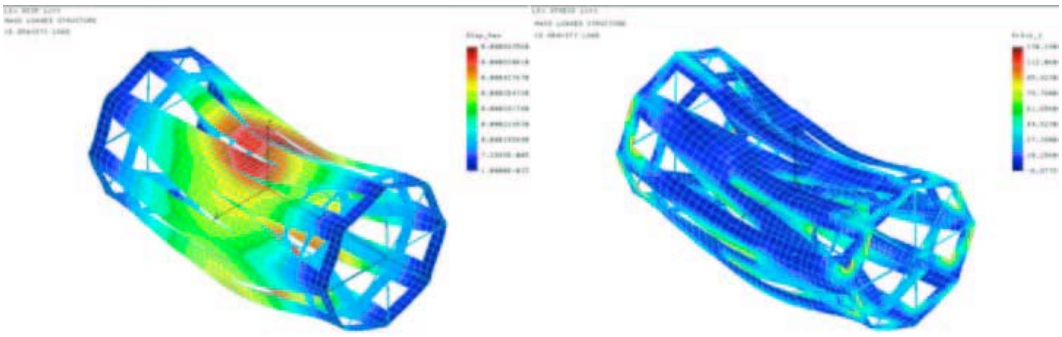

Figure 89 Displacement and principle stress from a 1.0g gravity load on a full mass loaded structure

4.6.3 Endcap Ladder Wedge Structure

The forward regions consist of 4 disk arrays of wedge modules oriented normal to the beam pipe. Conceptually, we have chosen a flat panel structure with sensors and electronics mounted on either side of the panel so that we can achieve hermetic coverage.

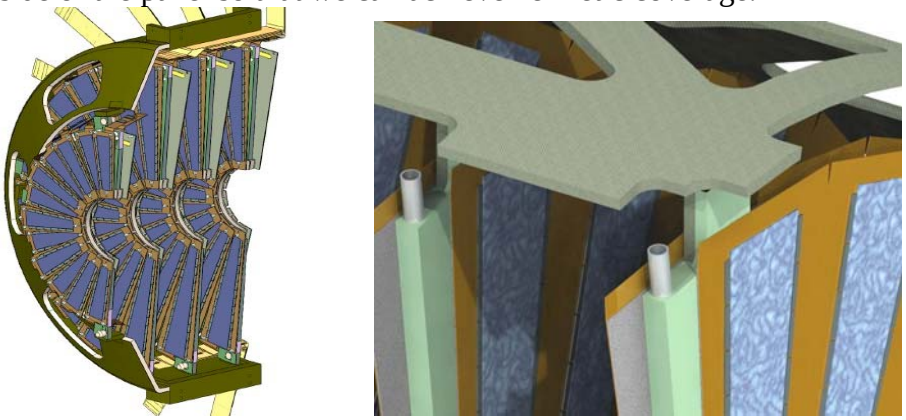

Figure 90 The forward region disk assembly is shown on the left and a close up of the detail showing the individual wedges is at right.

The forward region disk array is shown in Figure 90. The new FPHX chip has a heat load of 90 uW per channel so the total for each end cap is ~50 W. In comparison to the barrel this is a very small heat load and greatly simplifies the removal of heat. The disk panel structure consists of thermally conducting carbon composite with cooling tubes mounted on the outer radius. Heat generated by the wedge assemblies is conducted through the wedge carbon composite backplane to the outer radius cooling tubes. Thermal and gravity sag calculations were performed and no serious distortions were observed. The results of thermal calculations are shown in Figure 91. With only the outer radius cooled the temperature gradient across the wedge is only 2.5 deg C verifying that the wedge stackup design is adequate to transfer heat to the cooling system. This is primarily because the heat load of the wedge is quite small (.3 W) and the carbon backing is an excellent heat conductor.

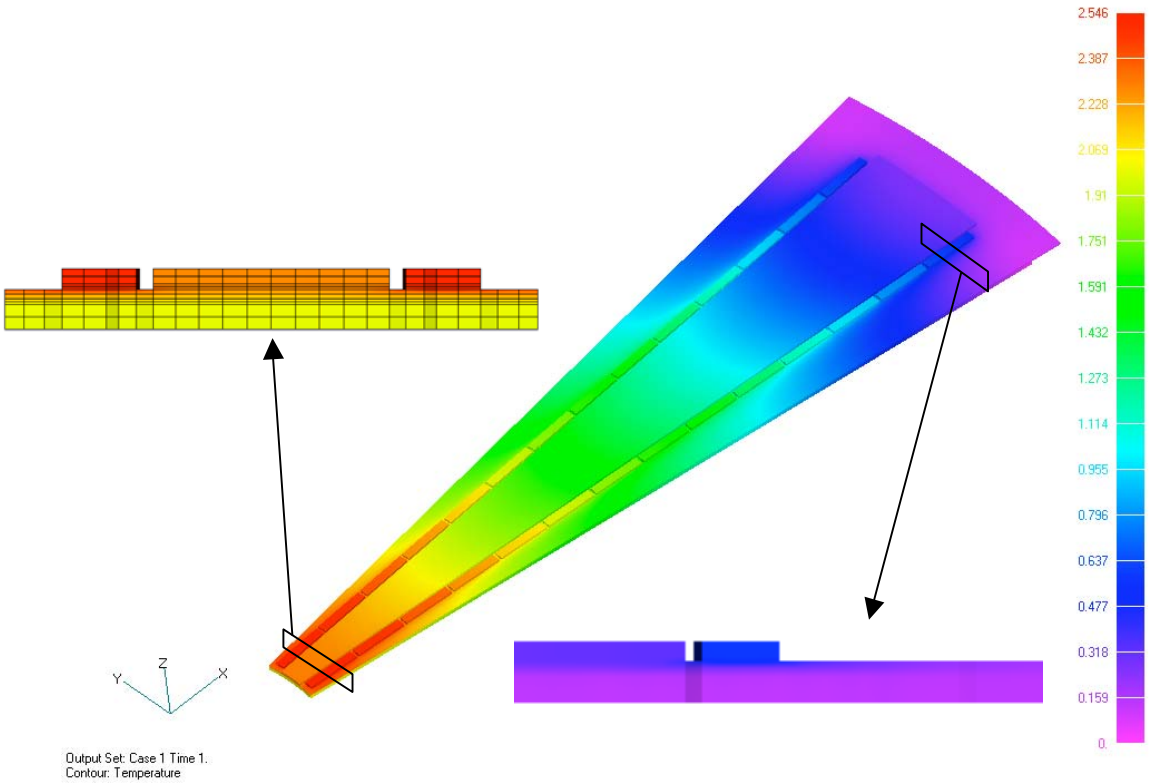

Figure 91 Thermal analysis of the wedge assembly. The temperature gradient from top to bottom is 2.5 deg C.

A modal analysis of the FVTX endcap has been performed and the results are shown in Figure 92. Evident in this picture is the first model frequency of 83.9 Hz seen as a pivoting about the attachment fixture at the top and bottom. The FVTX disk thermal and gravitational distortion summary is shown in Table 7. The largest distortions come from gravity sag but are still only 24 microns. Since this is a static deformation, it can be removed either by metrology of the assembled endcap or by using high energy straight through particles.

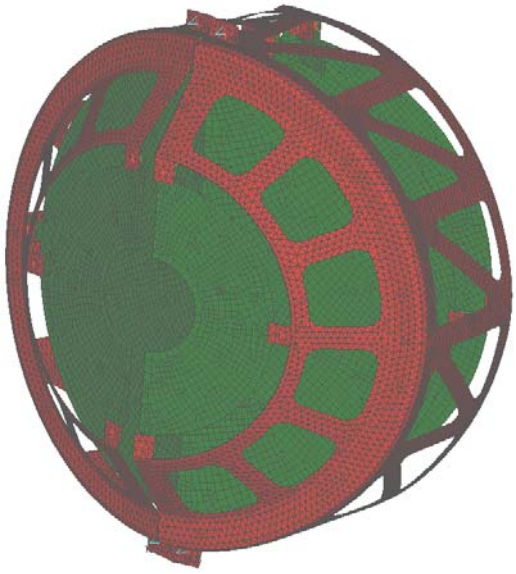

Figure 92 The FVTX modal analysis. The first modal frequency is 83.9 Hz is seen as a pivoting about the attachment points.

FVTX Disks Absolute Deformations (microns) Bottom and Top Kinematic Supports VTX with Barrel Mount Bracings									
Layer	Gravity			Thermal (-21.11°C)			Gravity+Thermal		
	X	Y	Z	X	Y	Z	X	Y	Z
1	-10.9	0.9	2.6	0.3	0.3	-0.2	-10.9	1.2	2.6
2	-11.2	-0.5	2.6	0.5	0.3	0.4	-11.4	0.7	2.6
3	-17.9	-4.4	3.9	0.5	0.3	0.2	-18.3	4.5	4.1
4	-24.1	-8.8	3.3	0.5	0.4	0.4	-24.5	8.8	3.7

Table 7 FVTX distortions from gravity and temperature gradients.

4.6.4 Analysis of the Full VTX/FVTX Structure

Since the VTX design effort has been proceeding and construction is now beginning, it was important for the FVTX to keep pace with its design so that we could insure that the two projects could coexist in the same enclosure without interference. A complete mechanical study has been completed. The results of the FEA of the complete structure demonstrate that the FVTX introduces no change in the VTX first mode and does not change the VTX deformation. The FEA model is shown in Figure 93.

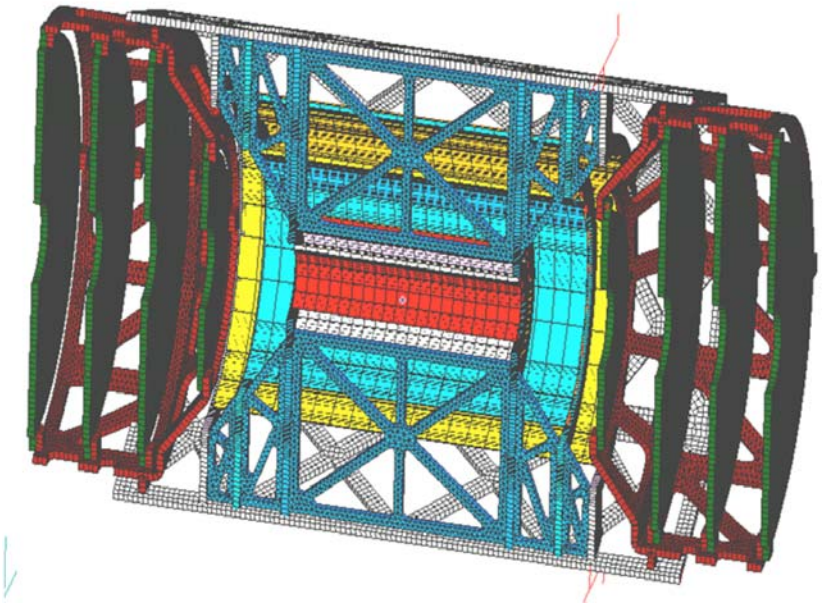

Figure 93 FEA model of the combined VTX and FVTX. The first modal frequency is 38.5 Hz

A full system level analysis has also been finished for the combined system. The model is shown in Figure 94..

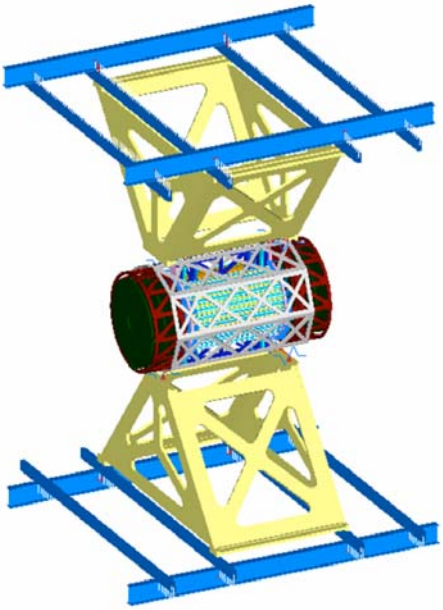

Figure 94 Full system FEA. The first frequency mode is 24 Hz.

4.7 Endcap Analysis Summary

The conceptual design studies revealed the following:

- Single phase cooling is well suited to the endcaps.
- Only one cooling loop is required on the outer radius of the disk.
- 2mm cooling tubes and panel thickness are adequate.
- The radiation length of the octant panel exclusive of sensor and electronics is ~ 0.6 %.
- The FVTX and VTX coexist in the enclosure without interference.
- No mechanical show stoppers.

The R&D issues consist of refining the calculations, designing attachment points to the main support structure, and prototyping the octant panels.

4.8 Assembly and Integration

4.8.1 Assembly

We can categorize the assembly into a few distinct categories; wedge, disk, cage, electronics.

4.8.1.1 Wedge

The wedge assembly consists of putting the HDI, sensor, and chips onto the backplane, affixing the passive components, wirebonding, testing and potting the wire bonds. We will use precision jigs to accomplish this assembly. We expect to do three wedges per day when the production cycles starts. The concept for attaching the HDI to the backplane is shown in the left panel in Figure 95. Vacuum jigs hold the HDI and backplane in each jig and the pieces are glued together as shown. Pins align the two jigs. For attaching the sensor to the HDI we first optically align the sensor to the alignment pin holes in the jig using fiducial marks on the sensor (shown in the right panel in Figure 95) and then put the two sides together. It will take 8-24 hours for the glue to cure so we will have 3 identical setups for these assembly tasks.

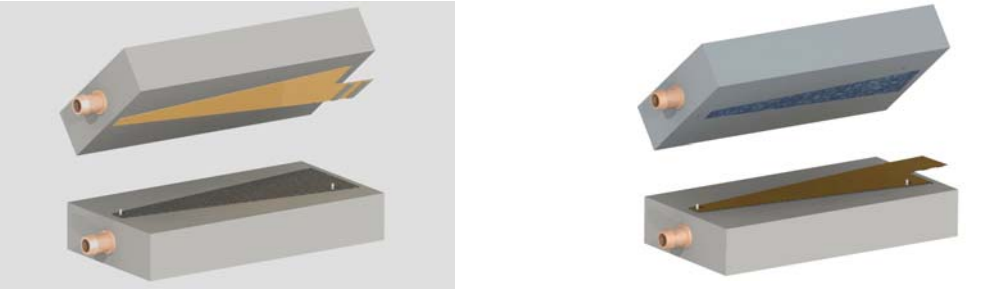

Figure 95 Assembly jigs for Backplane to HDI in the left panel and the sensor to HDI in the right panel.

At this stage the sensor, HDI, backplane assembly is complete and the next step is to send the completed units to a vendor for chip and passive component attachment and wire bonding. A QA system test will be done on the completed unit and then the wire bonds will be potted for protection before the completed wedge assembly is shipped back. A second QA procedure will be done when received. The details of the QA procedures will ultimately wait until a later date but the outline is given in section 4.9.

4.8.1.2 Disk

The wedges populate both sides of the disk. An exploded view is shown in Figure 96. Visible around the inner and outer radius are the alignment pins for the wedge assemblies. These pins locate the wedge assemblies to an accuracy < 25 μm. The assembly procedure will be to place the certified wedge assemblies onto the disk and fasten with nylon screws.

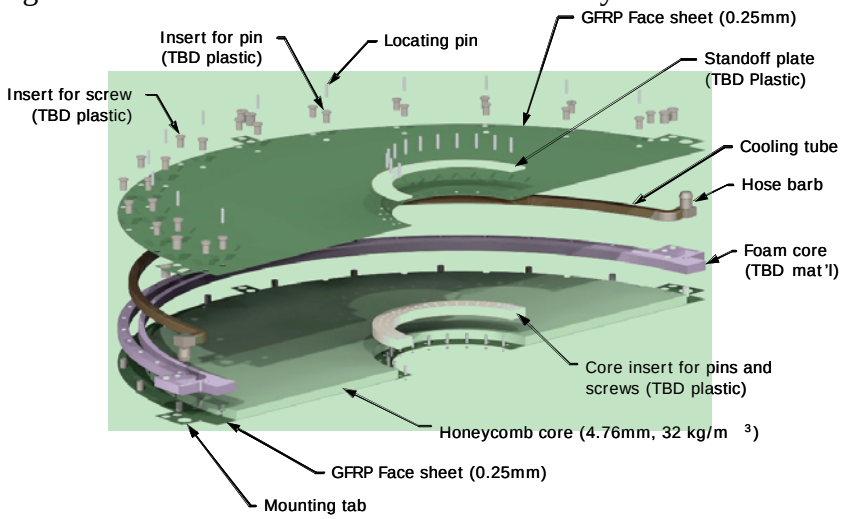

Figure 96 Exploded view of the disk showing the series of alignment pins on the outer and inner radius. The alignment pins accurately locate the wedges on the disk.

4.8.1.3 Cage

A holding jig assembly will be fabricated that will allow the disk to be held while the wedges are placed. After assembly the disk assembly will be surveyed to accurately locate the sensors to ~10 μm.

The assembly into the cage is reasonably straight forward owing to the simplicity of the disk assembly. The disk assembly has three tabs at the outer boundary for attachment to the cage assembly. As shown in Figure 97 the tab contains an alignment pin hole and a screw hole for fastening the disk in place. The general procedure for the cage assembly will be to, attach the disks starting with the smallest disk and working toward the back of the endcap, and as each disk is mounted route the cable with the cable extensions to the rear of the cage. The cable extensions will be connected to the FVTX Readout Cards (ROC) located in the "Big Wheel" area It has been determined that the ROC and it's cooling plate will not be attached to the enclosure back plate but will be supported on the same structure that holds the VTX electronics boards.

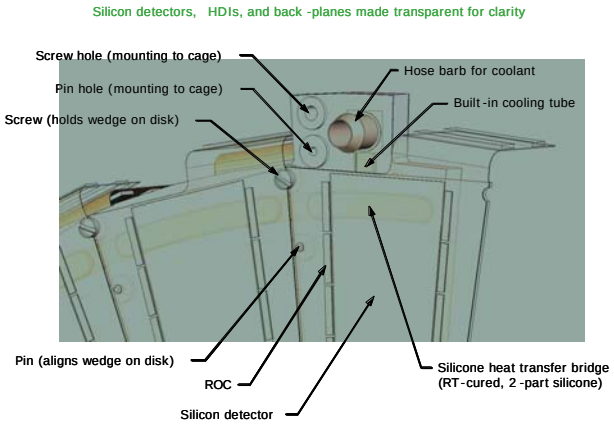

Figure 97 Closeup view of the outer boundary of the disk assembly showing the tab for attachment to the FVTX cage. Located at three points on the circumference, the disk is pinned accurately to the cage and then fastened with a screw.

4.8.2 Integration

Integration involves coordinating the mechanical and electronic activities within the FVTX project and across subsystem boundaries with the VTX, NCC, and the rest of PHENIX. We have put in place integration engineers who are responsible for ensuring that the FVTX integrates seamlessly into the VTX and other subsystems. The two integration engineers, Eric Mannel and Walt Sondheim, have identical responsibilities in the VTX and the FVTX projects. In addition, Robert Pak is working with both projects as the responsible person for infrastructure and mechanics and provides the interface to the BNL engineering team and the external subsystems.

4.8.2.1 Mechanical Integration

The mechanical integration has been an ongoing task for the FVTX since FY2006-7. Supported under R&D funds we have provided substantial input to the efforts by the VTX group to keep the design of the FVTX moving along as the VTX design evolves so that no show stoppers remain and the VTX effort can proceed on schedule. This has been very successful and the FVTX design has matured to the point where we have been able to do the thermal and finite element analysis of the entire VTX-FVTX system to ensure that the two projects coexist without interference. This is an ongoing effort that will last the full length of the project. Periodic reviews will be held.

4.8.2.2 Electronic Integration

Electrical Integration:

The tight space constraints of the VTX enclosure and the close proximity of the electronics for the the VTX detector requires that close attention be paid to the electrical integration of the detector. To facilitate this, the project electrical engineer will develop a set of plans, with the

assistance of the subsystem managers from both the VTX and FVTX projects, along with members of the PHENIX experimental team responsible for overall electronics at PHENIX. The integration can be broken into three separate sub-tasks; power and ground, systems control, and electrical design review.

Power and Ground:

A preliminary plan for power and ground for the VTX and FVTX projects requires that the three subdetectors, VTX pixels, VTX stripixels, and FVTX be electrically isolated from each other to minimize crosstalk and noise. Each of the three systems will provide the means for all grounds to be tied together at a single point, most likely at the power supplies. It is envisioned that the detectors will have several independent grounds within the detector - digital, analog, and shield - which will be specific to each of the detectors and requirements of the electronics chosen in the design. During the design phase of the electrical components, each detector system needs to insure that their grounding plans are appropriate and provide the flexibility to connect or isolate grounds at different points to allow for studies of crosstalk and noise issues, if necessary.

The three subdetectors will also have their own power requirements and it is up to the design teams to specify the power requirements, voltages, current, and noise limits, during the design phase. To maintain the electrical isolation, each of the subdetectors will have their own power supplies. Once full power specifications are known based on the measurements during the proto-type stages, power systems will be evaluated based on performance and cost. However, to minimize the effort required, it is planned that the three subdetectors will use the same vendor if possible.

Systems Control and PHENIX Integration:

Overall electrical integration into PHENIX requires the coordination of the VTX and FVTX design teams and various teams from PHENIX responsible for the overall operations of PHENIX. The project electrical engineer will be responsible for coordinating with the electrical group responsible for power and ground within PHENIX, the DAQ group responsible for data readout of all PHENIX detectors, and the Online Computing Group(ONC) that oversees the slow control and monitoring systems. The project engineer will work with each of these groups to ensure that when the FVTX detector is ready for installation, the detector can be quickly integrated into the PHENIX DAQ and Control systems.

Design Review:

Performing internal design reviews of the electronics is a critical step to ensure that the final design meets not only the readout requirements of the detector, but is compatible with PHENIX overall, and meets all PHENIX, BNL CAD and BNL safety requirements. The FVTX project will use a review procedure similar to the one developed and implemented by the VTX project.

The over all design phase has three primary stages, proto-type, pre-production, and final production. Once the proto-type testing has been completed, and the pre-production design work is nearing completion, the project electrical engineer will call for an internal electronics review

of the component design. The review process will be headed up by the project electrical engineer, and will include other electronics experts from within PHENIX with strong knowledge of the PHENIX detector and DAQ system. The design team will be required to provide in advance sufficient information for the review team to make an assessment as to the viability of the unit to perform to the required specifications and work within the PHENIX detector. This information should include, but is not limited to, electrical schematics, layout files, component list and data sheets, fpga/pld code, power and heat loads as measured on the proto-type, and a detailed Q/A and testing plan. This documentation will be archived for future reference. Once the design has been approved by the review team, pre-production can go forward. Should significant design changes be required following the pre-production review, then a second review may be required. Once the the pre-production units have been made and tested, a second mini-review will be held to verify the performance of the unit and address any final changes that might be required. Upon second approval, full production may go forward. In the case of simple designs, or cases where only a couple of modules are needed, the electrical project engineer can reduce the scope or wave the review process in consultation with the design team, FVTX project management, and PHENIX project management.

4.9 Q/A procedures

The FVTX is a complex assembly of silicon sensors, electronics, mechanical support and thermal management components. The individual pieces that comprise the final complete assembly will be designed, tested and produced at different stages of the project. The Q/A plan will contain a detailed set of test procedures, along with specific pass/fail criteria, to guide the various stages of the project from prototype to Q/A test, from Q/A test to production, and from production to Q/A acceptance for assembly.

4.9.1 Silicon sensors, design and prototype

The design of the silicon sensor will be initiated within the FVTX project. The responsibility for the layout design will be shared by LANL and the Prague collaborators. Major sensor design parameters include:

Wafer diameter and thickness	6”(preferred), 300μm
Implant Width	min 25 μm
Metallization Width	min 25 μm
Readout pitch	75 μm
Polysilicon resistors	1-5MΩ
Capacitor oxide specifications	≥ 200pf
Passivation material	SiO_2 or SiNi
Bond Pad Area	min 50 μm
Test Pad Area	min 50 μm
Guard ring structure	>1 with bond pads

Scratch pad for sensor ID and pass/fail marks
Scribe lines for cutting
Alignment targets for metrology

Test Structures (Large Area Diode, polysilicon, capacitor)

The CAD design will be sent to the vendor and the vendor will evaluate the design in the context of the company's design rules. The final mask design will be created by the vendor, and will be the result of iteration between the FVTX and the vendor. The LANL and Prague collaborators responsible for the sensor design will perform a final review of the proposed mask set, and mutually agree that it is correct, before giving the vendor permission to produce the mask set. The produced mask set will be qualified by the vendor according to their process rules.

The vendor will produce a prototype round of sensors from the mask set. The FVTX project will present a set of performance criteria to the vendor, which must be achieved in order to qualify each sensor for acceptance. Major acceptance criteria with typical values will include:

Wafer resisitivity	2-5 kohm
Wafer thickness and planarity	300 μm, < 10 μm
Maximum leakage current	2 $\mu A/cm^2$
Maximum slope of leakage current versus voltage	
Sensor capacitance versus voltage	
Minimum sensor breakdown voltage	200V
Polysilicon resistor value (if applicable)	1-5MΩ
Integrated capacitor value (if applicable)	200pf
Oxide breakdown voltage	>50V
Visual inspection for defects and flaws	

The prototype batch of silicon sensors will be re-tested by the FVTX project. The exact location where these tests will take place is undetermined at this time, but laboratories with suitable equipment exist at Prague and at UNM. The test laboratory should have an adequate clean area and a semiconductor characterization station.

All the acceptance criteria tests that the vendor performs will be repeated by the project. The sensor depletion voltage and breakdown voltage will be measured on each individual sensor. The overall sensor leakage current/voltage characteristic will also be measured on each sensor. Additionally, we will design a custom probe card that exactly matches the test pad geometry on the sensors. We will measure the leakage current/voltage characteristic on each individual strip using this probe card. Deviation from a relatively uniform characteristic across the sensor could be indicative of problems in the interstrip isolation or the quality of the passivation layer. We will measure the polysilicon resistance on test resistors on the wafer. We will measure the capacitance/voltage characteristic on a MOS test structure on the wafer. Another test structure will be used to measure the oxide breakdown voltage. Almost all of the test measurements will be controlled by a software interface, such as Labview. The program will record and store all the test data. We will use scratch pads on the wafer to record pass/fail results for each sensor.

A subset of the prototype detectors will be more extensively tested with radioactive sources and a 1064 nm laser diode to evaluate signal response performance of the sensor. Both methods can produce signals with large enough amplitude that the detector output can be recorded without an

amplifier. The amplitude and pulse shape response to source or laser will test the quality of the integrated coupling capacitors and the sensor depletion voltage characteristics versus bias voltage. By scanning the sensor with the laser diode, we will be able to evaluate the charge sharing characteristic of the sensor.

A typical anticipated yield for sensors fabricated in 4-inch wafer technology is approximately 70%. Because most sensor failures are due to volume defects in the silicon wafer, the number of defects scales with sensor area. We can expect a higher incidence of defects, and therefore a lower yield for sensors fabricated in 6-inch wafer technology. A minimum 50% yield in the prototype round would suggest that the failures were caused by material defects, and probably not process related. This would be sufficient basis to authorize the production run.

4.9.1.1 Silicon Sensors, Production Runs

The same procedures and criteria used for the prototype sensor Q/A will be used for the production runs.

4.9.2 FPHX Readout Chips, Design and Prototyping

The FVTX project will work with the electronics design group at Fermilab to develop the performance specifications of the FPHX readout chip. LANL is leading this effort for the FVTX project. These specifications include:

Front end coupling, ac/dc
Amplification
Shaping time
Noise floor and noise slope
ADC
Zero suppression
Channel mask
Test inject
Kill
Readout architecture and controls
Clock speeds
Data format
Power

The Fermilab design group and the FVTX project, led by LANL, will iterate between the design specifications provided by the project and the chip layout designed by the Fermilab group. The final prototype design will be reviewed by the FVTX project and approved before it is released for submission to the foundry. The Fermilab group will work with the foundry to ensure that the chip layout conforms to the foundry's process rules. The foundry will produce the mask set, and they will be responsible for reviewing and accepting the mask set.

The foundry will perform in-house quality checks on the wafer; however these will likely be basic tests which will not reflect die performance.

The Fermilab team will have a vested interest in qualifying the prototype round of wafers. We will work with them to prepare a probe station at Fermilab and to write software to perform a variety of automated measurements using the probe station. The Fermilab team will write specifications regarding the set points for reference voltages, filter requirements, and the performance metrics. We will test all the die on the wafers before they are diced. Die that fail to meet the acceptance criteria are typically inked on the wafer. The wafers will be sent to a vendor to have them thinned and diced. The die that have passed the acceptance test will be grouped according to similar performance characteristics.

Once they are diced, a subset of the readout chips will be tested extensively in the lab to gather as much operating experience as possible with the chips. Some number of die will be powered for approximately 72 hours to determine if there is any infant mortality concern. Die will be tested with various input configurations, both varying input capacitance over the expected range, and with a range of input amplitudes. The signal-to-noise will be measured over this range of input conditions. The front-end saturation response will be measured. The sensitivity of the chip performance to bias voltages and other hardware and programmable set points will be studied. The ADC pedestals and linearity will be measured. A variety of test patterns using the masking capability will be exercised to look for crosstalk or neighboring channel correlations. Clock frequencies will be varied and measurements made to look for edge coupling from the clock to the other parts of the circuitry. Kill and reset functions will be tested. Test data will be readout under a variety of operating conditions and clock speeds. Tests will be performed to determine failure modes of the data output. Some die will be wire-bonded to a prototype sensor, and the response to an injected charge, either a source or laser diode, will be measured. The filter components between the sensor and the readout chip will be tested and optimized. The ambient temperature can be manipulated to test the system with elevated leakage currents in the sensor. A test in a particle beam would be useful, but not considered necessary to decide whether to move forward to full production of the readout wafers.

If, during these tests, a serious flaw or performance deficiency is found in the readout chip, there will be another design round. This is explicitly written into the Project schedule.

4.9.3 High Density Interconnect (HDI)

There will be an initial prototype round of the HDI. The first test of the HDI is a careful visual inspection. Common failure modes in kapton circuits are opens in the traces, and (often tiny) metal hairs that short adjacent traces. The quality of the trace edge is also an important indicator of good high frequency isolation. The kapton circuit is a precision component in the overall wedge assembly, and so accurate metrology will be performed to measure length, height, width, thickness die pad locations, and sensor bias pad location. The LCR characteristics of the kapton circuit will be tested with test pulses. The fidelity of a test signal will be measured end-to-end. Cross talk between output lines will be studied and electrical characteristics of the HDI will be measured at operating frequencies. UNM is leading the HDI effort

4.9.4 Composite Backplane (Support/Heat Spreader)

Hytec Inc. will determine the composition and specifications for the backplane based on finite element simulations which indicate that our operating temperature specification will be maintained. On receipt of the first articles, we will perform metrology to confirm the length, width, thickness, and planarity of the composite backplane. We will measure the thermal conductivity, in consultation with Hytec. These tests will most likely take place at LANL or at Hytec.

4.9.5 Adhesives

The wedge assembly components are mainly glued together. The kapton HDI will be glued to the composite backplane. The bond must have adequate strength, a uniform and repeatable bead deposition pattern, provide a flat assembly, and provide adequate rigidity under the wire bond pads on the HDI to ensure reliable wire bonding from the readout chip to the HDI. There are two classes of adhesives that we will evaluate; adhesive tape and epoxies. Types of adhesives will include electrically conductive, non-conductive and thermally conductive. We will evaluate various products in close consultation with Hytec, because the company has experience and expertise with these products. If we choose to work with epoxies, we may have to evacuate the mix to get rid of bubble formation. It is very likely that we would use an automated glue dispenser in order to achieve a reproducible epoxy bead pattern.

We will perform precision metrology on the assembly to evaluate the accuracy of the assembly procedure. We will perform a heat conduction evaluation using a suitable heat source on top of the HDI and measuring the temperature distribution on the backplane. We will thermal cycle the assembly to test for mechanical integrity and to determine whether the assembly retains acceptable planarity.

The sensor will be glued to the HDI/backplane. In addition to the requirements stated above, the bias connection has to be made to the underside of the sensor and brought to the perimeter of the HDI. This will most likely be done using a conductive adhesive. We will also test this assembly as above for thermal and mechanical characteristics.

Each of these assemblies will require custom designed vacuum jigs and precision location tooling. The lab where these assemblies and tests will take place has not yet been determined.

4.9.6 Wedge Assembly

The wedge assembly will be built in the following sequence.

Kapton HDI glued to composite backplane
Sensor glued to HDI plus composite backplane

Filter components and bias resistors soldered to HDI
FPHX chips glued to HDI
FPHX output pads wire bonded to HDI
Sensor outputs wire bonded to FPHX input pads
Wire bonds encapsulated

Production quantities of the wedge assembly, prior to wire bonding, can be done at a lab within the project, or at the vendor who does the wire bonding. This will be determined according to cost/benefit. If the assembly is done at the vendor, the work will be carried out in accordance to written procedures, specifications and measurements, and it will be monitored by someone from the FVTX project.

The filter components, bias resistors and FPHX die will likely be attached at the vendor. The surface mount components will be soldered and the FPHX will be attached with adhesive. We will work with the vendor to approve component and die attach procedures. The readout wafer thinning and sawing into individual die will be performed by a qualified vendor, either the one who is awarded the wire bond contract or a different source. The vendor will use a diamond saw, and we will visually inspect the die under a microscope to ensure good cut-edge quality from the saw before sawing the entire wafer lot.

The wire bonding from sensor to readout chip and from readout chip to the HDI will be performed by an approved vendor. We expect the vendor to use a semi-automated wedge bonder and to use aluminum bond wire. The vendor will qualify a process to achieve bonds with reproducible length and loop height. Test bonds will be made to ensure bond strength of approximately 7 grams or greater pull strength.

The wire bonds on the wedge will be encapsulated to protect them during shipping and handling. There are several candidate products, opaque and clear, that will be evaluated. We have had experience using both clear and opaque encapsulant. The advantage to the clear product is that one can observe if a wire is bent over to its neighbor during application of the viscous encapsulant, and this can be corrected before the encapsulant sets. The encapsulant will most likely be applied by the vendor who is selected to do the wire bonding. We would evaluate the integrity of prototype assemblies before we had them encapsulated. We would require visual inspection to confirm that the wire bond pattern is correct on subsequent production assemblies before they are encapsulated.

5 R+D Schedule, Responsibilities and Budget

5.1 R+D Areas

The R&D associated with the endcaps involves designing the FPHX chip, developing the interface between the FPHX chip and the existing PHENIX DCMs, sensor design, developing the wedge structure, and developing the bus and flex cable. The FPHX and data interface is the most involved of the R&D projects. The rest are starting from existing technology or use standard commercial concepts. The R&D for the endcaps will be supported at LANL and BNL.

At LANL we will complete the R&D for the interface, the mechanical support and ladder, and the sensor design. BNL will support the R&D for the FPHX design and modification.

5.1.1 FPHX

The FPHX chip design will borrow elements from previously successful chips such as the FPIX2, SVX4, FSSR, etc. The FPHX is a 1 column x 128 channel structure designed for holes rather than electron collection. It has a data-push architecture similar to the FPIX2.1 chip and ~ 70 micron channel pitch. The R&D issues involve optimizing the front-end for the mini-strips, designing the digital readout specifically for the PHENIX DAQ and converting the chip to wire bonds. FNAL electronics group (Ray Yarema, head) has completed the conceptual design of FPHX and the next phase will be to do the wafer layout and prototype. We expect that this phase will proceed in mid calendar 2007.

5.1.2 Sensor

The sensor will be a standard p on n DC coupled silicon diode. This is a very conventional design that is available from many vendors. The R&D consists of mainly developing the prototype masks and producing prototypes for testing. The Czech group has made an initial design of the sensor and procured the first prototype wafer. We expect to have the wafer diced and begin testing in mid calendar year 2007.

5.1.3 Interface

The ROC and FEM boards that will connect between the PHX chip and PHENIX DCMs will need to provide the following functions:

- Strip the sync words out of the data stream, retaining only data words
- Combine the data from several chips into one serial stream which will go via fiber to a FEM
- Provide buffering of the continuously streaming data from the PHX chips for 64 beam clocks, and this buffering must be adequate for everything from pp running to central Au-Au events
- Upon a lvl-1 accept, retrieve the data from the buffer for the appropriate beam clock and package it into a format acceptable by the DCM
- Pass beam clock to the PHX chip, assure sychronization
- Provide an interface to download initialization settings to the PHX chips
- Perhaps provide ability to reset PHX chip(s)

We expect the board designs to be largely completed by our LDRD grant which will put a prototype forward silicon tracker in to PHENIX, and will be using FPIX chips which will have very similar digital output to the FPHX chips. Some details will need to be modified to accept the somewhat different segmentations of the FVTX detector compared to the LDRD detector. A

large portion of the designs have already been prototyped via efforts at LANL and Columbia, using FPIX chips and FPGA evaluation boards. The FPIX chips have been successfully read out, with one or more data lines per chip, the data have been buffered into 64 clock buffers, and the correct event from a given chip has been shown to be properly pulled out from the clock buffers upon a trigger. Prototyping began in mid 2006 and board design will begin in mid 2007.

5.1.4 Mechanics

The R&D necessary for the mechanical structures for the FVTX is closely coupled to the designs that are already underway for the VTX. LANL already has a major responsiblitity to coordinate the VTX mechanical activities with the local design firm and LANL will continue to do the same for the FVTX. The majority of the R&D and design effort involves a design for the FVTX ladder assemblies, ladder support disks and the cage assembly that will hold the disks. Because it was important that the design of the VTX and FVTX mechanical proceed in parallel to prevent the two designs from interfering with each other, the FVTX designs began in mid 2006 and was funded out of LANL's base program and LDRD. Prototyping is expected to begin in the 3rd quarter of FY07.

5.2 Schedule

The schedule for the FTVX project is shown in Figure 98. Included in the schedule is the R&D timeline. We have assumed R&D money begins in the second quarter of FY06 and construction funds begin in the second quarter of FY08. Task durations are based on previous experience of the engineering teams and quotes. The total project duration is due primarily to the sensor and PHX R&D and procurement times.

ID	WBS	Task Name	Start	Finish
1	1	FVTX Project	Fri 10/21/05	Tue 5/24/11
2	1.1	Start Construction	Tue 1/1/08	Tue 1/1/08
3	1.2	Start R&D BNL	Mon 1/2/06	Mon 1/2/06
4	1.3	Start R&D LANL	Mon 1/2/06	Mon 1/2/06
5	1.4	Wedge Components	Mon 1/15/07	Tue 2/9/10
6	1.4.1	Wedge sensors	Mon 1/15/07	Tue 2/9/10
7	1.4.1.1	design sensors	Mon 1/15/07	Fri 2/23/07
8	1.4.1.2	procure prototype sensor	Mon 2/26/07	Mon 3/16/09
9	1.4.1.2.1	mask set	Mon 2/26/07	Fri 3/23/07
10	1.4.1.2.2	sensor manufacture	Mon 2/26/07	Fri 5/18/07
11	1.4.1.2.3	test prototype sensor	Mon 5/21/07	Fri 8/31/07
12	1.4.1.2.4	wire bond FPHX	Tue 4/29/08	Mon 7/7/08
13	1.4.1.2.5	test wedge assembly(system test)	Tue 7/8/08	Mon 3/16/09
14	1.4.1.3	procure sensors	Wed 10/1/08	Tue 2/9/10
15	1.4.1.3.1	procure sensor	Wed 10/1/08	Tue 4/28/09
16	1.4.1.3.2	Sensor Q/A	Wed 11/12/08	Tue 5/5/09
17	1.4.1.3.3	Attach flex cable	Fri 4/10/09	Thu 11/5/09
18	1.4.1.3.4	Attach sensor	Fri 4/17/09	Thu 11/12/09
19	1.4.1.3.5	wire bond assembly	Wed 6/17/09	Tue 1/12/10
20	1.4.1.3.6	test chip,sensor + cable assemblies	Wed 7/15/09	Tue 2/9/10
21	1.4.2	FPHX Chip	Thu 3/15/07	Tue 6/16/09
22	1.4.2.1	design(FNAL)	Thu 3/15/07	Wed 6/20/07
23	1.4.2.2	Review design	Mon 6/25/07	Mon 6/25/07
24	1.4.2.3	layout	Tue 6/26/07	Mon 12/10/07
25	1.4.2.4	procure prototype chip	Tue 12/11/07	Tue 12/9/08
26	1.4.2.4.1	First MOSIS run	Tue 12/11/07	Mon 3/31/08
27	1.4.2.4.2	test prototype(FNAL)	Tue 4/1/08	Mon 5/26/08
28	1.4.2.4.3	redesign	Tue 5/27/08	Mon 7/21/08
29	1.4.2.4.4	submit 2nd MOSIS run	Tue 7/22/08	Mon 11/10/08
30	1.4.2.4.5	test 2nd proto	Tue 11/11/08	Mon 12/8/08
31	1.4.2.4.6	review and approve	Tue 12/9/08	Tue 12/9/08
32	1.4.2.5	procure production chips	Wed 12/10/08	Tue 6/16/09
33	1.4.2.5.1	engineering run	Wed 12/10/08	Tue 3/24/09
34	1.4.2.5.2	test chips(FNAL)	Wed 3/25/09	Tue 6/16/09
35	1.4.3	Kapton flex cables HDI	Mon 9/3/07	Thu 4/9/09
36	1.4.3.1	design	Mon 9/3/07	Fri 9/21/07
37	1.4.3.2	procure prototype HDI	Mon 9/24/07	Mon 1/28/08
38	1.4.3.2.1	prototype	Mon 9/24/07	Fri 10/26/07
39	1.4.3.2.2	test	Mon 10/29/07	Fri 11/9/07
40	1.4.3.2.3	redesign	Mon 11/12/07	Fri 11/23/07

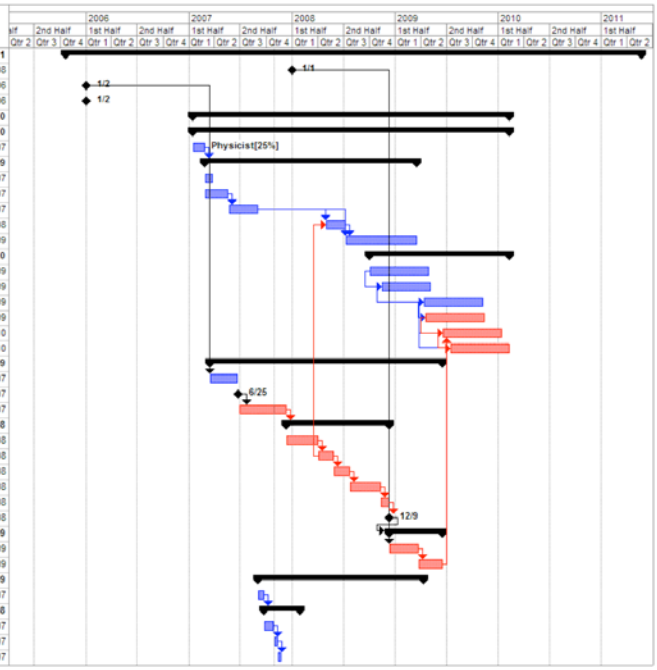

ID	WBS	Task Name	Start	Finish
40	1.4.3.2.3	redesign	Mon 11/12/07	Fri 11/23/07
41	1.4.3.2.4	prototype	Mon 11/26/07	Fri 12/28/07
42	1.4.3.2.5	test 2nd prototype	Mon 12/31/07	Fri 1/25/08
43	1.4.3.2.6	review and approve HDI	Mon 1/28/08	Mon 1/28/08
44	**1.4.3.3**	**procure production HDI**	**Fri 1/2/09**	**Thu 4/9/09**
45	1.4.3.3.1	procure	Fri 1/2/09	Thu 3/12/09
46	1.4.3.3.2	test cable	Fri 3/13/09	Thu 4/9/09
47	**1.4.4**	**Kapton HDI to ROC interconnect**	**Mon 12/31/07**	**Wed 4/8/09**
48	1.4.4.1	design	Mon 12/31/07	Fri 2/1/08
49	1.4.4.2	prototype	Mon 2/4/08	Fri 3/7/08
50	1.4.4.3	test prototype	Mon 3/10/08	Fri 3/21/08
51	1.4.4.4	procure	Thu 1/1/09	Wed 3/11/09
52	1.4.4.5	test cable	Thu 3/12/09	Wed 4/8/09
53	**1.5**	**DAQ**	**Mon 10/23/06**	**Mon 3/29/10**
54	**1.5.1**	**Fiber output ROC-FEM**	**Mon 3/10/08**	**Wed 7/8/09**
55	1.5.1.1	design	Mon 3/10/08	Fri 3/14/08
56	1.5.1.2	prototype	Mon 3/17/08	Fri 6/1/08
57	1.5.1.3	procure	Thu 1/1/09	Wed 6/24/09
58	1.5.1.4	test cable	Thu 6/25/09	Wed 7/8/09
59	**1.5.2**	**ROC Electronics**	**Tue 1/30/07**	**Mon 7/20/09**
60	1.5.2.1	design	Tue 1/30/07	Mon 3/19/07
61	**1.5.2.2**	**procure prototype**	**Tue 3/20/07**	**Mon 7/20/09**
62	1.5.2.2.1	prototype	Tue 3/20/07	Mon 5/21/07
63	1.5.2.2.2	test prototype	Tue 5/22/07	Mon 7/30/07
64	1.5.2.2.3	redesign	Tue 7/31/07	Mon 9/24/07
65	1.5.2.2.4	2nd prototype	Tue 9/25/07	Mon 11/26/07
66	1.5.2.2.5	test second proto	Tue 11/27/07	Mon 1/21/08
67	1.5.2.2.6	PHENIX system test	Tue 5/12/09	Mon 7/20/09
68	1.5.2.2.7	preproduction prototype	Tue 1/22/08	Mon 5/12/08
69	1.5.2.2.8	review and approve ROC	Tue 5/13/08	Tue 5/13/08
70	**1.5.2.3**	**procure production ROC**	**Thu 1/1/09**	**Mon 6/15/09**
71	1.5.2.3.1	production	Thu 1/1/09	Wed 4/8/09
72	1.5.2.3.2	QA - 28 units	Thu 4/9/09	Mon 6/15/09
73	**1.5.3**	**FEM Electronics**	**Tue 1/30/07**	**Mon 5/25/09**
74	1.5.3.1	design	Tue 1/30/07	Mon 3/19/07
75	**1.5.3.2**	**procure prototype FEM**	**Tue 3/20/07**	**Mon 5/25/09**
76	1.5.3.2.1	prototype	Tue 3/20/07	Mon 6/4/07
77	1.5.3.2.2	test prototype	Tue 6/5/07	Mon 8/13/07
78	1.5.3.2.3	redesign	Tue 8/14/07	Mon 10/8/07
79	1.5.3.2.4	2nd prototype	Tue 10/9/07	Mon 11/26/07
80	1.5.3.2.5	test second proto	Tue 11/27/07	Mon 1/21/08
81	1.5.3.2.6	PHENIX system test	Tue 3/17/09	Mon 5/25/09
82	1.5.3.2.7	preproduction prototype	Tue 1/22/08	Mon 5/12/08
83	1.5.3.2.8	review and approve FEM	Tue 5/13/08	Tue 5/13/08
84	**1.5.3.3**	**procure production FEM**	**Wed 5/14/08**	**Fri 10/24/08**
85	1.5.3.3.1	production	Wed 5/14/08	Tue 8/19/08
86	1.5.3.3.2	QA - 28	Wed 8/20/08	Fri 10/24/08
87	**1.5.4**	**Calibration**	**Mon 10/23/06**	**Fri 12/29/06**
88	1.5.4.1	Design Pulse injection	Mon 10/23/06	Fri 11/17/06
89	1.5.4.2	prototype	Mon 11/20/06	Fri 12/15/06
90	1.5.4.3	test prototype	Mon 12/18/06	Fri 12/29/06
91	**1.5.5**	**Ancillary**	**Tue 12/30/08**	**Mon 3/29/10**
92	1.5.5.1	Racks	Thu 1/1/09	Wed 3/11/09
93	1.5.5.2	LV,HV,crates,etc	Tue 12/30/08	Mon 7/27/09
94	1.5.5.3	DCM-24	Thu 1/1/09	Wed 3/11/09
95	1.5.5.4	Slow controls	Tue 12/30/08	Mon 7/27/09
96	1.5.5.5	Misc lab equip	Tue 7/28/09	Mon 10/5/09
97	1.5.5.6	install	Tue 10/6/09	Mon 3/29/10
98	**1.6**	**Mechanics**	**Fri 10/21/05**	**Wed 7/29/09**
99	**1.6.1**	**specifications**	**Fri 10/21/05**	**Thu 2/9/06**
100	1.6.1.1	endcaps - specify heat load	Tue 11/15/05	Mon 2/6/06
101	1.6.1.2	specify mechanical tolerances/distortions	Fri 10/21/05	Thu 2/9/06
102	1.6.1.3	specify disassembly/configuration options	Fri 10/21/05	Thu 2/9/06
103	**1.6.2**	**Support structure cage**	**Mon 4/9/07**	**Wed 7/29/09**
104	1.6.2.1	design	Mon 4/9/07	Fri 6/29/07
105	**1.6.2.2**	**procure prototype cage**	**Mon 7/2/07**	**Mon 11/19/07**
106	1.6.2.2.1	prototype	Mon 7/2/07	Fri 11/16/07
107	1.6.2.2.2	Review and approve cage design	Mon 11/19/07	Mon 11/19/07
108	**1.6.2.3**	**procure**	**Wed 1/2/08**	**Wed 7/29/09**
109	1.6.2.3.1	final design	Wed 1/2/08	Tue 1/15/08
110	1.6.2.3.2	detail drawings	Wed 1/16/08	Tue 2/5/08
111	1.6.2.3.3	laison	Thu 1/1/09	Wed 7/29/09
112	1.6.2.3.4	tooling	Thu 1/1/09	Wed 1/14/09
113	1.6.2.3.5	material	Thu 1/1/09	Wed 3/11/09
114	1.6.2.3.6	Fabrication	Thu 3/12/09	Wed 7/29/09
115	**1.6.3**	**wedge backplane**	**Mon 2/26/07**	**Wed 4/22/09**
116	1.6.3.1	design	Mon 2/26/07	Fri 4/20/07
117	**1.6.3.2**	**procure prototype wedge backplane**	**Mon 7/2/07**	**Fri 10/19/07**
118	1.6.3.2.1	prototype	Mon 7/2/07	Fri 9/21/07
119	1.6.3.2.2	test	Mon 9/24/07	Fri 10/19/07

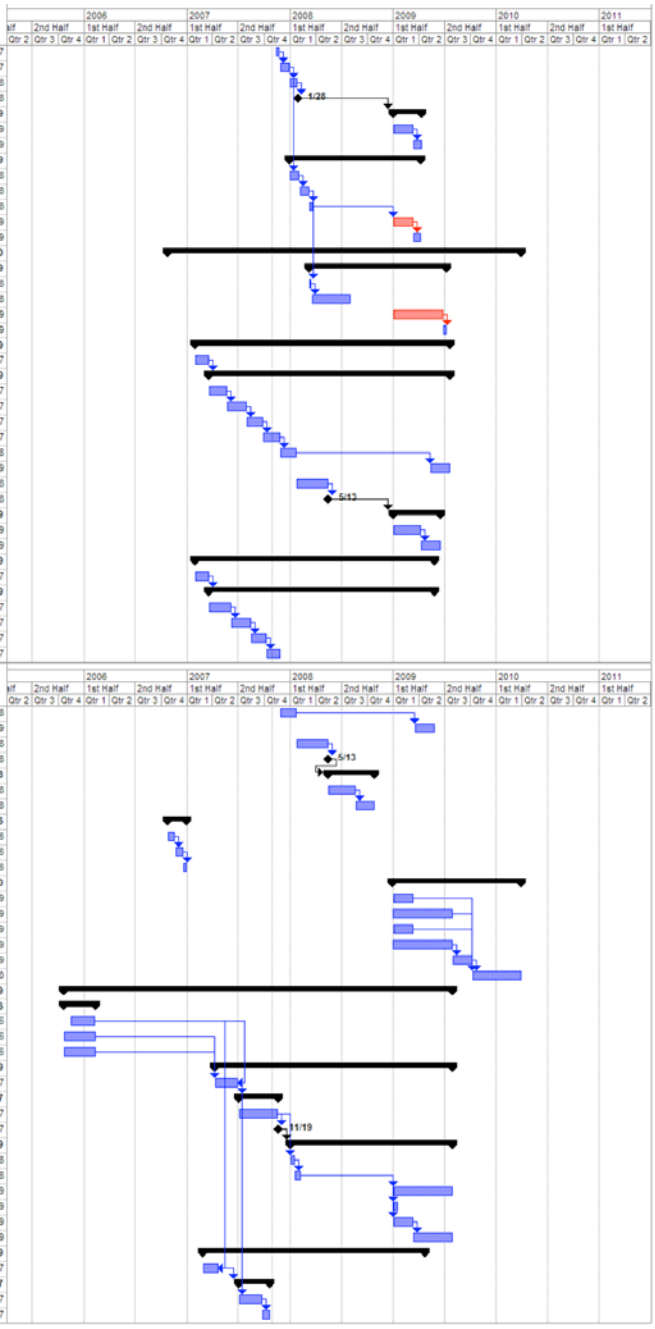

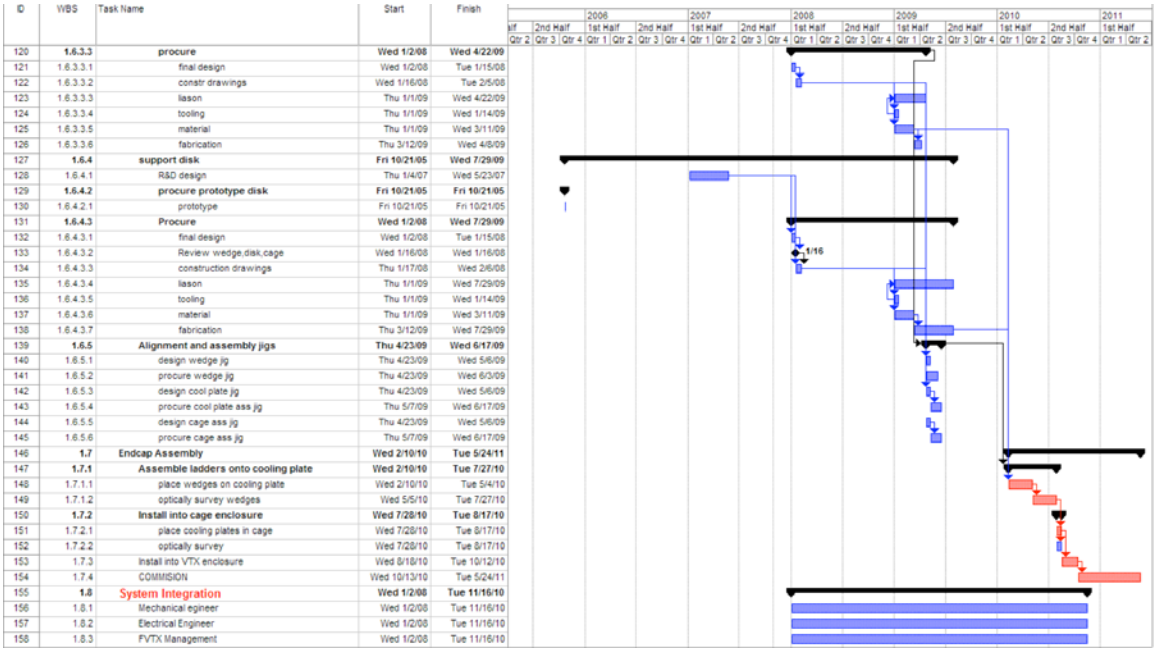

ID	WBS	Task Name	Start	Finish
120	1.6.3.3	procure	Wed 1/2/08	Wed 4/22/09
121	1.6.3.3.1	final design	Wed 1/2/08	Tue 1/15/08
122	1.6.3.3.2	constr drawings	Wed 1/16/08	Tue 2/5/08
123	1.6.3.3.3	liason	Thu 1/1/09	Wed 4/22/09
124	1.6.3.3.4	tooling	Thu 1/1/09	Wed 1/14/09
125	1.6.3.3.5	material	Thu 1/1/09	Wed 3/11/09
126	1.6.3.3.6	fabrication	Thu 3/12/09	Wed 4/8/09
127	1.6.4	support disk	Fri 10/21/05	Wed 7/29/09
128	1.6.4.1	R&D design	Thu 1/4/07	Wed 5/23/07
129	1.6.4.2	procure prototype disk	Fri 10/21/05	Fri 10/21/05
130	1.6.4.2.1	prototype	Fri 10/21/05	Fri 10/21/05
131	1.6.4.3	Procure	Wed 1/2/08	Wed 7/29/09
132	1.6.4.3.1	final design	Wed 1/2/08	Tue 1/15/08
133	1.6.4.3.2	Review wedge,disk,cage	Wed 1/16/08	Wed 1/16/08
134	1.6.4.3.3	construction drawings	Thu 1/17/08	Wed 2/6/08
135	1.6.4.3.4	liason	Thu 1/1/09	Wed 7/29/09
136	1.6.4.3.5	tooling	Thu 1/1/09	Wed 1/14/09
137	1.6.4.3.6	material	Thu 1/1/09	Wed 3/11/09
138	1.6.4.3.7	fabrication	Thu 3/12/09	Wed 7/29/09
139	1.6.5	Alignment and assembly jigs	Thu 4/23/09	Wed 6/17/09
140	1.6.5.1	design wedge jig	Thu 4/23/09	Wed 5/6/09
141	1.6.5.2	procure wedge jig	Thu 4/23/09	Wed 6/3/09
142	1.6.5.3	design cool plate jig	Thu 4/23/09	Wed 5/6/09
143	1.6.5.4	procure cool plate ass jig	Thu 5/7/09	Wed 6/17/09
144	1.6.5.5	design cage ass jig	Thu 4/23/09	Wed 5/6/09
145	1.6.5.6	procure cage ass jig	Thu 5/7/09	Wed 6/17/09
146	1.7	Endcap Assembly	Wed 2/10/10	Tue 5/24/11
147	1.7.1	Assemble ladders onto cooling plate	Wed 2/10/10	Tue 7/27/10
148	1.7.1.1	place wedges on cooling plate	Wed 2/10/10	Tue 5/4/10
149	1.7.1.2	optically survey wedges	Wed 5/5/10	Tue 7/27/10
150	1.7.2	Install into cage enclosure	Wed 7/28/10	Tue 8/17/10
151	1.7.2.1	place cooling plates in cage	Wed 7/28/10	Tue 8/17/10
152	1.7.2.2	optically survey	Wed 7/28/10	Tue 8/17/10
153	1.7.3	Install into VTX enclosure	Wed 8/18/10	Tue 10/12/10
154	1.7.4	COMMISION	Wed 10/13/10	Tue 5/24/11
155	1.8	System Integration	Wed 1/2/08	Tue 11/16/10
156	1.8.1	Mechanical egineer	Wed 1/2/08	Tue 11/16/10
157	1.8.2	Electrical Engineer	Wed 1/2/08	Tue 11/16/10
158	1.8.3	FVTX Management	Wed 1/2/08	Tue 11/16/10

Figure 98 – PHENIX Forward Silicon Vertex (FVTX) project timeline.

5.2.1 Cost

Since the FVTX will be added to the existing barrel vertex detector, VTX, much of the needed infrastructure, cooling, enclosure, cable routing, installation procedures, etc. will already have been done and be in place. In this cost estimate only those items needed for fitting the FVTX into the VTX enclosure are considered. The costs in Table 8 are generally obtained from cost estimates by the engineering team who will be doing the work and from cost estimates for work already done by those teams. For example, the cost estimate for the FPHX chip came from the FNAL engineers who designed the FPIX2 chip. The HYTEC engineering team previously designed the ATLAS pixel mechanical structures and is currently working on the VTX and that forms the basis for the mechanical cost estimates. The cost basis for the sensors are from quotes from ON Semiconductor Inc. in Prague, Czech Republic and CIS Semiconductor obtained in 2006 and on drawings of the wafers with the FVTX wedges. The contingency analysis method is listed in Appendix A (Section 6).

Forward Endcap Cost Estimate - FVTX

FY2007 dollars

2 endcaps	WBS	Construction(k$)	comments	total contingency	Cost with Contingency	2008
Mechanics	1.6					
Mechanical ladder and support structure	1.6.2-1.6.4	352	HYTEC Estimate	0.27	445.90	
Alignment and Assembly jigs	1.6.5	60	engineering estimate	0.25	75.00	
Sensor and Readout Chip						
Silicon Sensor	1.4.1					
prototype sensor and test	1.4.1.2	85	mask,prototype,wire bond,test	0.22	103.60	103.60
purchase	1.4.1.3	410	Vendor quotes	0.26	516.60	100
sensor Q/A and testing	1.4.1.3.2	50	University students + engineer	0.16	58.00	
PHX chip, tested	1.4.2					
2 nd Mosis run and test	1.4.2.4.4	95	FNAL esimate	0.29	122.10	122.10
engineering run	1.4.2.5.1	240	FNAL estimate	0.48	355.20	
testing	1.4.2.5.2	50	FNAL tech	0.16	58.00	
attach HDI to backplane	1.4.1.3.3	30	engineering estimate	0.22	36.60	
attach sensor	1.4.1.3.4	30	engineering estimate	0.22	36.60	
wire bond assembly	1.4.1.3.5	188	Promex quote	0.26	236.88	
test wedge assembly	1.4.1.3.6	40	engineering estimate	0.22	48.80	
Readout Electronics						
ROC electronics	1.5.2					
preproduction proto	1.5.5.2	71.11	engineering estimate	0.36	96.71	96.71
production	1.5.5.3.1	337.27	engineering estimate	0.33	448.57	
Q/A	1.5.5.3.2	14	engineering estimate	0.14	15.96	
FEM electronics	1.5.3					
preproduction	1.5.3.2	79.63	engineering estimate	0.36	108.30	108.30
production	1.5.3.3.1	301.39	engineering estimate	0.33	400.85	
Q/A	1.5.3.3.2	14	engineering estimate	0.14	15.96	
Ancillary Systems	1.5.5					
Racks,LV,HV,DCM,crates,install	1.5.5.1-1.5.5.6	99.2	existing designs	0.12	111.10	
slow controls	1.5.5.4	5	existing designs	0.18	5.90	
calibration system	1.5.4					
Assembly, Integration and Management						
Assemble endcap	1.7	30	techs and students	0.26	37.80	
Electronics Integration	1.8.2	165	Engineer	0.14	188.10	62.70
Mechanical Integration	1.8.1	250	Engineer	0.14	285.00	95.00
HDI bus	1.4.3	116.4	440 HDI, 10% spares, $250 ea.	0.24	144.04	
flex cables, sensor to ROC	1.4.4	56.2	784 flex, 10% spares, $42 ea.	0.16	65.28	
fibercables, ROC-FEM	1.5.1	17.23	440 ea. 54 units	0.16	19.99	
lab equipment	1.5.5.5	100	probe, test equipment	0.10	110.00	110.00
Management	1.8.3	200		0.14	228.00	76.00
total		3486.43		0.26	**4374.84**	**874.41**
			Inflation adjusted(.035 per year)		**4683.51**	**905.01**
BNL overhead 18%			DOE Guidence		4950.00	900
LANL overhead and GRT 19.5%						
All labor fully burdened						

Table 8 – Cost estimate for the FVTX endcaps with contingency. The methodology used for contingency is in Appendix A (Section 6).

5.2.2 Project Management and Responsibilities

The LANL Group will work together with HYTEC inc. to develop the design for the Endcap mechanical ladder and cooling. LANL has formed collaboration with FNAL to design, prototype and test the PHX readout chip. An MOU with PHENIX, BNL physics department and FNAL for R&D of the PHX chip was signed in 2004.

The organizational chart for the FVTX project is shown inFigure 99.

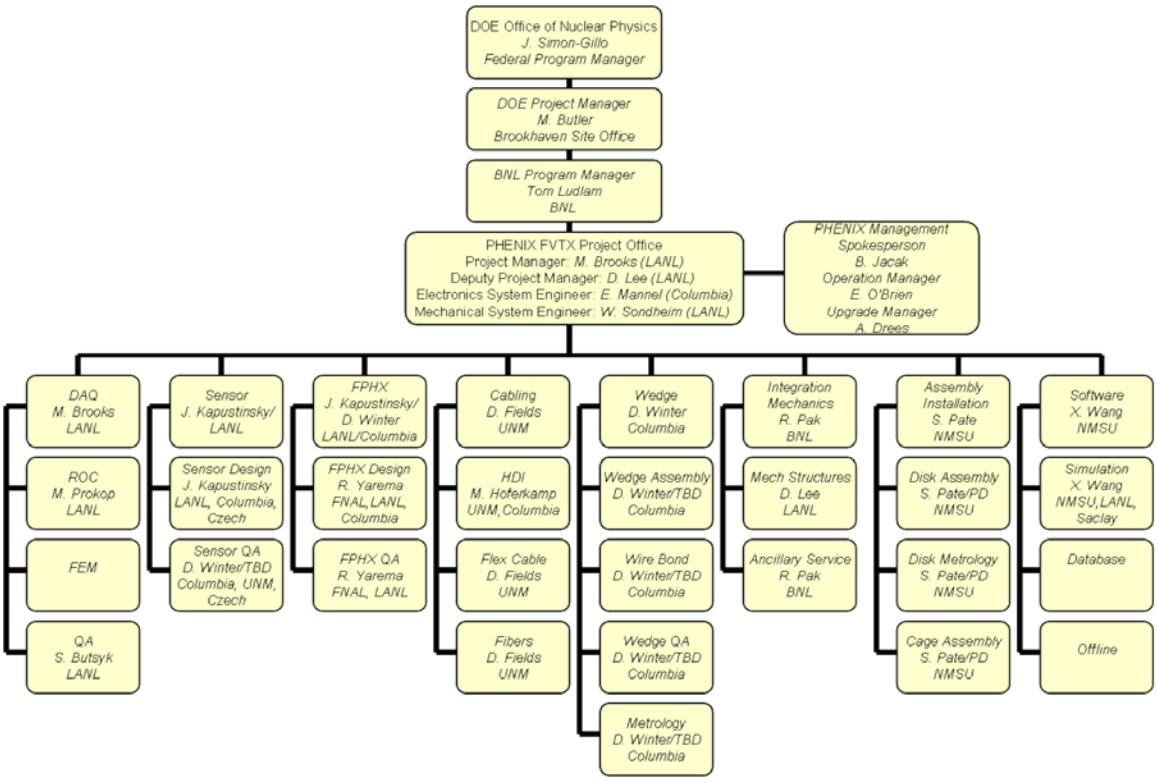

Figure 99 - Organizational Chart for the FVTX project.

Institutional Responsibilities

Los Alamos National Laboratory

LANL coordinate work to design and procure the silicon sensors, work with FNAL on the development of the FPHX chip, development of the interface to PHENIX DAQ, and on the simulation effort with NMSU. Los Alamos is currently leading the mechanical engineering and the integration effort for the barrel detector, and will continue those efforts for the FVTX.

Brookhaven National Laboratory

Brookhaven is responsible for the overall Mechanical Integration and Infrastructure for the VTX project and will do the same for the FVTX. They will coordinate activities at BNL and also work on simulations.

Columbia University

Columbia University will have the responsibility of the wedge assembly. The wedge is the fundamental unit for the FVTX. Columbia will be involved with all aspects of the design and

specification of the components that form the wedge. They will work with LANL and FNAL on the FPHX and sensors and with UNM on the HDI. They will be responsible for the assembly and testing of the wedge assembly, wire bonding and doing all QA. If other institutions are involved, they will coordinate all of the activities. Columbia is also responsible for the overall electronic integration.

Iowa State University

Iowa State University is currently working on management details with the barrel detector and working on an (funded) SBIR effort addressing the level-1 trigger capabilities of the FVTX. They are also involved with the interface module.

Charles University, Czech Technical University, Institute of Physics, Academy of Sciences, Prague, Czech Republic

Czech institutions have been active in the development, testing, assembly, and commissioning of the ATLAS pixel sensors. They will do the same for the FVTX effort and additionally participate in software development.

New Mexico State University

NMSU will work on comprehensive simulations for the FVTX effort. They will work on the wedge assembly in coordination with Columbia, and are responsible for the coordination of the assembly of the disks and cages at BNL. In addition, NMSU is contributing to the LDRD effort.

University of New Mexico

UNM has experience in testing, Q/A and a laboratory for characterization of sensors. They are currently working on the barrel strip sensors and will do the same for the FVTX effort. UNM is responsible for the HDI, flex, and fiber cables and will assist with sensor QA and testing.

Saclay

Saclay will work on software.

Yonsei University, Seoul, Korea

The Yonsei group has worked on electronics and software for the muon system. They have not defined their scope of work.

University of Jyvaskyla, Finland

The university of Jyvaskyla will work on simulations and assist in assembly.

6 Appendix A – Contingency Analysis

6.1 Contingency Analysis

The average contingency for the FVTX is 26 %.

This section describes how the contingency for a given WBS element was calculated. Risk is a function of the following factors: the sophistication of the technology, the maturity of the design effort, the accuracy of the cost sources and the impact of delays in the schedule. Risk analysis is performed for each WBS element at the lowest level estimated. Results of this analysis are related to a contingency, which is listed for each WBS element. The goal is to make the method of contingency determination uniform for all project WBS elements.

Definitions

Base Cost Estimate – The estimated cost of doing things correctly the first time. Contingency is not included in the base cost.

Cost Contingency – The amount of money, above and beyond the base cost, that is required to ensure the project's success. This money is used only for omissions and unexpected difficulties that may arise. Contingency funds are held by the Project Manager.

Risk Factors

Technical Risk – Based on the technical content or technology required to complete the element, the technical risk indicates how common the technology is that is required to accomplish the task or fabricate the component. If the technology is so common that the element can be bought "off-the-shelf", i.e., there are several vendors that stock and sell the item, it has very low technical risk, therefore a risk factor of 1 is appropriate. On the opposite end of the scale are elements that extend the current "state-of-the-art" in this technology. These are elements that carry technical risk factors of 10 or 15. Between these are: making modifications to existing designs (risk factor 2-3), creating a new design which does not require state-of-the-art technology (risk factor 4 & 6), and creating a design which requires R&D, and advances the state-of-the-art slightly (risk factor 8 & 10).

Cost Risk – Cost risk is based on the data available at the time of the cost estimate. It is subdivided into 4 categories.

The first category is for elements for which there is a recent price quote from a vendor or a recent catalog price. If the price of the complete element, or the sum of its parts, can be found in a catalog, the appropriate risk factor to be applied is 1. If there is an engineering drawing or specification for the element, and a reliable vendor has recently quoted a price based on these, the cost risk factor to be applied is 2. Similarly, if a vendor has quoted a price based on a sketch that represents the element, and the element's design will not change prior to its fabrication, the appropriate cost risk factor would be 3.

The second category is for elements for which there exists some relevant experience. If the element is similar to something done previously with a known cost, the cost risk factor is 4. If the element is something for which there is no recent experience, but the

capability exists, the cost risk is 6. If the element is not necessarily similar to something done before, and is not similar to in-house capabilities, but is something that can be comfortably estimated, the risk factor is 8.

The third category is for elements for which there is information that, when scaled, can give insight into the cost of an element or series of elements. The cost risk factor for this category is 10.

The fourth category is for elements for which there is an educated guess, using the judgment of engineers or physicists. If there is experience of a similar nature, but not necessarily designing, fabricating or installing another device, and the labor type and quantity necessary to perform this function can be estimated comfortably, a cost risk factor of 15 is appropriate.

Schedule Risk – If a delay in the completion of the element could lead to a delay in a critical path or near critical path component, the schedule risk is 8. If a delay in the completion of the element could cause a schedule slip in a subsystem which is not on the critical path, the schedule risk is 4. Only elements where a delay in their completion would not affect the completion of any other item have schedule risks of 2.

Design Risk – is directly related to the maturity of the design effort. When the element design is nearly complete, quantity counts and parts lists finished, the risk associated with design is nearly zero; therefore a risk factor of 0 is applied. This is also the case when the element is an "off-the-shelf" item and the parts counts and quantities are finalized. When the element is still just an idea or concept, with crude sketches the only justification for the cost estimate, the risk associated with design state is high or 15. Between these two extremes are the stages of conceptual design and preliminary design. In conceptual design, when layout drawings of the entire element are approaching completion, some preliminary scoping analyses have been completed, and parts counts are preliminary, the design risk factor is 8. During preliminary design, when there are complete layout drawings, some details worked out, complete parts counts, and some analysis for sizing and showing design feasibility, the appropriate design risk is 4.

Weighting Factors

The weight applied to the risk factors depends on whether there are multiple or single risks involved in completing an element.

The weights applied to technical risk depend upon whether the element requires pushing the current state-of-the-art in design, manufacturing, or both. If the element requires pushing both, the weight to be applied is high, or 4; if either the design or manufacturing are commonplace, the weighting factor is 2.

For weights applied to cost risk, the two factors are material costs and labor costs. If either of these are in doubt, but not both, the weight to be applied to cost risk is 1. If they are both in doubt, the weight applied is 2.

The weight factor given to schedule risk is always 1.

The weight factor given to design risk is always 1 and so is not shown explicitly.

Procedure

The following procedure is used for estimating contingency.

Step 1 – The conceptual state of the element is compared with Table 4 to determine risk factors. A technical risk factor is assigned based on the technology level of the design. A design risk factor is assigned based upon the current state (maturity) of the design. A cost risk factor is assigned based on the estimating methodology used to arrive at a cost estimate for that element. Similarly, a schedule risk factor is identified based on that element's criticality to the overall schedule.

Step 2 – The potential risk within an element is compared with Table 5 to determine the appropriate weighting factors.

Step 3 – The individual risk factors are multiplied by the appropriate weighting factors and then summed to determine the composite contingency percentage.

Step 4 – This calculation is performed for each element at its lowest level.

Step 5 – The dollar amount of contingency for an element is calculated by multiplying the base cost by the composite contingency percentage.

Risk Factor	**Technical**	**Cost**	**Schedule**	**Design**
0	Not used	Not used	Not used	Detail design > 50% done
1	Existing design and off-the-shelf H/W	Off-the-shelf or catalog item	Not used	Not used
2	Minor modifications to an existing design	Vendor quote from established drawings	No schedule impact on any other item	Not used
3	Extensive modifications to an existing design	Vendor quote with some design sketches	Not used	Not used
4	New design; nothing exotic	In-house estimate based on previous similar experience	Delays completion of non-critical subsystem item	Preliminary design >50% done; some analysis done
6	New design; different from established designs or existing technology	In-house estimate for item with minimal experience but related to existing capabilities	Not used	Not used
8	New design; requires some R&D but does not advance the state-of-the-art	In-house estimate for item with minimal experience and minimal in-house capability	Delays completion of critical path subsystem item	Conceptual design phase; some drawings; many sketches
10	New design of new technology; advances state-of-the-art	Top-down estimate from analogous programs	Not used	Not used

15	New design; well beyond current state-of-the-art	Engineering judgment	Not used	Concept only

Table 9 - Technical, cost and schedule risk factors.

Risk Factor	Condition	Weighting Factor
Technical	Design OR Manufacturing	2
	Design AND Manufacturing	4
Cost	Material Cost OR Labor Rate	1
	Material Cost AND Labor Rate	2
Schedule	Same for all	1
Design	Same for all	1

Table 10 - Technical, cost, schedule and design weighting factors.

7 Appendix B – The FVTX Level-1 Trigger System

7.1 Introduction

In this Appendix we present the current status of a conceptual design for a Level-1 trigger system utilizing the FVTX detector. While many of the details remain to be worked out, the design outlined here is a powerful, flexible trigger system that exploits synergies between many PHENIX upgrades and can address a wide array of physics observables.

We begin by summarizing the additional required event rejection for single and di-muon physics with the PHENIX detector beyond that currently available with the existing Muon Identifier Local Level-1 (MuID LL1). We outline a trigger strategy starting with an FVTX LL1 system for the identification of tracks from both the primary and displaced vertices. This trigger strategy requires combining the FVTX LL1 output with additional information from the PHENIX Muon Trigger Upgrade, which we describe in detail. We then report on the current hardware research and development effort, and conclude with a cost estimate for the FVTX LL1

7.2 Required Event Rejection

The required event rejection for heavy flavor physics with the PHENIX muon arms in future RHIC and RHIC-II running can be divided into two classes of trigger signals – single muons and muon pairs.

The existing trigger option for single muons is to trigger on at least one deep muon road in the Muon Identifier (MuID). A deep road is defined as a track in LL1 that penetrates all layers of the MuID. The achieved rejection factors for the 1-Deep MuID LL1 trigger in both p+p and Au+Au are shown in Table 11 (taken from Table 26 in this proposal). Also shown are the required rejections for the end of RHIC-I running as well as for RHIC-II. The required rejections are what are needed to ensure that the triggers are not prescaled (Table 27 this proposal). Prescaling means that valid triggers are not written to disk because the rate exceeds a bandwidth limit at Level-1 (1kHz). For convenience the required rejections are factorized into the current rejection and the required improvement.

Table 11 - Event rejection required beyond the MuID LL1 for RHIC-I (2008) and RHIC-II running for single muon triggers.

Existing Trigger MuID 1-Deep	Achieved Rejection	Rejection needed 2008	Rejection needed RHIC-II
p+p	478	478*21	478*71
Au+Au	5	5*15	5*116

Table 12 demonstrates that a new Level-1 trigger needs to increase the rejections already at the end of RHIC-I era (2008) and definitely by RHIC-II in order to maximize the collected statistics on open charm and bottom from a given time running the experiment.

The existing trigger option for muon pairs is to trigger on two roads in the MuID LL1. In order to maximize the efficiency for the physics signals of interest, combinations with shallow roads (only utilizing the first three MuID gaps) are used in p+p collisions, where the MuID occupancy is low. The achieved rejection factors for the 1-Deep 1-Shallow trigger in p+p and 2-Deep trigger in Au+Au are shown in the Table 12 (taken from Table 26 in this proposal). Also shown are the required rejections for the end of RHIC-I running as well as for RHIC-II. Again, the required rejections are factorized into the current rejection and the needed improvement.

Table 12 - Event rejection required beyond the MuID LL1 for RHIC-I (2008) and RHIC-II running for di-muon triggers.

Existing Trigger MuID	Achieved Rejection	Rejection needed 2008	Rejection needed RHIC-II
p+p 1-Deep 1-Shallow	23500	< 23500	23500*1.4
Au+Au 2-Deep	15.7	15.7*5	15.7*37

Table 12 demonstrates that a new Level-1 trigger needs to increase the rejections already at the end of Au+Au RHIC-I era (2008) and definitely by RHIC-II in order to get the most statistics in the $B \rightarrow J/\psi$ channel from a given time running the experiment. Another way of expressing this is that if no increase in rejection is obtained, then in Au+Au 2008 only one in every 5 produced $B \rightarrow J/\psi$ will be recorded, the other events will have to be prescaled away. Note that for p+p running very little to no increase in muon pair trigger rejection is needed.

7.3 FVTX LL1 Trigger Strategy

Based on the physics that the FVTX is designed to address and on the expected collision rates of p+p and A+A collisions at RHIC, there are three main types of triggers that a new Level-1 trigger needs to deliver; displaced single tracks for use in open charm and bottom production, a pair trigger for $B \rightarrow J/\psi$ and upsilon production, and an event-trigger to improve the efficiency of min-bias and ultra-peripheral collisions. More details on each are given below. We begin by presenting details of the trigger strategy to be used in the FVTX, followed by a combination with the downstream Muon Trigger.

7.3.1 Single Displaced Tracks

The goal of this trigger is to select events that have a track in the FVTX (comprised of hits in three to four stations) that are displaced from the collision vertex. Large additional sources of

displaced tracks are pion and kaon decays, that have a much larger decay lifetime. This leads to a strategy of requiring tracks that are displaced from the collision vertex but are still within several charm/bottom lifetimes to reduce the contamination from pions and kaons. As an example consider a trigger on z-displacement, how far the z-coordinate of the track is from the collision vertex (a similar cut could be placed on the radial distance of closest approach, or DCA)

$$\Delta z_{LOWER} < \Delta z < \Delta z_{UPPER}$$

Since most charm and bottom decays occur close to the collision vertex (exponential decay is largest at t=0), you would like to make Δz_{LOWER} as small as possible while still maintaining an acceptable rejection factor. Since the resolution of pointing back to the collision vertex depends on the momentum, you may be able to afford a tighter Δz_{LOWER} cut at higher momentum in order to catch more of the charm and bottom decays.

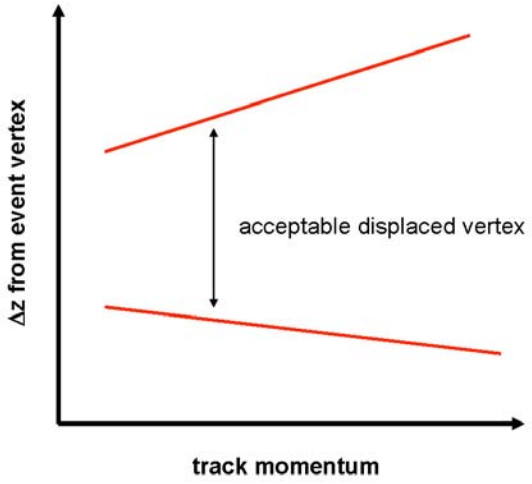

Figure 100 - A schematic representation a displaced vertex cut in the FVTX Level-1 as a function of momentum. The upper limit is designed to reject muons from pion and kaon decays, while the lower cut defines a minimum distance from the event vertex. To avoid potential bias against high momentum decays and still achieve a reasonable rejection factor, it will be necessary to change the upper cut as a function of momentum.

A different reason compels us to also consider that the Δz_{UPPER} cut also needs to be momentum dependent. One would like to make Δz_{UPPER} as small as possible that is consistent with catching several lifetimes of charm/bottom decays ($c\tau$ ~ 300-500 μm). The smaller you can make Δz_{UPPER}, the fewer pion decays you trigger on and the better the trigger rejection. This is shown schematically in Figure 100.

The need to have Δz_{LOWER} and Δz_{UPPER} cuts momentum dependent drives the need for information to be combined from the displaced tracks of the FTVX LL1 and the momentum information from tracks in the downstream Muon Trigger.

7.3.2 Muon Pair Trigger

The requirements for the two main physics cases are exactly complementary: the $B \rightarrow J/\psi$ requires a trigger on two tracks that are both displaced, while the upsilon and continuum physics require a trigger on two tracks that come from the main collision vertex.

A potentially powerful pair trigger is to require that both FVTX tracks come from a region that is within a distance a few times the track resolution, or $(\Delta z_1 - \Delta z_2) < n\sigma$, where n=2-3. This trigger will only achieve a sizeable rejection if both FVTX tracks are matched to muon tracks in the downstream Muon Trigger, otherwise the trigger will be satisfied by any pair of primary tracks that do not decay (primary protons, for example). This trigger satisfies all the pair physics goals and should remove many of the random combinations of decaying pions, and therefore it has the potential to reach high rejections.

7.4 Combined Forward Muon Trigger

As emphasized above, much of the physics to be addressed by the FVTX requires the ability to trigger effectively on the presence of a displaced vertex which results in a downstream track in the PHENIX Muon Tracker (MuTr) and Muon Identifier (MuID) detectors. While the FVTX is designed to accurately measure tracks whose origin is displaced from the main event vertex, it cannot identify these tracks as muons nor classify them according to momentum (for large momenta). Because of this, the FVTX LL1 is envisioned to operate as a key part of a combined forward physics trigger that makes use of additional information from the existing PHENIX MuID Local Level-1 and the planned Muon Trigger Upgrade funded by the National Science Foundation.

In the sections that follow we introduce and describe the PHENIX Muon Trigger Upgrade and describe how the FVTX and MuonTrigger systems can be combined to provide a trigger that can address a wide array of physics observables.

7.4.1 The PHENIX Muon Trigger Upgrade

The planned PHENIX Muon Trigger Upgrade is designed primarily to address the needs of the PHENIX spin program in polarized p+p collisions at $\sqrt{s} = 500$ GeV. In order to measure the antiquark contribution to the nucleon spin, it is necessary to trigger on very high momentum muons originating from the decay of polarized *W* bosons. Low momentum muons from pion and kaon decay, as well as from charm (and to some extent, bottom) decays occur at a substantial rate, so that a trigger is required that can select muons based on momentum as measured in the PHENIX muon arm.

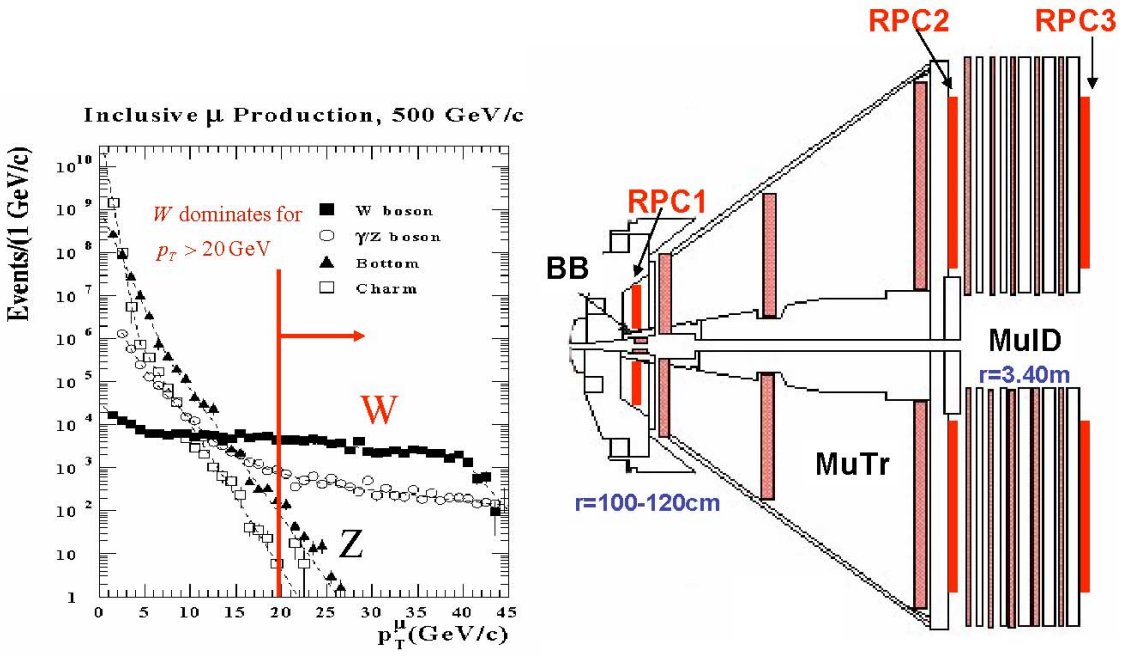

Figure 101 - The PHENIX Muon Trigger Upgrade is designed to provide an effective trigger on muons from the decay of polarized W bosons in polarized p+p collisions at 500GeV. Such muons dominate the inclusive muon production above a momentum of ~20GeV/c. The location of the additional RPC chambers that will be added to the PHENIX muon arm are shown at right.

The Muon Trigger Upgrade will consist of three additional resistive plate chambers (RPC's), two of which will provide tracking in the magnetic field volume and a third that will be used for the rejection of beam-associated backgrounds. These chambers are planned to have a segmentation of 1^o in the phi angle, with 24 segments in theta, although current plans only call for two theta segments at the trigger level. The momentum of the track is measured by the difference in angle between the track hit at the first and second RPC stations. A cut at 2^o corresponds roughly to a cut at a muon momentum of 12 GeV and yields sufficient rejection for the spin program, although the possibility of simultaneously selecting lower-momentum regions (possibly prescaled) will be retained. Finally, track candidates in the RPC chambers will be matched to deep roads in the existing MuID LL1 trigger system. This matching will be done by passing the deep road information along a backplane in the trigger crate to the new Muon RPC (MuPC) Level-1 trigger.

The hardware for the RPC-based Level-1 trigger system will be based on an improved design of the trigger boards used for the MuID LL1. These boards, designated GenLL1 Rev2, are based on a generic design that uses Xilinx FPGA's to implement the trigger algorithm and incorporate up to twenty 1Gbit fiber transceivers as input. We plan to make use of the generic nature of this design to implement the Combined Trigger Processor (described below) that will combine the output of the FVTX and Muon Level-1 trigger into an extremely flexible and powerful trigger system.

The Muon Trigger Upgrade is funded by a grant from the National Science Foundation, and is planned to be installed and commissioned in PHENIX in 2007-2008, and ready for operation in 2009.

7.5 Combining the FVTX with the Downstream Muon Trigger

We envision a trigger strategy where the information from the FVTX is combined and matched with track momentum information from the downstream Muon Trigger. Because the displaced vertex cut needs to be a function of momentum, and the FVTX does not accurately determine the track momentum, it will generate several sets of trigger primitives based on assumed momentum range. Likewise, the Muon Trigger will generate primitives for a selection of candidate momenta. The exact granularity of the trigger primitives in Δz and track momentum will need to be determined by simulation and event rejection requirements.

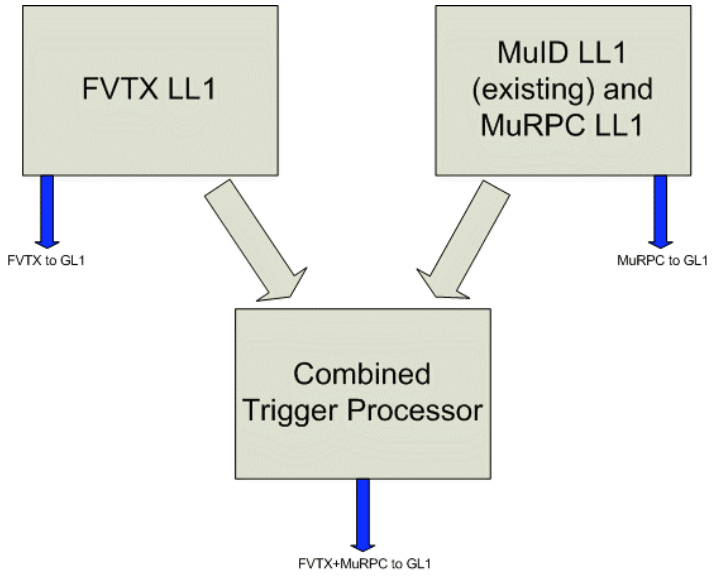

Figure 102 - Block diagram showing the communication between the FVTX and combined MuID and MuRPC triggers with the Combined Trigger Processor. Each LL1 system will have the ability to send trigger data to Global Level-1 (GL1) for independent triggering, or the primitives can be combined in the Combined Trigger Processor (as described in the text) to generate trigger primitives based on information from both systems.

This primitive information will be sent to a combined in a Combined Trigger Processor, as shown in Figure 102 Assuming four FVTX sets of trigger primitives, corresponding to a "low" and "high" momentum assumption (and therefore cut as outlined in Figure 102) combined with a displaced or primary track, and three sets of momentum regions defined by the Muon Trigger as "low", "middle" and "high" we show in Table 13 possible combinations of trigger primitives for different physics signals. For the sake of being concrete we assume p+p collisions at $\sqrt{s} = 500\text{GeV}$ and therefore the inclusive muon distribution shown in Figure 55. The Muon

Trigger momentum selections correspond to regions where charm ("low"), bottom ("middle") or W decay ("high") dominate the inclusive muon spectra.

Physics Signal	FVTX Primitives	Muon Trigger Primitives	Min. No. of Tracks
$D, B \rightarrow \mu X$ (single muon, displaced vertex)	displaced vtx ("low" and "high")	"low" and "middle" momentum	1
$B \rightarrow J/\psi$ (pair, displaced vertex)	displaced vtx ("low" and "high")	"low" and "middle" momentum	2
$J/\psi, \psi'$ (pair, primary vertex)	primary vertex ("low" and "high")	"low" and "middle" momentum	2
Υ, $\mu\mu$ continuum (pair, primary vertex)	primary vertex ("low" and "high")	"low" and "middle" momentum	2 (same arm, high η) 2 (opposite arm, central)
$W \rightarrow \mu\nu$	(not required)	"high" momentum	

Table 13 - Physics signals and potential FVTX and muon trigger primitive combinations that could be used to generate Level-1 triggers.

7.5.1 Hardware Integration of FVTX and Muon Trigger Systems

In previous sections we have outlined a trigger strategy that requires the integration of trigger information from the downstream muon arm with information from the FVTX. We plan to do this by transmitting trigger primitives from both the FVTX LL1 and the Muon Level-1 trigger to a Combined Trigger Processor. We envision that the primitives will consist of mappings of candidates in (θ,φ) space at the back of the FVTX detector with a granularity that is determined by the resolution of the RPC trigger. Each element in the mapping will be a "1" if the system detected a candidate matching a set of requirements in that (θ,φ) element, and a "0" otherwise. There may be several groups of these primitives based on momentum region of interest and vertex origin of the FVTX tracks, as described above.

The combination of the trigger primitive mapping is relatively straightforward in the Combined Trigger Processor, and is essentially an AND operation on the individual map elements. The generation of the trigger data sent to the Global Level-1 trigger will then consist of a count of the number of elements in each combined primitive map that satisfies the AND operation.

As an example, a trigger on a pair of tracks originating away from the event vertex (for example, the decay $B \rightarrow J/\psi$) would be generated by a trigger primitive map from the FVTX trigger for tracks originating within a window away from the event vertex and a trigger primitive map (or

several maps) from the Muon Trigger indicating candidates within selected momentum ranges. If more than two elements in the trigger primitive array survive the AND operation between the FVTX and Muon Trigger, the pair trigger is satisfied.

The exact method by which trigger primitive data is pushed from the FVTX and Muon Trigger LL1 systems into the Combined Trigger Processor will be determined based on the number of maps (and hence the amount of data) that will need to pass between the systems. It is possible that all three systems could coexist in a single crate for each arm, or that individual crates for each system will communicate over fiber or copper links.

We note that some modification of the Muon Trigger design may be necessary to allow an optimal combined trigger. While it is already envisioned that the Muon Trigger will allow lower momentum selections (possible prescaled at GL1) to allow triggering on tracks from charm and bottom decay, it is possible that additional segmentation in theta will be required by the combined trigger, especially in the heavy ion environment. Simulations are underway to determine the required segmentation and the potential impact on the Muon Trigger.

Finally, we note that additional elements could be incorporated into this Combined Trigger Processor approach could be used to incorporate additional PHENIX detectors into the trigger if required by the physics program. For example, the PHENIX Nose Cone Calorimeter is a calorimeter proposed to cover the same rapidity region as the PHENIX muon arms. Such a calorimeter could be included to provide an isolation cut at the trigger level, for example.

7.6 Research and Development on FVTX LL1 Trigger Design

An FY2005 Phase I Small Business Technology Transfer (STTR) award was granted to to Northern Microdesign and ISU. The key personnel in this project are

- Bill Black, President Northern Microdesign previously at Xilinx, Inc. (until September 2003) where he was responsible for the analog portion of the 10Gb/s serial transceivers on the newly introduced Virtex II Pro-X chips
- Nader Badr, Engineer Northern Microdesign with experience in high-speed chip to chip communications and protection circuits
- Gary Sleege, Engineer Iowa State University who has worked on previous PHENIX Level-1 trigger projects, including the MuID LL1
- John Lajoie, Craig Ogilvie at Iowa State University

A Phase II STTR has since been awarded to this group for FY06/07 to continue the Phase-I development and produce a hardware prototype.

During the Phase I project displaced vertex calculations were successfully run on an FPGA using simulated events into one FVTX arm with the simulated event preloaded into memory. The goals of Phase I were to

- Develop a starting algorithm for displaced vertices

- Test if the calculation is feasible for central Au+Au, i.e. to calculate DCAs for all tracks within the maximum PHENIX Level-1 of 4μs.

Single and multiple-track events were simulated using standard PHENIX packages of GEANT for zero magnetic field. This case was chosen as the simplest starting algorithm to set the overall scale for the size and timing of the tracking algorithm. Extension of the Phase-1 algorithms to nonzero magnetic fields is being developed in Phase II.

Within the FPGA we implemented a pipelined four stage algorithm that consisted of (see Figure 103):

1. Hit sorting and preparation
2. Straight-line finding
    a. Hits in station 0 paired with max/min collision point
    b. Searched for hits in station 1 within tolerance
    c. Line between station-0 and station-1 hits
    d. Searched for hits in 2, 3 within tolerance
3. Collision vertex from found lines
4. DCA from collision vertex calculated for each track

The timing for this algorithm was established for single- and multiple-track events then scaled to the full central Au+Au event. The test was done for a single Xilinx XC2VPX70 FPGA, but the scaling for a full central Au+Au event assumes eight XC4VLX200 FPGAs on a board (or equivalent logic in a smaller number of units, such as the Virtex-4). Such a prototype board is the major goal of the Phase-II STTR grant. The timing for the algorithm is shown in Table 14.

Task	Time (ns) Central Au+Au
Hit Format converter	30
Hit Sorter	30
Line-finder	960*
Collision Vertex	70
Secondary Tracks	120
Total	1210

Table 14 - Time budget for the STTR Phase-I FVTX algorithm as described in the text. Notes that the time required for the line finding algorithm could be reduced with added parallelization.

Since the time required to calculate track DCA's is less than the maximum PHENIX Level-1 latency of 4 μs, it seems that an FVTX displaced-vertex trigger is feasible for Au+Au collisions.

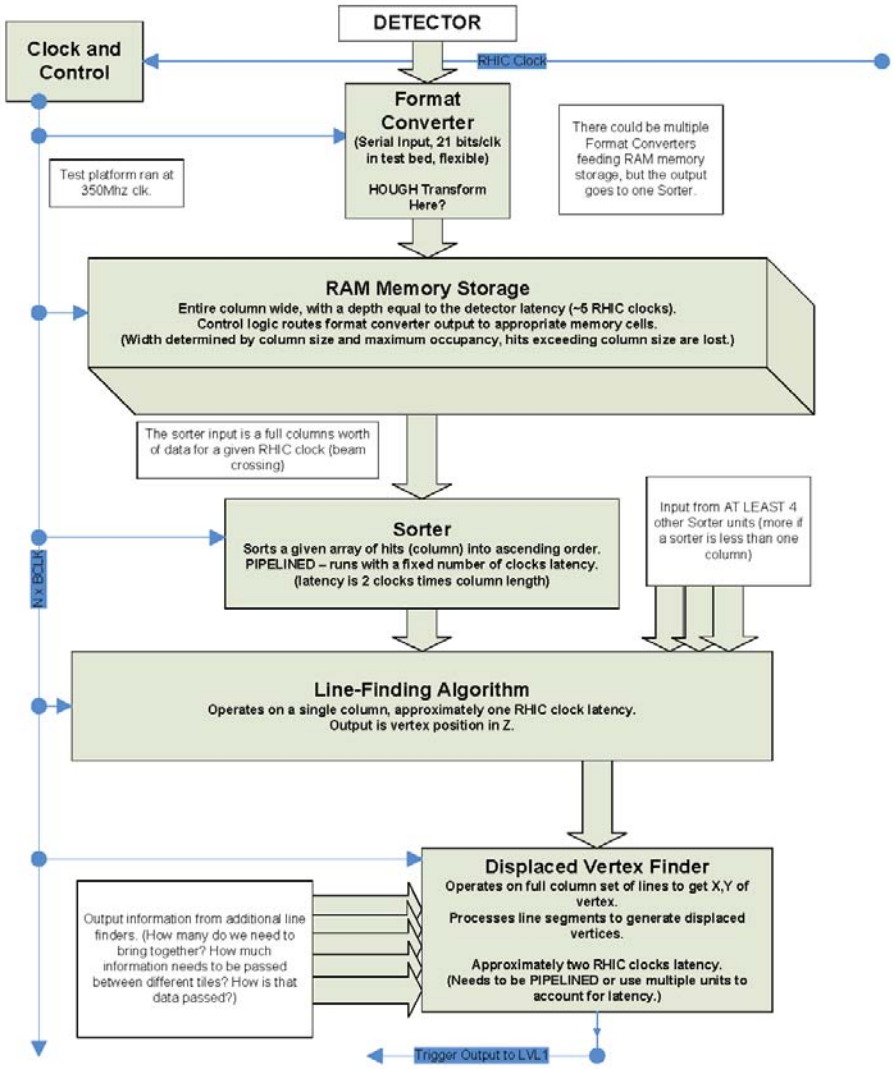

Figure 103 - Block diagram of the FVTX LL1 trigger algorithm, as implemented by Northern Microdesign for STTR Phase-1 feasibility testing.

The major goal of the Phase-II STTR is to produce a prototype board that could be used with the prototype FVTX being installed in PHENIX using LANL's LDRD grant. The result of this development should be a well-developed design for the trigger hardware required for the full FVTX LL1.

7.7 FVTX LL1 Cost Estimate

The full FVTX detector consists of 48 wedges per station, four stations per arm, with 5632 channels per wedge. We plan to develop a Level-1 trigger board that can service eight wedges over four stations, or a total of 5632 x 8 x 4 = 180k channels.

Each wedge will send a single fiber to the trigger board, for a total of 32 fibers per trigger board. For a AuAu event, assuming 1.5% occupancy and 24 bits per hit channel yields 8.3kB per event input to the trigger tile, or 0.259kB per fiber. This can be easily accommodated in a modern 7.5Gbit/s serial link (the Xilinx Virtex-4 FPGA's incorporate transceivers capable of speeds up to 10Gbit/s).

Item Description	Est. Cost
Trigger Tile Boards: **(assumes 12 boards + 3 spares)**	**$510k**
Cost Breakdown per board:	
Board Manufacture	$3k
Assembly	$2k
Interface, Monitoring and Control Logic (Ethernet interface)	$5k
Xilinx Virtex-4 FPGA's (four per board @ $5K per FPGA)	$20k
Fiber Transceivers	$4k
Total Cost Per-Board:	$34k
Combined Trigger Processor: **(assumes 1+1 spare)**	**$25k**
Engineering Design:	**$60K**
Production Board Design	$20k
Systems Integration Support	$20k
Backplane Design	$10K
Combined Trigger Processor FPGA Design	$10K
Crates, Power Supplies and Controllers	**$25k**
Estimated Total System Cost:	**$620k**

Table 15 - Cost estimate breakdown for the FVTX LL1 trigger. The estimate is based on the conceptual design as outlined in the proposal and assumes that the prototype board design is completed as part of the Northern Microdesign Phase-II STTR. The Combined Trigger Processor is assumed to be a GenLL1 Rev2 board, as used in the Muon RPC trigger, so the costs shown are for materials and additional programming.

A breakdown of the estimated cost of a full FVTX LL1 system, consisting of 12 FVTX LL1 trigger boards with two spares and all required infrastructure, is shown in Table 15. This cost estimate assumes the use of Xilinx Virtex-4 FPGA's based on current prices; however, we emphasize that no final technology choice has been made. We also assume that we will be able to use the existing design of the GenLL1 Rev2 boards to implement the Combined Trigger Processor, so that new hardware for this purpose does not need to be developed. The costs listed in Table 1 are based on price quotations for the FPGA's as well as our previous experience in designing trigger hardware.

The cost estimate presented in Table 15 should be viewed as setting that expected scale of the cost of the Level-1 trigger project. Additional refinement will be possible once continued development has refined trigger algorithms that can achieve the required rejections.

Note that the cost listed in Table 15 is not included in the baseline FVTX budget. It is assumed that once the FVTX project is approved we will pursue additional independent funding for this FVTX trigger. We also view the triggering problem as an issue to spans multiple forward PHENIX subsystems that should be addressed in a global way.

8 Appendix C – Estimates for Rates and Triggers for the PHENIX FVTX

8.1 Cross sections, branching ratios and acceptances:

8.1.1 D → mu X

We take the PHENIX result from hep-ex-/0508034,

$$\sigma_{c\bar{c}} = 920 \pm 150 \pm 540 \mu b$$

which gives a single-charm cross section of 1840 μb.

We get the branching ratio to a muon from the PDB and use the average of the charged and neutral D branching ratios (since the number of charged and neutral D's is about equal),

$D^+ \to l + X$ is 17.2%.
$D^0 \to \mu + X$ is 6.6%,

and use 11.9%

For the acceptance we use a Pythia simulation which gives 2.32% (after taking out the branching ratio) for muons with theta 10-35 degrees and a total momentum greater than 2.5 GeV. An additional factor of 0.84 is included on top of the Pythia acceptance to account for octant boundary gaps, etc.

3826/1000000 muons pass the 10-35 degree and p>2.5 GeV cuts, so,
Acc = 3826/1000000/11.9%*84% = 2.32%

Pythia version 6.205 is used with CTEQ5L, M_{charm} = 1.25 GeV and K=1.

To estimate the p_T dependence of the yields we use the p_T shape of the spectra from the above simulations, given as follows as fractional yield in each bin:

All	$0<p_T<1$	$1<p_T<2$	$2<p_T<3$	$3<p_T<4$	$4<p_T<5$
1.00	0.68	0.31	0.012	0.00073	0.000147

8.1.2 B → mu X

We take the $b\bar{b}$ cross section from Ramona Vogt's FONNL calculations as shown in her RHIC-II workshop talk (April 2005),

$$\sigma_{b\bar{b}} = 2\mu b$$

(Her calculations, see below, varied between 1.25 and 2.7 μb for different parameters)

Bottom Cross Sections

m (GeV)	μ_F/m	μ_R/m	σ(all y) (μb)	$\sigma(\lvert y\rvert \le 0.75)$ (μb)	$\sigma(1.2 \le \lvert y\rvert \le 2.2)$ (μb)
$\sqrt{s} = 200$ GeV					
4.5	1	1	2.38	1.100	0.320
4.75	1	1	1.82	0.846	0.242
5	1	1	1.40	0.661	0.185
4.75	0.5	0.5	2.72	1.253	0.365
4.75	0.5	1	1.87	0.864	0.249
4.75	1	0.5	2.67	1.236	0.357
4.75	2	2	1.25	0.589	0.166
4.75	2	1	1.74	0.814	0.231
4.75	1	2	1.33	0.621	0.176
$\sqrt{s} = 500$ GeV					
4.5	1	1	12.26	4.69	1.81
4.75	1	1	9.77	3.78	1.44
5	1	1	7.87	3.08	1.16
4.75	0.5	0.5	13.51	5.19	1.99
4.75	0.5	1	8.98	3.47	1.38
4.75	1	0.5	14.29	5.50	2.11
4.75	2	2	7.40	2.88	1.09
4.75	2	1	10.09	3.91	1.49
4.75	1	2	7.16	2.78	1.05

Table 4: Bottom cross sections obtained from the parameter sets used to determined the theoretical uncertainty band in pp collisions at $\sqrt{s} = 200$ and 500 GeV with the CTEQ6M densities.

Figure 104 - Cross section calculations for bottom with FONNL for various parameters from Ramona Vogt.

Which gives a single-bottom cross section of 4 μb.

For the branching ratio we take 10.87% from the PDB for an admixture of B^+/B^0.

For the acceptance we use 14.5% from a Pythia simulation that requires the muon be within theta 10-35 degrees and with a total momentum above 2.5 GeV. An additional factor of 0.84 is included on top of the Pythia acceptance to account for octant boundary gaps, etc.

1880/100000 muons pass the 10-35 degree and p>2.5 GeV cuts
Acc = 1880/100000/10.87%*84% = 14.5%

All	$0<p_T<1$	$1<p_T<2$	$2<p_T<3$	$3<p_T<4$	$4<pT<5$	$5<p_T<6$
1.00	0.131	0.572	0.234	0.0496	0.0103	0.00258

8.1.3 B → J/ψ X

We use the 4 μb cross section for B given above.

For the combined branching ratio we use 1.094% (B → J/ψX) and 5.9% (J/ψ → μμ) which gives 0.065%

For the acceptance we use 4.6% from a Pythia simulation that requires both muons to lie within theta 10-35 degrees and have a total momentum above 2.5 GeV. An additional factor of 0.70 for a pair is included on top of the Pythia acceptance to account for octant boundary gaps, etc.

(42/1000000)/(1.094%*5.9%)*0.7 = 4.6%

A Z_{vtx}>1 mm vertex cut is made with an efficiency for B → J/ψX of 39%.

8.2 Luminosities

We use the RHIC-II luminosities from T. Roser as given at,

http://www.phenix.bnl.gov/phenix/WWW/publish/leitch/rhicii-forward/RHIC_II_Luminosity_Roser.xls

Table 16 - Luminosity estimates for RHIC-II from Thomas Roser.

W. Fischer, T. Roser, I. Ben-Zvi, A. Fedotov, BNL
C-AD, 16-Mar-2005

Classical proton radius [m]	1.53E-18

Maximum Luminosity Estimates for RHIC II

Beams	unit	p	p	unit	Si	Cu	d	p	Au	unit	Au
Charge number Z	…	1	1	…	14	29	1	1	79	…	79
Mass number A	…	1	1	…	28	63	2	1	197	…	197
Relativistic γ	…	108	271	…	108	108	107	108	107	…	107
Revolution frequency	kHz	78.2	78.2	kHz	78.2	78.2	78.2	78	78.2	kHz	78.2
Normalised emittance, 95%, min	mm mrad	12	12	mm mrad	12	12	12	12	12	mm mrad	10
Ions/bunch, initial	10^9	200	200	10^9	10.7	5.2	150	200	1.0	10^9	1.0
Charges per bunch	10^9e	200	200	10^9e	150	150	150	200	80	10^9e	80
No of bunches	…	110	110	…	110	110	110	110	110	…	110
Average beam current/ring	mA	275	275	mA	206	206	206	275	110	mA	110
Luminosity at one IP	**unit**	**p-p**	**p-p**	**unit**	**Si-Si**	**Cu-Cu**	**d-Au**	**p-Au**	**Au+Au**	**unit**	**Au+Au**
Beam-beam parameter per IP	…	0.0123	0.0123	…	0.0046	0.0043	0.0024 0.0036	0.0048 0.0048		…	0.0024
β*	m	1.0	0.5	m	1.0	1.0	2.0	2.0		m	0.5
Peak luminosity	10^{30} $cm^{-2}s^{-1}$	150	750	10^{28} $cm^{-2}s^{-1}$	42	10	28	37		10^{26} $cm^{-2}s^{-1}$	90
Peak / average luminosity	…	1.5	1.5	…	1.3	1.3	1.5	1.5		…	1.3

Average store luminosity	10^{30} $cm^{-2}s^{-1}$	100	500	10^{28} $cm^{-2}s^{-1}$	32	8	19	25		10^{26} $cm^{-2}s^{-1}$	70
Time in store	%	55	55	%	55	55	55	55		%	60
Luminosity/week	pb^{-1}	33	166	nb^{-1}	108	25	62	83		nb^{-1}	2.5
Luminosity/week, achieved	pb^{-1}	0.9		nb^{-1}		2.4	4.5			nb^{-1}	0.16

and to get an estimate of RHIC-I luminosities we scaled these down according the ratios for average store luminosity given also by T. Roser in a RHIC-II talk,

pp: $1.5x10^{32} / 5x10^{32} = 0.3$
AuAu: $8x10^{26} / 70x10^{26} = 0.114$

For dAu we take the RHIC-I luminosity from the PHENIX Run6 BUP for dAu in Run7 of 2.8 nb^{-1}/wk.

These luminosities per week are:

Table 17 - Summary of luminosities used in these rate calculations for RHIC-II and RHIC-I (2008).

collision	RHIC-II	RHIC-I (2008)
Pp	33 pb^{-1}/wk	9.9 pb^{-1}/wk
dAu	62 nb^{-1}/wk	2.8 nb^{-1}/wk
AuAu	2.5 nb^{-1}/wk	0.327 nb^{-1}/wk

8.3 Reality factors

We use the following reality factors for pp:

- 55% for |Zvtx| < 10 cm
- 60% PHENIX duty factor
- 79% for the min-bias part of the pp trigger
- 90% trigger efficiency
- 90% reconstruction efficiency

For AuAu we use the same factors except:

- 90% for min-bias part of the AuAu trigger
- 70% reconstruction efficiency

8.4 Summary of Changes from Old Numbers

Changes from older estimates include:

- Explicit calculation of the B → μ X acceptance which is much larger than the D → μ X given the higher momentum muons from the B.
- Use FONNL calculations of the B cross section.
- Use the PHENIX measured D cross section.
- Update the branching ratios from the latest online Particle Data Book (PDB).
- Adding various efficiency and reality factors.
- Using the 'Roser luminosities
- Lowering the single-muon momentum threshold to 2.6 GeV from 2.5 GeV.

Table 18 - Comparison of new and old values for various parameters used in these rate calculations.

	D → μ X		B → μ X		B → J/ψ X → μ μ X	
	new	old	New	old	New	old
σ(pair)	920 μb	325 μb	2 μb	0.73 μb	2 μb	0.73 μb
BR	11.9%	9.6%	10.87%	10.49%	1.094% • 5.9%	1.2% • 5.9%
Acc(1-arm)	2.32%	4.7%	14.5%	2.08%	4.6%	2.83%
eff	84%	1	84%	1	70%	1
p_T> (Gev)	2.5	2.6	2.5	2.6	2.5	2.6
eff_{vtx}	1	n/c	1	n/c	39%	n/c

8.5 Rates

pp	Ccbar								
	(μb)	Acc	BR	Type	(pb-1)	Counts	Reality	Dzvtx	dzvtx
D→μ	920	0.0232	0.119	RHICII	33	3.4E08	7.1E07	1	7.1E07
	920	0.0232	0.119	2008	9.9	1.0E08	2.1E07	1	2.1E07
B→μ	2	0.145	0.1087	RHICII	33	4.2E06	8.8E05	1	8.8E05
	2	0.145	0.1087	2008	9.9	1.2E06	2.6E05	1	2.6E05
B→j/ψ	2	0.046	0.00065	RHICII	33	7.9E03	1.7E03	0.39	6.5E02
	2	0.046	0.00065	2008	9.9	2.4E03	5.0E02	0/39	2.0E02

Table 19 Estimated rates per week for p+p collisions

pp	**0<pT<1**	**1<pT<2**	**2<pT<3**	**3<pT<4**	**4<pT<5**	**6<pT<6**
D -> mu	4.8E+07	2.2E+07	8.5E+05	5.2E+04	1.0E+04	---
	1.4E+07	6.6E+06	2.5E+05	1.6E+04	3.1E+03	---
B -> mu	1.2E+05	5.0E+05	2.1E+05	4.4E+04	9.1E+03	2.3E+03

3.5E+04	1.5E+05	6.2E+04	1.3E+04	2.7E+03	6.8E+02	

Table 20 – p+p rates vs p_T for same estimates as in Table 19.

dAu	ccbar								
	Sigma	1-arm		Lumi	Lumi		with	eff	with
process	(ub)	Acc	BR	type	(nb-1)	counts	reality	dzvtx	dzvtx
D → μ	920	0.0232	0.119	RHIC-II	62	2.5E+08	6.0E+07	1	6.0E+07
	920	0.0232	0.119	2008	2.8	1.1E+07	2.7E+06	1	2.7E+06
B→ μ	2	0.145	0.1087	RHIC-II	62	3.1E+06	7.4E+05	1	7.4E+05
	2	0.145	0.1087	2008	2.8	1.4E+05	3.3E+04	1	3.3E+04
B → J/ψ	2	0.046	0.0007	RHIC-II	62	5.8E+03	1.4E+03	0.39	5.5E+02
	2	0.046	0.0007	2008	2.8	2.6E+02	6.3E+01	0.39	2.5E+01

Table 21 Estimated rates per week for d+Au collisions.

dAu	0<pT<1	1<pt<2	2<pt<3	3<pt<4	4<pt<5	5<pt<6
D → μ	4.1E07	1.9E07	7.2E05	4.4E04	8.8E03	
	1.8E06	8.4E05	3.2E04	2.0E03	4.0E02	
B→ μ	9.7E04	4.2E05	1.7E05	3.7E04	7.6E03	1.9E03
	4.4E03	1.9E04	7.8E03	1.7E03	3.4E02	8.6E01

Table 22 d+Au rates vs p_T for same estimates as inTable 21.

AuAu									
	Sigma	1-arm		Lumi	Lumi		With	Eff	With
Process	(ub)	Acc	BR	Type	(nb-1)	Counts	Reality	Dzvtx	Dzvtx
D → μ	920	0.0232	0.119	RHICII	2.5	9.9E08	1.8E08	1	1.8E08
	920	0.0232	0.119	2008	0.327	1.3E08	2.4E07	1	2.4E07
B→ μ	2	0.145	0.1087	RHICII	2.5	1.2E07	2.3E06	1	2.3E06
	2	0.145	0.1087	2008	0.327	1.6E06	3.0E05	1	3.0E05
B → J/ψ	2	0.046	0.00065	RHICII	2.5	2.3E04	4.3E03	0.39	1.7E03
	2	0.046	0.00065	2008	0.327	3.0E03	5.7E02	0.39	2.2E02

Table 23 Estimated rates per week for Au+Au collisions.

AuAu	0<pT<1	1<pT<2	2<pT<3	3<pT<4	4<pT<5	6<pT<6
D → μ	2.2E+07	1.0E+07	3.9E+05	2.4E+04	4.8E+03	
	1.6E+07	7.5E+06	2.9E+05	1.8E+04	3.5E+03	

B → μ	3.0E+05	1.3E+06	5.4E+05	1.1E+05	2.4E+04	5.9E+03
	3.9E+04	1.7E+05	7.0E+04	1.5E+04	3.1E+03	7.7E+02

Table 24 Au+Au rates vs p_T for same estimates as in Table 23.

8.6 Rates for Prompt Vector Mesons: J/ψ, ψ' and ϒ

Although the rates for the prompt vector mesons, J/ψ, ψ' and ϒ, have been estimated elsewhere (e.g. in Tony Frawley's RHIC-II studies[xlviii]); we give estimates here that are consistent with the single heavy-quark rates estimates above. The following inputs are used and the rates for one RHIC-II week are shown in Table 25.

- For the cross sections we use the recently published J/ψ cross section of 2.61 μb from PHENIX[xxxiii]. For the ψ' we use the cross section ratio of 14% to the J/ψ from Ref. [xlix]; and for the ϒ we use the preliminary estimate from PHENIX at QM05 of 2.1 nb.
- We take the Branching ratios from the particle data book as 5.9% (J/ψ), 0.76% (ψ') and 2.1% (ϒ); where the latter is an average over the three Upsilon states as calculated in PHENIX Analysis Note AN401.
- For the acceptance we use values from recent PHENIX analysis: 1.08% (J/ψ) and 1.19% (ϒ). And we assume the ψ' acceptance is the same as that for the J/ψ.

Table 25 - Counts for prompt vector mesons per week into both muon arms at RHIC-II luminosity.

Signal	Luminosity/week	J/ψ → μμ	ψ' → μμ	ϒ → μμ
Au+Au	2.5 nb^{-1}	60k	1.1k	200
d+Au	62 nb^{-1}	20k	360	65
p+p	33 nb^{-1}	23k	420	77

Although not shown in the table, the rates for ϒ's at y=0 from detecting their decay into one muon in each of the two muon arms is approximately equal to the rate into one muon arm shown in Table 25.

8.7 Trigger considerations

8.7.1 Rejection factors

For pp triggers we use Lajoie's estimate from run5 data and simulations oof 478 (1-deep), 23500 (1-deep & 1-shallow) and 133500 (2-deep). An independent check of these numbers was done by looking at the run5 pp triggers for several runs (179809, 170190, 174696, 177185) where one sees about a factor of 500 rejection for 1-deep muons (south arm) and 10^4 rejection for 1d1s dimuons (south arm).

For AuAu we use simulations of the level-1 run on 2004 AuAu raw data files (since the level-1 hardware was not working fully during that run yet). Lajoie gets rejection factors of 5 for 1-deep

and 1-deep * 1-shallow triggers and 15.7 for 2-deep triggers.

As shown in Table 26, we will then use the averages over the two arms, with the North arm generally being somewhat worse than the South due to its coverage at smaller angles with its smaller piston.

Table 26 - Level-1 muon trigger rejection factors for pp and AuAu based on previous data and simulations of the level -1 triggers.

Species	Arm	Source	Trigger	Reject. factor
pp	N	Run5	1-deep	580
		"	1-deep & 1-shallow	28700
		"	2-deep	20000
	S	"	1-deep	376
		"	1-deep & 1-shallow	18300
		"	2-deep	67000
	N&S avg	"	1-deep	478
		"	1-deep & 1-shallow	23500
		"	2-deep	133500
AuAu	N	Sim on run4 prdf	1-deep	5.1
		"	1-deep & 1-shallow	5.3
		"	2-deep	15.3
	S	"	1-deep	4.8
		"	1-deep & 1-shallow	5.3
		"	2-deep	16.1
	N&S avg	"	1-deep	5
		"	1-deep & 1-shallow	5
		"	2-deep	15.7

8.7.2 Trigger Rates and Needed Rejection Factors

For these estimates we will use a 2-deep (2d) dimuon trigger in AuAu and a 1-deep & 1-shallow (1d1s) trigger in pp.

We use the luminosities quoted above in the discussion of FVTX rates. To calculate the peak luminosity from the average, we will follow Tony's example again and use a factor of 4.48 from the average instantaneous luminosity.

Min-bias rates are calculated from luminosities using the full inelastic cross sections for pp and AuAu of 42 mb and 6847 mb respectively. This assumes that the FVTX itself can provide a min-bias trigger that is very close to 100% of the inelastic cross section. In any case this is an upper limit on the min-bias trigger rate.

We use event sizes of 180 kb and 250 kb for pp and AuAu respectively. These sizes will need to be updated as the additional contributions from the various PHENIX upgrades become clear.

Additional trigger rejections needed from the FVTX (or from combination with other upgrades such as the muon RPC trigger upgrade) will be calculated assuming a 60 Mb/s limit for each muon trigger, which corresponds to 10% of an assumed DAQ limit of 600 Mb/s. I.e. if one uses ½ of the 600 Mb/s for min-bias, and the remaining 300 Mb/s is split between 5 types of triggers, then that leaves 60 Mb/s per trigger (sum over the two arms).

Table 27 – Estimated trigger rates and addition rejection factors needed for p+p and Au+Au collisions in PHENIX.

					MB	evt	1d		1d	1d1s		1d1s
		L/wk	Zvtx	*L* pk	pk rate	size	pk rate	1d	presc.	pk	1d1s	presc.
	era	(pb-1)	<10cm	10^32	Mhz	(kb)	(khz)	Mb/s	needed	(hz)	Mb/s	needed
pp	RHICII	33	0.55	1.34	5.65	180	23.63	4253	71	481	87	1.4
	2008	9.9	0.55	0.40	1.69	180	7.09	1267	21	144	26	0.4
					MB	evt	1d		1d	2d		2d
		L/wk	Zvtx	*L* pk	pk rate	size	pk rate	1d	Presc.	pk rate	2d	presc.
	era	(nb-1)	<10cm	10^26	khz	(kb)	(khz)	Mb/s	needed	(hz)	Mb/s	needed
AuAu	RHICII	2.5	0.55	101.85	69.74	250	27.9	6974	116	8884	2221	37
2008	0.327	0.55	13.32	9.12	250	3.65	912	15	1162	291	4.8	

9 Appendix D – Synergy with other PHENIX Upgrades

Although the FVTX detector adds a lot of important physics, as has been discussed at length in the body of the proposal, it also can work together with many of the ongoing or other proposed upgrades to strengthen or add physics capability beyond what any subsystem of PHENIX brings by itself. Here we will discuss briefly some of these strengthened or added capabilities. Since integration with the muon tracker and muon identifier has already been extensively discussed, we will not repeat that discussion here.

9.1 Central Barrel Vertex Detector (VTX) Upgrade

The most obvious coupling of the upgrades is with the VTX detector, which provides similar vertexing capability in the central rapidity region to what this FVTX detector provides. When used together they can provide a very accurate primary vertex which can then be used by both detectors as a origination point for determining detached vertices for the various processes already discussed in this proposal. As shown in Section 3.3, the FVTX can do this quite well by itself even in p+p collisions and can do it at the level-1 trigger level for fast triggers; but the VTX can improve this further. Unfortunately the VTX does not give a fast output and cannot contribute at the fast trigger level.

Together the two detectors, as has been discussed in the body of this proposal, give a quite large range in rapidity, -2.2 to +2.2. However at the boundary between them, some tracks will give hits in both detectors. This should help with internal alignment between the two vertex detectors and will also help make a smooth picture of the physics across the boundary between the VTX and FVTX parts of the vertex detector.

9.2 Muon Trigger Upgrade

The Muon Trigger Upgrade is a NSF funded upgrade with the main goal being to allow selective triggering on very high momentum (> 10 GeV) muons from W decays for measurements of the flavor dependence of spin structure functions. Three Resistive Plate Cathode strip (RPC) detector planes will be added to each muon arm with one in just in front of station-1, one in between station-3 and the front of the muon identifier, and a third plane behind the muon identifier. The RPC's will have 1^0 segmentation in ϕ (the bend direction in the muon magnet's field) and up to 24 segments in the radial direction.

http://www.npl.uiuc.edu/phenix/publish/nsf/muon-mri.pdf

The coarse momentum resolution of the MuTrig can provide a momentum measurement (fast enough to be used for a level-1 trigger) that would help to:

- Allow momentum dependence vertex cuts in the FVTX or prescaling of lower momentum ranges.

- Help eliminate any tracks that do not point to the primary vertex and do not satisfy time-of-flight cuts for tracks originating from the primary vertex.
- Allow track matching at the fast trigger level between roads through the MuTrig RPC's and the muon identifier with the FVTX tracks.
- Help eliminate soft pion tracks in the FVTX that do not match tracks above.
- And also provide a space (x-y) point to help the muon tracker pattern recognition in high occupancy events (central Au+Au collisions) that will reduce incorrect tracks in the muon tracker. This will also benefit the FVTX by providing cleaner muon tracks to match with.

9.3 Nose Cone Calorimeter (NCC) Upgrade

The NCC upgrade would turn the present copper nosecone absorbers, that lie in front of the muon magnets and behind where the FVTX would go, into an active Silicon-tungsten electromagnetic and partial hadronic calorimeter for detecting various particles including photons and neutral pions. This would extend much of the capability of the PHENIX central arms calorimeters into the forward and backward regions now covered only for muons. Highlights of the physics this upgrade could add include direct photons, extending the study of pion suppression to these rapidities and measurements of the χ_C by its decay into a photon and a photon. The proposal for this upgrade, along with out FVTX proposal, is now being prepared for submission to DOE for funding, although contributions from RIKEN may also help fund the total $7M cost of two NCC endcaps.

https://www.phenix.bnl.gov/WWW/publish/seto/NCC/ncccdr.pdf

A number of physics issues could be addressed with the combination of the NCC and the FVTX, these include:

- Identification of hadron jets in the NCC to help reduce backgrounds for single muons from punch-through hadrons that penetrate deep into the muon identifier and otherwise look like muons. Although the FVTX in combination with the muon tracker can eliminate many of these, the possibility of reducing punch-throughs further could be quite valuable. A detailed study of shower probabilities and characteristics in the 1.5 lamba NCC needs to be made in order to make a quantified estimate of the level to which the NCC can help here.
- Can aid in the study of associated particle production with hard processes such as J/ψ production, especially by adding detection capability for neutral particles such as π^0's and photons. These associated particles, may help understand the production mechanism for J/ψ and could also give information on the interaction with co-moving light quarks in heavy ion collisions.
- The combination of the FVTX and NCC in the forward and backward rapidity regions would allow detection of charm and bottom decays via their decay to electrons with the electron identification coming from the NCC and the detached vertex from the FVTX. This would give a second measurement of these heavy quarks, in addition to that with single muons; and might even allow extending these measurements to lower momentum with the electrons compared to the ~2.5 GeV momentum threshold for detection via detached vertices with muons.

- The additional measurements in the NCC might also help in overall definition of the muon track in combination with the FVTX mini-strip hits, muon tracker cathode-strip hits, muon identifier hits and MuTrig RPC hits. (if one NCC plane has smaller pixels, it would help most – need to check NCC proposal about this) It may also be able to help identify kinks in tracks that result from decay-in-flight of hadrons to muons, and thereby reduce the contributions of these decays-in-flight to the final single muon spectra.
- This matching between FVTX and NCC might also help with low energy tracks in the forward direction, by looking for consistency between the multiple scattering of the track in the FVTX and the energy observed for the matching track in the NCC.
- Electrons and muons, both with detached vertices, could be combined into $D\overline{D} \rightarrow \mu e$ pairs which would provide a additional wayto study the di-lepton continuum under and near the J/ψ peak. Identification of these lepton pairs would also help in isolating the Drell-Yan di-leptons which are otherwise over-whelmed by copious random pairs from heavy quark decays. This could include back-to-back μe pairs where an electron is seen in one endcap and a muon in the other.
- The FVTX can act as a charged particle veto for the NCC, to help solidify the identification of neutral particles, e.g. photons and π^0's.

9.4 Muon Piston Calorimeter (MPC)

The Muon Piston Calorimeter (MPC) is a small electromagnetic calorimeter composed of an array of $PbWO^4$ crystals (240/arm) with photo-diode readout that is installed inside the muon magnet piston of each muon arm, and adds detection jets in the 3 to 4 rapidity range, providing measurements of jets, pions and eta's for the study of spin asymmetries in the very forward region in p+p collisions and to search for effects of shadowing or the color glass condensate in that region in d+A collisions. Like the NCC, it may be useful in sampling particles near those in the FVTX, e.g. in terms of associated particle production for instance. But it has no tracking, only calorimetry – so would likely not be useful in Au+Au collisions.

---

[i] M.C. Abreu et al., "Observation of a threshold effect in the anomalous J/y suppression", Physics Letters B 450 (1999) 456-466

[ii] HERMES collaboration, Phys. Rev.Lett. 94, 012002 (2005)

[iii] COMPASS collaboration, Phys. Rev. Lett. 94, 202002(2005)

[iv] http://spin.riken.bnl.gov/rsc/write-up/dy_final.pdf

[v] V. Guzey, M. Strikman, W. Vogelsang, Phys. Lett. B, 603, 173 (2004).

[vi] S. S. Adler, et al, "Nuclear Modification Factors for Hadrons at Forward and Backward Rapidities in Deuteron-Gold Collisions at sqrt(s_NN)=200 GeV," Phys. Rev. Lett. 94 (2005) 82302.

[vii] http://p25ext.lanl.gov/phenix/fvtx/

[viii] X-N Wang, M. Gyulassy, Phys. Rev. Lett. **68**, 1480 (1992).

[ix] M. Gyulassy, P. Levai, I. Vitev, Phys. Rev. Lett. **85**, 5535 (2000).

[x] I. Vitev, Phys. Lett. B **562**, 36 (2003).

[xi] PHENIX Collaboration, Nucl. Phys. A 757, 184 (2005).

[xii] A. Adare *et al*. (PHENIX Collaboration), "Energy Loss and Flow of Heavy Quarks in Au+Au Collisions at $\sqrt{s_{NN}}$ = 200 GeV", nucl-ex/0611018 and submitted to Phys. Rev. Lett.

[xiii] Yuri L. Dokshitzer, D.E. Kharzeev Phys. Lett.**B519**:199-206,2001

[xiv] M. Djordjevic, M. Gyulassy nucl-th/0305062
[xv] M. Djordjevic, M. Gyulassy, Phys. Lett. **B560**, 37 (2003)
[xvi] B. H. Zhang, E. Wang, X-N. Wang, nucl-th/0309040
[xvii] A. Adil, I. Vitev, hep-ph/0611109.
[xviii] E. Shuryak Phys. Rep **61**, 71 (1980)
[xix] P. Levai *et al*, Phys. Rev C **51**, 3326 (1995)
[xx] Z. Lin and M. Gyulassy, Phys. Rev. C **51**, 2177 (1995)
[xxi] R. Vogt, FONLL NLO calculation of charm cross section vs rapidity, RHIC-II presentation - http://rhicii-science.bnl.gov/heavy/doc/April05Meeting/ramona-nlo.pdf
[xxii] A. Adare *et al*. (PHENIX collaboration), "J/ψ Production vs Centrality, Transverse Momentum and Rapidity in Au+Au collisions at $\sqrt{s_{NN}}$ = 200 GeV", nucl-ex/0611010 and submitted to Phys. Rev. Lett.
[xxiii] M. Arnedo, Phys. Rep. **240**, 301 (1994), K.J. Eskola et al., hep-ph/9906484.
[xxiv] L. McLerran and R. Venugopalan, Phys. Rev. D **49**, 2233 (1994); A.H. Mueller and J.W. Qui, Nucl. Phys. B **268** 427 (1986) and L.V. Bribox, E.M. Levin and M.G. Ryskin, Phys. Rept. **100**, 1 (1983).
[xxv] J.-W. Qui, I. Vitev, Phys. Lett. B632, 507 (2006).
[xxvi] B. Kopeliovich *et al*.,, Phys. Rev. C72, 054606 (2005) & hep-ph-/0501260 (2005).
[xxvii] K.J. Eskola, V.J. Kolhinen, R. Vogt, Nucl. Phys. **A696**, 729 (2001) & hep-ph/0104124.
[xxviii] L. Frankfurt, M. Strikman, Eur. Phys. J **A5**, 293 (99)
[xxix] B.Z. Kopeliovich, A.V. Tarasov, J. Huefner, Nucl. Phys. **A696**, 669 (2001) or hep-ph/0104256.
[xxx] I. Vitev, T. Goldman, M. Johnson and J. Qiu, Acta. Phys. Hung. **A27**, 275 (2006).
[xxxi] Talk given by Xiaorong Wang at Hawaii Division of Nuclear Physics meeting, September 18 2005.
[xxxii] T. Goldman, M.B. Johnson, I. Vitev, J.W. Qui, to be published.
[xxxiii] S. Adcox *et al.* (PHENIX collaboration), Phys. Rev. Lett. **96**, 012304 (2006) & nucl-ex/0507032.
[xxxiv] R. Vogt, Phys. Rev. C **61**, 035203 (2000).
[xxxv] M.J. Leitch et al., (E866/NuSea), Phys. Rev. Lett. **84**, 3256 (2000).
[xxxvi] J. Badier *et al.*, (NA3), Z. Phys. **C20**, 101 (1983).
[xxxvii] I. Arsene *et al*., Phys. Rev. Lett. **93**, 242303 (2004).
[xxxviii] T. Gehrmann and W. J. Stirling, Z. Phys. C65, 461 (1995).
[xxxix] C. Aidala *et al*., Research Plan for Spin Physics at RHIC.
[xl] G.L. Kane, J. Pumplin, and W. Repko, Phys. Rev. Lett. **41** (1978) 1689.
[xli] D.W. Sivers, Phys. Rev. D41 (1990) 83; Phys. Rev. D**43** (1991) 261.
[xlii] J.C. Collins, S.F. Heppelmann, G.A. Ladinsky, Nucl. Phys. **B420** (1994) 565.
[xliiixliii] S.J. Brodsky, D.S. Hwang and I. Schmidt, Phys. Lett. **B530** (2002) 99.
[xliv] M. Burkardt, Phys. Rev. D**69** (2004) 091501.
[xlv] M. Anselmino et al., Phys. Rev. D**70** (074025) 2004.
[xlvi] E. Norrbin, T. Sjostrand, Eur. Phys. J. C **17**, 137 (2000)
[xlvii] G.C. Nayak, J. Smith, Phys. Rev. D **73**, 014007 (2006) or hep-ph/0509335.
[xlviii] http://www.phenix.bnl.gov/WWW/publish/abhay/panic05/frawley.pdf
[xlix] R. Gavai, *et al.*, Int. J. Mod. Phys. A**10**, 3043 (1995) & hep-ph/9502270.